



# Single Molecule Studies of $F_1$ -ATPase and the Application of External Torque

Thomas Bilyard

Balliol College, Oxford

The Life Sciences Interface Doctoral Training Centre  
and  
The Physics Department

The University of Oxford

Hilary 2009

A thesis submitted for the degree of  
Doctor of Philosophy

# Single Molecule Studies of F<sub>1</sub>-ATPase and the Application of External Torque

Thomas Bilyard  
Balliol College, Oxford

A thesis submitted for the degree of  
Doctor of Philosophy  
at the University of Oxford, Hilary 2009

## Abstract

F<sub>1</sub>-ATPase, the sector of ATP synthase where the synthesis of cellular ATP occurs, is a rotary molecular motor in its own right. Driven by ATP hydrolysis, direct observation of the rotation of the central axis within single molecules of F<sub>1</sub> is possible. Operating at close to 100% efficiency, F<sub>1</sub> from thermophilic *Bacillus* has been shown to produce ~40pN-nm of torque during rotation.

This thesis details the groundwork required for the direct measurement of the torque produced by F<sub>1</sub> using a rotary angle clamp, an optical trapping system specifically designed for application to rotary molecular motors. Proof-of-concept experiments will be presented thereby demonstrating the ability to directly manipulate single F<sub>1</sub> molecules from *Escherichia coli* and yeast mitochondria (*Saccharomyces cerevisiae*), along with activation of F<sub>1</sub> out of its inhibited state by the application of external torque.

Despite in-depth knowledge of the rotary mechanism of F<sub>1</sub> from thermophilic *Bacillus*, the rotation of F<sub>1</sub> from *Escherichia coli* is relatively poorly understood. A detailed mechanical characterization of *E.coli* F<sub>1</sub> will be presented here, with particular attention to the ground states within the catalytic cycle, notably the ATP-binding state, the catalytic state and the inhibited state. The fundamental mechanism of *E.coli* F<sub>1</sub> appears to depart little from that of F<sub>1</sub> from thermophilic *Bacillus*, although, at room temperature, chemical processes occur faster within the *E.coli* enzyme, in line with considerations regarding the physiological conditions of the different species. Also presented here is the verification of the rotary nature of yeast mitochondrial F<sub>1</sub>. The torque produced by F<sub>1</sub> from thermophilic *Bacillus*, *E.coli* and yeast mitochondria is the same, within experimental error, despite their diverse evolutionary and environmental origins.

---

## Acknowledgements

The DPhil experience is one of ups and downs. This one has been no different. The first few years were a struggle against unexplainable no-results, operator error and frustration. Occasionally popping their head out of this general malaise, dotted sparingly, were joyous and encouraging results. Almost by definition, results in an experimental project come in the final year, whether that be your second or your seventh. As it was for me, January to March 2008 were joyous months and full of much relief!

Throughout it all, I have been fortunate to have shared my time with a fantastic group, full of wonderful people and some truly great friends. Conducting this merry band of assorted scientists is my supervisor Richard Berry, someone who can always be relied upon to have one hundred and one ideas for the next thing to try and to whom I express my earnest gratitude.

Next in line is Teuta, who initially (maybe reluctantly) took on the maternal/matriachal role until I found my feet and, from thereon, provided me with numerous humourous moments, some deliberate, some not. Teuta is one of the most honest people I know and her blunt assessment of results or ideas has been refreshing.

A good postdoc is worth their weight in gold and the group has been lucky to have had two of the best in the business in Lo and Yoshi. Their recent departures have been felt massively already but thankfully I got to pick their brains with such regularity that I'm sure they won't miss me in their new jobs! Yoshi, especially, has held his own in discussions about all things Japanese during our late nights in the office together.

The thought of spending one week alone in Biochemistry still keeps me awake at night and I am indebted to Wei Meng for making the long days of protein purification slightly less tedious. Wei is, perhaps, the most industrious people I have met as well as the most resilient. He also has worse OCD than me. Along with Wei and myself, the latest addition to the F<sub>1</sub> team, Bradley, has brought with him a new slant on maths and computing and has been a font of knowledge in a short space of time.

---

To all other members of the group during my time, past and present - Matt, Richard Branch, Bai Fan, James, Mark, Stu and Tania - thanks.

Outside of my group, but staying within physics, I should thank the DNA guys for still inviting me to the occasional social event despite my rejection of them for the Motors group all those years ago.

I have been very fortunate to have been able to develop a close collaboration with members of Masamitsu Futai's group in Iwate, Japan. In particular, Mayumi Nakanishi-Matsui has always been receptive to my full-range of ideas and Hiroyuki Hosokawa has fielded many emails regarding trivial questions about biochemistry.

Closer to home, I wish to thank my sponsors - the EPSRC and the LSI DTC - especially Dave Gavaghan and Maureen York. I also want to thank Balliol for their support over the last two years, although free food, gluttony and a sedentary thesis-writing lifestyle is not a good combination!

I have been entertained during my time in Oxford by a varied selection of friends both in and outside of the university. I won't list them here because I know that more than one will take offence if they're not listed first. I will, however, single out Tim (a.k.a. The Rat) for putting a roof over my head for the past eight months.

On a personal level Anne has been with me throughout my graduate life and we have experienced the roller-coaster of each other's DPhils. Anne has been continually supportive and her own incredible work ethic has slowly begun to rub off on me. Despite running away to Japan to avoid the horror of living with me while I write-up, she has never been far away (how did people ever have relationships before Skype/broadband?) and always has the right thing to say when needed.

To my Mum and Sister, a big thank you, for everything, for leaving me be for the most part, but also for being there for me if I ever need you.

Finally, this thesis is dedicated to my Father, a humble and gentle man who would have been immensely proud that I've got this far. Despite the passing years, his love and support stay with me and my memories of him are just as strong as ever.

Tom Bilyard

March 2009

# Contents

|          |  |           |
|----------|--|-----------|
| <b>1</b> | <b>Introduction</b>  | <b>1</b>  |
| 1.1      | Molecular Motors   | 2         |
| 1.1.1    | Linear Motors  | 3         |
| 1.1.2    | Rotary Motors  | 6         |
| 1.1.3    | Synthetic Molecular Motors and Nanotechnology Devices                            | 14        |
| 1.2      | The Current Understanding of the Rotary Mechanism of F <sub>1</sub> -ATPase      | 15        |
| 1.2.1    | The Rotary Nature of F <sub>1</sub> -ATPase                                      | 17        |
| 1.2.2    | F <sub>1</sub> F <sub>o</sub> Experiments  | 21        |
| 1.2.3    | The Structure of F <sub>1</sub> -ATPase  | 22        |
| 1.2.4    | The Catalytic Cycle of ATP Hydrolysis by F <sub>1</sub> -ATPase                  | 29        |
| 1.3      | A Summary of Suitable Optical Techniques for the Study of F <sub>1</sub> -ATPase | 33        |
| 1.3.1    | Detecting Rotation by Back-Focal-Plane Interferometry                            | 34        |
| 1.3.2    | The Use of Optical Traps with Biological Samples                                 | 35        |
| 1.3.3    | Feedback Theories  | 36        |
| 1.4      | The Objectives and Layout of this Thesis   | 38        |
| <b>2</b> | <b>Techniques and Methods</b>  | <b>41</b> |
| 2.1      | A Definition of the Buffers Used   | 41        |
| 2.2      | Purification of F <sub>1</sub> derived from <i>E.coli</i>                        | 41        |
| 2.3      | Activity Measurements of <i>E.coli</i> F <sub>1</sub> -ATPase                    | 43        |
| 2.3.1    | Activity Measurement by Colourimetry   | 43        |
| 2.3.2    | Activity Measurement by a Coupled Reaction with NADH                             | 44        |
| 2.4      | Preparation of Biomolecule-Compatible Surfaces                                   | 46        |
| 2.5      | Preparation of Biotinylated Bead-Duplexes  | 47        |
| 2.5.1    | Biotinylation of Polystyrene Beads   | 49        |
| 2.5.2    | Purification of Bead-Duplexes  | 49        |
| 2.6      | Rotation Assays  | 50        |
| 2.7      | Detection of Rotation and Optical Trapping                                       | 51        |
| 2.8      | Data Analysis  | 54        |
| 2.8.1    | Obtaining AVI files from DVD Files   | 54        |
| 2.8.2    | Analysing AVI Files  | 55        |
| 2.8.3    | Obtaining Angle Data from Position Data  | 57        |
| <b>3</b> | <b>F<sub>1</sub> Rotation Studies</b>  | <b>58</b> |
| 3.1      | The Philosophy of F <sub>1</sub> Rotation Analysis                               | 59        |
| 3.2      | Obtaining Compatible Surfaces and an Optimized Assay                             | 60        |
| 3.3      | Load-Dependence of EF <sub>1</sub>   | 63        |
| 3.3.1    | An Estimate of EF <sub>1</sub> Torque  | 71        |

---

|          |  |            |
|----------|--|------------|
| 3.3.2    | A Summary of EF <sub>1</sub> Load Dependence . . . . .                         | 77         |
| 3.4      | Enzymatic Kinetics of EF <sub>1</sub> Over a nM–mM [ATP] Range . . . . .       | 77         |
| 3.4.1    | Michaelis-Menten Fitting . . . . .   | 78         |
| 3.4.2    | A Summary of the [ATP] Dependence of EF <sub>1</sub> . . . . .                 | 81         |
| 3.5      | ATP-Binding Dwells in EF <sub>1</sub> Rotation . . . . .                       | 81         |
| 3.5.1    | Analysis of Dwell Times . . . . .  | 81         |
| 3.5.2    | Estimation of the ATP-Binding Rate, $k_{on}$ . . . . .                         | 86         |
| 3.5.3    | An Estimate of Torque from Step Alignment . . . . .                            | 87         |
| 3.5.4    | A Summary of the EF <sub>1</sub> ATP-Binding State . . . . .                   | 90         |
| 3.6      | High-Speed Experiments on EF <sub>1</sub> . . . . .                            | 91         |
| 3.6.1    | Calculating Dwell Times . . . . .  | 92         |
| 3.6.2    | Correlation Analysis . . . . .   | 94         |
| 3.6.3    | Analysis of Dwell Times . . . . .  | 98         |
| 3.6.4    | Using an ATP Analogue, ATP $\gamma$ S . . . . .                                | 102        |
| 3.6.5    | Attempts to Observe ATP-Binding and Catalytic<br>Dwells Concurrently . . . . . | 103        |
| 3.6.6    | An Alignment of EF <sub>1</sub> Catalytic Dwells . . . . .                     | 109        |
| 3.6.7    | A Summary of EF <sub>1</sub> Rotation Under Low-Load . . . . .                 | 111        |
| 3.7      | The Inhibited State of EF <sub>1</sub> . . . . .                               | 112        |
| 3.7.1    | An Automated Method for Determining Pauses . . . . .                           | 114        |
| 3.7.2    | Load-Independent Pausing . . . . .   | 116        |
| 3.7.3    | The Distribution of Pause Lengths . . . . .                                    | 117        |
| 3.7.4    | Angular Position Relative to ATP-Waiting and Cat-<br>alytic States . . . . .   | 121        |
| 3.7.5    | Occasional Clicking Between States . . . . .                                   | 123        |
| 3.7.6    | A Summary of the Inhibited State of EF <sub>1</sub> . . . . .                  | 123        |
| 3.8      | Verification of the Rotary Nature of YF <sub>1</sub> . . . . .                 | 125        |
| <b>4</b> | <b>Applying External Torque with an Optical Trap</b>                           | <b>128</b> |
| 4.1      | The Optical Angle Clamp . . . . .  | 129        |
| 4.1.1    | Programmable Control of the DSP Board . . . . .                                | 131        |
| 4.1.2    | Shutter Control . . . . .  | 132        |
| 4.2      | Successful Stalling of F <sub>1</sub> with the Optical Angle Clamp . . . . .   | 135        |
| 4.2.1    | The Use of Feedback . . . . .  | 137        |
| 4.2.2    | Issues Encountered . . . . .   | 139        |
| 4.3      | Mechanical Activation . . . . .  | 142        |
| <b>5</b> | <b>Discussions and Conclusions</b>   | <b>145</b> |
| 5.1      | Future Work . . . . .  | 147        |
| 5.2      | Other Ideas . . . . .  | 149        |

|          |   |            |
|----------|---|------------|
| <b>A</b> | <b>Purification of <math>F_1</math>-ATPase from <i>Escherichia coli</i></b>       | <b>156</b> |
| A.1      | Buffers and Media Used . . . . .  | 156        |
| A.2      | Day 1 . . . . .   | 157        |
| A.3      | Day 2 . . . . .   | 157        |
| A.4      | Day 3 . . . . .   | 158        |
| A.5      | Day 4 . . . . .   | 159        |
| <b>B</b> | <b>A Guide to Nonlinear Curve Fitting</b>   | <b>160</b> |
| B.1      | Likelihood Estimator . . . . .  | 160        |
| B.2      | Minimization of $\chi^2$ . . . . .  | 162        |
| B.2.1    | Method of Steepest Descent . . . . .  | 162        |
| B.2.2    | Newton's Method . . . . .   | 163        |
| B.2.3    | Levenberg-Marquardt Method . . . . .  | 164        |
| B.2.4    | The Simplex Method . . . . .  | 165        |
| B.3      | Obtaining a Measure of the Goodness of Fit . . . . .                              | 166        |
| B.4      | Estimating the Errors on the Best-Fit Parameters . . . . .                        | 167        |
| B.5      | A Procedure for Fitting to Histogram Data . . . . .                               | 168        |
| <b>C</b> | <b>A Simulation of <math>F_1</math> Rotation</b>                                  | <b>170</b> |
| <b>D</b> | <b>An Estimate of the Catalytic Process Length from Step Alignment</b>            | <b>172</b> |
| <b>E</b> | <b>Applying the Switch-Time Algorithm to Rotation Data from <math>EF_1</math></b> | <b>175</b> |
| <b>F</b> | <b>Wiring Connection Panels for the Control of Hardware by the DSP Board</b>      | <b>178</b> |

# 1

## Introduction

*“... What she saw made her head spin. At first it looked like a motorcycle gang. Then she thought it was a herd of wheeled animals. But that was impossible. No animal could have wheels. She wasn't seeing it. But she was ... somehow they had evolved, on their fore and rear single legs, a wheel. But wheels did not exist in nature, her mind insisted; they couldn't; you needed an axle with a bearing that was completely separate from the rotating part, it couldn't happen, it was impossible...”*

**Mary's encounter with the Mulefa,  
taken from Philip Pullman's 'The Amber Spyglass' [1].**

Despite countless iterations of evolution and natural selection, the world to which we are accustomed to today does not appear to favour rotation. Birds do not fly using a propellor. Fish do not swim with a screw. Indeed, it is only through works of fiction that we find animals that can skate about on wheels. However, at the microscopic, sub-cellular level, it turns out that fact is actually as strange as fiction, as two distinct types of rotary molecular motor are now known to exist.

Recent advances in bioinformatics, genetics and protein structural knowledge, along with the merging of traditional scientific areas, have lead to an elementary understanding as to the role of molecular motors and how they

function. Nanotechnology is an exciting area of engineering, exerting an important influence on the direction of academic research. For tomorrow's machines to be based upon natural motors, first we require a complete understanding of the underlying mechanisms of the proteins involved. This drive for understanding and explanation, in itself, makes the study of single-molecule biophysics fascinating.

In this thesis, I present an investigation into one of the known rotary motors,  $F_1$ -ATPase - a  $\sim 10\text{nm}$ , highly-efficient enzyme - applying dry physical techniques to the very wet subject of proteins. I will attempt to carefully straddle the two traditional disciplines of Physics and Biochemistry, taking care to realise that both areas are essential to work of this type. I will summarize the work carried out in Section 1.4 but first, in Sections 1.1–1.3, I will outline our motivations for the study with respect to the academic field.

## 1.1 Molecular Motors

---

A motor is a device that creates motion from an energy source. Molecular motors are complexes that couple potential energy to mechanical work within the cellular environment. Naturally-occurring molecular motors are proteins, ranging from  $10\text{nm}$  up to  $50\text{nm}$  in size. On these length scales, molecular motors operate at energies only slightly higher than the thermal bath [2]. Indeed, thermal fluctuations are an essential part of the mechanism of molecular motors. Unlike macroscopic motors, which can be assumed to be completely deterministic in nature, molecular motors are stochastic and subject to large, random fluctuations. It would appear that molecular motors are the cell's solution to the randomness at the molecular level and their way of producing directional and choreographed processes.

The world experienced by a protein motor is not always intuitive, since they exist in the low Reynolds number regime [3], where inertial effects are negligible and where there is a strong influence by Brownian motion. Mech-

anisms must be described by probability distributions and averages, rather than equations of Newtonian physics for individual motors, to account for these thermal effects. It is true that molecular motors are governed by potential energy landscapes. However, unlike their macro-scale counterparts, their trajectory towards the point of lowest energy is simply a random walk, biased by the underlying potential.

Molecular motors require an energy source, provided by either the hydrolysis of adenosine triphosphate (ATP) or from the flow of ions down the electrochemical gradient. The thermal bath has characteristic energies of  $\sim k_B T$ , giving a natural energy unit on these scales, where  $k_B$  and  $T$  are the Boltzmann constant and the absolute temperature respectively. By way of comparison, the free energy available through ATP hydrolysis ( $\text{ATP} \rightarrow \text{ADP} + \text{P}_i$ ) is  $\sim 20k_B T$  under typical physiological conditions, and an ion crossing the membrane may gain  $\sim 6k_B T$  [4].

An essential element of a molecular motor is the coupling of potential energy to the motion of the motor, or part of the motor, relative to a track. Evolutionary pressure has dictated that there are two geometries within which this can be achieved - either by using a linear or rotary track. We will now discuss each of these in turn.

### 1.1.1 Linear Motors

At the sub-cellular level, the world is teeming with vesicles and other cargoes being carried along the cellular highways, tracks of actin or microtubules, by the cell's transporters, myosin, kinesin and dynein. These three classes of molecular motors contain a huge number of variants, each with a specific cellular function. A brief description of each motor is presented here. It should be noted that DNA/RNA polymerases and helicases could also be broadly classified as linear motors, albeit precessing about a helical track, but will not be discussed here for purposes of brevity.

## Myosin

Myosin is a superfamily of motors that bind to actin filaments, powered by ATP hydrolysis. Myosin contains a motor domain of  $\sim 80$ kDa [5], known as the heavy chain, that binds actin and hydrolyzes ATP. The heavy chain is linked to a light chain, which acts as a lever arm. The lever arm amplifies small changes at the point of ATP hydrolysis into large movements of the light chain [6]. Within the superfamily, at least 18 subfamilies are known [7], grouped by the different phylogeny of the well-conserved motor domain. Myosin motors can be processive and unidirectional, with the subfamily defining whether the motor moves towards the plus-end or minus-end of the actin filament. Since the arrangement of actin filaments within a cell is generally with the plus-ends towards the cell periphery, this distinction suggests different cargoes are carried by each type of myosin. Using a double optical trap technique, the stall force of myosin V has been measured to be 2–3pN [8].

## Kinesin

Kinesin is a superfamily of related molecular motors that move along microtubules, using the hydrolysis of ATP to do mechanical work. First purified in 1985 from squid giant axons [9], there are many variants known, with  $\sim 45$  found to be encoded in the human genome alone [10]. The kinesin superfamily can be subdivided into 14 subfamilies (known as Kinesin 1–14), with each subfamily sharing common attributes such as structure and function. Kinesins fulfil many roles within the cell, including the transportation of diverse cargoes and microtubule spindle organization. One subfamily (Kinesin 13) is responsible for the rapid depolymerization of microtubules, a process required during cell mitosis [11]. Generally kinesin consists of an N-terminal head group and a C-terminal cargo-carrying domain. The head group is a highly-conserved domain consisting of  $\sim 350$

amino acids [10], with the ability to bind tubulin and hydrolyze ATP. The C-terminus cargo-carrying domain differs across kinesin classes, implicative of the different cellular functions achieved by each subfamily. Depending upon the subfamily, kinesin can exist as either monomers, dimers, trimers or tetramers. ‘Conventional kinesin’, the kinesin first discovered, is a rod-like structure consisting of two head groups connected by a short neck region, a stalk and the cargo-carrying domain. The majority of the double-headed kinesins (dimers), including conventional kinesin, move towards the fast-growing plus-end of the microtubule in a step-wise manner. The walking mechanism of kinesin has been shown to be hand-over-hand (as opposed to shuffling along with one hand always in front of the other) with each hand making steps of  $\sim 17\text{nm}$  [12]. This means that the kinesin dimer is actually making steps of  $\sim 8.5\text{nm}$ , consistent with the hydrolysis of one ATP molecule per step [13, 14]. The force required to stall the progress of kinesin has been measured by optical techniques to be  $\sim 8\text{pN}$  [15].

## Dynein

Dynein is a family of motors that use ATP hydrolysis to power the translocation of cargo to the minus-end of a microtubule. Dyneins are large proteins, constructed from one to three heavy chains (each  $\sim 520\text{kDa}$ ) that contain the ATPase active site and the microtubule binding site [7]. Dyneins can be classified into two types: axenomal dynein found in cilia and flagella, and cytoplasmic dynein involved in the organization of the mitotic spindle and chromosome separation alongside many other roles [16]. Despite their different locations and specialities, axenomal dynein and cytoplasmic dynein share a number of structural similarities and stretches of conserved amino acid sequence. Whereas myosin and kinesin have a number of different forms in each cell, dynein is only found in one isoform per cell, with different functionality achieved with the assistance of accessory proteins.

Compared to myosin and kinesin, the mechanism of dynein motor activity is poorly understood, but dynein does seem to have a gearing mechanism since it is capable of producing small but powerful steps under high load [17]. The step size changes from a 24/32nm mixture under no load to 8nm upon 1pN opposing forces. Various mechanisms have been proposed (see [16]) and will not be discussed here.

### 1.1.2 Rotary Motors

Quite distinct from the linear molecular motors discussed up to this point, two classes of rotary molecular motors are known to exist: the bacterial flagellar motor and the V- and F-type ATPases. Both couple the flux of ions across the cell membrane to create rotational motion. Structurally, however, the two classes are diverse and it would appear that they are evolutionarily distant. It seems that nature not only invented the wheel, but may have done so more than once. Rotary motors share a common requirement - a need for a stator to provide a mechanism of creating torque, and a rotor on which the stator acts.

#### **The Bacterial Flagellar Motor**

In order to find nutrients, bacteria need to be able to sense their environment and to migrate towards the more favourable regions. The chemotactic pathway for sensing external chemicals is well-studied (for a review, see [18]) and will only be touched upon here. Bacteria live in a low Reynolds number world. A swimming cell will be randomly oriented within  $\sim 3$ s due to Brownian motion [19]. Within this time-frame, bacteria must be able to sense their surroundings and respond accordingly. It has been shown that bacteria have a short-term memory of  $\sim 3$ s for sensing chemotactic signals [20]. If a bacterium senses that it is moving towards more advantageous conditions it will want to carry on in that direction. If, however, the conditions are

becoming more unfavourable, the bacteria will need to change direction.

Most bacteria swim by means of flagella,  $\sim 10\mu\text{m}$  long and  $\sim 20\text{nm}$  wide helical filaments that protrude outwards from the cell body. Propulsion can be achieved by rotation of the base of the flagellum by the bacterial flagellar motor, a rotary motor powered by the transmembrane ion gradient. Bacteria have multiple flagella ( $\sim 5$ ) which bundle together in a constructive manner to allow the bacterium to swim. If one of the flagellar motors changes direction, the bundle falls apart. When this happens, the cell undergoes a ‘tumble’ and its direction is randomly re-oriented [21]. This is the method that bacteria use to respond to external stimuli. If ‘good’ signals are received, the chance of one of the motors changing direction reduces. If a ‘bad’ signal is received, the probability of a switch is increased. The result is that the bacterium explores by way of a random walk, biased towards beneficial regions.

The overall structure of the bacterial flagellar motor has been obtained by electron microscopy and the structure is summarized in Figure 1.1. The flagellar motor is a huge protein complex ( $\sim 11\text{MDa}$ ) with  $\sim 13$  different component proteins. The MotA/MotB stator units are anchored to the cell membrane due to interactions with the peptidoglycan layer. A ring of  $\sim 26$  FliG proteins [22] acts as the rotor, sitting on top of the 35-fold symmetric C-ring [23]. Protruding from the cell is a flexible hook, which acts as a universal joint, connected to the helical flagellar filament. The MotA/MotB stator units are ion channels and are in constant dynamic turnover [24, 25]. This mechanism might allow the replacement of damaged stator units or for the cell to respond to environmental conditions by regulating motility.

The rotary nature of the bacterial flagellar motor was first observed in 1973 by attaching a flagellar filament to a coverslip and watching the rotation of the large cell body [27] in a so-called tethered cell assay. Since then bacteria from many species have been studied, with the most work

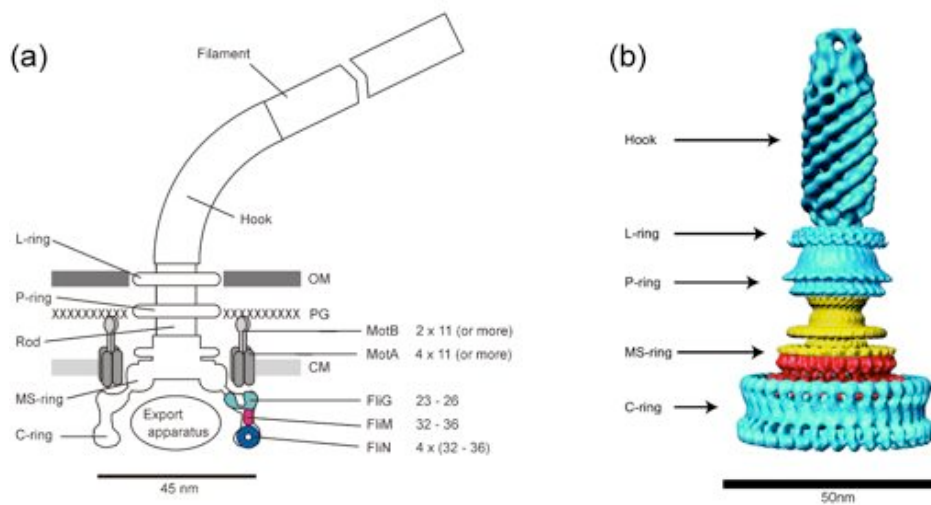


**Figure 1.1:** The structure of the  $H^+$ -driven bacterial flagellar motor. (a) A cartoon of the flagellar motor in the cell membrane, adapted from [4]. Four MotA and two MotB proteins are thought to form the embedded stator units. FliG, FliM and FliN form the rotor, though they are composed from rings of different periodicities. OM, PG and CM stand for outer membrane, peptidoglycan cell wall, and cytoplasmic membrane respectively. (b) A 3D electron micrograph representation of the isolated rotor from *S. typhimurium* shows the periodicities of the various ring structures, adapted from [26] with permission.

done on the flagellar motor from *E.coli*. Current methods for investigation of the bacterial flagellar motor no longer rely on tethered cell methods but, instead, the cell body is stuck to a coverslip and a small (200-1000nm) polystyrene bead attached to a truncated filament. The rotation of the bead is then observed by back-focal-plane interferometry (to be discussed in Section 1.3.1). The bacterial flagellar motor is a powerful rotary molecular motor, and the bacterial flagellar motor from *Vibrio alginolyticus* has been shown to create torques of up to 4000pN·nm [28] and to rotate at 1700Hz at 37°C [29].

The bacterial flagellar motor is powered by the flux of ions through the cytoplasmic membrane [4]. The free energy available from a single ion crossing is defined as the ionic charge multiplied by the Ion Motive Force (IMF), which is given by

$$\text{IMF} = V_m + \frac{k_B T}{q} \ln \frac{C_i}{C_o} \quad (1.1)$$

where  $V_m$  is the membrane voltage due to the distribution of charges,  $q$  the charge of each ion,  $k_B$  the Boltzmann constant,  $T$  the absolute temperature, and  $C_i$  and  $C_o$  the concentrations of the ions inside and outside the cell respectively. Typically, the IMF is around  $-150\text{mV}$  [4], meaning that the energy gained from a proton crossing the membrane is  $\sim 6k_B T$ , 6 times the energy of the thermal bath. The two terms in Equation 1.1, the contribution from the membrane potential and the contribution from the chemical potential, have been shown to contribute equivalently for a flagellar motor operating under high load, however, under low load, the chemical potential contribution is greater [30, 31].

Recent low-load experiments using cells expressing only one stator and with a low IMF have shown step-wise rotation with  $\sim 26$  steps per revolution [32]. This stepping frequency is consistent with the periodicity of the FliG ring, the track on which rotational torque is believed to be generated.

Analysing the torque produced by single-stator cells, an estimate of  $\sim 38$  ions per revolution has been given [24], consistent with the periodicity of the C-ring, leaving open questions regarding the symmetry mismatch and the number of ions required per step.

### ATP Synthase

ATP synthase is the  $\sim 530$ kDa enzyme responsible for the rapid regeneration of ATP within cells. Using the flow of ions (typically  $H^+$ ) down the electrochemical gradient, ATP synthase synthesizes ATP from ADP and inorganic phosphate,  $P_i$ . The method by which potential energy is coupled to the production of ATP within the enzyme has slowly been elucidated, initially from a high-resolution crystal structure [33] and then by single-molecule techniques [34] to confirm that rotation of part of the enzyme ensemble was required for ATP synthesis.

$F_1F_o$  is essentially ubiquitous in the cellular membrane of bacteria, the thylakoid membrane of chloroplasts and the inner membrane of mitochondria. This thesis is chiefly concerned with  $F_1F_o$  derived from *E.coli*, the simplest form known with only eight different subunits, with stoichiometry  $\alpha_3\beta_3\gamma\delta\epsilon c_{10}ab_2$ . In contrast, the vast majority of structural determination has been achieved using mitochondrial  $F_1F_o$ , in particular bovine  $F_1F_o$ , a more complex assembly. However, there is considerable shared subunit homology between the two sources and, in general, the enzyme appears to be well-conserved across all species. The *E.coli* complex appears to be the basic structure upon which some species have added further subunits. The addition of subunits may be a regulatory requirement [35], however, the role of many of the subunits is still unclear. Unless otherwise stated, we shall employ the subunit nomenclature of the *E.coli* enzyme from hereon. A cartoon of the *E.coli* and bovine mitochondrial structures is shown in Figure 1.2a. Flux of ions through the *a*-subunit forces rotation of the *c*-ring, a

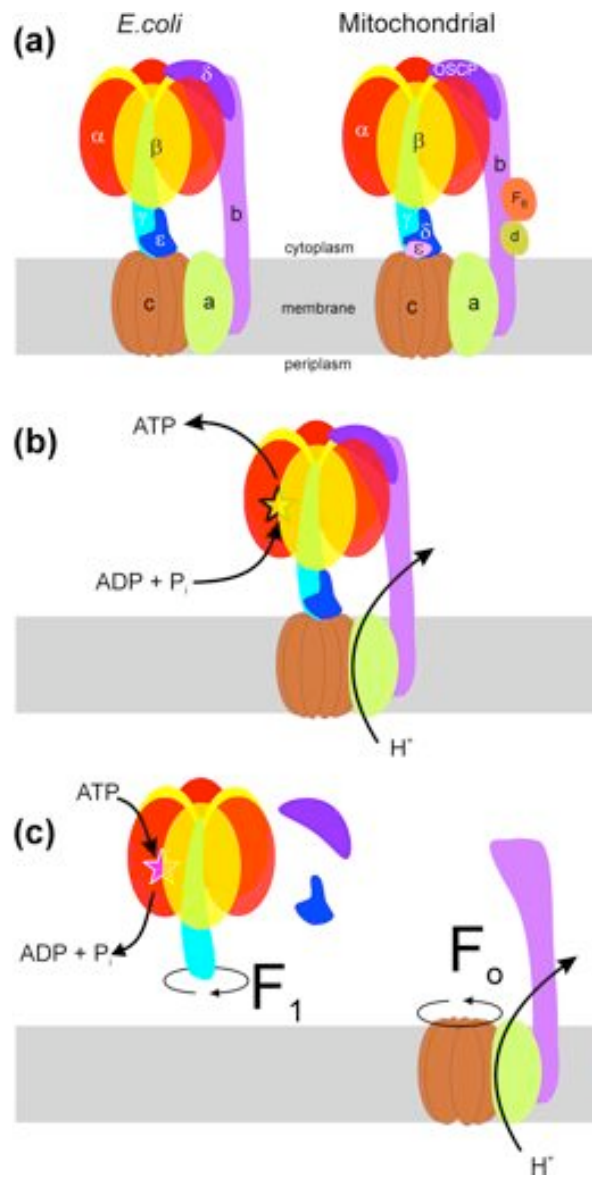


**Figure 1.2:** (a) A subunit comparison of ATP synthase from *E. coli* and bovine mitochondrial cells. The mitochondrial complex has a number of additional subunits compared to the *E. coli* ensemble. (b) The flux of ions (in most species, protons) down the electrochemical gradient through an ion channel in the  $a$ -subunit is coupled to synthesis of ATP from ADP and  $P_i$  in a remote part of the enzyme. The hypothesis for this coupling is for the internal rotation of the  $c_{10-15}\epsilon\gamma$  rotor relative to the  $ab_2\delta\alpha_3\beta_3$  stator. (c) When the enzyme is placed into a low ionic strength medium, the enzyme splits into two distinct components, a membrane embedded  $F_0$  sector and the soluble  $F_1$  portion. In their own right,  $F_1$  and  $F_0$  are thought to be rotary motors.  $F_0$  is powered by the electrochemical gradient as in the complete  $F_1F_0$  ensemble. In solution,  $F_1$  is uncoupled from the electrochemical energy source. Instead,  $F_1$  uses ATP hydrolysis to generate the reverse rotation compared to the ATP synthesizing  $F_1F_0$ .

barrel-type assembly formed from 10–15 identical  $c$ -subunits. The  $c$ -ring is tightly coupled to the  $\gamma$ -subunit, a central stalk that runs up and into a cylindrical headgroup formed from alternating  $\alpha$ - and  $\beta$ -subunits with stoichiometry  $\alpha_3\beta_3$ . The headgroup does not rotate with the  $\gamma$ -subunit because it is fixed by a peripheral stalk formed by two  $b$ -subunits. In *E.coli*  $F_1F_o$ , the  $\delta$ -subunit is part of the peripheral stalk and interacts with one of the  $\alpha$ -subunits [36, 37]. The *E.coli*  $\delta$ -subunit is a direct homolog of the mitochondrial OSCP<sup>1</sup> subunit. In turn, it is thought that the  $b_2$  stalk contacts  $\delta$ /OSCP, and not the  $\alpha$ -subunit, directly [38]. The  $\epsilon$ -subunit in *E.coli* attaches to the  $\gamma$ -subunit and is equivalent to the mitochondrial  $\delta$ -subunit. Additionally, the mitochondrial enzyme has extra subunits (of which only some are shown in Figure 1.2a) that have no equivalents in the *E.coli*  $F_1F_o$ . Using engineering terminology, the *E.coli*  $F_1F_o$  motor is composed of the  $ab_2\delta\alpha_3\beta_3$  stator and the  $c_{10-15}\epsilon\gamma$  rotor, however the exact definition of rotor and stator is interchangeable since neither part is fixed within the membrane.

Various parts of the  $F_1F_o$  ensemble are currently lacking high-resolution structural determination, importantly including the membrane-embedded sector and the peripheral stalk. The structure of the mitochondrial  $F_1F_o$  complex has been obtained by electron cryomicroscopy [39], as shown in Figure 1.3, at a resolution of 32Å. The blue section represents the parts of the ensemble where higher resolution structural information has been obtained by x-ray crystallography (the  $\alpha_3\beta_3\gamma\delta\epsilon$  complex), whereas the structure of the green portion is still undetermined at sufficient resolution.

The membrane-embedded  $c$ -ring is composed of 10–15 subunits depending on species: 10 in yeast mitochondrial [40], *E.coli* [41] and the thermophilic *Bacillus* PS3 [42]; 11 in *Ilyobacter tartaricus* [43], *Propionigenium modestum* [44] and *Clostridium paradoxum* [45]; 13 in *Methanopyrus kandleri* [46]; 14 in chloroplasts [47]; and 15 in alkaliphilic cyanobacteria [48].

---

<sup>1</sup>OSCP: Oligomycin sensitive conferral protein

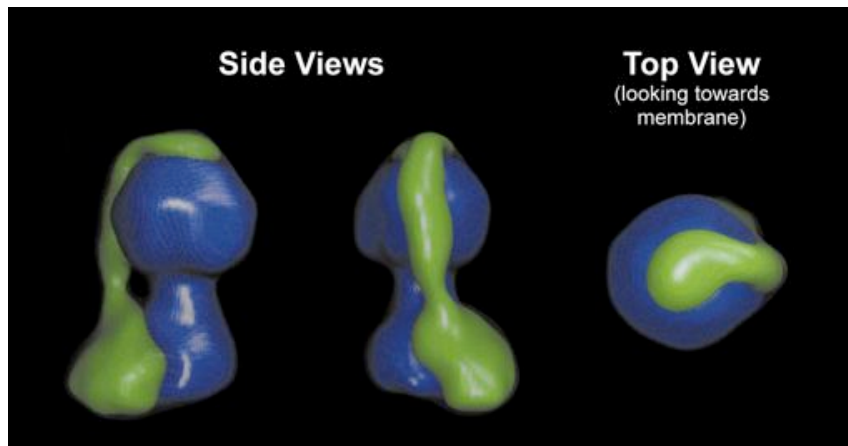


**Figure 1.3:** The structure of bovine mitochondrial  $F_1F_0$  obtained by electron cryomicroscopy at  $32\text{\AA}$  resolution, adapted from [39] with permission. The blue regions represent parts of the enzyme with high-resolution crystal structures available. The green regions still require high-resolution structural determination.

This variation in the number of  $c$ -subunits might be the result of species' adaptations to particular environmental and physiological conditions [49], although it would appear that a particular species cannot change its  $c$ -subunit composition in response to different growth conditions [47, 50]. The  $c$ -ring is tightly-connected to the  $\gamma$ - $\epsilon$  complex ( $\gamma$ - $\delta$  in mitochondrial  $F_1$ ) via polar loops in the  $c$ -subunits [51], a coupling that is reversible but sufficiently tight such that motion of the  $c$ -ring can be translated to motion in the  $\gamma$ -subunit.

When  $F_1F_0$  is placed into a low-ionic strength medium, the enzyme separates into two distinct parts, a membrane-embedded portion referred to as  $F_0$ , and a soluble  $F_1$  sector. The  $F_0$  portion,  $ab_2c_{10-15}$ , consists of the ion-channel and it is proposed that  $F_0$  can still use the electrochemical potential to rotate the  $c$ -ring. Purification of  $F_0$  requires the use of detergents to remove the lipids of the cell membrane. The solubilized  $F_1$  sector, with stoichiometry  $\alpha_3\beta_3\gamma\delta\epsilon$ , by contrast, is completely de-coupled from the electrochemical potential and therefore is unable to synthesize ATP independently. However,  $F_1$  uses the free energy available from ATP hydrolysis to drive the reverse rotation of the  $\gamma$ -subunit and is hence referred to as  $F_1$ -

ATPase. In this manner, purified  $F_1$  can be used in single molecule studies by isolating individual  $F_1$  motors and supplying the necessary ATP fuel.

This thesis is centred upon the rotary nature of *E.coli*  $F_1$ . A brief review of the current understanding of the  $F_1$  rotation field will be presented in Section 1.2, along with a discussion on the structure of  $F_1$  with regards to the mechanism of rotation.

### **V-ATPase**

The F-type ATP synthase we have just discussed, consisting of  $F_1F_o$ , is a subclass of the ATPase/ATP-synthase superfamily. Members of this superfamily perform the role of the exchange of energy between ATP-stored chemical energy and electrochemical potential energy. Aside from the F-type ATPases, another subclass in this superfamily is the Vacuolar-ATPases, or the  $V_1V_o$ -ATPases.  $V_1V_o$ -ATPase is a  $\sim 900$ kDa protein responsible for the acidification of various intracellular compartments [52]. Analogous to  $F_1F_o$ ,  $V_1V_o$ -ATPase consists of a membrane-embedded  $V_o$  sector responsible for proton translocation and a peripheral  $V_1$  portion that acts as an ATPase. There is shared homology between the nucleotide-binding subunits and the proton-pumping subunits of  $V_1V_o$ -ATPase and  $F_1F_o$ , indicating a common evolutionary ancestor. One striking structural difference between the V-type and F-type ATPases is the relatively large diameter of  $V_o$  compared to  $F_o$  [53]. The ATP hydrolysis-driven rotary nature of  $V_1V_o$ -ATPase has been shown by using similar methods to the  $F_1F_o$  rotation assays [54].

### **1.1.3 Synthetic Molecular Motors and Nanotechnology Devices**

The study of  $F_1$ -ATPase sits broadly within the field of bionanotechnology. Therefore, and for completeness, we should take a moment to discuss some nanotechnology devices that have been inspired by our knowledge of natural

molecular motors.

Unsurprisingly, the best examples are based upon the linear motors, with the aim of being able to replicate the cellular transportation function of linear motors to a synthetic environment. DNA has proven to be a formidable building-block on these length-scales. Tracks and motors can be carefully designed to maintain high specificity (for a review, see [55]). Obviously, synthetic motors require an energy source to achieve work and, to this end, DNA-based linear motors have employed the hydrolysis of the DNA backbone [56, 57], the hydrolysis of ATP by a restriction enzyme [58] and the free energy of DNA hybridization [59]. Unidirectional processivity has been achieved but at rates much slower than the natural linear motors.

Much less has been achieved in constructing synthetic rotary motors. An attempt to use F<sub>1</sub> in a nano-fabricated assembly has been demonstrated by attaching F<sub>1</sub> from thermophilic *Bacillus* to nano-engineered ~100nm-wide posts [60], although this is some way off from being truly synthetic.

We have reached the point at which our understanding of the natural motors and our ability to synthesize DNA oligonucleotides and proteins have become complementary. It is the dream of many to be able to design a functional protein at the computer and then create it in the lab. With our current knowledge it may now be possible to create a new linear or rotary motor from bottom-up techniques (H. Noji, private communication) but we are still some way off being able to improve upon the naturally-occurring motors.

## 1.2 The Current Understanding of the Rotary Mechanism of F<sub>1</sub>-ATPase

---

F<sub>1</sub>-ATPase has long been studied by traditional biochemistry techniques. In recent years, the advancement in novel single molecule techniques and

the determination of the enzyme's structure at atomic resolution have resulted in a rapid gain in understanding of the molecule's rotary mechanism. F<sub>1</sub> is a highly-conserved enzyme and is virtually ubiquitous across all living species. The most studied F<sub>1</sub> enzymes for single molecule or structural studies have been derived from bacterial sources or from eukaryotic mitochondrial cells respectively. The vast majority of recent single molecule rotation work has been using the thermophilic *Bacillus* PS3 strain, a bacterium found in Japanese thermal springs, operating optimally at 75°C [61], with comparatively few studies using the *E.coli* F<sub>1</sub> enzyme. In contrast, the seminal structural determination was achieved using F<sub>1</sub> derived from bovine heart mitochondria. More recently, the structure of yeast mitochondrial (*Saccharomyces cerevisiae*) F<sub>1</sub> has been resolved [62, 63]. In keeping with convention, and for purposes of brevity, from hereon, we will refer to F<sub>1</sub> derived from the thermophilic *Bacillus*, *E.coli*, bovine mitochondria and yeast mitochondria as TF<sub>1</sub>, EF<sub>1</sub>, MF<sub>1</sub>, and YF<sub>1</sub> respectively.

F<sub>1</sub> is a ~380kDa [64, 35] complex of three  $\alpha$ - and  $\beta$ -subunits, alternating to form a cylinder enclosing the central  $\gamma$ -subunit, a coiled-coil structure that acts as a central axis. The  $\alpha$ -,  $\beta$ -, and  $\gamma$ -subunits have molecular weights of 55kDa, 52kDa, and 30kDa respectively [65]. The  $\alpha_3\beta_3\gamma$  complex is the minimum stoichiometry required for ATPase function. The  $\alpha$ -,  $\beta$ - and  $\gamma$ -subunits have high homology across all species, as shown in Table 1.1, and it appears likely that the structure of F<sub>1</sub> remains highly conserved across all species. Indeed, even for the relative low homology of the  $\gamma$ -subunit in the MF<sub>1</sub> and EF<sub>1</sub> enzymes, the two  $\gamma$ -subunit structures have been found to be highly similar [66]. Various sections within the sequences of the  $\alpha$ -,  $\beta$ - and  $\gamma$ -subunits are extremely well-conserved, indicating not only the structural importance of these residues but also their functional significance.

The single molecule F<sub>1</sub> field was catalyzed by two breakthroughs: the 2.8Å resolution structure of MF<sub>1</sub> in 1994 [33], followed in 1997, by the first

| $\alpha$ -subunit     |                       |                       |                       |
|-----------------------|-----------------------|-----------------------|-----------------------|
|                       | <b>EF<sub>1</sub></b> | <b>TF<sub>1</sub></b> | <b>MF<sub>1</sub></b> |
| <b>TF<sub>1</sub></b> | 53                    | -                     | -                     |
| <b>MF<sub>1</sub></b> | 56                    | 58                    | -                     |
| <b>YF<sub>1</sub></b> | 53                    | 56                    | 70                    |

| $\beta$ -subunit      |                       |                       |                       |
|-----------------------|-----------------------|-----------------------|-----------------------|
|                       | <b>EF<sub>1</sub></b> | <b>TF<sub>1</sub></b> | <b>MF<sub>1</sub></b> |
| <b>TF<sub>1</sub></b> | 67                    | -                     | -                     |
| <b>MF<sub>1</sub></b> | 72                    | 69                    | -                     |
| <b>YF<sub>1</sub></b> | 68                    | 69                    | 77                    |

| $\gamma$ -subunit     |                       |                       |                       |
|-----------------------|-----------------------|-----------------------|-----------------------|
|                       | <b>EF<sub>1</sub></b> | <b>TF<sub>1</sub></b> | <b>MF<sub>1</sub></b> |
| <b>TF<sub>1</sub></b> | 37                    | -                     | -                     |
| <b>MF<sub>1</sub></b> | 25                    | 29                    | -                     |
| <b>YF<sub>1</sub></b> | 21                    | 25                    | 38                    |

**Table 1.1:** Homology relations, as given by pairwise alignment scores [67], for each of the  $\alpha$ -,  $\beta$ - and  $\gamma$ -subunits from *E.coli*, thermophilic *Bacillus*, bovine mitochondrial and yeast mitochondrial F<sub>1</sub>, calculated from sequence alignment using ClustalW 2.0.10 [68]. Sequences obtained from the National Centre for Biotechnology Information (NCBI) database (<http://www.ncbi.nlm.nih.gov/>).

direct evidence of the rotary nature of TF<sub>1</sub> [34]. The obtention of the crystal structure provided further evidence for the ‘Binding Change Mechanism’ proposed previously by Boyer [69], initiating a flurry of work aimed at proving the rotation of the central axis of F<sub>1</sub>.

### 1.2.1 The Rotary Nature of F<sub>1</sub>-ATPase

Direct evidence of the rotary nature of F<sub>1</sub> was obtained in 1997 [34], confirming various previous indirect methods [70, 71, 72]. Isolation of the TF<sub>1</sub> enzyme onto a coverslip and the attachment of a fluorescent actin filament to the central  $\gamma$ -subunit allowed observation of unidirectional rotation in the presence of ATP.

This technique has been employed by the vast majority of subsequent single molecule rotation assays. Due to the small size of F<sub>1</sub> and, in particular, the  $\gamma$ -subunit, it is not possible to directly visualize the rotation of the  $\gamma$ -

subunit by optical methods. As a result, the method employed is to attach a probe to the central axis and observe the rotation of the probe. In the initial experiments, fluorescently-tagged actin filaments ( $\sim 1\mu\text{m}$  in length) were used as the detection probe [34, 73] but various forms of probe have been used since, including single or double beads [74, 75], a metal bar [60], a single fluorophore [76] and a FRET pair [77, 78]. At 2mM ATP, the speed of rotation of the actin molecules ( $\sim 1\text{-}5\text{rps}^2$ ) was consistent with TF<sub>1</sub> producing  $\sim 40\text{pN}\cdot\text{nm}$  of torque during ATP hydrolysis. The TF<sub>1</sub> enzyme has been observed to behave according to Michaelis-Menten type kinetics [73, 74] as a function of substrate (ATP) concentration, with corresponding values of  $K_M$  and  $v_{\text{max}}$ .

At high concentrations of ATP (ie.  $[\text{ATP}] \gg K_M$ ), the speed,  $v_{\text{max}}$ , of TF<sub>1</sub> is independent of  $[\text{ATP}]$ . In this regime, binding of ATP is fast and the rate-limiting process is the rotation of the  $\gamma$ -subunit. With the actin filament, the rotation rate is severely limited by viscous drag.

At low  $[\text{ATP}]$ ,  $[\text{ATP}] \ll K_M$ , binding of ATP molecules into the catalytic sites is the rate-limiting step and the rate of rotation is proportional to  $[\text{ATP}]$ . In the nM– $\mu\text{M}$  ATP range, the rotation of TF<sub>1</sub> was resolved into discrete steps of  $120^\circ$  [73]. We shall define these  $120^\circ$  steps as ‘ATP-binding steps’ and the angle at which the enzyme dwells, waiting for an ATP molecule to bind, as the ‘ATP-binding angle’. The work done by the motor during one  $120^\circ$  step will be given by the motor torque ( $40\text{pN}\cdot\text{nm}$ ) multiplied by the angle covered ( $\frac{2\pi}{3}$  radians), and is equal to  $\sim 80\text{pN}\cdot\text{nm}$ . If each ATP-binding step is due to the binding and hydrolysis of one ATP molecule, we can compare the work done to the free energy available from ATP hydrolysis. The standard free energy change of ATP hydrolysis per molecule is  $\Delta G_0 = -50\text{pN}\cdot\text{nm}$ . The intracellular free energy available,  $\Delta G$ ,

---

<sup>2</sup>rps, revolutions per second. This has been the unit of rotation traditionally employed in F<sub>1</sub> literature, as compared to the use of Hz in the bacterial flagellar motor field. Both are, of course, interchangeable.

will be given by

$$\Delta G = \Delta G_0 + k_B T \ln \frac{[\text{ADP}][\text{P}_i]}{[\text{ATP}]} \quad (1.2)$$

with  $k_B T = 4.1 \text{pN}\cdot\text{nm}$  at  $23^\circ\text{C}$ . Typical physiological conditions are in the region of  $[\text{ATP}] = 1 \text{mM}$ ,  $[\text{P}_i] = 1 \text{mM}$  and  $[\text{ADP}] \approx 100 \mu\text{M}$  [79], giving  $\Delta G = -90 \text{pN}\cdot\text{nm}$ , implying a motor efficiency of close to 100%.

Replacing the  $\mu\text{m}$ -sized actin filaments with  $40 \text{nm}$  gold particles allowed the resolution of sub-steps within each  $120^\circ$  step due to the reduced viscous drag of the gold particles [74]. The viscous drag of the probe is no longer limiting and the TF<sub>1</sub> enzyme rotates at  $\sim 130 \text{rps}$  under these conditions. At an angle  $+80^\circ$  forward from the ATP-binding dwell [80], a very short dwell (on average  $\sim 2 \text{ms}$ ) was observed, corresponding to at least two  $\sim 1 \text{ms}$  events [74]. The dwells were independent of ATP concentration and, as such, were named the ‘catalytic dwells’ since the dwells must be due to internal chemical processes occurring within the enzyme. Individual catalytic steps have been overlaid to analyze the torque profile during a  $120^\circ$  step [74] and indicate that the torque produced might be constant with angle throughout the step. The method used to achieve this, however, would not be able to resolve torque variation over angles less than  $30^\circ$ , for example.

The rotation of TF<sub>1</sub> is unidirectional but not continuous, even on the timescales of seconds at saturating ATP concentrations. Occasionally and stochastically, TF<sub>1</sub> lapses into a long paused state ( $\sim 30 \text{s}$ ), shown to be due to MgADP-inhibition<sup>3</sup> [75]. This state is either due to the failure of TF<sub>1</sub> to release MgADP from the catalytic site or to the enzyme re-binding MgADP from solution<sup>4</sup>. MgADP-inhibition was shown to be a transient event, with

---

<sup>3</sup>It is expected that MgADP-inhibition is a feature of only the ATP-hydrolyzing F<sub>1</sub> enzyme and not the ATP-synthesizing F<sub>1</sub>F<sub>o</sub> complex. *In vivo*, MgADP-inhibition of uncoupled F<sub>1</sub> may be a method employed to avoid the unwanted hydrolysis of cellular ATP. Future single molecule assays of ATP-synthesizing F<sub>1</sub>F<sub>o</sub> should test this hypothesis.

<sup>4</sup>The likelihood of rebinding MgADP from solution is greatly diminished by the use of an ‘ATP-regenerating system’ in the reaction buffers. The regenerating system is an enzymatic coupled reaction that re-produces ATP from ADP and P<sub>i</sub> at the expense of the conversion of, for example, phospho(enol) pyruvate into pyruvate by pyruvate kinase.

active and inactive (inhibited) forms of TF<sub>1</sub> constantly interchanging, resulting in a steady-state rate of ATP hydrolysis in bulk assays. At 23°C, the result is that only ~30% of TF<sub>1</sub> molecules are active at any moment [81]. The position of the MgADP-inhibited long pauses was coincidental with the catalytic dwell position at +80°. The stability of this paused state was investigated by replacing the gold particle with a similarly sized magnetic bead. In this manner, MgADP-inhibited TF<sub>1</sub> was manipulated by external torque [82]. When the TF<sub>1</sub> molecule was rotated in the forwards direction, the probability of the activation of TF<sub>1</sub> from the paused state increased, indicating that the external manipulation was twisting the  $\gamma$ -subunit and lowering the binding affinity of the catalytic site to MgADP.

Using the same method, the reversibility of the TF<sub>1</sub> enzyme has been demonstrated. The F<sub>1</sub> sector, in solution, uses ATP hydrolysis to power the rotary motor. *In vivo*, coupled to the electrochemical gradient and to the F<sub>o</sub> sector, F<sub>1</sub> synthesizes ATP from ADP and P<sub>i</sub>. The ability of TF<sub>1</sub> to synthesize ATP was confirmed by externally rotating the  $\gamma$ -subunit in the *in vivo* direction in the presence of ADP and P<sub>i</sub> [83]. The produced ATP was detected by the luciferase-luciferin reaction [84]. In order to capture the produced ATP molecules, TF<sub>1</sub> was isolated within a manufactured femto-litre chamber [85]. When the external magnetic field was removed, the TF<sub>1</sub> molecules began to rotate back in the opposite direction by hydrolyzing the ATP molecules that had just been created. Despite the knowledge that the  $\alpha_3\beta_3\gamma$  complex is sufficient for ATP hydrolysis driven rotation, inclusion of the  $\epsilon$ -subunit was required to improve the efficiency of ATP synthesis from 10% to 70% [86].

The rotary nature of F<sub>1</sub> from sources other than the thermophilic *Bacillus* has been demonstrated. F<sub>1</sub> from *E. coli* (EF<sub>1</sub>) was shown to rotate by two independent studies [87, 88], using fluorescent actin as the rotation probe, along with chloroplast F<sub>1</sub> (obtained from spinach) in a similar manner [89],

showing that rotation is a characteristic of eukaryotic F<sub>1</sub> as well as prokaryotic. Furthermore, F<sub>1</sub> from thermophilic cyanobacteria, an enzyme with similar properties to chloroplast F<sub>1</sub>, has been observed to rotate and to be inhibited both by its  $\epsilon$ -subunit [90] and by tentoxin [91].

Recently, EF<sub>1</sub> has been investigated in the low-load regime, using 40-60nm gold beads, and has been shown to rotate at up to 450rps, on average. On the millisecond timescale, the rotation rate is stochastic [92]. Therefore, under the same laboratory conditions, the maximal rotation rate of TF<sub>1</sub> and EF<sub>1</sub> differs by almost four-fold. One possible explanation for this is the different *in vivo* conditions that the two species inhabit. At 23°C in the laboratory, EF<sub>1</sub> is only 14°C from its optimal operating temperature. The thermophilic *Bacillus* is found in 75°C hot springs. Even taking into account that the best growth condition for TF<sub>1</sub> is 65°C [93], TF<sub>1</sub> in the initial studies detailed above is more than 40°C sub-optimal. Increasing the temperature, increases the rate at which TF<sub>1</sub> can rotate [81]. Extrapolating to *in vivo* temperatures, rotation rates greater than 1000rps might be expected.

### 1.2.2 F<sub>1</sub>F<sub>o</sub> Experiments

F<sub>1</sub>F<sub>o</sub> consists of two back-to-back motors. When the electrochemical potential is sufficiently large, proton flow through the membrane results in the synthesis of ATP. We shall refer to this mode as ‘synthesis mode’. When the Proton Motive Force drops, the enzyme can use ATP hydrolysis to pump protons back across the membrane. This scenario shall be called ‘hydrolysis mode’.

It is postulated that F<sub>o</sub> is a rotary motor powered by ion flux. Direct visualization of this rotation has still not been achieved. However, evidence that the *c*-ring of F<sub>o</sub> rotates during ATP synthesis has been obtained using the variation in polarization of a single Cy3 fluorophore [94], and step-wise motion of the  $\alpha\beta$ -hexamer relative to the peripheral stalk has been shown

using FRET [95]. Reconstituted F<sub>1</sub>F<sub>o</sub> carrying FRET pairs into freely-diffusing lipid bilayers has revealed step-wise movements under conditions of ATP synthesis [95]. These movements most likely correspond to clockwise rotation of the stator units (i.e., in the reverse direction to hydrolysis mode rotation) but are not completely definitive.

However, obtaining a stable F<sub>1</sub>F<sub>o</sub> assay in synthesis mode, with directly observable probes attached, has proven to be difficult. Two main challenges arise. Firstly, F<sub>1</sub>F<sub>o</sub> is a membrane protein. Consequently, the single molecule F<sub>1</sub>F<sub>o</sub> assay would require F<sub>1</sub>F<sub>o</sub> to be successfully reconstituted into an artificial lipid bilayer, possibly on a surface. Secondly, F<sub>1</sub>F<sub>o</sub> requires control of the proton concentrations either side of the bilayer and therefore electrical contacts would be required. These issues, though not insurmountable, are sufficiently challenging to keep this ultimate goal out of reach as yet.

Coupling of F<sub>1</sub> to F<sub>o</sub> has been demonstrated through rotation studies of F<sub>1</sub>F<sub>o</sub> under hydrolysis mode. Without the requirement for a lipid bilayer, detergent-purified F<sub>1</sub>F<sub>o</sub> can be isolated onto a glass surface, akin to the F<sub>1</sub> assays, and ATP-dependent rotation can be observed [96,97,98,99,100,101]. The torque produced by F<sub>1</sub>F<sub>o</sub> in this manner has been estimated to be similar to that of TF<sub>1</sub> [99].

### 1.2.3 The Structure of F<sub>1</sub>-ATPase

The resolution of the atomic structure of MF<sub>1</sub> at 2.8Å was achieved in 1994 [33]. The protein crystals were prepared in the presence of AMP-PNP<sup>5</sup> and sodium azide<sup>6</sup>. From hereon, we will refer to this structure as the ‘Reference Structure’ in line with recent convention. Following on from this work, the structure of MF<sub>1</sub> has been determined in the presence of many different

---

<sup>5</sup>AMP-PNP, adenosine-5'-(β,γ-imino)-triphosphate, is a non-hydrolyzable ATP analogue, competitively inhibiting ATP-dependent enzyme systems.

<sup>6</sup>Sodium azide, NaN<sub>3</sub>, is a known F<sub>1</sub> inhibitor that stabilizes the MgADP-inhibited state [102].

inhibitors (aurovertin B [103], efrapeptin [104], NBD-CI<sup>7</sup> [105], AlF<sub>3</sub> [106], DCCD<sup>8</sup> [107], ADP.AlF<sub>4</sub><sup>-</sup> [108], IF<sub>1</sub><sup>9</sup> [109], and ADP.BeF<sub>3</sub><sup>-</sup> [110]) and the structures obtained are all similar, with the exception of the  $\gamma$ -subunit of the ADP.AlF<sub>4</sub><sup>-</sup> structure [108] which will be discussed later. Figure 1.4 shows one such atomic-level structure of MF<sub>1</sub> at 1.9Å resolution. The alternating  $\alpha_3\beta_3$  hexamer forms a flattened ball  $\sim 100\text{\AA}$  wide and  $\sim 80\text{\AA}$  high. Protruding  $\sim 44\text{\AA}$  from the hexamer is a  $114\text{\AA}$  coiled-coil asymmetric  $\gamma$ -subunit. There is no axis of rotational symmetry running through F<sub>1</sub>, not only due to the asymmetric  $\gamma$ -subunit, but also due to different conformations taken on by the  $\beta$ -subunits.

The  $\alpha$ - and  $\beta$ -subunits are 20% homologous [113], and include the P-loop nucleotide-binding motif [64]. The nucleotide-binding domains are found in the interfaces between the  $\alpha$ - and  $\beta$ -subunits – three non-catalytic domains mainly in the  $\alpha$ -subunits and three catalytic domains predominantly in the  $\beta$ -subunits. It has been suggested that ATP binding onto the non-catalytic sites on the  $\alpha$ -subunits is required for full ATPase activity [114]. In the Reference Structure, each of the  $\beta$ -subunits was in a unique conformational state, designated as  $\beta_{TP}$ ,  $\beta_{DP}$  and  $\beta_E$ , indicating AMP.PNP, ADP or no nucleotide being bound to the subunit respectively, as shown in Figure 1.4b. Figure 1.5 shows the conformation of the  $\beta$ -subunits under the conditions of crystallization. Both  $\beta_{TP}$  and  $\beta_{DP}$  are in the ‘closed’ conformation with the nucleotide tightly bound. However,  $\beta_E$  is in a state with the nucleotide-binding domain opened by  $\sim 30^\circ$  with respect to  $\beta_{TP}$  and  $\beta_{DP}$ . This observation suggests that there is a distinct ‘hinge’ region within the  $\beta$ -subunit and that conversion of the ‘open’ form into the ‘closed’ form (or vice versa) involves a bending of the hinge and the storage of energy in the form of elastic strain.

---

<sup>7</sup>NBD-CI, 4-chloro-7-nitrobenzofurazan

<sup>8</sup>DCCD, dicyclohexylcarbodiimide

<sup>9</sup>A natural inhibitory protein, IF<sub>1</sub>, prevents ATP hydrolysis by F<sub>1</sub> under cellular conditions of low PMF [109]

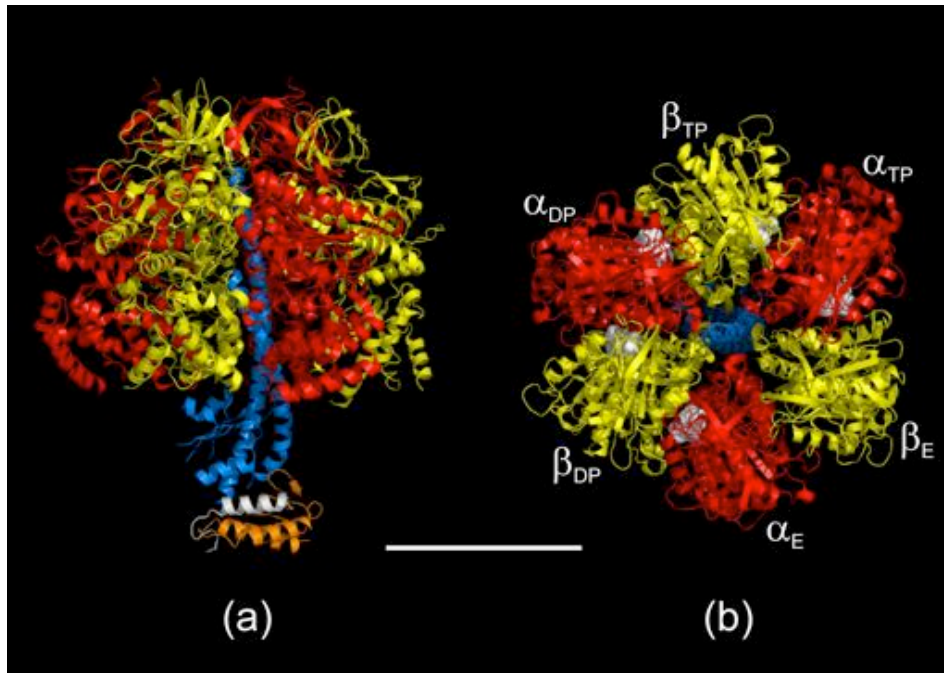


**Figure 1.4:** The structure of MF<sub>1</sub> at 1.9Å resolution, PDB file 2JDI [111]. The central scale bar represents 50Å. (a) MF<sub>1</sub> as viewed from the side. The  $\alpha$ -,  $\beta$ -,  $\gamma$ -,  $\delta$ - and  $\epsilon$ -subunits are shown in red, yellow, blue, orange and white respectively. It should be noted that the MF<sub>1</sub>  $\delta$ -subunit is analogous to the EF<sub>1</sub>  $\epsilon$ -subunit. (b) The minimal  $\alpha_3\beta_3\gamma$  complex of MF<sub>1</sub> as viewed from the N-terminal domains (from the top of (a)). Bound nucleotides are shown by white spheres. Three non-catalytic and three catalytic nucleotide-binding sites are found in the interfaces of the  $\alpha$ - and  $\beta$ -subunits, with the non-catalytic sites predominantly on the  $\alpha$ -subunits and the catalytic site correspondingly on the  $\beta$ -subunits. All three non-catalytic sites have bound nucleotide. The three  $\beta$ -subunits take on different conformations, named  $\beta_{TP}$ ,  $\beta_{DP}$ , and  $\beta_E$  with AMP.PNP, ADP or no nucleotide bound in the Reference Structure [33]. In this particular structure, grown in the absence of sodium azide, both  $\beta_{TP}$  and  $\beta_{DP}$  bind AMP.PNP. From this viewpoint, the  $\gamma$ -subunit would rotate in a clockwise direction under conditions of ATP hydrolysis. The crystal structure was visualized with PyMOL [112].

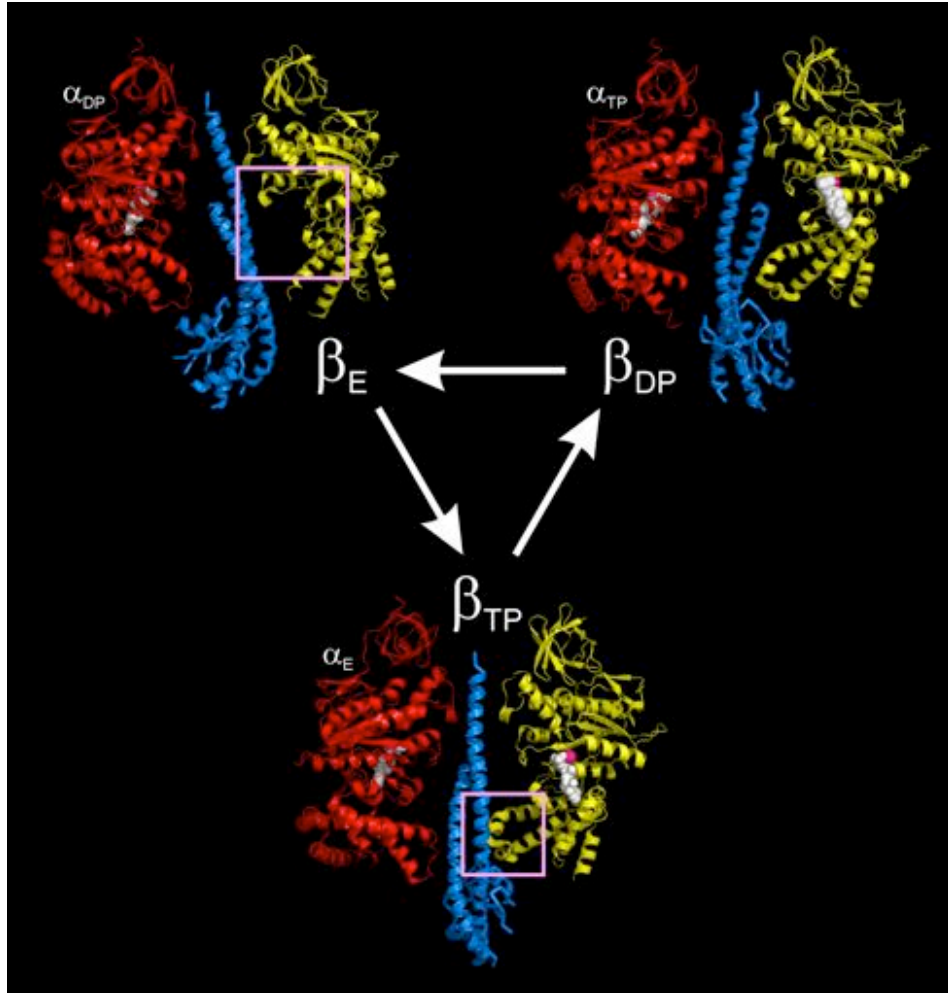


**Figure 1.5:** The crystal structure is consistent with cyclic conformational changes of the  $\beta$ -subunits - the Binding Change Mechanism. Three side views of MF<sub>1</sub> are shown. In each case one  $\beta$ -subunit is shown in yellow, along with the opposing  $\alpha$ -subunit in red and the  $\gamma$ -subunit in blue. Bound nucleotides are shown by white dots and bound  $\text{Mg}^{2+}$  ions by dark pink spheres.  $\beta_{TP}$  contacts the  $\gamma$ -subunit via the DELSEED region (indicated by the lower pink box). The binding site of  $\beta_E$  is opened by  $\sim 30^\circ$  with respect to the corresponding site in  $\beta_{TP}$  and  $\beta_{DP}$  (indicated by the upper pink box). Rotation of the asymmetric  $\gamma$ -subunit during ATP hydrolysis cycles each  $\beta$ -subunit through each of the three conformational states in the direction shown by the white arrows. Crystal structure visualized with PyMOL [112].

The  $\beta$ -subunits of different species have a number of highly-conserved regions, as shown in the sequence alignment shown in Figure 1.6. These sequences are presumably important structural features, and include the nucleotide-binding motif GXXXXGKT/S, the residues that make up the nucleotide-binding pocket and the so-called ‘DELSEED’ region. As can be seen in Figure 1.5,  $\beta_{TP}$  interacts with the  $\gamma$ -subunit via the DELSEED region. The DELSEED region was originally thought to be involved in torque generation but studies using ‘DELSEED mutants’ of TF<sub>1</sub><sup>10</sup> showed that this was not true [115]. Subsequent work suggested that this region is likely to be involved in the binding of the inhibitory  $\epsilon$ -subunit [116].

Crystal structures are invaluable for understanding the mechanism of protein function. Ideally, structures and single molecule data should be used collectively. At best, crystal structures represent a snapshot of the protein in a stable state undergoing normal function. At worst, due to the method of growing crystals, they may represent a stable state well off the catalytic cycle. The difficulty is understanding how to align the two forms of knowledge.

Of all the structures determined for MF<sub>1</sub>, only one deviates significantly from the Reference Structure, namely, the structure of MF<sub>1</sub> inhibited with ADP.AIF<sub>4</sub><sup>-</sup> [108]. This structure has ADP and sulphate bound to  $\beta_E$ , which is a ‘half-closed’ conformation, and the  $\gamma$ -subunit is rotated 20° in the synthesis direction with respect to the Reference Structure. This suggests that, with bound nucleotide at all three catalytic sites, the structure may represent a pre-product release state of the catalytic cycle. This one structure apart, the Reference Structure, and subsequent similar structures, probably represent one particular stable conformational state of the catalytic cycle. The Reference Structure was grown in the presence of sodium azide, ADP and AMP.PNP, as discussed previously. AMP.PNP and ADP were bound

---

<sup>10</sup>The corresponding sequence in TF<sub>1</sub> is actually DELSDED

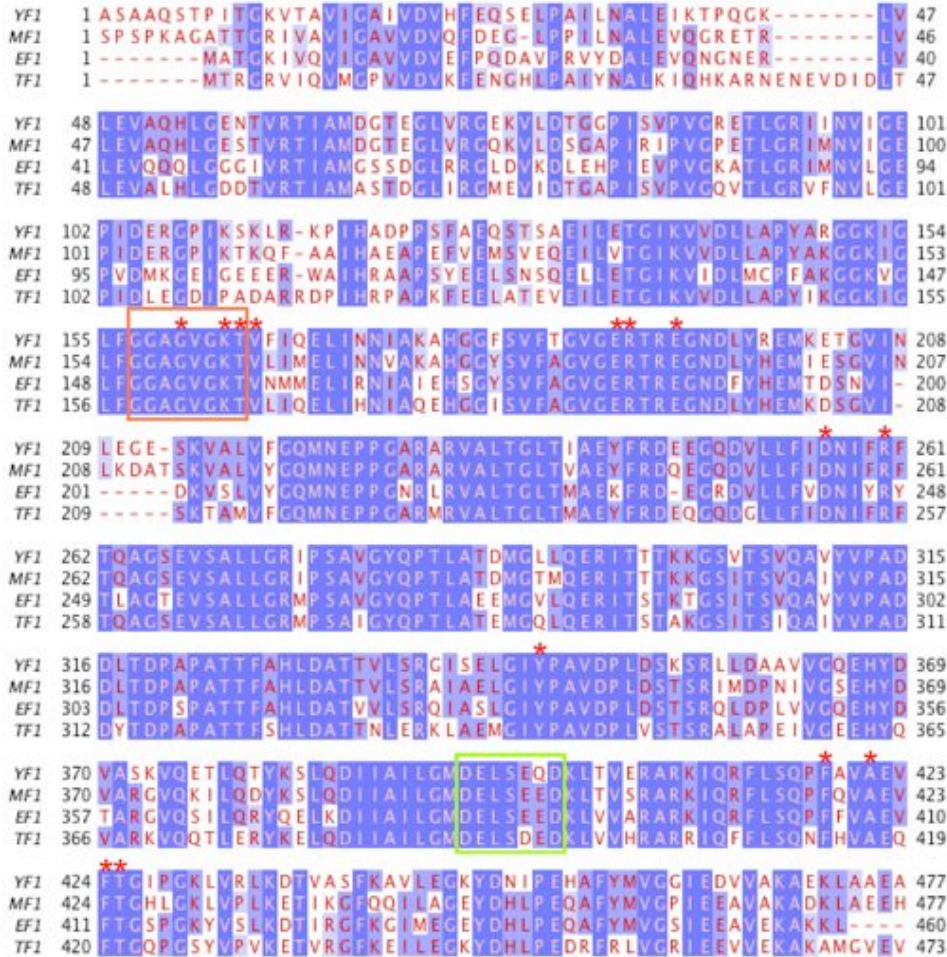


**Figure 1.6:** The sequence alignment of the  $\beta$ -subunits from the mitochondrial YF<sub>1</sub> and MF<sub>1</sub>, and from the bacterial EF<sub>1</sub> and TF<sub>1</sub>. Alignment achieved using ClustalW 2.0.10 [68] and displayed using Jalview [117]. The numbers down the left-side and right-side of the figure correspond to the first and last residue number, respectively, for the sequence shown on each line. The degree of residue conservation is indicated by the blue background for each residue - the darker the background, the more conserved the residue. Various parts of the sequence are highly conserved. One region, the so-called ‘DELSEED’ region, contacts the  $\gamma$ -subunit in the crystal structures when the  $\beta$ -subunit is in the  $\beta_{TP}$  form. This conserved region is indicated by the green box. A highly-conserved nucleotide-binding motif is found in both the  $\alpha$ - and  $\beta$ -subunits [113]. The motif, GXXXXGKT/S, is shown by the dark orange box. Residues indicated by a red asterisk are those residues found to be part of the nucleotide-binding pocket in the Reference Structure. Completing the pocket are residues S<sub>344</sub> and R<sub>373</sub> of the  $\alpha$ -subunit.

to two of the  $\beta$ -subunits and the third was empty. As a result, it has been postulated that this structure was that of the MgADP-inhibited state since azide stabilizes the binding of ADP [102, 118]. A structure from crystals grown in the absence of azide has AMP.PNP bound in both  $\beta_{DP}$  and  $\beta_{TP}$ , despite the presence of ADP during growth [111]. Since the enzyme is not in the azide-stabilized MgADP-inhibited form, this structure may represent a ground state in the catalytic cycle of MF<sub>1</sub>. By way of comparison, the first structure of YF<sub>1</sub>, obtained in the absence of azide but with AMP.PNP and ADP present, also had AMP.PNP bound at both  $\beta_{TP}$  and  $\beta_{DP}$ .

Tallying structural knowledge and single molecule data requires a slight leap of faith. Except for the recent determination of the YF<sub>1</sub> structure [62], only the structure of MF<sub>1</sub> has been studied in depth. By contrast, the vast majority of single molecule rotation studies have used TF<sub>1</sub>, an enzyme accessible to genetic modification and rigorously stable under the demands of the single molecule assay [119]. As we have discussed earlier, F<sub>1</sub> is well-conserved across all species. Furthermore, even subunits with relatively low homology appear to share the same essential structural features. For example, despite only having a low-resolution structure of the entire EF<sub>1</sub> complex [120, 121], the central portion of the EF<sub>1</sub>  $\gamma$ -subunit has been determined at 2.1Å resolution [66]. The structure of this section of EF<sub>1</sub> is almost identical to the corresponding section of the MF<sub>1</sub> enzyme, despite the two species only having 25% homology in the entire  $\gamma$ -subunit and 34% in the central region. These observed similarities between species has allowed possible identification of the catalytic state of the crystal structures in relation to the single molecule rotation work on TF<sub>1</sub>.

The crystal structures show that  $\beta E_{391}$  and  $\gamma R_{75}$  are in close contact when the  $\beta$ -subunit is in the  $\beta_{DP}$  form, but further apart in both  $\beta_{TP}$  and  $\beta_E$ . By introducing cysteine mutations into TF<sub>1</sub> at the corresponding residues, a cross-link could be formed under oxidising conditions. It was

found that upon formation of the cross-link, the mutant TF<sub>1</sub> stopped at the same angle as the catalytic dwell angle or the MgADP-inhibited angle (since they are coincident) [119]. This suggests that the Reference Structure is probably that of the azide-stabilized MgADP-inhibited state, whilst the structure obtained without azide [111] is either the catalytic dwell state or the MgADP-inhibited state (not stabilized by azide). Contrary to the observed single state shown by the MF<sub>1</sub> structure studies (with the exception of the ADP·AlF<sub>4</sub><sup>-</sup> half-closed structure [108]), TF<sub>1</sub> has been shown to have two stable states – the catalytic dwell state and the ATP-binding state – in the single molecule rotation assays. The determination of an ATP-binding state structure remains a significant challenge for crystallographers.

#### 1.2.4 The Catalytic Cycle of ATP Hydrolysis by F<sub>1</sub>-ATPase

Putting together the single molecule and structural data has allowed the postulation of the basic coupling scheme for TF<sub>1</sub> rotation driven by ATP hydrolysis at 23°C over nM–mM ATP concentrations [122,119]. The scheme is illustrated in Figure 1.7. The 120° step has been split into two substeps of 80° and 40° [74,80]. The three β-subunits work in a coordinated manner – binding on one β-subunit allows the hydrolysis of ATP and the release of ADP or P<sub>i</sub> from the other two β-subunits. We shall number the three β-subunits in a counterclockwise manner, starting with the β-subunit that is about to bind an ATP molecule. The ATP-binding dwell is ATP concentration dependent [73]. ATP-binding onto subunit 1, probably followed by rapid ADP release on subunit 2 [122,93,81], initiates the 80° step. At least two processes occur during the short catalytic dwell. In TF<sub>1</sub>, two ~1ms events have been suggested [74], corresponding to ATP hydrolysis [80] on subunit 3 and P<sub>i</sub> release [122]. In the scheme presented here, P<sub>i</sub> is released from subunit 2 immediately after hydrolysis occurs on subunit 3. All-in-all, an ATP molecule bound at 0° is thought not to be hydrolyzed until the

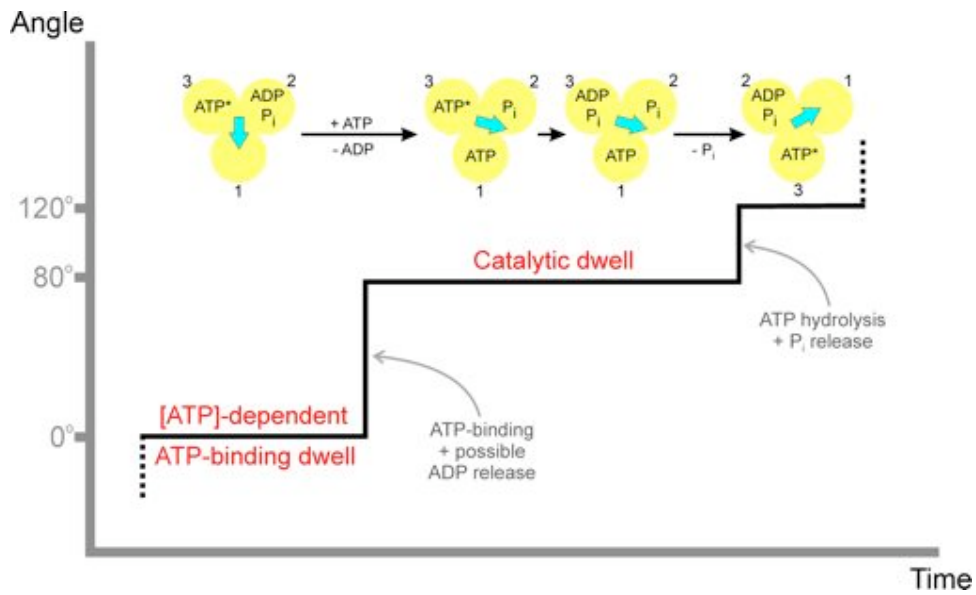


**Figure 1.7:** A possible coupling scheme for ATP-driven rotation of TF<sub>1</sub> as proposed by [119]. The three  $\beta$ -subunits of TF<sub>1</sub> are shown in yellow, the  $\gamma$ -subunit is shown in blue and bound nucleotides are indicated. ATP\* represents tightly-bound ATP. ATP-binding onto  $\beta$ -subunit 1, immediately followed by ADP release from subunit 2, initiates the 80° step. Hydrolysis of ATP on subunit 3 and release of P<sub>i</sub> precede the 40° step. This scheme is consistent with the crystal structures of MF<sub>1</sub> being of the catalytic state. In the numbering system used here subunits 1, 2 and 3 would represent the  $\beta_{TP}$ ,  $\beta_E$  and  $\beta_{DP}$  subunits of the crystal structure respectively. The exact timing of the release of P<sub>i</sub> is still a point for conjecture. Either P<sub>i</sub> leaves immediately after ATP hydrolysis or, as presented here, P<sub>i</sub> remains bound for 120° and ATP hydrolysis on subunit 3 is immediately followed by P<sub>i</sub> release on subunit 2.

$\gamma$ -subunit has rotated  $+200^\circ$  and its ADP product will not be released until at least  $+240^\circ$  [123, 122].

One final question we should ask is: How might the F<sub>1</sub> protein use ATP hydrolysis to drive rotation of the  $\gamma$ -subunit? The TF<sub>1</sub> studies have suggested that the work done by the enzyme is almost exactly the free energy available from hydrolysis of one ATP molecule. We also know, from the crystal structures, that the  $\gamma$ -subunit is asymmetrical and that each of the three  $\beta$ -subunits takes on a unique conformation. Therefore, we can conclude that rotation of the  $\gamma$ -subunit is linked to conformational changes of the  $\beta$ -subunits. Isolated  $\beta$ -subunits [124] and nucleotide-free  $\beta$ -subunits in  $\alpha_3\beta_3$  complexes [125] adopt a similar conformation to  $\beta_E$  in the Reference Structure, i.e., with the nucleotide-binding site opened up. This conformation would appear to be the ground (or unstressed) conformation of the  $\beta$ -subunit.

Theoretical models have been developed to explain ATP hydrolysis-driven F<sub>1</sub> rotation [126, 127, 128], including molecular simulations [129] and Markov-Fokker-Planck models [130]. A much simplified version will be presented here.

A  $\beta$ -subunit, in the  $\beta_E$  conformation, has an affinity to bind ATP. When ATP enters into the  $\beta$ -subunit binding pocket, a number of weak bonds, mainly hydrogen bonds, are formed between the binding pocket and ATP molecule, primarily to the phosphate groups. As each subsequent bond is formed (bending the  $\beta$ -subunit into the tightly-bound ‘closed’ form), the affinity for ATP greatly increases. This ‘zipping’ of the binding pocket, forcing the conformational change in the  $\beta$ -subunit, will also initiate a rotation of the  $\gamma$ -subunit. As more bonds are formed between the  $\beta$ -subunit and the ATP molecule, the  $\gamma$ -subunit rotates through  $80^\circ$  due to a force from the  $\beta$ -subunit exerted onto the off-axis portion of the  $\gamma$ -subunit. The free energy of ATP binding, as a result, is stored as elastic strain within the

$\beta$ -subunit. In this manner, ATP-binding corresponds to the primary power stroke of the F<sub>1</sub> mechanism.

So far, it has been ATP binding, and not ATP hydrolysis, that has driven rotation. In fact, ATP hydrolysis would appear to be mechanically quiet [74, 128], with  $\text{ATP} \rightleftharpoons \text{ADP} + \text{P}_i$  lying near to equilibrium within the binding pocket. So, what of the role of ATP hydrolysis? Well, as the ATP-driven conformational change and rotation occurs, the affinity of the binding pocket for ATP increases concomitantly. Without ATP hydrolysis, which acts to reset the motor, the motor would become stalled after this one step with ATP very strongly bound. ATP hydrolysis allows the release of the small  $\text{P}_i$  ion from the pocket, driving the secondary power stroke, the relaxation of the  $\beta$ -subunit to the ‘open’ conformation (in line with experimental results [131]) and initiating the next 40° step. Of course, these power strokes are occurring on different  $\beta$ -subunits in a highly coordinated manner and the exact timing of the  $\text{P}_i$  release is still a point of conjecture. The YF<sub>1</sub> crystal structure indicates that  $\text{P}_i$  remains bound for 120° after ATP hydrolysis [62], although this is only true of one of the available crystal structures. Single molecule studies suggest that  $\text{P}_i$  is released immediately after hydrolysis in TF<sub>1</sub> [122]. From experiment, it appears that ADP is not released until the  $\beta$ -subunit is back into the ‘open’ form and ATP binding occurs on a different subunit.

The observed near-100% efficiency of TF<sub>1</sub> has direct implications for its mechanism. This result implies tight-coupling between the mechanical and chemical reactions, where all of the free energy available from ATP hydrolysis goes into generating the driving torque on the  $\gamma$ -subunit. The ~100% efficiency also leads to constant torque predictions during the 120° catalytic cycle [127, 132, 74, 128]. This implication is in no way conclusive however, since a periodic torque profile would lead to ~90% efficiency [127], a value within the experimental uncertainty.

### 1.3 A Summary of Suitable Optical Techniques for the Study of F<sub>1</sub>-ATPase

---

The original method for observing TF<sub>1</sub> rotation [34] involved the isolation of TF<sub>1</sub> molecules onto a glass coverslip and the attachment of a fluorescent actin filament to the  $\gamma$ -subunit. The subsequent ATP-dependent rotation of the actin filament was recorded via a video-rate (30Hz) CCD camera on an epifluorescence microscope. In this study, TF<sub>1</sub>, under the high viscous load of the actin filament, rotated at only a few revolutions per second and therefore video rate recording was sufficient to obtain rotation information. When the actin filament is replaced by large (>300nm) bead-duplexes, as is the case in the majority of experiments presented in this thesis, F<sub>1</sub> experiences a comparable viscous drag. This means that video rate recording (25–30Hz) can still be used, albeit in conjunction with conventional bright-field microscopy.

Replacement by beads (both single and duplex) below this limit results in fast rotation that cannot be recorded effectively by a video-rate camera. One technique applied has been to use commercially-available fast-speed cameras [74, 92] that can record at up to 100kHz. These cameras can be used with either bright-field imaging or via laser dark-field microscopy depending on the size of the beads. Typically, bright-field imaging is diffraction limited to the observation of 200nm bead-duplexes and larger, whilst bead sizes smaller than this are imaged in laser dark-field where gold beads have to be used. Laser dark-field is also diffraction-limited but the signal-to-noise ratio is much higher than in bright-field mode, allowing higher spatial resolution. The location of the centre of a Gaussian-shaped diffraction spot has been calculated by the centroid method (see Section 2.8.2) by all studies in the field. More accurate methods are available, either by fitting a 2D Gaussian curve explicitly to each frame of an image (a computationally-

expensive method prone to instability due to background noise), or by the Gaussian Mask method [133] (an iterative approach that appears to be the best compromise between computational time and accuracy).

Other techniques for monitoring rotation have been successfully applied to TF<sub>1</sub>. Single fluorophore imaging by direction of fluorescence polarization has been used to observe 120° ATP-binding dwells of TF<sub>1</sub> under truly low load [134] (the 40–60nm single gold beads are not rate-limiting but do impose a viscous drag on the enzyme, as will be discussed in Section 3.3). FRET has also been used to study the conformation of the ATP-binding dwell [78] by placing a donor fluorophore (Cy3) onto the periphery of one of the  $\beta$ -subunits and the acceptor (Cy5) onto the asymmetric  $\gamma$ -subunit and imaged onto a CCD at video rate.

### 1.3.1 Detecting Rotation by Back-Focal-Plane Interferometry

The technique of image capture by CCD has one obvious drawback – image analysis is computationally intensive. Peak detection can only be achieved in real-time using specialist Data Acquisition Boards (DAQ), with a limitation of less than 1kHz sampling rate [135]. To obtain faster, ‘on-the-fly’ position detection a method known as Back-Focal-Plane Interferometry can be used. In this method, a low-power focussed laser can be used to locate the position of a dielectric particle in the specimen plane. Interference between forward-scattered light from the bead and unscattered light is monitored by a quadrant photodiode (QD) in a plane conjugate to the back-focal-plane of the condenser<sup>11</sup>. By imaging in the back-focal-plane, the position detection is not sensitive to the position of the bead within the image plane, but sensitive only to the relative displacement of the bead away from the laser axis [136]. The pattern on the back-focal-plane is independent of the

---

<sup>11</sup>For an example see Figure 2.5 in Chapter 2.

focal height and represents the angular-intensity distribution of scattered light [136]. The incident light onto the QD, in the form of four voltages, can be converted into both lateral dimensions by suitable pair-wise subtraction. This technique can also be used to measure the relative position of live cells within the specimen plane. A distinct advantage of this method is that it can afford real-time position detection at sampling rates in excess of 50kHz.

### 1.3.2 The Use of Optical Traps with Biological Samples

The manipulation of nano-metre sized objects is an oft-desired application in many biophysical single molecule experiments. The aim is to be able to apply and measure forces and torques without physical damage to your object of interest. Atomic Force Microscopy (AFM) has long deviated from its original imaging role to become a multi-function option capable of molecular manipulation (for a review see [137]), electrorotation has been used to apply torque to particles attached to the bacterial flagellar motor [138], whilst magnetic tweezers have allowed the visualization of the rotation of DNA during transcription [139] and to apply torque to TF<sub>1</sub> [83]. However, it is the technique of optical tweezers that remains the most popular method for the study of force (torque) production by molecular motors.

Since their inception almost forty years ago [140], optical traps have been used in applications ranging from physics to biology, initially with the entrapment of dielectric particles, up to the manipulation of live bacteria and viruses [141, 142]. The ability to apply picoNewton forces to micron-sized particles, whilst accurately measuring position, has made optical traps attractive to biophysicists.

Using a high numerical aperture (NA) objective lens, an optical trap formed by a tightly-focused Gaussian laser beam can be used to trap dielectric particles in three dimensions. The position of the trap centre is coincident with the optical axis and slightly downstream from the focal point

of the objective. For small displacements ( $\sim 150\text{nm}$  [135]) away from the trap centre, the restoring force exerted onto the dielectric particle is simply proportional to the displacement and, therefore, the trap acts as a Hookean spring on this length-scale, with corresponding trap stiffness,  $k$ . The exact forces on a dielectric sphere of radius  $a$  due to an optical trap created from a Gaussian laser beam of wavelength  $\lambda$  can be calculated in the extremes from simple ray optics (when  $a \gg \lambda$ ) or from the theory of Rayleigh scattering (when  $a \ll \lambda$ ). Unfortunately, the majority of particle sizes used in biophysics experiments, and those used in this thesis, lie in the intermediate range ( $a \sim \lambda$ ). Complete electromagnetic theories are required in this regime (for a review see [143]). Further complications arise from non-spherical particle shapes. Fortunately, the trap stiffness,  $k$ , can, in general, be obtained through accurate calibration of the set-up, of which the simplest method is by the Principle of Equipartition of Energy  $\frac{1}{2}k\langle x^2 \rangle = \frac{1}{2}k_B T$ , where  $x$  is the displacement from the trap position of the particle [135].

Optical traps have been used to measure the forces produced by the linear motors kinesin (firstly in 1D [144, 145, 146] and then in 2D [147, 15]) and myosin [148, 149, 150], and to estimate the torque of the bacterial flagellar motor [151]. The more recent linear motor force measurements have used optical traps as force clamps by the addition of beam steering and the implementation of control algorithms. In this manner, position clamping, in which the trap location is constantly varied to keep the particle at a fixed position, affords greater spatial and temporal resolution since the precise particle location is known and removes complications due to elastic compliance between the trap and the motor [147, 15].

### 1.3.3 Feedback Theories

Optical position clamps have been successfully applied to the linear motors using conventional control theory, or feedback algorithms (for a review see

[152]). The aim of the feedback algorithms is to precisely clamp the location of the particle attached to the molecular motor whilst measuring relative displacements of the particle from the trap.

For a particle within an optical trap, the equation of motion in 1D is given by

$$\zeta \frac{dx}{dt} = -k[x(t) - u(t)] + f_b(t) + F_d(t) \quad (1.3)$$

where  $\zeta$  is the viscous drag coefficient of the particle in the medium,  $x$  is the position of the particle,  $u$  is a feedback term governing the trap position,  $f_b$  describes the Brownian noise of the particle and  $F_d$  is an external driving force (perhaps due to the molecular motor).

If  $u_t = 0$  and  $F_d = 0$ , Equation 1.3 represents a conventional fixed optical trap and the power spectrum of the particle behaves as a Lorentzian [135]. The most common form of feedback control is Proportional Integral Derivative (PID). If the aim of control is to make the system follow a control signal of  $r(t)$ , feedback works by minimizing the error,  $e(t)$ , between the control signal and the particle position,  $x(t)$ , with  $e(t) = r(t) - x(t)$ . PID control is expressed as

$$u(t) = K_p e(t) + K_i \int e(t) dt + K_d \frac{de(t)}{dt} \quad (1.4)$$

parameterized by constants  $K_p$ ,  $K_i$ ,  $K_d$ .

The control parameters have to be tuned for the system [152]. Very simple control could be obtained just using the proportional gain term (setting  $K_i = K_d = 0$ ), however, this can suffer from oscillations, slow response and systematic offsets. Introduction of memory by including integral gain and tuning  $K_i$  helps to eliminate systematic offsets but may introduce a time lag. The derivative gain can be used to preempt fast changes in the system but becomes de-stabilising in systems with high-frequency noise.

The PID control given here describes 1D control but could easily be

extended to 2D, by independent control of an orthogonal direction, or into polar coordinates with control of  $r$  or  $\theta$  or both.

## 1.4 The Objectives and Layout of this Thesis

---

So far we have discussed the field of molecular motors, in particular the study of  $F_1$ -ATPase at the single molecule level. We have seen that the majority of rotation assays have used  $F_1$  from thermophilic *Bacillus* and that we have excellent structural information of mitochondrial  $F_1$ , predominantly from bovine mitochondria. We have also summarized suitable experimental techniques that can be applied to  $F_1$  and how, in theory, optical position clamps can be used to measure the piconewton forces created by molecular motors. Here we shall outline the aim of the work presented in this thesis and expound the layout of the remaining sections.

To place this thesis into context, we should make a note of the original aim and detail the natural evolution of the project up to the final presented body of work. The grand aim, first held as long as four years ago, was to measure the torque profile of  $F_1$  during the hydrolysis of ATP as a function of angle. We hoped that, using an optical angle clamp developed by the group, we would be able to map out the potential energy profiles of the enzyme during rotation, relating interesting features back to predictions derived from theory and structure. Needless to say, this has remained the motivation but other important landmarks have had to be achieved on the way. In this respect, this thesis does not present a completed piece of work with all questions answered. Instead, the work presented here is a major step towards attaining this ambitious goal.

Chapter 2 will cover the experimental and analysis techniques that have been central to this work. The protocols detailed represent the optimized methods obtained from experience and, as such, may be considered as small results in their own right.

In Chapter 3, a mechanical characterization of  $F_1$  from *E. coli* will be presented, along with steps that were required to produce a reliable, high-yield rotation assay. This characterization will be in reference to the substantial work carried out on  $TF_1$ . This characterization is important due to the limited knowledge regarding the  $EF_1$  enzyme at the single molecule level. It should be noted that we were unable to obtain the  $TF_1$  enzyme despite requests to the relevant groups. We will observe an underlying similarity between the two enzymes, perhaps unsurprising, but also that the observed biochemical parameters differ in accordance with the natural operating environments of the two species. Characterization of  $EF_1$  rotation over a wide range of ATP concentrations and viscous loads has been achieved. It will be noted that elements of this work were in close collaboration with Dr Mayumi Nakanishi-Matsui and Prof Masamitsu Futai, currently in Iwate Medical University, Iwate Prefecture, Japan. Initial results will also be presented verifying the rotary nature of  $F_1$  from yeast mitochondria, an enzyme provided by Prof David Mueller, Rosalind Franklin University, Chicago Medical School, Illinois, US. The initial success of this project has spawned a spin-off project in its own right.

In order to make inference from any optical trapping experiments on  $EF_1$ , we first needed to be able to conclusively understand the ATP hydrolysis mode of  $EF_1$  rotation. The assumption that  $EF_1$  and  $TF_1$  would be operationally similar at room temperature is not valid, especially since features such as the ATP-waiting step and MgADP-inhibition were debated in  $EF_1$ . The group of Junge and Engelbrecht (University of Osnabrück) also study  $EF_1$  under high load and have had little luck observing the ATP-waiting step, to the extent that they began to believe that it may not a feature of  $EF_1$  at all (S. Engelbrecht, private communication). Understanding the rotation of  $EF_1$  affords angular knowledge about the catalytic cycle, essential information if we wish to map out the angular torque profile. Without

a suitable frame of reference marker, we would not be able to confidently overlay the data from many different molecules. I propose that this angular marker should be that of the inhibited form of  $EF_1$ .

In Chapter 4, investigation of  $F_1$  with an optical angle clamp will be presented. The optical angle clamp was developed in the group of Dr Richard Berry by Dr Teuta Pilizota and is an extension of the optical position clamps used previously on linear motors. The difficulties we encountered applying the optical trap to  $F_1$  will be discussed, as will interesting initial results. Precise torque measurements have not been obtained as yet but activation of  $EF_1$  with the optical trap has been achieved, albeit without quantification. Work on developing a second-generation optical trap will be detailed, in particular the use of a new digital signal processing board (DSP) and improved automation of hardware. This second-generation trap essentially builds upon the original but with extra developments to enable additional experimental options for use not only with  $F_1$  studies, but also for investigation of the bacterial flagellar motor.

Finally, in Chapter 5, a summary of the thesis will be given along with ideas for the future direction of  $F_1$  torque measurements. Also discussed will be ideas relating to novel DNA attachment chemistries, with the aim of obtaining biocompatible surfaces for use with  $F_1$  rotation studies.

# 2

## Techniques and Methods

### 2.1 A Definition of the Buffers Used

---

- **Buffer A.** 10mM 3-(N-Morpholino)propanesulfonic acid (MOPS; Sigma), 50mM KCl, 2mM MgCl<sub>2</sub>, adjusted to pH7.0 with 4M KOH.
- **Buffer B.** Buffer A containing 10mg/ml bovine serum albumin (BSA; Sigma).
- **Buffer C.** 10mM sodium bicarbonate, pH8.0.
- **Buffer D.** 10mM 4-(2-Hydroxyethyl)piperazine-1-ethanesulfonic acid (HEPES), pH 7.8.
- **Buffer E.** 50mM 2-morpholinoethanesulfonic acid (MOPS), pH5.5.
- **Buffer F.** 20mM TrisHCl, pH 8.0 at 37°C, 2μg/ml BSA.

### 2.2 Purification of F<sub>1</sub> derived from E.coli

---

Unless otherwise stated, the F<sub>1</sub>-ATPase used throughout this work was the enzyme derived from *Escherichia coli* and obtained by collaboration with the group of Prof Masamitsu Futai<sup>1</sup>. Two F<sub>1</sub> variants were used by ex-

---

<sup>1</sup>Currently at Iwate Medical University, Iwate Prefecture, Japan

pression of different plasmids within the DK8 bacterial strain [153]. The plasmid pBUR17 $\gamma$ K108C expresses a  $F_1F_o$  mutant with His<sub>6</sub>-tags on the *N*-terminus of the  $\alpha$ -subunit and carries two cysteine mutants,  $\gamma$ Lys108Cys and  $\gamma$ Ser193Cys [87]. The plasmid pBUR17AH10GC2 expresses  $F_1F_o$  with His<sub>10</sub>-tags on the *N*-terminus of the  $\alpha$ -subunit and again carries the same two cysteine mutations on the  $\gamma$ -subunit. In particular, pBUR17AH10GC2 was a kind gift developed by Dr. Hiroyuki Hosokawa. The requirement for His<sub>10</sub>-tags will be covered in Section 3.2. The location of the Cys mutations was chosen such that they were on the surface of the  $\gamma$ -subunit from the crystal structure [121]. Ser193 was chosen since the corresponding residue in the chloroplast  $F_1$  is accessible to ferredoxin [87, 154]. Lys108 was chosen since it is the equivalent residue to Ser107 in TF<sub>1</sub>, the point of Cys mutation in the first rotation assays [34].

The protocol for the purification of *E.coli*  $F_1$  and  $F_1F_o$  was obtained by Dr Teuta Pilizota through work in the laboratory of Prof Masamitsu Futai<sup>2</sup>. The protocol for purification was refined by Dr Pilizota, assisted by Jelena Baranovic and Maja Petkovic<sup>3</sup>, for the available equipment at the University of Oxford. Purification of  $F_1$  used in this thesis was carried out in the laboratory of Prof Anthony Watts (Biochemistry Department, University of Oxford), initially by Dr Simon Ross<sup>4</sup>, and subsequently by myself and Wei Meng Ho<sup>5</sup>. The protocol for  $F_1$  purification can be found in Appendix A.

---

<sup>2</sup>At the time, Prof Futai's laboratory was at the Division of Biological Sciences, Institute of Scientific and Industrial Research, Osaka University, Japan.

<sup>3</sup>J. Baranovic and M. Petkovic were undergraduate students from the University of Zagreb, Croatia.

<sup>4</sup>Dr Simon Ross was a technician funded by the Bionanotechnology IRC, University of Oxford.

<sup>5</sup>Wei Meng Ho is currently a DPhil graduate student in the group of Dr Richard Berry, Physics Department, University of Oxford, attempting to reconstitute *E.coli*  $F_1F_o$  into energized lipid bilayers and to apply single molecule techniques.

## 2.3 Activity Measurements of *E.coli* F<sub>1</sub>-ATPase

---

Despite the recent trend towards single molecule techniques, more traditional biochemical measurements still hold many advantages for the Biophysicist. In our case, the measurement of bulk properties often allows quicker, more reliable and more reproducible analysis of enzyme activity and concentration. We have used two different approaches to obtain the functional ATPase activity of the purified F<sub>1</sub> enzyme.

### 2.3.1 Activity Measurement by Colourimetry

This method involves measuring the amount of inorganic phosphate produced upon ATP hydrolysis by the increased absorbance at 740nm when a molybdenum complex binds phosphate [155]. Care should be taken to ensure that ferrous sulphate solutions are new since ferrous sulphate undergoes spontaneous oxidation on the timescale of hours. Solutions of Buffer F containing  $x$ mM F<sub>1</sub> or 0.1–1mM KH<sub>2</sub>PO<sub>4</sub>, along with 10mM TrisHCl (pH8.0 at 37°C), 4mM ATP and 2mM MgCl<sub>2</sub>, were prepared. The solutions were incubated at 37°C for 10 minutes. Trichloroacetic acid (TCA) was added (at a final concentration of 330mM TCA) in order to suspend the reaction. The samples were then placed on ice. The Colouring Solution consisting of FeSO<sub>4</sub>, (NH<sub>4</sub>)<sub>6</sub>Mo<sub>7</sub>O<sub>24</sub>, H<sub>2</sub>SO<sub>4</sub> was added to final concentrations of 1.8% (w/v), 0.36% (w/v) and 180mM respectively. The solutions were shaken and incubated at 37°C for 30s. The absorbance of each solution was then measured at 740nm. The solutions containing KH<sub>2</sub>PO<sub>4</sub> allow calculation of a calibration curve for P<sub>i</sub> concentration.

### 2.3.2 Activity Measurement by a Coupled Reaction with NADH

ATP can be regenerated from ADP and P<sub>*i*</sub> by the coupled conversion of phospho(enol) pyruvate (PEP; Sigma) to pyruvate, catalysed by pyruvate kinase (PK; Roche Diagnostics). In turn, pyruvate can be converted to lactate by lactate dehydrogenase (LD; Sigma), resulting in the subsequent oxidation of β-Nicotinamide adenine dinucleotide (NADH; Sigma) [156, 157, 158]. The stoichiometry of each of the coupled reactions is 1:1. Whereas NADH absorbs strongly at 340nm, its oxidized form, NAD<sup>+</sup> does not, as demonstrated in Figure 2.1a. Therefore, the ATPase activity of F<sub>1</sub> can be calculated from the rate of decrease of absorbance at 340nm,  $\frac{dA_{340}}{dt}$ , of a solution containing both NADH and ATP upon the addition of F<sub>1</sub>, as shown in Figures 2.1b and 2.1c for data I obtained using EF<sub>1</sub>. The precise determination of the rate of ATP hydrolysis per mole of F<sub>1</sub>,  $R_{ATP}$ , is given in terms of the molar extinction coefficient,  $\epsilon$  (6220M<sup>-1</sup>cm<sup>-1</sup> for NADH), and the path length,  $l$ , by:

$$R_{ATP} = -\frac{1}{\epsilon l} \frac{1}{[F_1]} \frac{dA_{340}}{dt} \quad (2.1)$$

The precise method was as follows. 500μl of Buffer A containing 2mM MgATP, 10units/ml LD, 0.1mg/ml PK and 2mM PEP was placed into a quartz cuvette and the absorbance was measured using a Cary-UV spectrophotometer to obtain a background curve. 25μl 4mM NADH was added, stirred and left for ~2 minutes for sufficient mixing within the cuvette. The absorbance was measured to determine the exact concentration of the NADH present. 5μl of 0.1–1mg/ml F<sub>1</sub> was added to the cuvette, quickly stirred and the absorbance spectrum measured. The lag between adding F<sub>1</sub> and the initial measurement was ~10s. Absorbance spectra were obtained every 20s for the next 10–20 minutes.

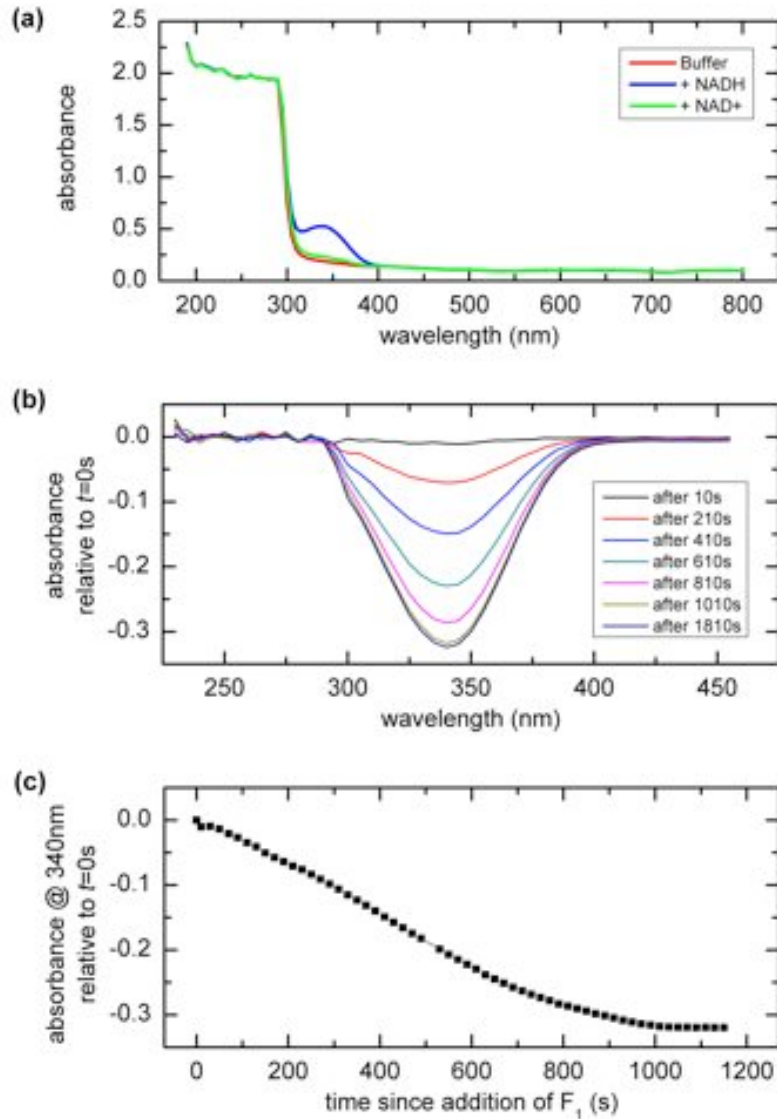


**Figure 2.1:** The measurement of ATPase activity by a coupled reaction with NADH. (a) NADH absorbs strongly around 340nm whereas its oxidized form, NAD<sup>+</sup> does not. (b) ATP hydrolysis by F<sub>1</sub> leads to a decrease in the concentration of NADH present and the subsequent decrease in absorbance at 340nm. (c) The rate of decrease in absorbance at 340nm can be equated to the ATPase rate by Equation 2.1.

## 2.4 Preparation of Biomolecule-Compatible Surfaces

---

F<sub>1</sub>-ATPase was isolated onto microscope cover-slips for direct observation of rotation. During this study, we used a number of different surfaces in an attempt to find the most compatible for the immobilization of the F<sub>1</sub> enzyme.

- **Clean Glass.** 22x22x0.15mm glass coverslips were immersed overnight in 95% ethanol containing saturating KOH, followed by washing, firstly in 95% ethanol then finally in H<sub>2</sub>O, before drying prior to use.
- **BSA Coating.** Clean Glass surfaces were coated with BSA by the addition of Buffer B for 10 minutes prior to the introduction of F<sub>1</sub>.
- **HRP Coating.** Clean Glass surfaces were coated with Collodion Solution (2% cellulose nitrate in amyl acetate; Sigma), dried and then 1μM Ni<sup>2+</sup>-NTA horseradish peroxidase (HRP; Sigma) was added for 10 minutes prior to F<sub>1</sub> addition.
- **Copper Surface.** The Copper Surfaces were commercially available cover-slips (Microsurfaces Inc., USA), offering Cu<sup>2+</sup> chelated ions, via a poly(ethylene) glycol (PEG) film, for the directed immobilization of His-tagged proteins [159].
- **Ni<sup>2+</sup>-NTA-Silane Surface.** Ni<sup>2+</sup>-NTA-silane surfaces were prepared essentially as described previously [84,114,160], with detailed method as follows. A beaker containing 95% ethanol with 0.02% (v/v) acetic acid and 2% (v/v) 3-mercaptopropyltrimethoxysilane (Sigma) was placed in a water bath at 80–90°C for at least 30 minutes. Under lab conditions, the ethanol solution was measured to be around 65°C. The coverslips were immersed into the ethanol solution and left for 1–2 hours. The coverslips were washed thoroughly with water, wrapped in

foil and baked at 120°C for 20 minutes and then left to dry for 1 hour. The cover-slips were transferred to an aqueous solution of 100mM dithiothreitol (DTT, Sigma) at room temperature for 15 minutes before thorough washing with water. 10 $\mu$ l of a solution of 10mg/ml maleimido-C3-NTA (Dojindo, Japan) in 10mM MOPS (pH7.0) was sandwiched between pairs of cover-slips to minimize the quantity of expensive reagents used and incubated for 30 minutes at room temperature. The cover-slips were separated and washed once more with water. Finally, the coverslips were immersed in an aqueous solution of 10mM NiCl<sub>2</sub> for 15 minutes, prior to thorough washing with water, and then dried overnight at  $\sim$ 50°C. The surfaces were typically used within one month of preparation and were discarded after two months of storage at room temperature free from dirt and dust.

## 2.5 Preparation of Biotinylated Bead-Duplexes

---

In order for direct observation of rotation and for external forces to be applied to the rotor of F<sub>1</sub>, we have attached duplexes of biotinylated polystyrene beads to the biotinylated  $\gamma$ -subunit of F<sub>1</sub> via a streptavidin linkage. Streptavidin is a tetrameric protein produced by *Streptomyces avidinii* and is able to bind up to four biotin molecules. This interaction is one of the strongest protein-ligand associations known with an estimated dissociation constant,  $K_d$ , of  $4 \times 10^{-14}$ M [161, 162], essentially making the binding of the beads to the F<sub>1</sub> molecule irreversible. The polystyrene beads can be trapped optically with a focussed laser trap, whilst the use of bead-duplexes results in a large handle for the exertion of external torque. Furthermore, the bead-duplexes have a much larger radius of gyration than single beads resulting in easier observation of rotating single molecules, as illustrated in Figure 2.2.

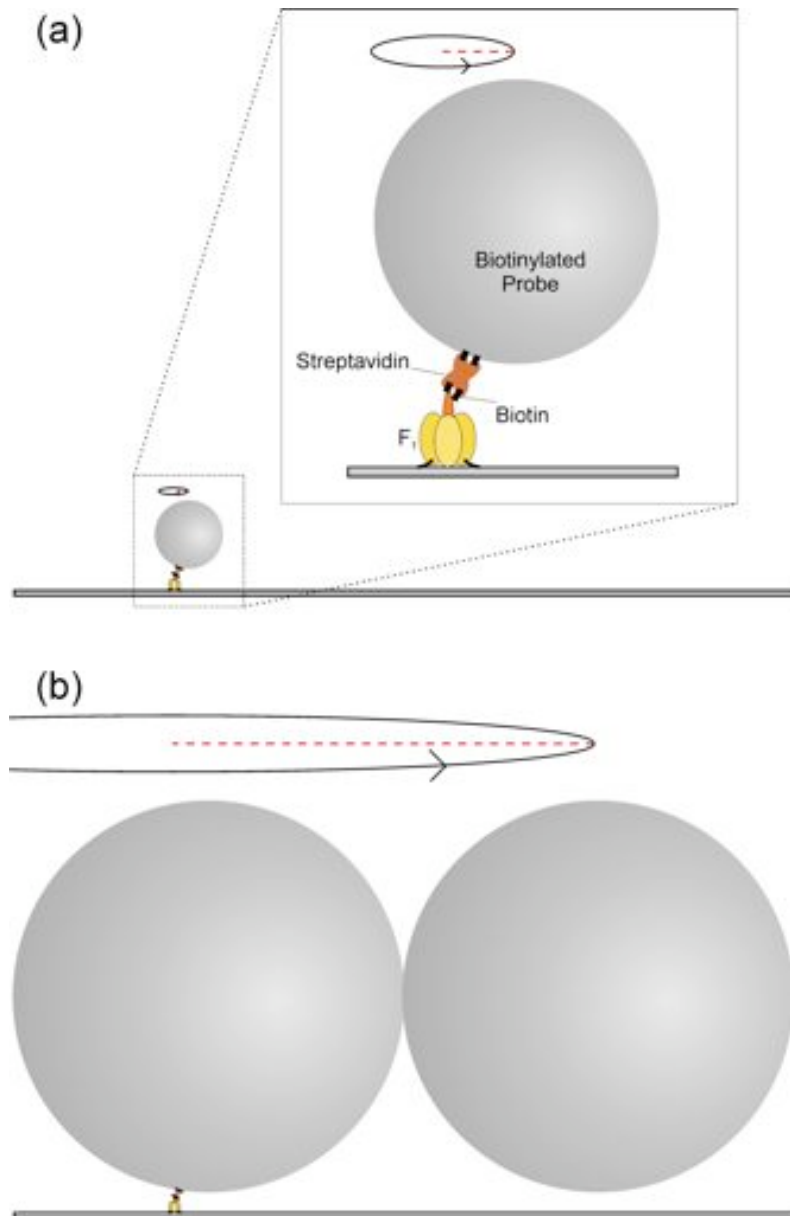


**Figure 2.2:** The advantage of using bead-duplexes (b) as opposed to single beads (a) is the vastly increased radius of gyration obtained, as indicated by the dotted red line. (a) The attachment of a single 40nm gold bead. (b) The attachment of a 220nm bead-duplex to F<sub>1</sub>.

### 2.5.1 Biotinylation of Polystyrene Beads

220nm and 495nm diameter amino-functionalized and 340nm diameter carboxy-functionalized polystyrene microspheres (Polysciences Inc., USA) were used due to available surface chemistry reactions to covalently attach biotin. 1% (w/v) amino-functionalized beads in Buffer C containing 2mM 6-(biotinamidocaproylamido)caproic acid N-hydroxysuccinimide ester (Biotin-XX-NHS; Sigma) were incubated at room temperature for 2 hours with gentle agitation, before extensive washing into Buffer D for storage at 4°C. 1% (w/v) carboxy-functionalized beads were incubated for 2 hours at room temperature with gentle agitation in Buffer E containing 200 $\mu$ M 1-ethyl-3-(3-dimethylaminopropyl)carbodiimide (EDAC; Sigma) and 2mM (+)-biotinyl-3,6-dioxaoctanediamine (Biotin-PEO-amine; Pierce), followed by washing into Buffer D for storage at 4°C.

### 2.5.2 Purification of Bead-Duplexes

The beads we have used carry a slight surface charge and therefore will repel each other in a non-ionic medium. We can overcome this repulsion by adding a small amount of ions to effectively screen the surface charges. In this situation, the beads can come sufficiently close that they can bind by induced-dipole interactions. This process must be controlled in both time and ionic concentration such that duplexes are formed, with only a small amount of larger complexes. Substantial trials have found suitable reaction parameters for duplex formation. 0.8% (w/v) of 220nm amino-, 340nm carboxy- and 495nm amino-functionalized biotinylated beads were incubated for 15, 28 and 15 minutes respectively in Buffer D containing 100mM MgCl<sub>2</sub>, prior to washing into Buffer D. At best this method resulted in around 15% bead-duplexes when studied under the microscope. In order to further increase the bead-duplex concentration, we separated the bead-duplexes by zonal centrifugation through a 10%(bottom)→5%(top) smooth sucrose gra-

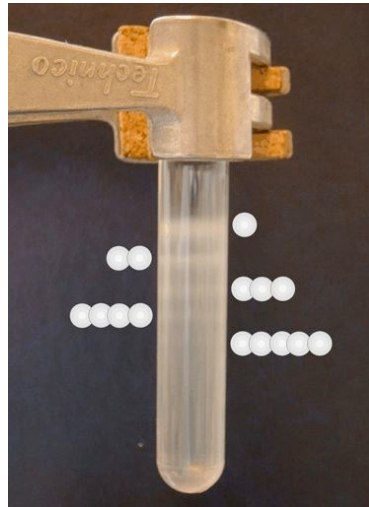


**Figure 2.3:** The purification of bead-duplexes by centrifugation through a sucrose gradient. It is just possible to make out five bands that decrease in population from the top of the centrifuge tube corresponding to single beads, bead-duplexes, triples, quadruples and quintuples. The exact geometry of the triples, quadruples and quintuples is variable and are shown as rods for illustrational purposes.

dient prepared with a home-made gradient maker. After centrifugation, the band corresponding to bead-duplexes could be visualized (see Figure 2.3) and then extracted.

## 2.6 Rotation Assays

---

$F_1$  rotation assays were carried out in a ‘Tunnel Slide’, a simple construct consisting of a modified glass cover-slip (see section 2.4), double-sided adhesive tape to act as spacers and a microscope slide (cleaned with 98% ethanol prior to use), as shown in Figure 2.4. The effective size of the tunnel produced was approximately  $22 \times 2 \times 0.1$  mm, with volume  $\sim 5 \mu\text{l}$ .  $10 \mu\text{l}$  of  $0.1\text{--}1 \text{ mg/ml}$   $F_1$  in Buffer B was added to the tunnel and left to incubate in a high-humidity chamber for 10 minutes. All incubation was done with the coverslip facing downwards to encourage immobilization onto the coverslip rather than onto the microscope slide.  $F_1$  was removed from the tunnel by the gentle flowing of  $\sim 50 \mu\text{l}$  of Buffer B through the tunnel.  $10 \mu\text{l}$  of  $4 \text{ mM}$

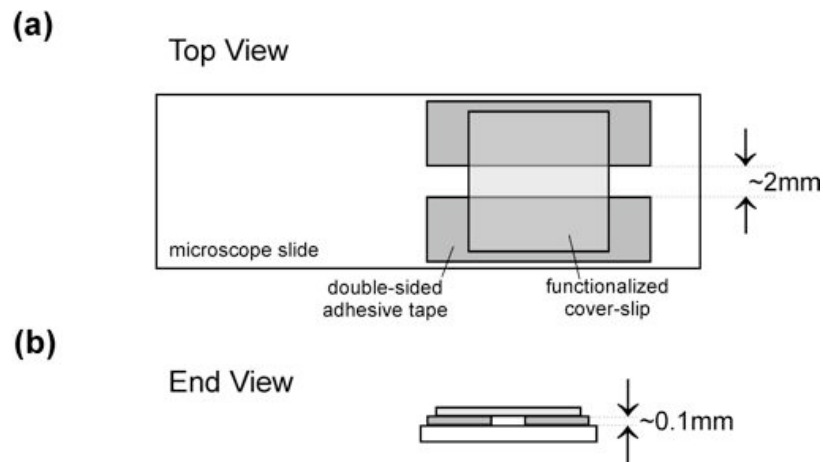


**Figure 2.4:** The construction of a tunnel slide as viewed from (a) above the coverslip and (b) from the end, looking through the tunnel. The produced tunnel has a volume of  $\sim 5\mu\text{l}$ . Note, the figure is not drawn to scale.

streptavidin in Buffer B was added and the slide was incubated for 10 minutes. The tunnel was cleared of unbound streptavidin by washing with  $50\mu\text{l}$  Buffer B. Finally, the biotinylated bead-duplexes were added at  $\sim 1\%$  (w/v) in Buffer B and incubated for 20 minutes. Loose beads were removed from the tunnel by gentle washing with  $50\mu\text{l}$  of Buffer B. Care was taken to ensure that the flow rate at this stage was slow as fast flow can remove the bead- $F_1$  complex from the surface. Just prior to observation,  $50\mu\text{l}$  of Buffer B containing a desired concentration of MgATP, 2mM PEP and 0.1mg/ml PK was infused into the channel to initiate rotation of  $F_1$ .

## 2.7 Detection of Rotation and Optical Trapping

The majority of  $F_1$  rotation results presented in this thesis were achieved using a custom-built microscope [160] developed by Dr Teuta Pilizota. The ray optics diagram is shown in Figure 2.5. The microscope was built to allow simultaneous position detection and optical trapping with a dual-laser system, with the express aim of applying pN forces and measuring the torque of rotary molecular motors. The microscope has three main features:

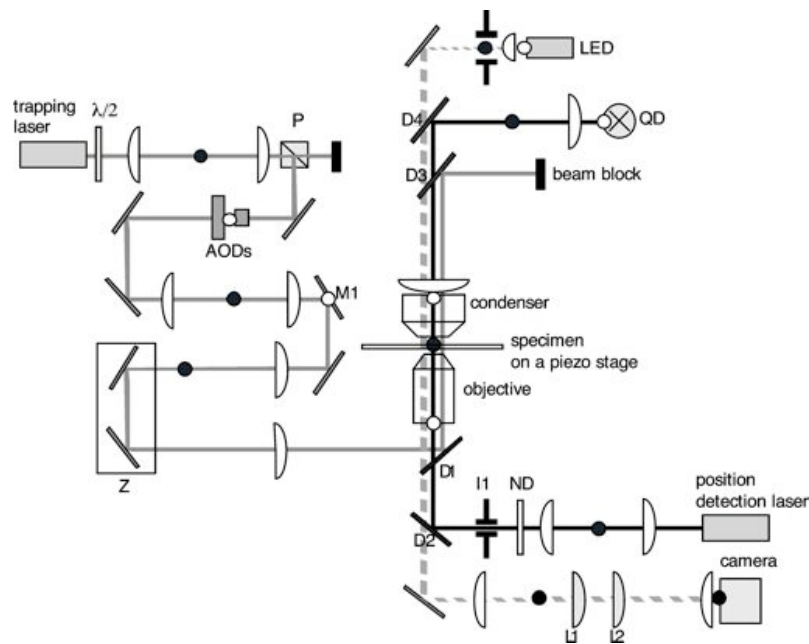


**Figure 2.5:** The optical set-up of a custom-built microscope, developed by Dr Teuta Pilizota, for the simultaneous position detection and optical trapping of dielectric particles. The main features include a 633nm laser for position detection via back-focal-plane interferometry onto a quadrant photodiode (QD), a 1064nm laser for the trapping of the particles in the specimen plane and an LED for simultaneous bright-field imaging. Acousto Optical Deflectors (AODs) are used to steer the position of the optical trap in two dimensions. Adapted from a figure by Dr Teuta Pilizota.

- The system can operate as a conventional inverted microscope operating in **bright-field imaging**. A high-power light-emitting diode (LED; Luxeon Star LEDs, Canada), high N.A. condenser and objective (both Nikon, Japan) allow imaging of micron-sized objects onto a black and white CCD camera (Watec, USA) operating at 25Hz. The image can be viewed on a TV monitor (Sony) via a commercial DVD recorder (LiteOn) with 250Gb hard-drive for direct recording. Videos can be recorded onto the hard-drive or directly to DVD, encoded by the MPEG-2 compression format.
- A Helium-Neon, 633nm laser (17mW; Coherent, USA) focused onto the specimen plane and specimen interference recorded onto a quadrant detector (QD; UDT Sensors, USA) allows position detection via **back-focal-plane interferometry**. A host PC including a digital signal processing board computes the  $xy$  signal from the 4 QD output voltages.
- An Ytterbium, 1064nm laser (3W; IPG Photonics Corporation, USA) forms an **optical trap** in the specimen plane. Home-built software routines running on the host PC allow fine control of the trap position via steering with acousto-optical deflectors (AODs; Opto-Electronique, France), allowing a **fast, programmable feedback loop** [160] on the trap position to be initiated.

The control of the optical trap with feedback will be discussed in more detail in Chapter 4.

For the study of the rotation of  $F_1$  with 340nm or 495nm bead-duplexes attached to the  $\gamma$ -subunit, use of the microscope in bright-field imaging mode is sufficient. The maximum rotation rate of  $F_1$  under the conditions studied was 10Hz, below the Nyquist frequency<sup>6</sup> of the CCD camera. In

---

<sup>6</sup>The Nyquist frequency corresponds to the maximum frequency that can be accurately sampled without aliasing issues and is equal to half of the sampling frequency. The

addition, the image obtained with these bead sizes is sufficient for analysis of the recorded DVD file to obtain  $xy$  position data (see Section 2.8.1). The microscope has been used in the back-focal-plane interferometry mode to record  $F_1$  rotation, predominantly with 220nm bead-duplexes, particles too small for bright-field imaging.

In addition, some  $F_1$  rotation has been observed using a custom-built dark-field microscope developed by Dr Yoshiyuki Sowa and Dr Bradley Steel. The microscope, in this study, was used solely in bright-field mode. The microscope is optimized for direct imaging and has a fast-speed camera for recording (up to 100kHz frame rate; Photron), allowing long-scale recording of 220nm bead-duplexes. Files can be downloaded from the camera as an Audio Video Interleave (AVI) file.

## 2.8 Data Analysis

---

### 2.8.1 Obtaining AVI files from DVD Files

Commercial DVD recorders and players require a stringent file directory structure on the read DVD, enabling cross-manufacturer playback of DVD videos. All DVD recorders create a folder called ‘:\VIDEO\_TS\’ in the root directory, containing IFO files (providing information as to the disk structure) and VOB files (relating to objects within the structure)<sup>7</sup>.

The DVD file structure can be ‘ripped’ into an AVI file by specialist software. We have been using the Auto Gordian Knot 2.40 (AutoGK; <http://www.autogk.me.uk>) freeware package. Subsequent temporal and spatial cropping of the AVI file was achieved using VirtualDubMod 1.5.10.2 (obtained concurrently with AutoGK). AVI files were saved uncompressed in order to maintain the maximal information.

---

sampling frequency of the CCD used was 25Hz, leading to a Nyquist frequency of 12.5Hz.

<sup>7</sup>Some DVD recorders, including our LiteOn recorders, also create a root folder called ‘:\VIDEO\_RM\’. For our intentions, this folder can be ignored.

### 2.8.2 Analysing AVI Files

AVI files were analysed using custom-built routines using LabVIEW (National Instruments), with the Image Acquisition (IMAQ) add-on. An AVI can be read by LabVIEW as a series of stacked 8-bit image files. A typical image obtained from experiment is shown in Figure 2.6. The centre of mass of a bead-duplex was calculated by the centroid method. To achieve this, the image was thresholded at a suitable pixel depth,  $I_t$ , corresponding to a pixel value slightly greater than the background intensity. A new image was obtained corresponding to all pixels being renormalized across the entire pixel spectrum depth. If pixel intensity on column  $i$  and row  $j$  is given by  $I(i, j)$ , the new image will have an pixel intensity  $I^*(i, j)$  given by:

$$I^*(i, j) = \frac{I(i, j) - I_t}{I_{max} - I_t} \times (2^8 - 1) \quad \text{if } I(i, j) \geq I_t \quad (2.2)$$

$$I^*(i, j) = 0 \quad \text{if } I(i, j) < I_t \quad (2.3)$$

where  $I_{max}$  is the maximum pixel value in each frame. Applying the centroid method allows determination of the centre point  $(x, y)$ .

$$x = \frac{\sum_i \sum_j I(i, j) \times i}{\sum_i \sum_j I(i, j)} \quad (2.4)$$

$$y = -\frac{\sum_i \sum_j I(i, j) \times j}{\sum_i \sum_j I(i, j)} \quad (2.5)$$

The minus sign in Equation 2.5 is required because, by definition, the rows of an AVI field start from 1 at the top of the image and the columns are numbered from the left, resulting in a left-handed coordinate system.

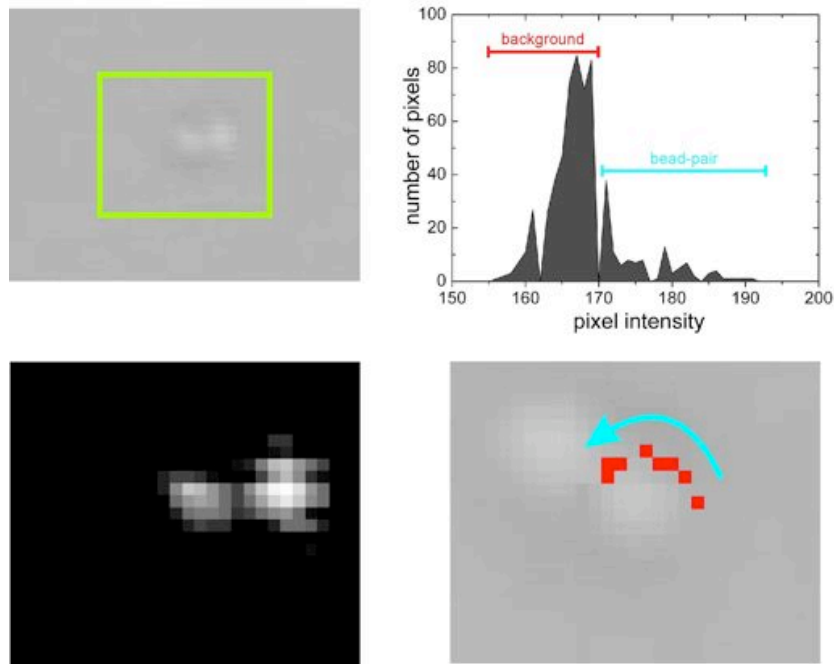


**Figure 2.6:** The extraction of  $xy$  position data from AVI images. Upper left: A region of interest (ROI) is selected containing only the bead-duplex of interest. Upper right: Due to contrast issues, the spread of pixels values within the ROI is limited to a small range. A pixel threshold is manually selected that separates the pixel intensities of the background from those of the bead-duplex. Since the highest pixel value is located at the centre of the beads, the centroid method employed is affected little by the precise placement of the threshold, assuming that the threshold chosen is greater than the background level. All pixels below the threshold are set to pixel value 0 and the rest are re-normalised over the full 8-bit range. Lower left: The resulting ROI after recalibration. The centroid method can now be used to calculate the centre of mass of the ROI. Lower right: After ten frames, the centre of mass is plotted and begins to describe an ellipse.

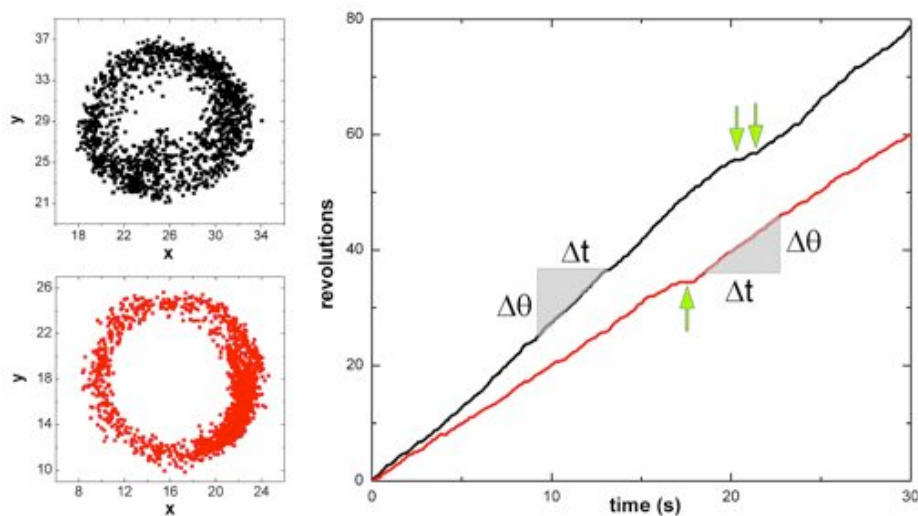


**Figure 2.7:** Two examples of  $xy$  position data obtained from the image analysis described in Section 2.8.2. The data refer to two EF<sub>1</sub> molecules with 495nm bead-duplexes attached to the  $\gamma$ -subunit. The  $xy$  data is converted to angle data for the analysis described in Chapter 3. The rotation contains clear pauses (indicated by the green arrows), due to EF<sub>1</sub> lapsing into an inhibited state, as described in Section 3.7. The rotation rate is calculated from the periods in between these pauses ( $= \frac{\Delta\theta}{\Delta t}$ ).

### 2.8.3 Obtaining Angle Data from Position Data

The  $xy$  position data obtained from the AVI analysis was converted into polar coordinates by a LabVIEW ellipse-fitting routine implementing the Simplex minimization algorithm (see Appendix Section B.2.4) and written by Dr Richard Berry. Typical  $xy$  data and the resulting angle data is shown in Figure 2.7 for a bead-duplex at 2mM ATP with a 495nm bead-duplex attached. EF<sub>1</sub> rotation data generally exhibits clear pausing, a phenomenon that will be discussed in Section 3.7. The rotation rate is found by calculating the average gradient (angular speed  $\omega = \frac{\Delta\theta}{\Delta t}$ , rotation rate  $v = \frac{\omega}{2\pi}$ ) in periods of rotation free from pauses.

# 3

## F<sub>1</sub> Rotation Studies

In this chapter I will detail the mechanical characterization of EF<sub>1</sub> rotation and make a comparison to the well-studied TF<sub>1</sub> enzyme. In Sections 3.1 and 3.2, I will discuss some general considerations that should be followed for work of this nature and summarize some of the initial problems, along with those still ongoing, that have been encountered in the development of EF<sub>1</sub> rotation assays. Following, EF<sub>1</sub> rotation over a wide-range of external loads (Section 3.3) and over nM to mM ATP concentrations (Section 3.4) will be presented, along with an investigation of single molecule binding effects (Section 3.5). In Section 3.6, data obtained in the low-load regime is analyzed allowing observation of the catalytic dwell in EF<sub>1</sub>, along with a new technique for obtaining dwell positions in F<sub>1</sub> data that may be useful in future work. An investigation into the inhibited state of EF<sub>1</sub>, a presumed off-the-catalytic pathway process, will be summarized in Section 3.7. Finally, in Section 3.8, verification of the rotary nature of F<sub>1</sub> from yeast mitochondria (*Saccharomyces cerevisiae*, YF<sub>1</sub>) will be presented.

As is the nature of this work, close collaborations have been essential to its success. Dr Mayumi Nakanishi-Matsui and Dr Hiroyuki Hosokawa, in the group of Prof Masamitsu Futai, have been my on-call biochemists when advice and guidance have been required. Indeed, the initial F<sub>1</sub> rotation assay

techniques came from Prof Futai's group, via Dr Teuta Pilizota who spent one month working in their laboratory. When I took over the project of  $EF_1$  rotation it was very much in its infancy in Oxford, with only a few rotating  $EF_1$  molecules having been observed. All the data obtained in this chapter, with the exception of the gold-bead data, were obtained by myself, but I am indebted to the work of the aforementioned for laying the foundations of the project. The low-load, 40–200nm single gold bead data were obtained by Dr Nakanishi-Matsui and passed to me as  $xy$  position data.  $YF_1$  enzyme was purified and sent to us by Prof David Mueller.

### 3.1 The Philosophy of $F_1$ Rotation Analysis

---

Before we begin, it is worth thinking about the problems involved with single molecule work, especially the analysis of  $F_1$  rotation data analysis.

A good scientific model should attempt to explain all that is observed in experiment. A model that only explains a subset of the data may be very accurate at what it is describing but, ultimately, it can be improved upon. Importantly, a model should make clear what it is ignoring and what it is trying to explain.

This concept is very important in the  $F_1$  field. In the large bead assays I will present in the following sections, rotating molecules were selected by eye in real-time. In all instances there was a subset of molecules that were rotating consistently, along with a smaller subset of molecules that rotated poorly. In addition to these species are all the visible beads that may or may not be connected to  $F_1$  - all we can tell is that they are definitely not rotating. Again, only those molecules that were rotating consistently were recorded.

This method would appear to be similar to that employed by most researchers in the field, i.e., to only select those molecules that show clean, beautiful data, especially if it agrees with your hypothesis! This method

feels unscientific and will, no doubt, be extremely susceptible to bias on the part of the researcher. That being said, an element of this selection process is unavoidable, especially when >90% of all available data is of insufficient quality for analysis. It is apparent that all current  $F_1$  models do not explain all of the experimental data obtained. Indeed, it may not be unfair to suggest that even the best models only accurately explain  $\sim 1\%$  of the data! Ideally, a dataset would be composed of two distinct sub-populations (i.e., those molecules that are functioning properly and those that are not) allowing rigorous statistical differentiation between the two groups. In  $F_1$  assays, the two sub-populations, whilst resolvable, are not always satisfactorily distinct and a careful choice of cut-off has to be made.

There is, however, one counter-argument - a caveat that I feel is very important - which is that this selection of data is preferential to the over-analysis of bad (noisy) data. If we accept my assertion that only 1% of all data are ‘perfect’, that means that 99% is available for mis-analysis. Single-molecule work, by definition, involves the analysis of single events. However, the results of single events should be expressed in terms of statistics describing a large population of events. Granted, it is not always possible to obtain a large dataset, but equally, analysis of just one molecule is not reliable and should be flagged as so.

## 3.2 Obtaining Compatible Surfaces and an Optimized Assay

---

At the commencement of this project, rotation of  $EF_1$  had only been observed by members of the group in a small handful of molecules. In these early assays, the most common problems were a very low number of rotating beads and insufficient adhesion between the beads and the coverslip. The assay preparation described in Section 2.6 represents the culmination of many

attempts to optimize the assay. In all honesty, a stable  $EF_1$  rotation assay has still not been obtained. For a stable assay, day-to-day repeatability and predictability are required - this is certainly not the case in our  $EF_1$  assays. This has been a cause of great frustration and annoyance. However, the assay has now been optimized such that, when it works, it works well.

One difficulty in optimizing the system is that we infer the amount of  $F_1$  protein on the coverslip surface by the number of beads stuck. Unfortunately, the biotinylated beads themselves will stick to many things through non-specific binding. Therefore, optimization involves obtaining the ‘stickiest’ surface for  $F_1$  to adhere to, but the least sticky for beads. The surfaces we have used will be listed here, if for nothing else, as an appreciation of the history of this project and will be presented in chronological order. Their preparations are described in Section 2.4.

- BSA-coated surface
- Horseradish Peroxidase-coated surface
- $Ni^{2+}$ -coated surface
- $Cu^{2+}$ -coated surface

In addition, we have used BSA and casein as options for blocking the surface from non-specific sticking of the beads. Of these, BSA gave the best results and all results presented in this thesis use BSA to block the surface. The exact origin of the blocking ability of BSA is not clear. BSA carries a long-range negative charge at pH7.0 [163], as do the polystyrene beads used. In turn, the absorption of BSA onto polystyrene beads has been shown to have contributions from electrostatics, hydrogen-binding and hydrophobic effects [164,165,166,167]. 1mg/ml BSA was insufficient to block non-specific sticking of the beads to the glass surface but 10mg/ml BSA reduced the background to insignificant levels and was the concentration used throughout.

One of the obvious advantages of using a chelated  $\text{Ni}^{2+}$  or  $\text{Cu}^{2+}$  surface is the controlled architecture of the enzyme-surface interaction. The His-tags are introduced into the  $N$ -terminus of the  $\alpha$ -subunits with the aim that this will determine the orientation of  $\text{F}_1$  with the  $\gamma$ -subunit facing away from the surface, available for attachment of beads. The initial  $\text{EF}_1$  used had three His<sub>6</sub>-tags (on the  $\alpha$ -subunit), as did  $\text{YF}_1$  (on the  $\beta$ -subunit). It was noted that rotating bead-duplexes came off from the surface on the time-scale of minutes, resulting in very few rotating molecules after 20 minutes. The most likely cause for this is that the  $\text{F}_1$  itself was coming off from the surface since the bead-duplexes are attached to  $\text{F}_1$  via the strong biotin-streptavidin linkage ( $K_D = 4 \times 10^{-14}\text{M}$  [162]). Indeed, the attachment of His<sub>6</sub>-tags to  $\text{Ni}^{2+}$ -NTA is only a transient binding, with dissociation rate  $k_d = 1.8\text{s}^{-1}$  [168], i.e., a His<sub>6</sub>-tag will dissociate from  $\text{Ni}^{2+}$ -NTA on average after only  $\sim 0.5\text{s}$ . Various schemes were discussed to solve this issue (some of which will be discussed in Section 5.2), chiefly based upon improving the His-tag/ $\text{Ni}^{2+}$ -NTA interaction. A His<sub>10</sub>-tag has a slightly improved attachment to  $\text{Ni}^{2+}$ -NTA ( $k_d = 1.4\text{s}^{-1}$  [168]) and, if three  $\text{Ni}^{2+}$ -NTA heads can be brought together in the correct topology, the dissociation constant drops almost five orders of magnitude to  $k_d = 5 \times 10^{-5}\text{s}^{-1}$  for His<sub>10</sub>-tags. A side project was spun-off trying to create a triple  $\text{Ni}^{2+}$ -NTA head (Tris-NTA), an important piece of work not only for  $\text{F}_1$  studies but also for other single molecule work. At the same time,  $\text{EF}_1$  with His<sub>10</sub>-tags was very kindly produced for us by Dr Hiroyuki Hosokawa (see Section 2.2) with the same bulk characteristics as  $\text{EF}_1$  with His<sub>6</sub>-tags. The observed improvement was marginal for use with the  $\text{Ni}^{2+}$ -NTA-silane surface, presumably due to the low surface density of  $\text{Ni}^{2+}$ -NTA on these surfaces. It is hoped, however, that if a Tris-NTA surface can be made in the near future, the  $\text{EF}_1$  with His<sub>10</sub>-tags will, in effect, be irreversibly bound to the surface. The data in this thesis were primarily obtained using  $\text{EF}_1$  with His<sub>10</sub>-tags, except for the

low-load data in Section 3.6 which were obtained using the His<sub>6</sub>-tag variety. The YF<sub>1</sub> data of Section 3.8 were obtained using YF<sub>1</sub> with His<sub>6</sub>-tags.

If we define the yield of the assay as the ratio of rotating beads to stuck beads, the original assays typically had yields of <1%, and rotating beads were often observed detaching from the surface in the first few minutes of recording. Of the surfaces tried, the Ni<sup>2+</sup>-NTA surfaces were comfortably the best for obtaining long-term recording. On these surfaces, I have observed EF<sub>1</sub> molecules rotate for up to two hours. Furthermore, using BSA as a blocker, the yield of the assay has been improved to 5–10%, typically. However, on the very best days (and I have no justification why some days are better than others), the yield has pushed close to 50%.

A further improvement to the assay was in the reliable production of bead-duplexes (as described in Section 2.5.2). Purification of bead-duplexes resulted in a ~5–10× increase in the fraction of bead-duplexes attached to EF<sub>1</sub> molecules.

In order to obtain the amount of data required for the characterization of EF<sub>1</sub> presented hereon, this initial optimization work was essential and should not be sacrificed in future similar projects.

### 3.3 Load-Dependence of EF<sub>1</sub>

---

At the length scales we are dealing with in F<sub>1</sub> rotation studies, the Reynolds number<sup>1</sup>,  $R$ , is typically in the range  $10^{-4}$ – $10^{-6}$ , indicating that inertial forces are negligible. In this regime, the Navier-Stokes equation is solvable for a sphere rotating about its axis with a creeping, non-slip boundary

---

<sup>1</sup>The Reynolds number is given by  $R = \frac{vL\rho}{\eta}$ , where  $v$ ,  $L$ ,  $\rho$  and  $\eta$  are the speed of the object relative to the medium, the size of the object, the density of the medium and the viscosity of the medium.  $R$  represents the ratio of inertial forces to viscous forces as experienced by the object when moving within the medium.

condition to be [3, 169]

$$T = \omega \zeta_r \quad (3.1)$$

$$\zeta_r = 8\pi\eta r^3 \quad (3.2)$$

where  $T$ ,  $\zeta_r$ ,  $\omega$ ,  $\eta$  and  $r$  are the torque on the sphere due to drag, the frictional drag coefficient, the angular speed, the viscosity of the surrounding medium and the radius of the sphere respectively. Equation 3.1 holds true for all rotational geometries. In F<sub>1</sub> rotation assays the sphere is not rotating about its own axis and therefore we need to translate Equation 3.2 to off-axis geometries, leading to

$$\zeta_{r,t} = \zeta_r + \zeta_t d^2 \quad (3.3)$$

$$= 8\pi\eta r^3 + 6\pi\eta r d^2 \quad (3.4)$$

where  $d$  is the distance between an axis parallel to the rotation axis running through the centre of the sphere and the rotation axis (for a full derivation see [169]). The second term in Equation 3.4 represents Stokes drag,  $\zeta_t$ , for a small sphere of radius  $r$  moving through a medium with translational linear speed  $v = d \times \omega$ ,  $\zeta_t = 6\pi\eta r$ .

Before I present results of EF<sub>1</sub> under varied loads, we should take a moment to carefully consider the geometry of F<sub>1</sub> rotation assays.

F<sub>1</sub> immobilized onto a surface is small ( $\sim 10\text{nm}$ ) compared to the size of the probes we attach ( $40\text{--}1000\text{nm}$ ). The beads we use are biotinylated and attach to F<sub>1</sub> at the  $\gamma$ -subunit via streptavidin. F<sub>1</sub> with streptavidin attached to the  $\gamma$ -subunit would constitute a  $\sim 15\text{nm}$  complex on the glass surface. It would appear likely that a bead will attach to the F<sub>1</sub>-streptavidin complex at an arbitrary angle,  $\phi$ , as shown in Figure 3.1a. If we make the coarse approximation that the surface is flat on this length scale, there will be a minimum angle,  $\phi_{\min}$ , due to the interaction of the bead with the surface.

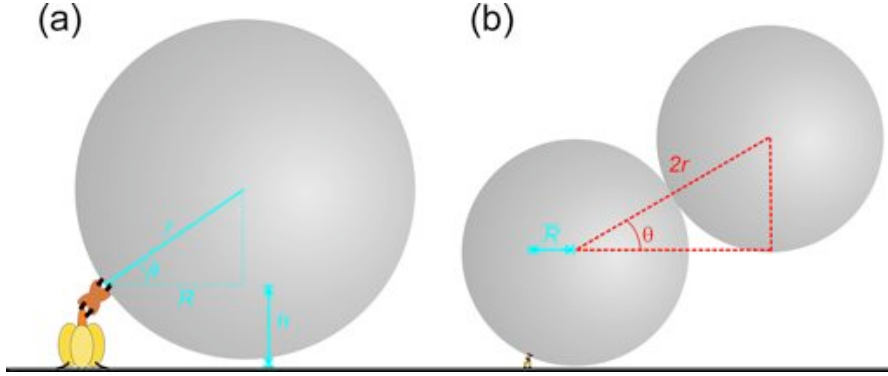


**Figure 3.1:** The attachment geometries of single beads and bead-duplexes to  $F_1$ -ATPase. (a) A single bead has a small radius of rotation, limited by the close proximity of the surface. If the distribution of attachment angles,  $\phi$ , is isotropic, the average radius of gyration,  $\bar{R}$ , can be calculated as given in Equation 3.8. (b) In general, a bead-duplex can attach at any angle,  $\theta$ , and the resulting radius of rotation of the outer bead will vary accordingly. We will assume that the bead-duplex attaches isotropically around a hemispheric shell of solid angle  $2\pi$ .

$\phi_{\min}$  will be a function of the bead radius,  $r$ , as given by

$$\sin(\phi_{\min}) = 1 - \frac{h}{r} \quad (3.5)$$

where the height,  $h$ , of the  $F_1$ -streptavidin complex is 15nm. The corresponding distance of the bead centre to the  $F_1$  rotation axis,  $R(\phi)$ , will be equal to  $r\cos(\phi)$ . In general,  $\phi$  can range from any angle between  $\phi_{\min}$  and  $\frac{\pi}{2}$ . If we make the assumption that there are no preferential angles, the angular distribution will be isotropic about a shell of solid angle  $\Omega = 2\pi(1 - \sin(\phi_{\min}))$  and the density of states,  $n(\phi)d\phi$ , will be proportional to  $\cos(\phi)d\phi$ . We can then calculate the mean gyration radius,  $\bar{R}$ , that a bead

| Bead Diameter, $2r$ (nm) | Average Rotation Radius, $\bar{R}$ (nm) |
|--------------------------|---|
| 40                       | 14                                      |
| 60                       | 18                                      |
| 80                       | 22                                      |
| 100                      | 25                                      |
| 200                      | 36                                      |
| 220                      | 37                                      |
| 340                      | 47                                      |
| 495                      | 56                                      |

**Table 3.1:** The expected average rotation radius,  $\bar{R}$ , of a single bead attached to a 15nm F<sub>1</sub>-streptavidin complex calculated from a simple geometry argument and given in Equation 3.8.

of radius  $r$  will make when attached to F<sub>1</sub>.

$$\bar{R} = \frac{\int_{\phi_{\min}}^{\frac{\pi}{2}} R(\phi)n(\phi) d\phi}{\int_{\phi_{\min}}^{\frac{\pi}{2}} n(\phi) d\phi} \quad (3.6)$$

$$= \frac{\int_{\phi_{\min}}^{\frac{\pi}{2}} r \cos^2(\phi) d\phi}{\int_{\phi_{\min}}^{\frac{\pi}{2}} \cos(\phi) d\phi} \quad (3.7)$$

$$= \frac{r^2}{2h} \left( \frac{\pi}{2} - \phi_{\min} - \frac{1}{2}\sin(2\phi_{\min}) \right) \quad (3.8)$$

Table 3.1 summarizes the expected average radii of rotation for the bead sizes used and the result is also plotted in Figure 3.2. We can see that as the size of the bead increases, only a small increase in the rotation radius is obtained. We can now use Equation 3.4 to calculate the average frictional drag coefficient,  $\bar{\zeta}_{r,t}$ , for a single bead in a similar manner to how we found

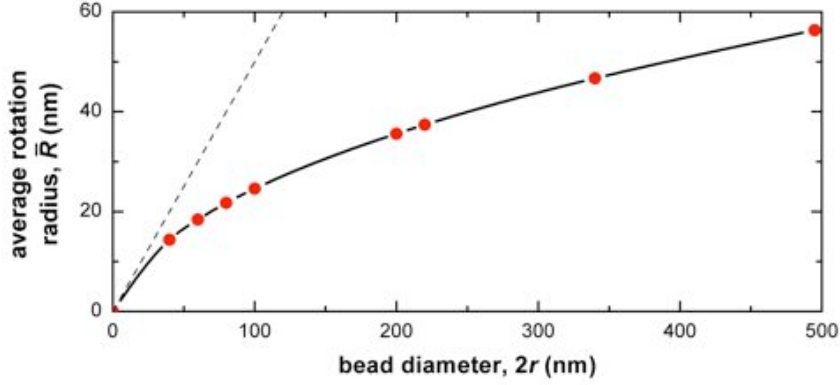


**Figure 3.2:** An illustration of the expected average rotation radius,  $\bar{R}$ , as predicted by Equation 3.8, for the beads sizes used in this thesis. The data plotted are also shown in Table 3.1. The dashed line indicates the departure of Equation 3.8 from  $\bar{R} = r$ .

the average rotation radius.

$$\bar{\zeta}_{r,t} = \frac{\int_{\phi_{\min}}^{\frac{\pi}{2}} \zeta_{r,t}(\phi) n(\phi) d\phi}{\int_{\phi_{\min}}^{\frac{\pi}{2}} n(\phi) d\phi} \quad (3.9)$$

$$= \frac{\int_{\phi_{\min}}^{\frac{\pi}{2}} \left( 8\pi\eta r^3 + 6\pi\eta r [r \cos(\phi)]^2 \right) \cos(\phi) d\phi}{\int_{\phi_{\min}}^{\frac{\pi}{2}} \cos(\phi) d\phi} \quad (3.10)$$

$$= \frac{\pi\eta r^3}{h} \left( 14 [1 - \sin(\phi_{\min})] - 2 [1 - \sin^3(\phi_{\min})] \right) \quad (3.11)$$

In the case of the attachment of a bead-duplex to F<sub>1</sub>, we have the complication that we do not know the rise angle of the bead-duplex with respect to the surface (angle  $\theta$  in Figure 3.1b). I have attempted to quantify the angle from the microscope images but this has not been possible since the microscope focus greatly affects the image and it is not constant between molecules. This means that, again, we will have to deal with average drag coefficients for each size of bead-duplex.

Figure 3.1b shows the geometry we must consider. We will assume that the rise angle  $\theta$  can be in the range of 0 to  $\frac{\pi}{2}$  and that the distribution will be isotropic about a hemispheric shell. The frictional drag coefficient,  $\zeta_{r,t}(\theta, \phi)$ , will be approximated by a linear combination of the drag coefficients for two off-axis single beads.

$$\zeta_{r,t}(\theta, \phi) = 2 \times 8\pi\eta r^3 + 6\pi\eta r \left( [R(\phi)]^2 + [R(\phi) + 2r \cos(\theta)]^2 \right) \quad (3.12)$$

We could then calculate the average drag coefficient for each size of bead-duplex by performing a double integral over both  $\phi$  and  $\theta$ . I do not feel that the simple geometrical argument and assumptions made justify this level of intricacy. To make the mathematics more straightforward, we will make the simplification that the inner bead attaches at the mean distance,  $\bar{R}$ , given by Equation 3.8. This simplification will only affect the cross-term in Equation 3.12 but since  $2r\cos(\theta)$  will generally be much larger than  $R(\phi)$ , the simplification will make little difference to the result. Equation 3.12 then reduces to

$$\zeta_{r,t}(\theta) = \pi\eta r [16r^2 + 12\bar{R}^2 + 24r^2\cos^2(\theta) + 24\bar{R}r\cos(\theta)] \quad (3.13)$$

This leads to a mean frictional drag coefficient for a bead-duplex of

$$\bar{\zeta}_{r,t} = \pi\eta r [32r^2 + 12\bar{R}^2 + 6\pi\bar{R}r] \quad (3.14)$$

In this thesis, we have used 40–200nm single gold beads and 220–495nm bead-duplexes. Table 3.2 shows the drag coefficients calculated from Equations 3.11 and 3.14.

| Bead Diameter, $2r$ (nm) | $\bar{\zeta}_{r,t}$ single (pN·nm·s) | $\bar{\zeta}_{r,t}$ double (pN·nm·s) |
|--------------------------|--------------------------------------|--------------------------------------|
| 40                       | $2.8 \times 10^{-4}$                 |                                      |
| 60                       | $8.7 \times 10^{-4}$                 |                                      |
| 80                       | $2.0 \times 10^{-3}$                 |                                      |
| 100                      | $3.7 \times 10^{-3}$                 |                                      |
| 200                      | $2.8 \times 10^{-2}$                 |                                      |
| 220                      |                                      | $1.7 \times 10^{-1}$                 |
| 340                      |                                      | $5.9 \times 10^{-1}$                 |
| 495                      |                                      | 1.8                                  |

**Table 3.2:** The average frictional drag coefficients,  $\bar{\zeta}_{r,t}$ , for single beads and bead-duplexes, using  $\eta = 10^{-9}$  pN·nm<sup>-2</sup>s, using Equations 3.11 (single beads) and 3.14 (bead-duplexes).

### Correcting $\zeta$ Due to the Close Proximity of the Surface

The Stokes drag,  $\zeta_t$ , and the frictional drag due to rotation (Equation 3.2),  $\zeta_r$ , are derived for a sphere moving in a medium with an infinite boundary condition, i.e., far from other spheres and boundaries. Unfortunately, F<sub>1</sub> rotation assays deviate far from this idealized system. By immobilizing F<sub>1</sub> onto a glass surface, the attached bead is very close to the surface and fluid flow lines will now become greatly affected by the surface's proximity. As a result, the drag coefficient has to be corrected, with the degree of correction becoming significant when the distance of the sphere centre from the surface,  $H$ , is of a similar order to the sphere radius,  $r$  [169, 170]. Unfortunately, the exact geometry of a bead or bead-duplex rotating close to the surface has not been solved. The closest approximation being for a free bead moving parallel to a non-slip boundary. Applying these correction factors gives the following relations for a sphere rotating off-axis close to a surface

$$\text{with } \zeta_t = \frac{6\pi\eta r}{1 - \frac{9}{16} \left(\frac{r}{H}\right) + \frac{1}{8} \left(\frac{r}{H}\right)^3 - \frac{45}{256} \left(\frac{r}{H}\right)^4 - \frac{1}{16} \left(\frac{r}{H}\right)^5 + \dots} \quad (3.15)$$

$$\text{and } \zeta_r = \frac{8\pi\eta r^3}{1 - \frac{1}{8} \left(\frac{r}{H}\right)^3 + \dots} \quad (3.16)$$

Equations 3.15 and 3.16 represent an underestimate of the true correction

| Bead Diameter, $2r$ (nm) | $\theta = 0$ | $\theta = \frac{\pi}{2}$ |
|--------------------------|--------------|--------------------------|
| 220                      | 81%          | 5%                       |
| 340                      | 97%          | 6%                       |
| 495                      | 106%         | 6%                       |

**Table 3.3:** The increase in the drag coefficient,  $\zeta_{r,t}$ , due to the close proximity of the surface as compared to the infinite boundary condition solution for bead-duplexes oriented flat ( $\theta = 0$ ) or fully raised ( $\theta = \frac{\pi}{2}$ ).

factors for our geometry. They are derived from a free bead which will begin to rotate about an axis in the plane of the boundary but perpendicular to the direction of motion (akin to the bead rolling directly along the surface) due to increased drag close to the surface. A bead attached to  $F_1$  is not free to rotate about this axis. Advanced theoretical calculations would be required to calculate the correction factors involved in a  $F_1$  rotation assay and are not attempted here. As a result, Equations 3.15 and 3.16 represent our best current correction factors.

Since,  $\frac{r}{H} \leq 1$ , the degree of correction required is much larger for the translational contribution to the total drag (Equation 3.15) compared to the rotational contribution (Equation 3.16). Therefore, little correction is required for single beads attached to  $F_1$  because the majority of the single bead drag is due to rotation ( $\geq 80\%$ ). The bead-duplex drag, however, requires a large correction, mainly due to the orbit of the outer bead. It is difficult to estimate the height of a bead-duplex from the surface,  $H$ , because of the unknown geometry. For the case of a ‘propellor-like’ bead-duplex ( $\theta=0$ ), the correction will be greatest. When  $\theta = \frac{\pi}{2}$ , the correction will only be in  $\zeta_r$  and will therefore be small. Assuming again that  $h \approx 15\text{nm}$ , and with  $H = r + h$ , the degree of increase of the total drag coefficient,  $\zeta_{r,t}$ , is summarized for these two cases in Table 3.3.

Owing to the angular distribution in  $\theta$ , it would appear that the average drag coefficient,  $\bar{\zeta}_{t,r}$ , should be in the range of 50–80% higher than that predicted from Equation 3.14 for the size bead-duplexes used in this study.

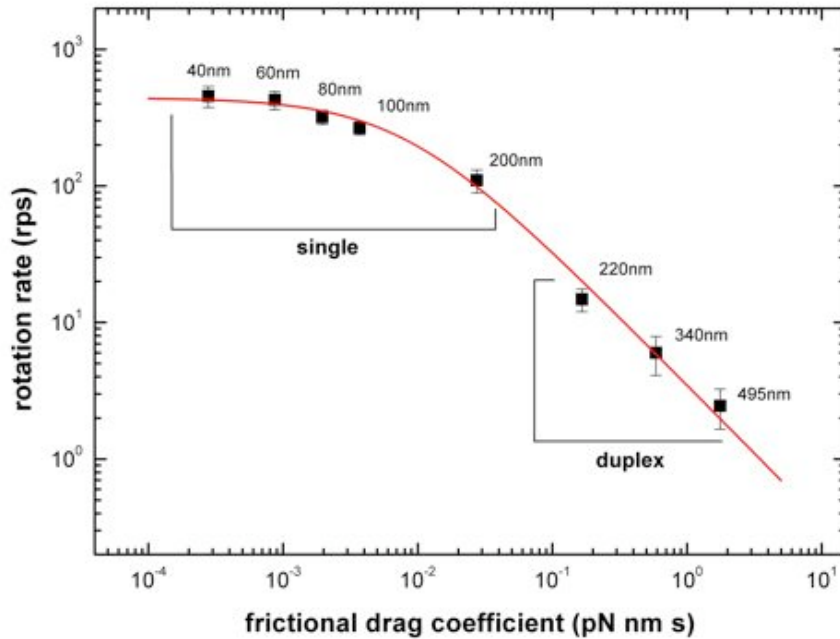


**Figure 3.3:** The rotation rate of EF<sub>1</sub> at 2mM ATP as a function of attached viscous load. Points plotted represent mean±std. The curve in red is a least-squares fit to the data using Equation 3.21. The fitting parameters give  $a = 3.5 \pm 0.3 \text{ pN} \cdot \text{nm}$  and  $b = 0.0079 \pm 0.0013 \text{ pN} \cdot \text{nm} \cdot \text{s}$ .

A 495nm bead-duplex represents an equivalent viscous drag to the fluorescent actin filaments used in the early rotation assays [34, 88, 87]. EF<sub>1</sub> with a 495nm bead-duplex attached rotates at only a few revolutions per second at 2mM ATP. Assuming that the actual (internal) torque produced by EF<sub>1</sub> is independent of viscous load, the reason EF<sub>1</sub> rotates so slowly with large bead-duplexes attached is that there is a finite time required for the bead-duplex to be rotated through the medium. We shall refer to this time as the bead ‘revolution transit time’. As the load decreases, this revolution transit time decreases accordingly.

### 3.3.1 An Estimate of EF<sub>1</sub> Torque

Figure 3.3 shows the average rotation rate of EF<sub>1</sub> as a function of viscous drag coefficient of the attached probe. As the size of the attached probe de-

increases (moving from right to left in the figure), the rotation rate of EF<sub>1</sub> increases until the speed reaches a plateau at  $\zeta_r < 10^{-3}$  pN·nm·s. The plateau region corresponds to single gold beads smaller than 60nm. Such small viscous loads do not significantly impede EF<sub>1</sub> rotation since the internal enzymatic steps are now the rate-limiting processes. The corner point in Figure 3.3 ( $\zeta_r \approx 5 \times 10^{-2}$  pN·nm·s) corresponds to the situation where the revolution transit time is approximately equal to the sum of the internal processes. The time for each revolution,  $t_{\text{rev}}$ , can be expressed as the sum of the revolution transit time contribution,  $t_{\text{tran}}$ , and the average contribution due to internal chemical processes,  $t_{\text{int}}$ , i.e.

$$t_{\text{rev}} = t_{\text{tran}} + t_{\text{int}} \quad (3.17)$$

Applying Equation 3.1 gives

$$t_{\text{rev}} = \frac{2\pi\zeta_{r,t}}{T} + t_{\text{int}} \quad (3.18)$$

Therefore, the observed average rotation rate,  $v_{\text{obs}}$ , should be given by

$$v_{\text{obs}} = \left( t_{\text{int}} + \frac{2\pi\bar{\zeta}_{r,t}}{T} \right)^{-1} \quad (3.19)$$

$$= \frac{T}{t_{\text{int}}T + 2\pi\bar{\zeta}_{r,t}} \quad (3.20)$$

$$= \frac{a}{b + \bar{\zeta}_{r,t}} \quad (3.21)$$

Equation 3.20 contains two unknowns which can be obtained from a two-parameter non-linear curve fit to the data using Equation 3.21, with  $a = \frac{T}{2\pi}$  and  $b = t_{\text{int}}a$ . A discussion on non-linear curve-fitting is included in Appendix B. The fit is shown by the red curve in Figure 3.3. The rotation rate at zero viscous load,  $v_0$ , can be found from  $t_{\text{int}}$  by  $v_0 = \frac{1}{t_{\text{int}}}$ . The curve fit is consistent with  $v_0 = 442 \pm 15$  rps and a torque of  $T = 21.9 \pm 1.8$  pN·nm.

Making the adjustment for the close proximity of the glass surface (discussed earlier and using the corrections given in Equations 3.15 and 3.16) predicts that the true torque produced by EF<sub>1</sub> is in the range of 33–40pN·nm.

In fact, this range probably represents a lower limit since unquantifiable factors, hitherto ignored, will result in an underestimate of the torque. For example, (1) any occasional interaction with the surface will appear as a slower speed, (2) any unobserved short pauses due to inhibition (see Section 3.7), will create a slower effective speed, and (3) due to biased recording, it may not always be possible to observe the rotation of highly-raised ( $\theta = \frac{\pi}{2}$ ), fast-rotating bead-duplexes by eye.

### Analysis of EF<sub>1</sub> Speed Distributions

To see if observational bias has a significant effect on the expected speed distribution I have plotted the speed distribution for all molecules recorded with 220nm, 340nm, and 495nm bead-duplexes attached in Figure 3.4b. If the assumption is made that all EF<sub>1</sub> molecules produce the same internal torque then the expected rotation rate will be determined only by the rise angle of the bead-duplex,  $\theta$ . To simplify matters we shall not be concerned at this point with the surface correction factor. The rotation rate should be given by

$$\omega = \frac{T}{\bar{\zeta}_{r,t}} \quad (3.22)$$

$$= \frac{T}{\pi\eta r [16r^2 + 12D^2 + 24r^2\cos^2(\theta) + 24Dr\cos(\theta)]} \quad (3.23)$$

To further simplify matters, we will let  $D = 0$ , since this correction only makes a ~20% contribution to  $\bar{\zeta}_{t,r}$  and varies little with bead-duplex size. This factor can then be approximated by a multiplicative constant. There-

fore, for each bead-duplex size, the rotation rate,  $\omega$ , will be given by

$$\omega \propto \frac{1}{2 + 3 \cos^2(\theta)} \quad (3.24)$$

However, we know that we should expect to see the number of molecules,  $N$ , with bead-duplex raised at angle  $\theta$  to be proportional to  $\cos(\theta)$  and the density of states in  $\theta$ -space will be given by  $N(\theta)d\theta \propto \cos(\theta)d\theta$ . By definition,  $\int N(\theta)d\theta = \int N(\omega)d\omega$ , and using Equation 3.24 we can determine the density of states in  $\omega$ -space to be

$$\begin{aligned} N(\omega) d\omega &= A \frac{1}{\omega^2} \left(5 - \frac{P}{\omega}\right)^{-\frac{1}{2}} d\omega && \text{for } \frac{P}{5} \leq \omega \leq \frac{P}{2} \\ N(\omega) d\omega &= 0 && \text{otherwise} \end{aligned} \quad (3.25)$$

where  $A$  and  $P$  are constants relating to the number of molecules observed and the motor torque respectively, and  $N(\omega) d\omega$  is the number of molecules in the area  $\omega d\omega$ . In fact  $P$  corresponds to the speed of rotation of the bead-duplex relative to the speed of rotation of a single bead attached to the motor and, hence,  $\omega_{\max} = \frac{P}{2}$  in Equation 3.25. An example of the shape of the distribution detailed in Equation 3.25 is shown in Figure 3.4a.  $N(\omega)$  tends to infinity at  $\omega = \frac{P}{5}$ . However, the integral is finite in this region and therefore Equation 3.25 does describe a physically-realistic distribution.  $A$  and  $P$  can be found from a non-linear curve fit to the distributions as shown in Figure 3.4b. Since the distribution is rapidly changing over each histogram bin width, care has to be taken to make the necessary transformation into ‘binned’ data, as covered in Appendix B. Equation 3.25 can be integrated

to yield the histogram distribution,  $g(\omega)d\omega$ , to be

$$g(\omega) d\omega = C \left[ \left( 5 - \frac{P}{\omega} \right)^{\frac{1}{2}} \right]_a^b d\omega \quad \text{for } \frac{P}{5} \leq \omega \leq \frac{P}{2}$$

$$g(\omega) d\omega = 0 \quad \text{otherwise} \quad (3.26)$$

where  $a$  and  $b$  are the lower and upper edges of each bin and  $C$  is a constant related to  $A$  in Equation 3.25.

Assuming that the maximum rotation rate,  $v_{\max}$ , occurs at the minimum drag coefficient,  $\zeta_{\min}$ , setting  $D = 0$  and  $\theta = \frac{\pi}{2}$  in Equation 3.23 gives

$$T = 2\pi v_{\max} \zeta_{\min} \quad (3.27)$$

$$= 2\pi \frac{P}{2} 16\pi\eta r^3 \quad (3.28)$$

The torques predicted from this fitting are 43pN·nm, 27pN·nm, and 21pN·nm for 495nm, 340nm, and 220nm bead-duplexes respectively. Unfortunately, due to the complexity of the fitting function, no errors can be computed for the fitted parameters. In theory, these torques require little calibration since they represent the  $\theta = \frac{\pi}{2}$  case. However, it is apparent that the torque decreases as the bead-duplex size decreases. One explanation would be that as the bead-duplex size decreases, observational bias against very fast rotation ( $\theta = \frac{\pi}{2}$ ) of small bead-duplexes increases. This is not unexpected since highly-raised small bead-duplexes are very difficult to see in the set-up we have. Perhaps automated recording and analysis of each field of view could go some way to eliminating this problem. The result is that the mean speed observed for the smaller bead-duplexes will actually be lower than the true mean. Indeed, the mean rotation rate for the 220nm bead-duplexes lies some way below the line in Figure 3.3. If there was observational bias in practice, the distribution described in Equation 3.25 should be broader than the experimental data in Figure 3.4b since the full range of speeds are not

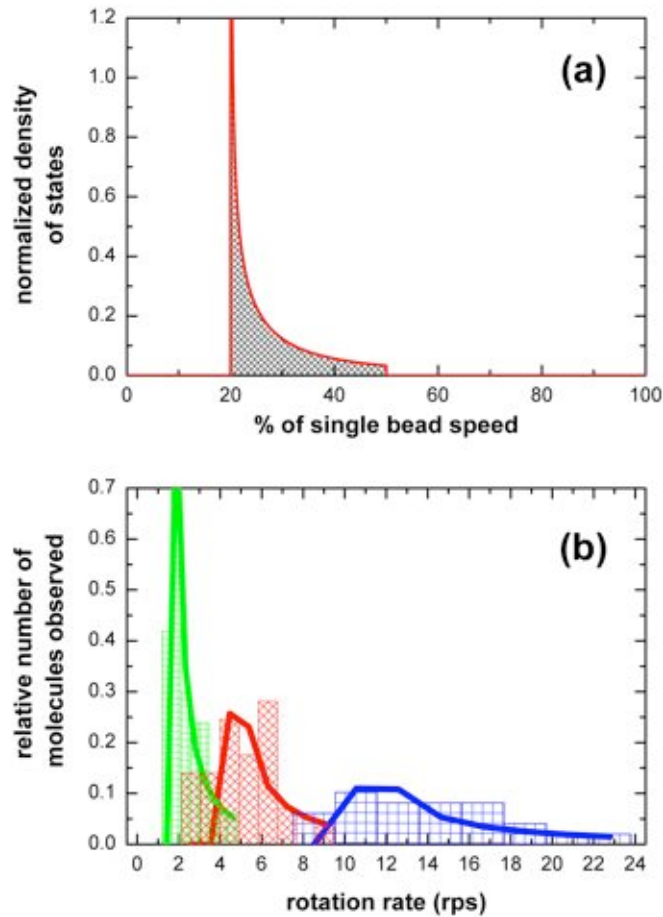


**Figure 3.4:** By considering the angular rise of the bead-duplex,  $\theta$ , a distribution of observed rotation rates of EF<sub>1</sub> can be predicted. (a) The theoretical distribution for the density of states, as given by Equation 3.25, is plotted. The maximum possible speed corresponds to half that of a single bead rotating about its axis. The more populous minimal speed is only 40% of the maximum rate for a bead-duplex (20% of maximal single bead rate). (b) The observed speed distributions for EF<sub>1</sub> with 495nm (green hatching; total number of molecules observed,  $n = 37$ ), 340nm (red hatching;  $n = 31$ ) and 220nm (blue hatching;  $n = 24$ ) bead-duplexes attached, with  $[\text{ATP}] = 20\mu\text{M} - 2\text{mM}$  (at these concentrations the rotation speed is independent of  $[\text{ATP}]$ , see Section 3.4). The non-linear curve fit of Equation 3.26 is shown by the overlaid thick line in each case.

recorded. Actually, the speed distributions obtained appear to be slightly broader than the theoretical function. Including the surface correction factors of Equations 3.15 and 3.16, ignored up to this point, will reduce the lower end of the predicted speed range, whilst keeping a similar predicted maximal speed. This suggests that bias against fast rotating molecules is minimal in this study.

### 3.3.2 A Summary of $EF_1$ Load Dependence

The work presented here suggests that  $EF_1$  produces torque in the range of 33–40pN·nm. The previous studies of  $EF_1$  have predicted 40pN·nm [88] and 50pN·nm [87] using actin filaments. The use of actin filaments in these studies has resulted in a large spread of speeds, possibly due to uncertainty in the filament length, but surface corrections to the drag coefficient are negligible because the actin filament is very thin. By comparison,  $TF_1$  has been reported to generate 40pN·nm using actin filaments [34, 73] and 20pN·nm using nano-engineered gold rods [60], whilst  $F_1$  from spinach chloroplasts was reported to produce torque in the range 10–40pN·nm [89]. A brief discussion as to the validity of these estimates will be presented in Chapter 5.

## 3.4 Enzymatic Kinetics of $EF_1$ Over a nM–mM [ATP] Range

---

We have seen that, at 2mM ATP, the rotation rate of  $EF_1$  can be explained by requiring a finite time for internal enzymatic processes to occur, and for the rotational transit of the attached probe due to viscous drag. As a result,  $EF_1$  with large probes rotates much slower than  $EF_1$  with smaller attached probes. If the ATP concentration is decreased below a certain level, the observed rotation rate of  $EF_1$  slows. Finally, at very low ATP

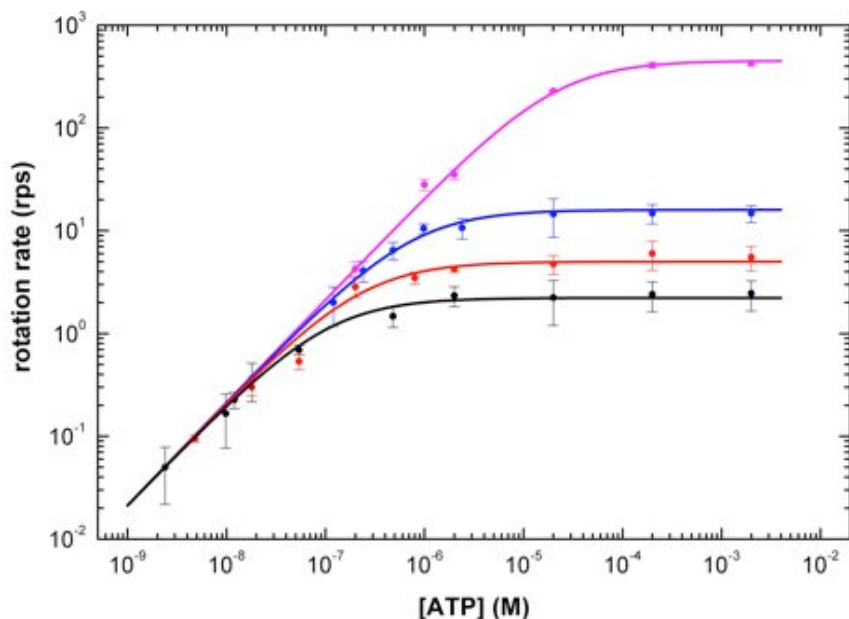


**Figure 3.5:** The rotation speed of EF<sub>1</sub> over a range of ATP concentrations and for four different attached probes, 60nm single bead (magenta), 220nm bead-duplex (blue), 340nm bead-duplex (red), and 495nm bead-duplex (black). Points shown are mean $\pm$ std. At low ATP concentrations, EF<sub>1</sub> rotates at the same speed irrespective of attached viscous load and at a speed proportional to the ATP concentration. The thick lines represent a global, five parameter, non-linear curve fit from Equation 3.31 describing Michaelis-Menten type kinetics, with shared  $c$  parameter, weighted by the square of the standard error. The obtained fitting parameters are  $c = 21.4 \pm 0.2 \text{ s}^{-1} \mu\text{M}^{-1}$ ,  $d_{60} = 0.0473 \pm 0.010 \mu\text{M}^{-1}$ ,  $d_{220} = 1.33 \pm 0.02 \mu\text{M}^{-1}$ ,  $d_{340} = 4.27 \pm 0.20 \mu\text{M}^{-1}$  and  $d_{495} = 9.63 \pm 0.18 \mu\text{M}^{-1}$ . The corresponding  $v_{\text{max}}$  and  $K_{\text{M}}$  for each probe are given in Table 3.4.

concentrations (a few nM), the rotation speed of EF<sub>1</sub> is independent of the size of the attached probe and is proportional to the ATP concentration, since the rate-limiting step now is binding of ATP into the nucleotide binding site. Figure 3.5 shows the average rate of rotation of EF<sub>1</sub> over nM–mM ATP concentration for four different viscous loads.

### 3.4.1 Michaelis-Menten Fitting

Assuming that three ATP molecules are produced per revolution from structural considerations, the speed of rotation,  $v$ , is a measure of the ATP hy-

hydrolysis rate,  $v_{\text{hyd}}$ , for a single EF<sub>1</sub> molecule by  $v_{\text{hyd}} = 3 \times v$ . Since the speed is calculated only from periods when EF<sub>1</sub> is rotating, we have ignored possible inhibition mechanisms and therefore we might expect the speed to be related to the ATP concentration, [ATP], by Michaelis-Menten type kinetics, given by

$$v = \frac{v_{\text{max}}[\text{ATP}]}{K_{\text{M}} + [\text{ATP}]} \quad (3.29)$$

$K_{\text{M}}$  is the Michaelis-Menten constant and signifies the characteristic ATP concentration where the rate of ATP-binding onto the enzyme is comparable to the rate due to internal processes and probe transit.  $v_{\text{max}}$  corresponds to the speed of rotation under saturating ATP concentrations and should relate to the speeds given in Figure 3.3. The four different probes used will each have a unique pair of  $v_{\text{max}}$  and  $K_{\text{M}}$ . We could use Equation 3.29 to obtain these four pairs of parameters by non-linear curve fitting to the data. However, we know that at low ATP concentrations, the rotation rate should be independent of attached load and only determined by the rate of ATP-binding onto the enzyme. Therefore, the four sets of parameters are not independent. Re-arranging Equation 3.29 gives

$$v = \frac{\frac{v_{\text{max}}}{K_{\text{M}}}[\text{ATP}]}{1 + \frac{1}{K_{\text{M}}}[\text{ATP}]} \quad (3.30)$$

$$= \frac{c[\text{ATP}]}{1 + d[\text{ATP}]} \quad (3.31)$$

Now, as  $[\text{ATP}] \rightarrow 0$ ,

$$v \rightarrow c[\text{ATP}] \quad (3.32)$$

as required. Therefore, parameter  $c$  ( $= \frac{v_{\text{max}}}{K_{\text{M}}}$ ) should be constant, irrespective of attached load. Conversely, parameter  $d$  ( $= \frac{1}{K_{\text{M}}}$ ) will vary according to the load. It is possible, then, to obtain a global fit to all the data in Figure 3.5, with 5 parameters (a shared  $c$  amongst the four load data-sets and four  $d$  parameters). The result of the global fit is shown by the thick lines.

| Attached probe    | K <sub>M</sub> | v <sub>max</sub> |
|-------------------|----------------|------------------|
| 60nm single bead  | 21.1±0.5μM     | 449 ± 15rps      |
| 220nm bead-duplex | 752 ± 11nM     | 16.0 ± 0.8rps    |
| 340nm bead-duplex | 234 ± 11nM     | 4.98 ± 0.25rps   |
| 495nm bead-duplex | 104 ± 3nM      | 2.22 ± 0.07rps   |

**Table 3.4:** K<sub>M</sub> and v<sub>max</sub> found from the global fit of the data in Figure 3.5 using Equation 3.31.

The corresponding K<sub>M</sub> and v<sub>max</sub> constants for each attached load can be calculated and are shown in Table 3.4. We know from Figure 3.3 and from Equation 3.21 that a 60nm single bead rotates at 90–100% of the maximal rotation rate of EF<sub>1</sub>. Therefore K<sub>M</sub> for this load should closely resemble the K<sub>M</sub> obtained by bulk activity measurements if there is no inhibition. We also know that parameter *c* from Equation 3.29 is globally conserved and equals  $\frac{v_{\max}}{K_M}$ . From the fitting of Equation 3.21 to Figure 3.3, we can estimate that, with zero attached load, the rotation rate of EF<sub>1</sub> should be 442 ± 15rps, and K<sub>M</sub> will correspondingly be ~20μM. However, the K<sub>M</sub> from bulk activity assays has been reported to be 100μM [171] and 70μM (M. Nakanishi-Matsui, private communication), with a v<sub>max</sub> of 30rps [92], in agreement with 17–33rps reported previously [172]. The difference, no doubt, is due to the inhibition of EF<sub>1</sub> by MgADP<sup>2</sup>. Additionally, bulk assays can be inhibited by the ε-subunit [92], though the ε-subunit is not present in the single molecule assays<sup>3</sup>, and may be a contributing factor to the difference between the bulk and single molecule assays. The increase in K<sub>M</sub> and the decrease in v<sub>max</sub> from single molecule results when assayed in bulk is consistent with a mixed inhibition scheme [174].

---

<sup>2</sup>It is thought that ADP inhibits ATPase activity in two ways [173]. Firstly through competitive inhibition with ATP and, secondly, by the spontaneous failure of F<sub>1</sub> to release the products of hydrolysis.

<sup>3</sup>The ε-subunit is only obtained in small quantities during our purification. The ε-subunit binds transiently to the γ-subunit and therefore, even if it is present at the start of single molecule studies, it is very unlikely to still be present after all the washing steps involved in preparation.

### 3.4.2 A Summary of the [ATP] Dependence of EF<sub>1</sub>

Over a range of ATP concentrations from 2.4nM up to 2mM, and with varied attached loads, EF<sub>1</sub> exhibits Michaelis-Menten type kinetics. This behaviour suggests that a change of mechanism at low ATP concentrations from trisite to bisite (or bisite to unisite) is unlikely since, if a change were to occur, the rotation rate would be expected to decrease faster than the ATP concentration [175]. The lack of an observable change in mechanism is in agreement with a similar study on TF<sub>1</sub> [114]. The K<sub>M</sub> for TF<sub>1</sub> for a negligibly small viscous load was found to be 15±6μM, with a  $v_{\max}$  of 129±27rps [74,114]. It appears, therefore, that in the absence of inhibition, EF<sub>1</sub> and TF<sub>1</sub> have similar K<sub>M</sub> values but that the true rotation rate of EF<sub>1</sub> is ~3.5× that of TF<sub>1</sub> under the same conditions.

## 3.5 ATP-Binding Dwells in EF<sub>1</sub> Rotation

---

Other than being able to factor out inhibition, one attractive feature of the single molecule assays is to be able to observe single molecule reactions. At low ATP concentrations ( $[ATP] \ll K_M$ ),  $v \approx \frac{v_{\max}}{K_M}[ATP]$ . In this regime, we have resolved the rotation of EF<sub>1</sub> into discrete 120° steps, each due to ATP-binding onto EF<sub>1</sub>. Figure 3.6 shows the ATP-binding dwells for EF<sub>1</sub> with a single 60nm bead attached at 200nM and 1μM ATP. Even with large probes attached, 120° stepping can still be resolved, albeit at correspondingly lower ATP concentrations due to the lengthened transit time. Figure 3.7 shows EF<sub>1</sub> rotating step-wise with a 220nm bead-duplex attached at 120nM.

### 3.5.1 Analysis of Dwell Times

The dwell times observed at low ATP concentrations are due to ATP-binding (plus a negligibly small contribution from bead transit and internal processes). In the case of Figures 3.6 and 3.7 the dwell times can easily be

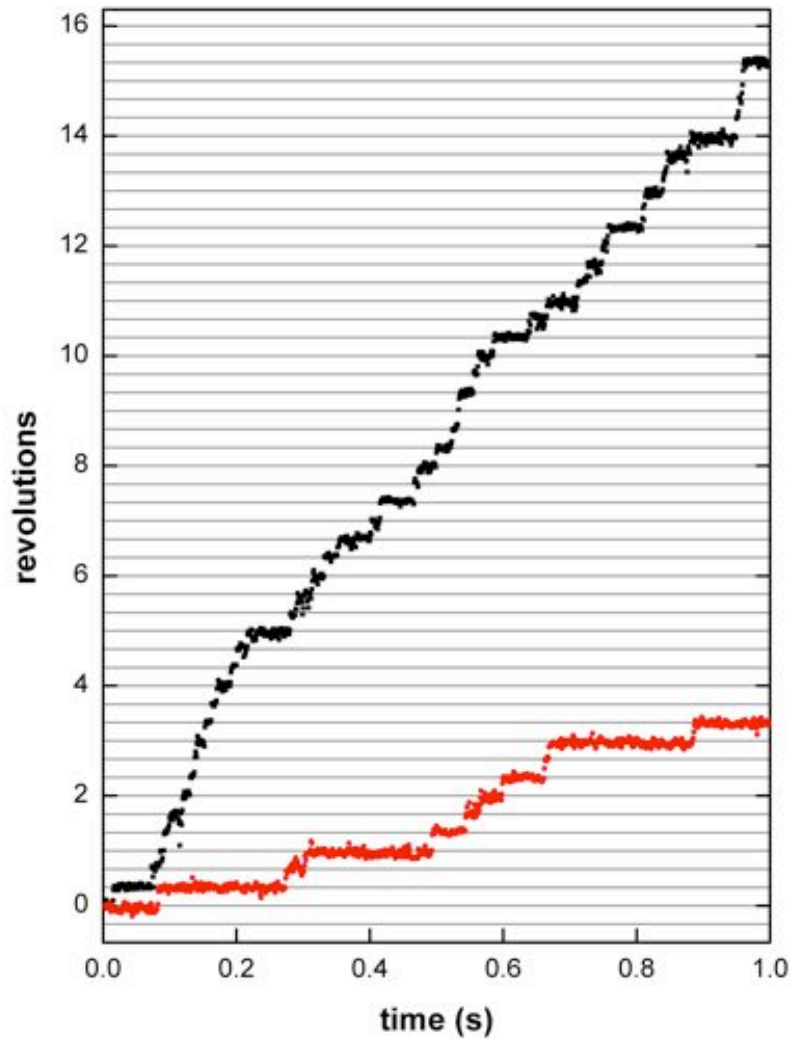


**Figure 3.6:** The step-wise rotation of  $EF_1$  at low ATP concentrations. With a 60nm bead attached, clear  $120^\circ$  steps can be seen at 200nM ATP (red) and  $1\mu$ M ATP (black). During the dwell times,  $EF_1$  is waiting for ATP to bind into the  $\beta$ -subunit binding pocket before it can hydrolyze a previously bound ATP molecule on a different  $\beta$ -subunit.

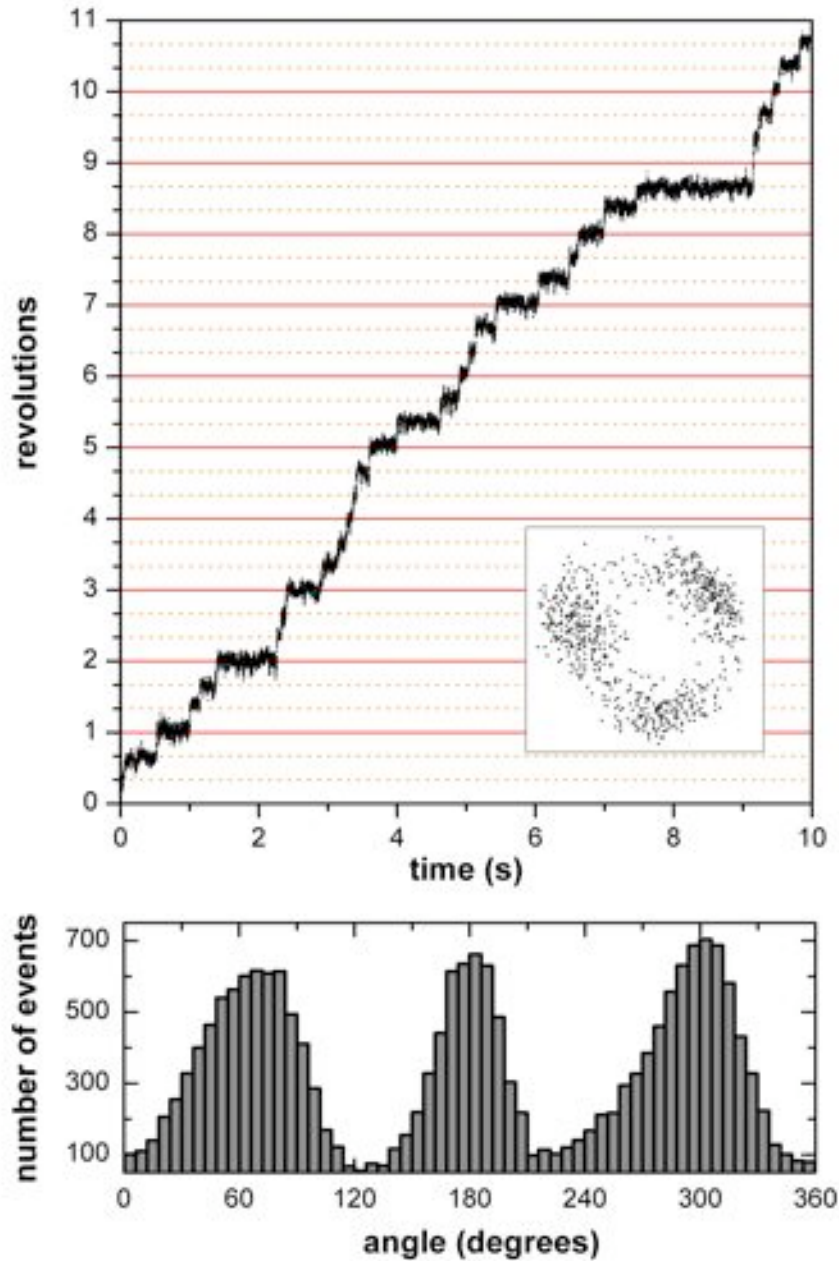


**Figure 3.7:** At 120nM, ATP-binding dwells of a 220nm bead-duplex ( $K_M = 629$ nM) have been observed using laser-based back-focal-plane interferometry at 2kHz sampling rate. Upper chart: The step-wise angle trace with loci of  $xy$  points shown in the inset. Lower chart: The corresponding angular histogram showing three broad states separated by  $\sim 120^\circ$ .

analyzed by eye, a method used often in the F<sub>1</sub> rotation field. The method, however, has two obvious drawbacks: (1) it is not suitable for dealing with a large amount of data, and (2) the method is susceptible to bias on the part of the researcher. In Section 3.6.2 I will present a method I have developed to extract information regarding steps and dwells from large, noisy data-sets. Here, I will show a basic approach for dealing with well-defined steps found at low ATP concentrations.

The angular histograms of well-defined ATP-binding steps show three clear angular states, e.g., as in Figure 3.7. In this manner, we can divide the bead orbit into thirds, each containing one state (i.e., by dividing at 0°, 120° and 240° in Figure 3.7). For each revolution, the total number of points in each third can be counted and, when divided by the sampling rate, are a good approximation for the time spent by EF<sub>1</sub> in that state. This method assumes that there are negligible numbers of back-steps and that the dwell states are clearly separated. This basic analysis will be the starting point for the extended method of Section 3.6.2.

For each stepping EF<sub>1</sub> molecule, the dwell times were analysed and their distribution found. Figure 3.8 shows the distribution of dwell times for four molecules at different ATP concentrations. If the dwell time is due to ATP binding onto the enzyme, the distribution should be that described by a Poisson process with form  $N(t) \propto e^{-k_{app}t}$ . A histogram is a summed transformation of a continuous function into a discrete function. This concept is covered in Appendix B. In the case of an exponential function with rate constant of the same order of magnitude, or longer, than the histogram bin width, the resulting discrete probability function closely resembles that of an exponential. For each molecule, an apparent rate constant,  $k_{app}$  can be found, along with associated error. The thick cyan lines in Figure 3.8 represents the exponential curves obtained for the four example molecules given. For 21 molecules found to be rotating in a step-wise manner,  $k_{app}$  was found

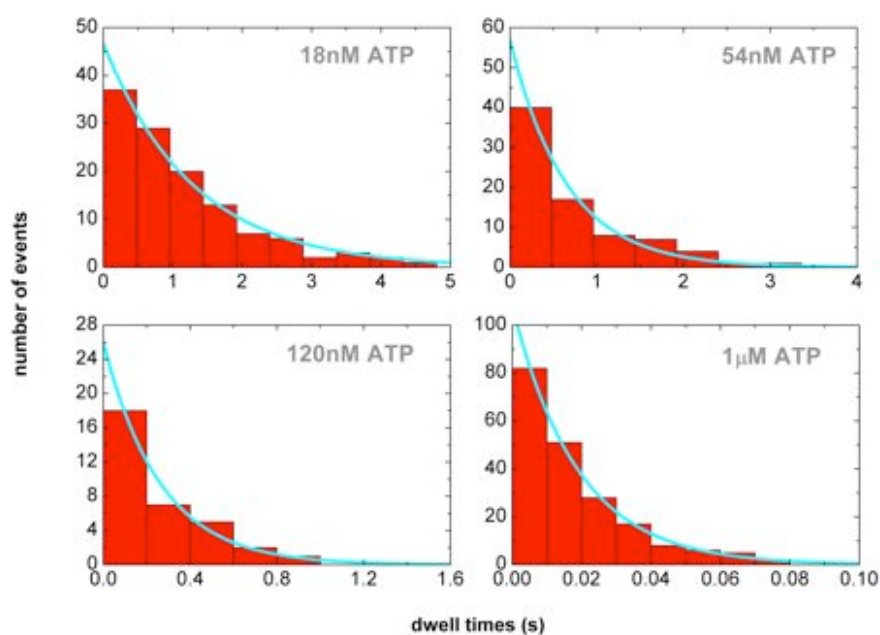


**Figure 3.8:** The dwell time histograms of four EF<sub>1</sub> molecules at 18nM, 54nM, 120nM and 1μM ATP obtained at 25Hz, 25Hz, 2kHz and 1kHz respectively. The distributions are fit with a single exponential function in blue and described in the text. The rate constant relating to the exponential distribution is plotted as a function of ATP concentration in Figure 3.9.

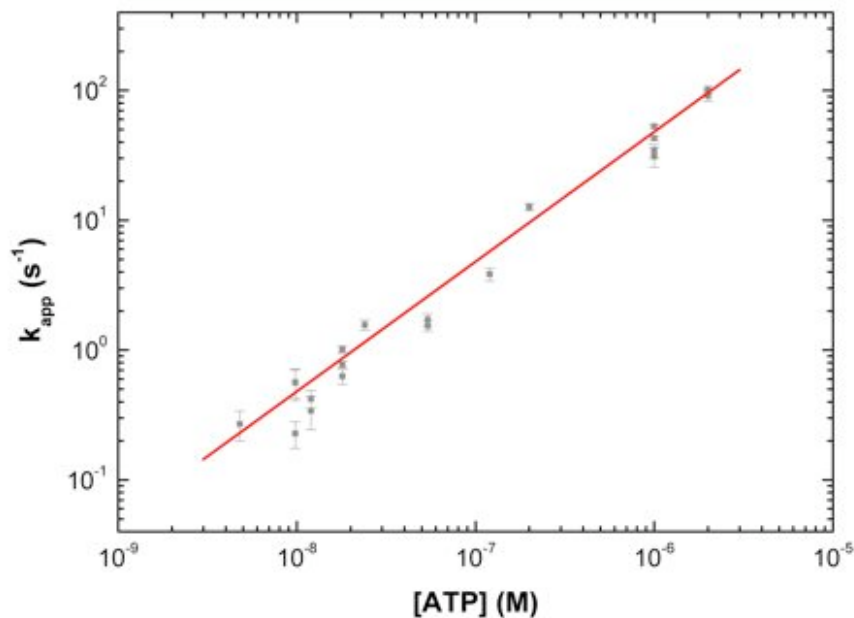


**Figure 3.9:** The apparent rate constant,  $k_{app}$ , is proportional to the ATP concentration over three orders of magnitude. The points plotted are the  $k_{app} \pm \text{error}$  obtained from the fitting of the discrete dwell histograms (e.g., those in Figure 3.8). The fit shown in red is  $k_{app} = k_{on}[\text{ATP}]$  with determined  $k_{on} = (4.81 \pm 0.14) \times 10^7 \text{M}^{-1}\text{s}^{-1}$ .

for each and are displayed in Figure 3.9.

### 3.5.2 Estimation of the ATP-Binding Rate, $k_{on}$

If we assume that the binding of ATP is first-order, consistent with Michaelis-Menten type kinetics, the binding rate of ATP onto EF<sub>1</sub> should be given by  $k_{app} = k_{on}[\text{ATP}]$ . Fitting the data of Figure 3.9 with a linear function, predicts  $k_{on}$  to be  $(4.81 \pm 0.14) \times 10^7 \text{M}^{-1}\text{s}^{-1}$ . To verify the first-order nature of  $k_{app}$  with respect to ATP concentration, a fit of  $k_{app} = a[\text{ATP}]^b$  gives  $b = 1.05 \pm 0.02$ , i.e., suitably close to linear to rule out mixed mechanisms (e.g., changing from trisite to bisite) at these concentrations. Indeed, the Michaelis-Menten kinetics of Section 3.4.1 also rule out a change of mechanism. The  $k_{on}$  value obtained here should be one-third of the value of

parameter  $c$  obtained from Michaelis-Menten kinetics in Figure 3.5. There is actually a disparity here between the two values, with  $c$  being 40% higher than expected. If anything, the average rotation rate should be slower than the single molecule binding events due to unresolved pauses and surface interactions. The value of  $c$  is probably slightly over-estimated in the fitting of Figure 3.5 due to relatively large errors in the rotation rate at nM ATP concentrations.

### 3.5.3 An Estimate of Torque from Step Alignment

The steps observed in Figure 3.7 are due to ATP-binding. The rate of transition from one state to the next can be calculated from Equation 3.1 using a torque estimate of 40pN·nm. For the 220nm bead-duplex used, the resulting rate should be  $\sim 200$  rad s<sup>-1</sup>, or the equivalent of  $\sim 10$ ms per transition. The approach I have taken is to align the transitions and, in effect, to average the rates. Figures 3.10a and 3.10b show the step-wise rotation of the same molecule as in Figure 3.7 and the corresponding angular histogram. An elementary step finding algorithm has been applied, based loosely on the Chung-Kennedy method [176], with the fitted steps shown in detail in the inset. Subtraction of the calculated step positions from the unfiltered data allows determination of the distribution within each state (Figure 3.10c). The dwell state is Gaussian in shape and the width of the distribution allows calculation of the effective stiffness of the state,  $k_f$ , from equipartition of energy, with  $k_f = 11.1$ pN·nm rad<sup>-2</sup>. This stiffness calculation may lead to a slight underestimate of  $k_f$  due to the convolution of detection noise onto the true width of the state. An alternative approach for obtaining  $k_f$  is from calculating the Lorentzian power spectrum and fitting the corner frequency. This method gives a similar value for  $k_f$  (data not shown).  $k_f$  is a combination of spring constants due to the series attachment of linkers, including flexibility due to the attachment of EF<sub>1</sub> to the surface,

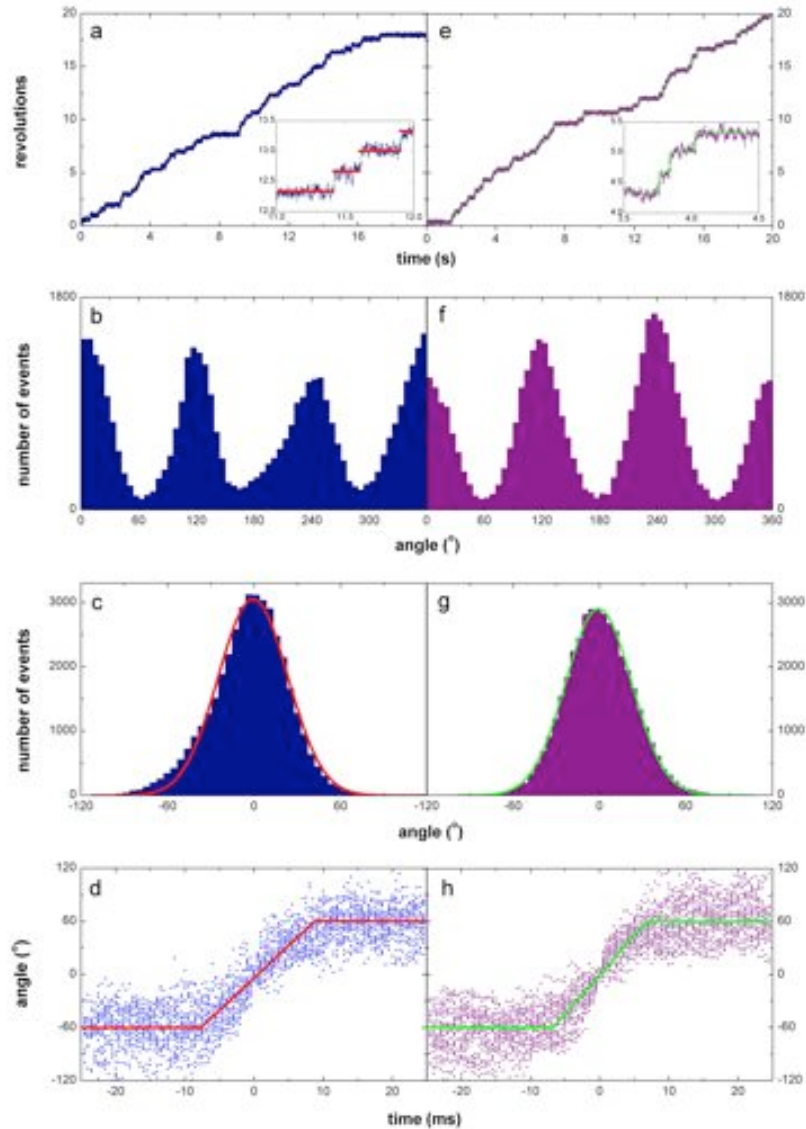


**Figure 3.10:** Estimating the effectiveness of the method of sequential step alignment. (a–d) Experimental data corresponding to the EF<sub>1</sub> molecule shown in Figure 3.7. (e–h) Simulated data using a model developed by Dr Bradley Steel and described in Appendix C. (a,e) The step-wise rotation of EF<sub>1</sub> with dwells fitted as described in the text. (b,f) The corresponding angular histograms. (c,g) The determination of the effective stiffness,  $k_f$ , by the Principle of Equipartition of Energy. (d,h) The alignment of  $\sim 50$  sequential steps and fitting with a step-like transition including finite transit speed. The obtained transit times are 16.4ms (experimental data) and 13.5ms (simulated data). Errors cannot be calculated for these functions.

flexibility due to the attachment of the bead-duplex to the  $\gamma$ -subunit, and an internal potential energy profile of the dwell state. Steps were aligned such that the central point ( $0^\circ$ ) of the transition from  $-60^\circ$  to  $+60^\circ$  was shifted to  $t = 0$ . The result of the alignment of 51 sequential steps is shown in Figure 3.10d. Overlaid is the fit of a step function between two states at  $\pm 60^\circ$  with a transition of constant speed between the two.

This method has been employed in previous TF<sub>1</sub> studies to suggest that the torque is constant throughout the transition and that it does not vary with ATP concentration [114]. Indeed, constant torque is required for a number of the present models of F<sub>1</sub>F<sub>o</sub> to hold [79, 128, 126]. Even with constant torque, the bead motion should be exponential in manner, with characteristic time constant  $\frac{k_f}{\zeta}$ , due to the elastic linkage between EF<sub>1</sub> and the bead-duplex. The transition appears to be smooth and step-like, though a small decay in the speed as it approaches  $+60^\circ$  cannot be ruled out. The transition time, obtained from fitting the step-like function is 16.4ms, suggesting a full speed rate of 20rps at saturating ATP concentrations, similar to the  $15.2 \pm 0.2$ rps average rate we obtained from the Michaelis-Menten kinetics. The alignment presented here is consistent with a constant torque but it does not rule out the possibility of more complicated torque profiles.

Also shown in Figure 3.10e–h is the same analysis obtained from a simulated data set. F<sub>1</sub> data was simulated using a model detailing one Poisson process at the ATP-binding angle, two Poisson processes at the catalytic dwell angle, a constant torque during the transition between states and an effective stiffness of the EF<sub>1</sub>/bead-duplex complex. The model was encoded by Dr Bradley Steel and is described in more detail in Appendix C. Using  $k_f$  found for the actual EF<sub>1</sub> molecule, a constant torque of 40pN·nm,  $\zeta = 0.17$ pN·nm·s (the uncorrected drag coefficient from Table 3.2), and suitable binding rates and catalysis rates (see Section 3.6.3), realistic angular traces were obtained (Figure 3.10e). Alignment of the simulated data reveals

similar properties to the real data, but in this instance, the transition only lasts 13.5ms, closely matching the expected time constant for the relaxation of a bead following F<sub>1</sub> via an elastic linker of  $\sim 15\text{ms}$  ( $\tau = \frac{\zeta}{k_f}$ ). Interestingly, using a backwards argument, a 13.5ms transition corresponds to a full speed of 25rps at saturating ATP concentrations. If this speed had been observed in practice, with a known drag of  $\zeta = 0.17\text{pN}\cdot\text{nm}\cdot\text{s}$ , the torque predicted would have been  $\sim 27\text{pN}\cdot\text{nm}$ , not the  $40\text{pN}\cdot\text{nm}$  that went into the simulation! Data simulated with a torque of  $80\text{pN}\cdot\text{nm}$  resulted in a transition time of 12.4ms, suggesting that the bead recoil is the rate-limiting step at these speeds. The longer transition time found for the real data implies that the bead drag of  $\zeta = 0.17\text{pN}\cdot\text{nm}\cdot\text{s}$  is underestimated in this instance.

#### 3.5.4 A Summary of the EF<sub>1</sub> ATP-Binding State

As expected, at ATP concentrations much lower than the  $K_M$  values,  $120^\circ$  step-wise rotation of EF<sub>1</sub> has been observed due to the binding of ATP molecules into the nucleotide binding sites. The rate of binding was found to be  $(4.81 \pm 0.14) \times 10^7\text{M}^{-1}\text{s}^{-1}$  from 5nM up to  $2\mu\text{M}$ . The corresponding binding rate in TF<sub>1</sub> has been reported to be  $2.2\text{--}2.7 \times 10^7\text{M}^{-1}\text{s}^{-1}$  [73],  $(2.6 \pm 0.14) \times 10^7\text{M}^{-1}\text{s}^{-1}$  [74] and  $\sim 2 \times 10^7\text{M}^{-1}\text{s}^{-1}$  [114]. Therefore, the rate of binding of ATP in EF<sub>1</sub> is twice that of TF<sub>1</sub>. This is probably due to the degree to which the experimental conditions depart from physiological conditions, namely the temperature. Since the binding rate is different for EF<sub>1</sub> and TF<sub>1</sub> under the same conditions, diffusion of ATP onto the molecule is not limiting. Instead, it would suggest that there is a greater energy barrier to ATP-binding in TF<sub>1</sub> compared to EF<sub>1</sub>. This is understandable because, *in vivo*, TF<sub>1</sub> must keep the ATP/ADP tightly bound during synthesis and would require a deeper potential well than EF<sub>1</sub>.

An attempt was presented to align ATP-binding steps to enable an estimate of EF<sub>1</sub> torque to be made. With comparison against simulated data,

it was shown that the method of step alignment is limited to the relaxation time of the bead-linkage. Despite the appearance of a smooth transition rate between states from the alignment, constant torque cannot be assumed since each transition is actually determined by elastic recoil. This method has been used to suggest the constant nature of the torque of 40pN·nm across the complete 120° transition in TF<sub>1</sub> [114]. The analysis here shows that constant torque will result in the observed alignment. However, the true motion of a bead-duplex attached to EF<sub>1</sub> will be exponential and therefore the alignment appears to smooth out this transition. As a result, it appears likely that small scale torque fluctuations would also be smoothed out, giving the appearance of a smooth transition. Further simulation, with non-constant torque, would be useful here.

### 3.6 High-Speed Experiments on EF<sub>1</sub>

---

I have been fortunate throughout this work to have been able to collaborate closely with Dr Mayumi Nakanishi-Matsui from Iwate Medical University, Japan. Dr Nakanishi-Matsui's work involves the study of mutant EF<sub>1</sub> kinetics in the low load regime, using 40–60nm gold beads and a commercial laser dark-field microscope, to probe the functional differences with regards to wild-type EF<sub>1</sub>. The data presented here were collected by Dr Nakanishi-Matsui but analyzed by myself. After the initial analysis, we have regularly discussed the direction of the project to ensure that experiment and analysis are complementary. A custom-made laser dark-field microscope has recently been built in Oxford by Drs Yoshiyuki Sowa and Bradley Steel. This will allow high-speed, low-load data to be collected on EF<sub>1</sub> in the future and is currently being used to observe YF<sub>1</sub> in this manner.

As we have seen in Section 3.3, EF<sub>1</sub> under low load can rotate at ~450rps. Laser dark-field microscopy is essential for this work. Sufficient illumination of 40–60nm gold beads, typically by a 532nm green laser in F<sub>1</sub> studies,

is required to allow fast image capture by a CCD camera. The expected average radius of gyration of a single 60nm gold bead is only 18nm (see Table 3.1). Detection noise and motion due to the flexible linkage between the enzyme and the bead creates a 2D Gaussian blur in the  $xy$  position of the bead. As a result, these studies are always significantly hindered by noise, with  $xy$  position data occasionally losing all resemblance of a clear orbit. With this in mind, and the philosophical discussions of Section 3.1, care has to be taken in the analysis of these data.

Two rotating molecules are shown in Figure 3.11 with 60nm single beads attached. These molecules represent neither excellent data nor poor data, they are simply representative of the data that needs to be analyzed. The insets show the  $xy$  position data for the bead. Three preferred angular positions are visible for both molecules in their angular histograms, though the positions are not distinct due to overlaid noise. 2mM ATP was present in this assay and, under these conditions, ATP-binding should occur within  $(\sim 5 \times 10^7 \text{M}^{-1} \text{s}^{-1})^{-1} \times (2 \times 10^{-3} \text{M})^{-1} \approx 10 \mu\text{s}$ . Therefore, the ATP-binding dwell should not be resolvable at the 4kHz sampling rate used in the assay. Therefore, the three preferential angles must be due to the catalytic dwell as observed in TF<sub>1</sub>. On average, each EF<sub>1</sub> rotation takes  $\sim 2\text{ms}$ . With a single 60nm gold bead, we would expect the revolution transit time to contribute  $\frac{2\pi\zeta}{T} \approx 2\pi \times (8.7 \times 10^{-4} \text{pN}\cdot\text{nm}) / (40 \text{pN}\cdot\text{nm}) \approx 0.14\text{ms}$ . Therefore, each dwell must be  $\sim 0.6\text{ms}$  long, a time comparable to the sampling rate available in these experiments. This complication adds considerable detection noise to the data, in addition to the experimental noise. Further analysis of these short catalytic dwells will be given in Section 3.6.3.

### 3.6.1 Calculating Dwell Times

The approach I have employed to analyse the high speed data is to use a large data-set such that noise that occurs on a short-time scale will be

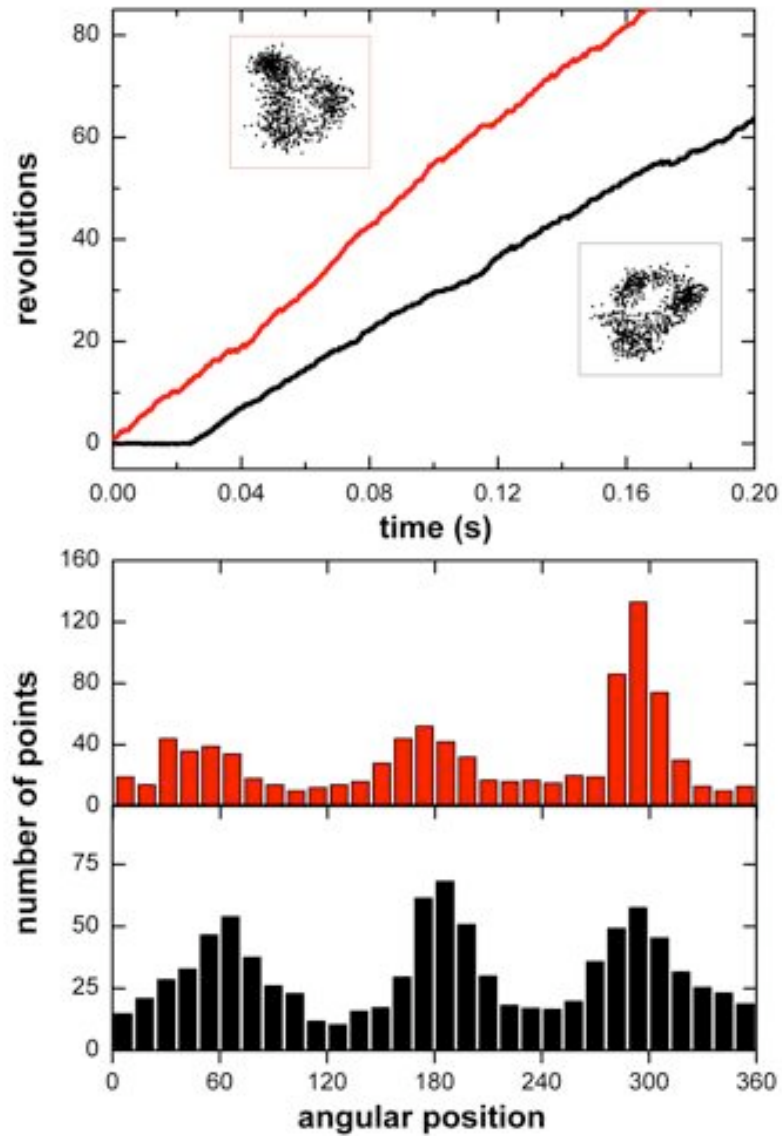


**Figure 3.11:** The rotation of two EF<sub>1</sub> molecules with a 60nm single gold bead attached at 2mM ATP, sampled at 4kHz. The insets show the  $xy$  positions of the two molecules with three preferred angular positions. The angular histograms are the result of ellipse fitting to the  $xy$  position data. The three preferred angular positions overlap, probably due to both experimental and detection noise.

averaged out. This means that individual steps within the motion of EF<sub>1</sub> may be subject to large noise fluctuations, but their long-time average should closely resemble the underlying processes.

The angular histograms of the two example molecules are shown in Figure 3.11. Since the transit time from one catalytic pause to the next is very short for a 60nm bead ( $\sim 0.05$ ms), nearly all of the time spent in each dwell will be due to the internal processes. Therefore, to approximate the length of each dwell we can divide the EF<sub>1</sub> orbit into thirds and then just sum the points spent within each third. Obviously, for the two example molecules shown in Figure 3.11, the best places to make the divisions are at 0°, 120° and 240°, i.e., at the minima in the angular histogram.

### 3.6.2 Correlation Analysis

For more noisy data, the minima in the angular histogram are not always clear. However, we can use our knowledge of the 3-fold stepping symmetry to attempt to determine the location of the dwells. Figure 3.12 shows the effect of placing the division in the wrong positions. If we assume that EF<sub>1</sub> is rotating in  $i$  independent steps of duration  $t_i$ , this division process will create a set of measured dwells,  $t'_i$ . In the case of perfect placement of the division,  $t'_i \approx t_i$  and, if the spread due to noise is less than 120°,  $t'_i = t_i$ , with each dwell time independent of its predecessor. In the case when the cut positions are completely in the wrong place (i.e., at the maxima of the angular histogram), the measured  $i$ th dwell time will be  $t'_i \approx f(t_i, t_{i+1})$ , where  $f(a, b)$  describes an arbitrary function of the variables  $a$  and  $b$ , and consecutive calculated dwell times will no longer be independent. In this manner, the measurement of the Pearson correlation coefficient,  $r$ , between the sets  $\tau_0 = \{t_1, t_2, \dots, t_{i-1}, t_i\}$  and  $\tau_{+1} = \{t_2, t_3, \dots, t_i, t_1\}$  will be a

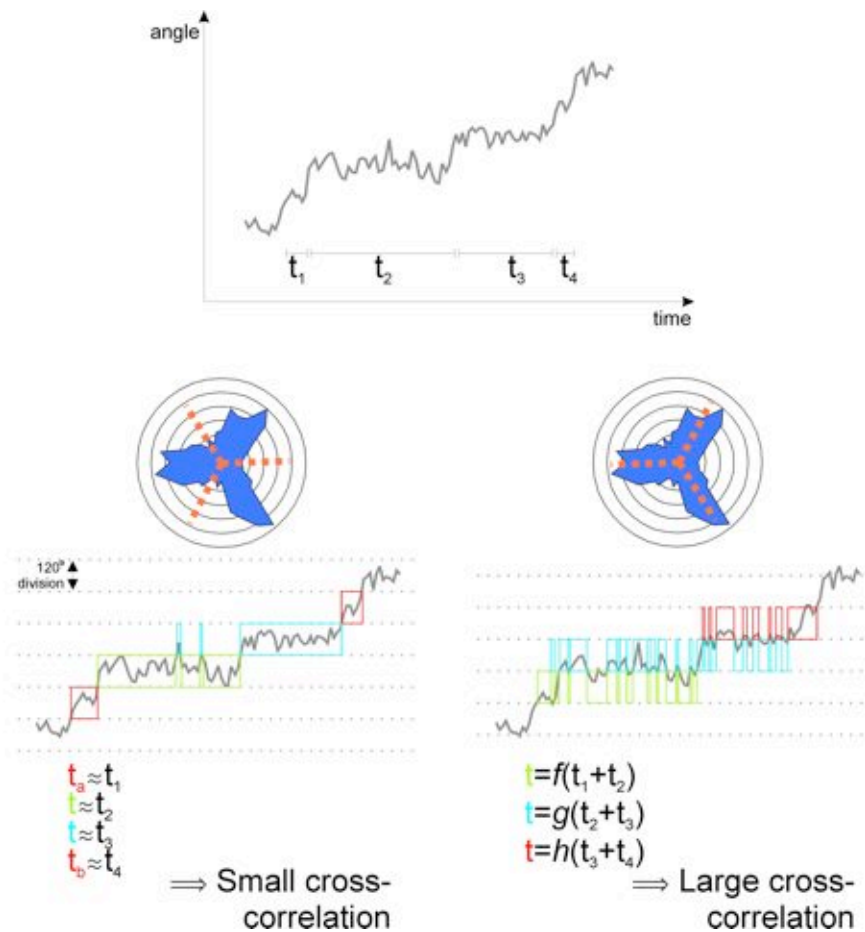


**Figure 3.12:** A graphical explanation of the correlation analysis. At the top of the figure is the angular progression of EF<sub>1</sub> in 120° steps with dwell times  $t_1, t_2, t_3$  and  $t_4$ . The steps are clear by eye but contain a degree of noise that means that the exact dwell positions are not well defined. Two radial angular histograms are shown in blue corresponding to the angular data above. The three dwell states are clearly visible in this case. The orange dashed lines represent the cut positions discussed in the text. On the left, the divisions are placed at the minima of the angular histogram. Simple counting of points within each third gives an approximation to the true dwell times. In the left-hand case, the approximation is very good. Since the dwell times are assumed to be due to underlying Poisson process, the true dwell times,  $t_i$ , are independent of one another. The Pearson correlation coefficient,  $r$ , is used to determine the degree to which neighbouring dwell times are dependent. The left-hand case corresponds to a minimal  $r$  coefficient whilst the right-hand case would be maximal  $r$ .

measure of the goodness of the division locations, with  $r$  defined by

$$r = \frac{1}{n-1} \sum_{j=1}^i \left( \frac{\tau_0(j) - \bar{\tau}_0}{s_{\tau_0}} \right) \left( \frac{\tau_{+1}(j) - \bar{\tau}_{+1}}{s_{\tau_{+1}}} \right) \quad (3.33)$$

and where  $s_\tau$  is the sample standard deviation of set  $\tau$ . Using this method we can vary the cut positions in small angular increments and find a relationship between  $r$  and the angular cut position.

It is yet to be proven whether this analysis will be sufficiently rigorous for the application to F<sub>1</sub> data. Using simulated data for EF<sub>1</sub> at 4kHz with a 60nm bead at 2mM ATP and with a similar noise profile to that found in Figure 3.7 (see Appendix C for details of the simulation model), catalytic dwells can be recreated, as shown by the angular histogram in Figure 3.13a. Three clear dwell positions are evident with only minimal overlap between the states. Application of the correlation analysis yields maximal correlation coefficient,  $r$ , at the simulation positions of the catalytic dwells. Further increasing the degree of noise, as shown in Figure 3.13b, destroys evidence of the states in the angular histogram and a researcher should be loathe to say that the catalytic dwells occur at 80°, 200° and 320°. Interestingly, maximal  $r$  does not occur at the expected positions of 80°, 200° and 320° but at -10–15° from these angles, possibly due to bead lag during transit between states. In Figure 3.13c, rotation close to the corresponding K<sub>M</sub> is simulated with the same noise level as used in Figure 3.13a. At this ATP concentration we would expect both the catalytic and ATP-binding dwells to be present. The noise level results in only three dwells being visible in the angular histogram, despite there being six underlying steps. Application of the correlation analysis reveals maximal  $r$  at 0°, 80°, 120°, 200°, 240° and 320°, i.e., the analysis has correctly located the positions of both the catalytic dwells and the ATP-binding dwells. Attempts to use this analysis on real data obtained around K<sub>M</sub> will be presented in Section 3.6.5.

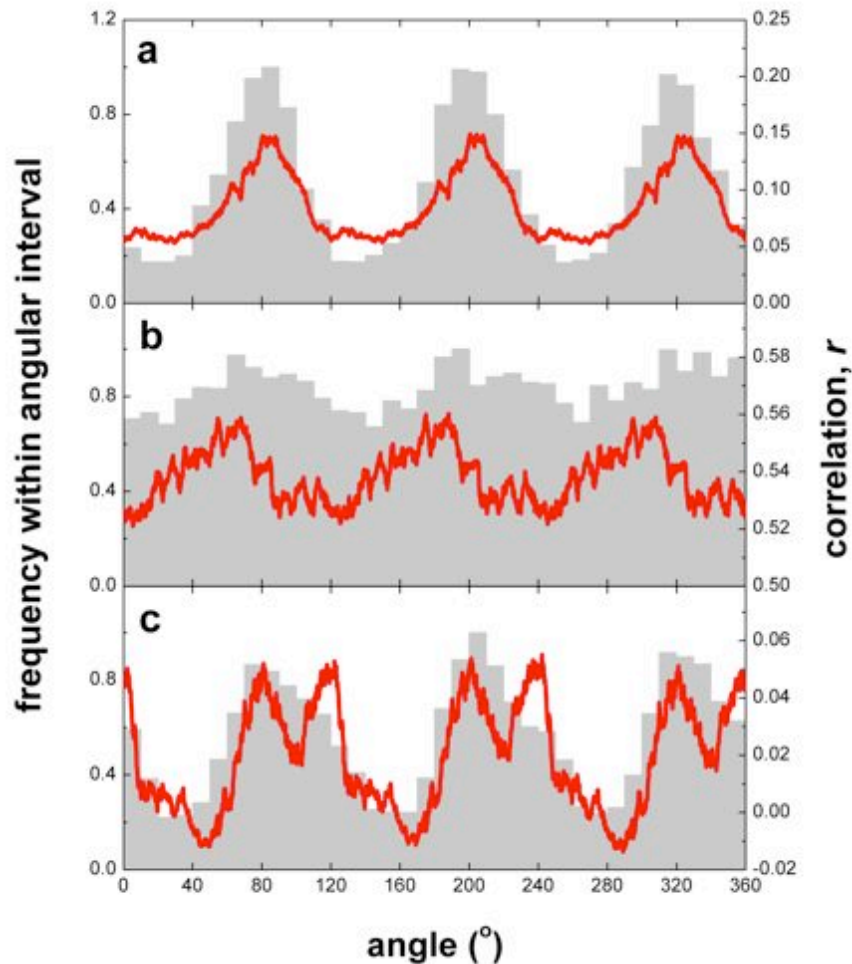


**Figure 3.13:** A test of the ability of the correlation analysis to find dwelling angles using simulated data for rotation with a 60nm bead at 4kHz sampling rate. In the simulation, EF<sub>1</sub> binds ATP at 0°, 120° and 240° and undergoes catalysis reactions at 80°, 200° and 320°. In each frame, the resulting angular histogram is shown in grey and the calculated correlation coefficient,  $r$ , is shown by the red line. (a) 2mM ATP with a noise profile similar to that found in the ATP-binding steps of Figure 3.7. Maximal  $r$  occurs almost directly at the catalytic dwelling angle. (b) 2mM ATP with 4× the noise of (a). Maximal  $r$  occurs at  $-15^\circ$  from the catalytic binding angles. (c) 60 $\mu$ M ATP (just slightly higher than the corresponding  $K_M$  for the bead size) and with the same noise profile as in (a). There are obvious double peaks in  $r$ , corresponding to the catalytic and ATP-binding dwells, despite the lack of resolution in the angular histogram.

### 3.6.3 Analysis of Dwell Times

Compared to TF<sub>1</sub>, EF<sub>1</sub> rotates fast at low load. One aspect of this high speed is that the required sampling rate for observation is raised accordingly. High-speed, low-load EF<sub>1</sub> rotation is observed on a commercial laser dark-field microscope and imaged onto a fast camera. Therefore, in theory, observing fast rotation should just involve increasing the laser power and camera sampling rates correspondingly. Unfortunately, Dr Nakanishi-Matsui has been unable to observe EF<sub>1</sub> rotation at sampling rates higher than 4kHz. The main reason for this is that increasing the laser power, required to maintain illumination at faster shutter speeds, results in an increased likelihood of bead detachment from the image plane, most likely due to EF<sub>1</sub> detaching from the surface. The mechanism for this is not obvious but is consistent with my own observations that EF<sub>1</sub>, even under high load conditions, falls off the surface more rapidly when illuminated by the 633nm laser than during normal bright-field conditions. Local heating would appear to be the most likely cause, although other mechanisms cannot be ruled out. If local heating is the source, a careful analysis of local temperature increase should be attempted to ensure that the enzyme is not being thermally activated (or deactivated in the laser). This could be achieved by using waxes with different melting points over a range of laser powers.

This experimental limit of 4kHz sampling rate has unfortunate effects on the degree to which we can analyze the data. At 4,000kHz sampling rate and with  $\sim 500$ rps rotation, one revolution will take on average 8 frames and the average catalytic dwell will last  $\sim 2$ – $3$  frames. Many dwells will be even shorter than this. A further complication comes from the nature of the image capture by the camera. Each frame is not an instant snapshot at each time point. Instead, each frame is an average image obtained over the exposure time. Due to the requirement to use minimal laser power, the exposure time is set to the complete length of one frame (i.e., to the reciprocal of the

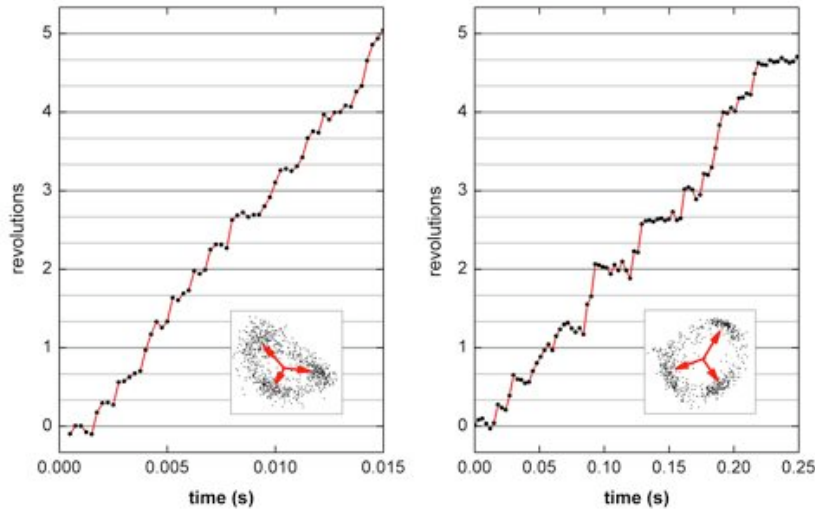


**Figure 3.14:** The stepwise rotation of EF<sub>1</sub> under low load due to catalytic processes. Left: Rotation in the presence of 2mM ATP recorded at 4kHz frame-rate. The lack of data points (shown as black dots) per dwell is evident. Right: Rotation in the presence of 2mM ATP $\gamma$ S, a slow hydrolyzing analogue of ATP, and recorded at 250Hz. The insets show the  $xy$  average position of each frame, with the three preferential angles indicated by the red arrows.

sampling rate). If, for example, EF<sub>1</sub> steps from state 1 to state 2 during the exposure time, the average position recorded will lie somewhere between the two states. In fact, as we discussed in Section 3.6, the transition time expected for a 60nm single bead is expected to be significantly shorter than one frame length. The net result is a ‘blurring’ of each state and less well-defined angular steps. The effect is similar to applying a low-pass filter to the angular data.

Analysis of dwell times that last only a few frames requires very clean  $xy$  orbits and the vast majority of data are rejected on this basis. The left-hand image in Figure 3.14 shows the rotation of one EF<sub>1</sub> molecule with 2mM ATP present. The 120° step-wise rotation is evident but so is the lack of data points in each step. The  $xy$  angular data, despite having three obvious positions, also includes a number of points in the transit region between states, most likely due to the averaging effect of the camera.

The catalytic dwell times of three EF<sub>1</sub> molecules are shown in Figure 3.15, calculated as described in Section 3.6.1. The distribution resembles that found for the TF<sub>1</sub> enzyme [74] which was fitted with a so-called ‘double exponential’ distribution. We shall use this terminology here but take careful note of what it means. For two sequential, independent Poisson processes with rate constants  $k_i$  and decay constants  $\tau_i$ ,



the probability of observing a transition of A→C of time  $t$  will be given by the ‘double exponential’ distribution of

$$p(t) = \frac{k_1 k_2}{k_2 - k_1} \left( e^{-k_1 t} - e^{-k_2 t} \right) \quad (3.35)$$

In the case where  $k_1 = k_2$ , Equation 3.35 becomes a Gamma distribution. Since  $\tau_1$  and  $\tau_2$  are of a similar order to the sampling rate, care has to be taken in the transformation into a histogram distribution, a topic covered in Section B.5 of Appendix B. Unfortunately, the catalytic dwell time distribution at 2mM ATP does not fit this function well at all (as shown by the red curve in Figure 3.15). There is an apparent lack of very short dwells observed. This is probably due to a finite transit time between states (estimated to be ~0.05ms, the equivalent of a fifth of a frame) plus an effect due to the averaging of state positions from the camera sampling. In a simple model, if we assume that the transit time and the averaging effect contribute a constant time to each dwell state,  $T_{\text{shift}}$ , in addition to the two assumed processes, Equation 3.35 becomes

$$p(t) = \frac{k_1 k_2}{k_2 - k_1} \left( e^{-k_1(t-T_{\text{shift}})} - e^{-k_2(t-T_{\text{shift}})} \right) \quad (3.36)$$

for  $t > T_{\text{shift}}$  and  $p(t) = 0$  for  $t \leq T_{\text{shift}}$ . Fitting this function to the catalytic

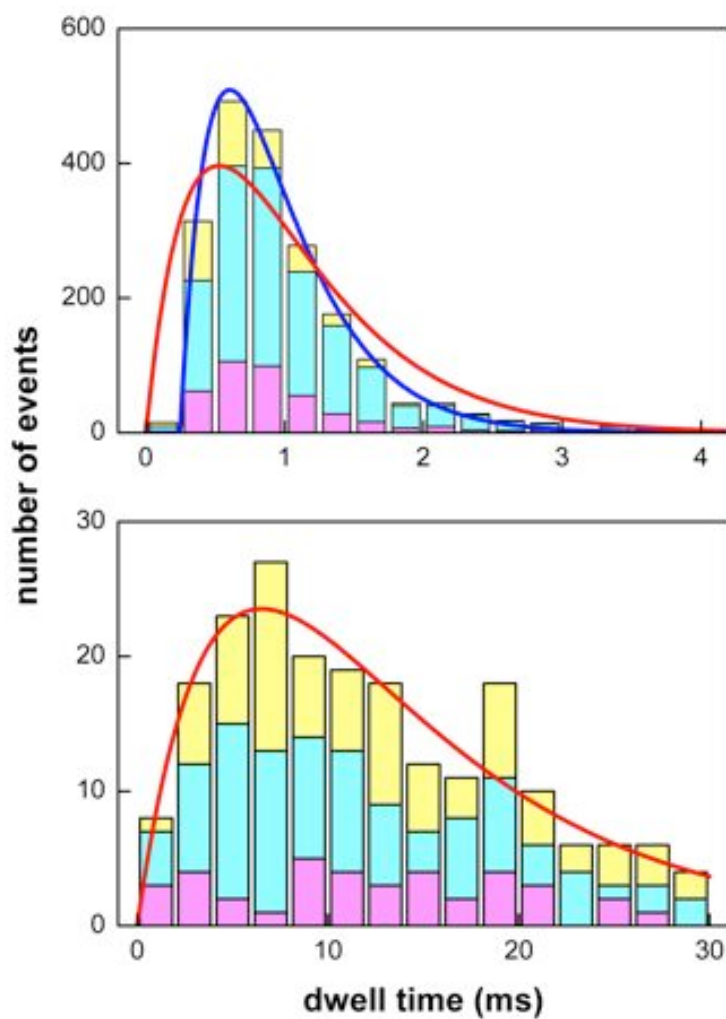


**Figure 3.15:** The distribution of catalytic dwell times. Top: The dwells of three different EF<sub>1</sub> molecules in the presence of 2mM ATP. The ‘double exponential’ distribution (red curve) does not represent the experimental data well, unlike the distribution including a finite additional time given in Equation 3.36 (blue curve). In this fit  $T_{\text{shift}} \approx 0.25\text{ms}$  and the two sequential Poisson processes are both  $\sim 0.3\text{--}0.4\text{ms}$ . Bottom: Three EF<sub>1</sub> molecules’ dwells at 2mM ATP $\gamma$ S. This distribution is consistent with the ‘double exponential’ distribution (shown in red) with time constants  $4.8 \pm 2.5\text{ms}$  and  $9.3 \pm 4.0\text{ms}$ .

dwells gives a better fit to the data, as shown by the blue curve in Figure 3.15.  $T_{\text{shift}}$  is approximately equal to one frame (or 0.25ms) and the two subsequent processes are both  $\sim 0.3\text{--}0.4\text{ms}$  in length. Trying to decompose  $T_{\text{shift}}$  into a transit time component and camera filtering component is difficult as the camera effect is highly non-linear. It should be noted that, if the sampling rate was higher, this method could allow the determination of the average transit time between states and, hence, the estimation of EF<sub>1</sub> torque, a topic which will be covered further in Section 3.6.6.

### 3.6.4 Using an ATP Analogue, ATP $\gamma$ S

The fast rotation speed and short catalytic dwell length of EF<sub>1</sub> has caused many problems from an analysis viewpoint. The finite length of the camera exposure time sets a resolution limit of 0.25ms on our experiments. Ideally, we would aim to lower this limit but we have been hampered by the problems of increased laser power as previously discussed.

A different approach is to slow the catalytic processes in the enzyme, resulting in the catalytic dwell becoming much longer than the exposure time. One technique would be to use a mutant of EF<sub>1</sub> that rotates slowly due to longer catalytic dwells, for example the  $\beta$ S174F,  $\beta$ S174L and  $\beta$ I163A mutants that have been shown to rotate slowly at saturating ATP concentrations [177, 178]. However, in terms of characterization of wild-type EF<sub>1</sub> this approach does not give any definitive answers since dwell positions may occur at different angles in the mutants.

Another approach is to replace ATP with its slow hydrolyzing analogue, ATP $\gamma$ S (adenosine 5'-[ $\gamma$ -thio]triphosphate). ATP $\gamma$ S has been used to slow the rotation of TF<sub>1</sub> and has been shown to only affect the catalytic dwells [80]. TF<sub>1</sub> catalytic dwells were increased from two  $\sim 1\text{ms}$  events to a  $\sim 2\text{ms}$  event and an  $\sim 8\text{ms}$  event upon replacement of 2mM ATP with 2mM ATP $\gamma$ S.

The same replacement in EF<sub>1</sub> slows the rotation down from  $\sim 450\text{rps}$  to

~20rps. 2mM ATP $\gamma$ S represents saturating concentrations (M. Nakanishi-Matsui, unpublished data, but consistent with TF<sub>1</sub> results [80]) and therefore the slow down is not due to slow diffusional binding onto the enzyme. At 2mM ATP $\gamma$ S, EF<sub>1</sub> rotates in clear 120° steps as shown in Figure 3.14. It should be noted that the three preferential dwell positions are much clearer with ATP $\gamma$ S than ATP due to the increased length of each dwell relative to the exposure time and the transit time. Analysis of the dwell times, shown in Figure 3.15, reveals that  $T_{\text{shift}} \approx 0$  since the dwells are well-described by the ‘double exponential’ function with time constants of each process of  $4.8 \pm 2.5\text{ms}$  and  $9.3 \pm 4.0\text{ms}$ . Since the dwells are much longer with ATP $\gamma$ S, the ~0.05ms transit time and any camera averaging will be negligible and the addition of  $T_{\text{shift}}$  is not required.

### 3.6.5 Attempts to Observe ATP-Binding and Catalytic Dwells Concurrently

In addition to understanding the underlying processes and rates occurring in the catalytic dwells of EF<sub>1</sub>, it was hoped that we would be able to determine the position of the catalytic dwell relative to the ATP-binding dwell. To observe both dwells concurrently, an ATP concentration equivalent to  $K_M$  has been sufficient to resolve six preferential angles in TF<sub>1</sub> studies, with the ATP-binding dwells at 0° and the catalytic dwells at +80° [74, 80].

Unfortunately this approach has not been successful with EF<sub>1</sub>. At  $[\text{ATP}] \gg K_M$ , three catalytic dwells are visible and at  $[\text{ATP}] \ll K_M$ , the ATP-binding dwells are clear. However, six positions have not been seen at  $[\text{ATP}] \approx K_M$ . No doubt this is due to the very short length of the catalytic dwells and our maximum sampling rate. Figure 3.16 shows the dwells observed at 2 $\mu$ M ATP for three EF<sub>1</sub> molecules, with the  $xy$  position data for each molecule. 2 $\mu$ M is just below the  $K_M$  of 18 $\mu$ M and we would expect ATP-binding to last ~10ms, compared to the ~0.7ms catalytic dwell. Each

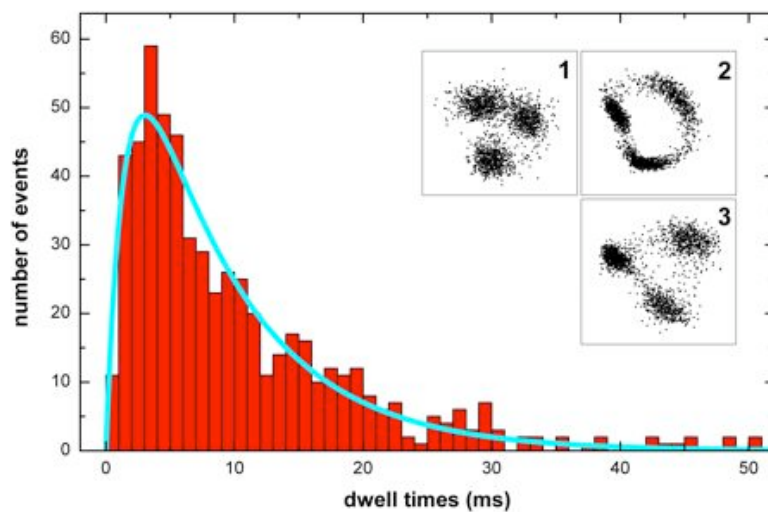


**Figure 3.16:** The dwell distribution for three EF<sub>1</sub> molecules at 1kHz frame rate with a 60nm gold bead at 2 $\mu$ M ATP. The dwells were obtained using the method described in Section 3.6.1. Also shown is the  $xy$  position data for each molecule. The dwell distribution is fitted with the ‘double exponential’ of Equation 3.35. The obtained parameters are  $7.9 \pm 0.7$ ms and  $1.5 \pm 0.3$ ms.

molecule only displays three stopping positions, due to the catalytic dwell being faster than the 1ms exposure time used. Fitting the dwell distribution with the ‘double exponential’ function of Equation 3.35 gives processes of  $7.9 \pm 0.7\text{ms}$  and  $1.5 \pm 0.3\text{ms}$ , consistent with ATP-binding of  $\sim 10\text{ms}$  and catalytic processes of  $\sim 0.7\text{ms}$ . The short process is perhaps slightly longer than expected but is consistent with the effect of camera sampling on simulated dwells (data not shown). Naturally, there remains the possibility that the ATP-binding dwells and the catalytic dwells occur at the same angle and that EF<sub>1</sub> departs significantly from the TF<sub>1</sub> enzyme. This would be interesting but would seem unlikely as the angular energy profile of the enzyme is theoretically linked to the torque production and the efficiency, concepts that would appear to be evolutionary important and, therefore, well-conserved.

Further suggestion that the two dwells occur at similar angles in EF<sub>1</sub> to TF<sub>1</sub> is the application of the correlation analysis of Section 3.6.2 to the three molecules from Figure 3.16, as shown in Figure 3.17. The most interesting  $r$  coefficient is that for molecule 2, where maximal  $r$  is found at angles separated by  $80^\circ$  and  $40^\circ$ <sup>4</sup>. Molecule 3 potentially shows small secondary maxima at  $-50^\circ$  from the binding angle. Molecule 1 perhaps shows secondary  $r$  maxima but is not clear. I feel that we would require a large number of molecules at the same ATP concentration to draw any firm conclusions from the correlation analysis method, however, these results suggest that the method might be useful in the future.

In addition to the correlation analysis, I will provide some evidence that the two dwells are distinct when compared to the position of the inhibited state of EF<sub>1</sub> presented in Section 3.7.4.

ATP $\gamma$ S seems like the best candidate to allow the simultaneous obser-

---

<sup>4</sup>It should be noted that despite the uneven angular distribution of the primary dwells in the histogram, the correlation analysis produces an ‘averaged’ assessment, three-fold symmetric about one revolution.

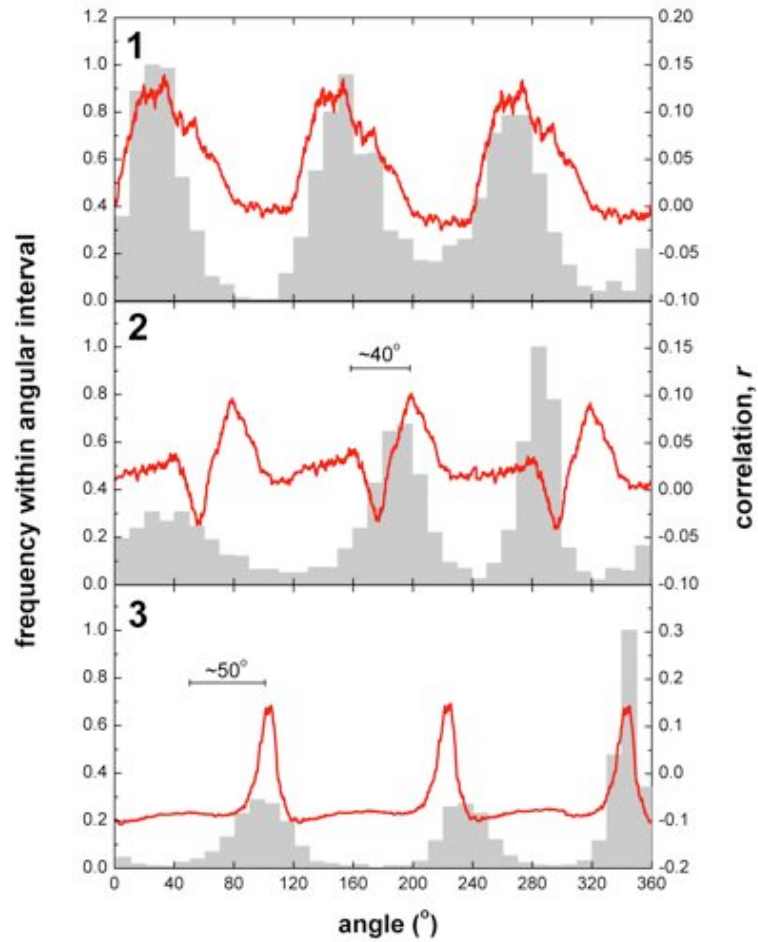


**Figure 3.17:** The application of the correlation analysis (shown by the red line) to the three EF<sub>1</sub> molecules rotation at  $[ATP] \approx K_M$  whose dwells and  $xy$  positions are given in Figure 3.16. Molecule 2 shows clear maximal  $r$  separated by  $80^\circ$  and  $40^\circ$ . The correlation analysis is less clear for molecules 1 and 3.

vation of the two states. By lengthening the catalytic dwells, we can go to correspondingly lower ATP concentrations and hopefully observe both catalytic and ATP-binding dwells of 10–20ms. Assuming the binding rate,  $k_{on}$ , is the same for both ATP and ATP $\gamma$ S, we would expect to need to use  $\sim 1\mu\text{M}$  ATP $\gamma$ S to obtain this condition. However, successful rotation has not been observed at these concentrations yet. This is probably due to the lack of an available regenerating system for ATP $\gamma$ S. As a result, the ATP $\gamma$ S concentration will decrease quickly due to hydrolysis. Rotation has been observed at  $10\mu\text{M}$  ATP $\gamma$ S and there is some evidence that at these concentrations, the sub-step is occasionally seen but we have only a few rotating molecules at  $10\mu\text{M}$  and only two that *possibly* exhibit such behaviour, one of which is shown in Figure 3.18. This example was only obtained using a frame rate of 125Hz, an insufficient sampling rate for clear resolution of the two states. Occasional sub-steps are visible that deviate significantly from the position of the catalytic dwell. They appear to be at the  $+40^\circ$  position if the catalytic dwell is defined at  $0^\circ$ . I am confident that the dominant steps observed are due to the catalytic dwells because at  $10\mu\text{M}$  ATP $\gamma$ S, the catalytic dwell should be  $\sim 5$ – $10$  times slower than the ATP-binding event.

I spent one week in the laboratory of Prof Masamitsu Futai and Dr Mayumi Nakanishi-Matsui attempting to observe the sub-step but with no success. This proves how hard these experiments are in practice and the element of good fortune required to obtain good data. I am completely confident that with time and effort, the binding dwell and the catalytic dwell could be observed concurrently. With the development of the new laser dark-field microscope in our lab in Oxford, this is certainly something that should be pushed further in the future. Again, the available EF<sub>1</sub> mutants may also be useful in this regard.

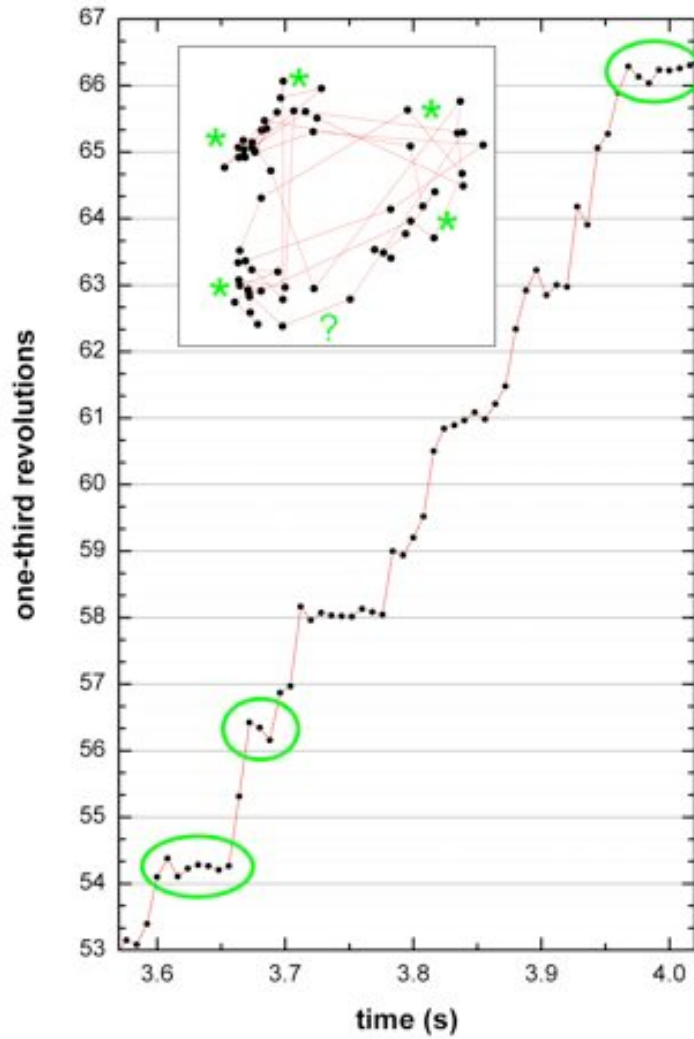


**Figure 3.18:** The possible simultaneous observation of the ATP-binding and catalytic states using  $10\mu\text{M}$  ATP $\gamma$ S. The catalytic binding states have been aligned with the solid grey grid-lines. Three possible dwells are highlighted whose position deviate from the catalytic position. The data were only obtained at 125Hz and therefore there are very few points per dwell. The  $xy$  position data shows possible sub-step positions.

### 3.6.6 An Alignment of EF<sub>1</sub> Catalytic Dwells

From the analysis of Section 3.6.3 and our understanding of the physics of the motor, it is expected that there is a finite transit time for the stepping from one state to another. The method employed in TF<sub>1</sub> studies [74] was to align sequential steps and to look at the transition from one state to the next. This method is analogous to my own alignment of ATP-binding steps presented in Section 3.5.3 but, in the case of catalytic dwell alignment, far fewer data points can be recorded per transition due to the considerably shorter dwell time. For this reason, I feel that this method actually yields very little information for EF<sub>1</sub> studies. In fact, I am surprised that the technique allowed such clear stepping motions to be observed in TF<sub>1</sub>. However, the approach used was to select only a small sample of steps (16 consecutive steps [74]) and the subset may have been chosen to emphasize their point. Sequential automated alignment of 160 EF<sub>1</sub> catalytic steps is shown in Figure 3.19. The alignment is done such that the steps occur ‘in between’ frames at  $t = 0$ . For two states at  $-60^\circ$  and  $+60^\circ$ , the alignment was achieved by placing the two consecutive frames either side of  $0^\circ$  as the two frames about  $t = 0$ ms. The transition from the frame immediately before the step and the frame immediately after appears to be smooth. This however is most likely due to the camera averaging effect. Indeed, an expected transition time of 0.05ms will be lost since the averaging effect can only make transitions appear longer than the true value.

It is evident from the alignment that for frames away from the step, there is a distribution of observed angular position. This is not unexpected. We know that the catalytic dwell is stochastic and fast ( $\sim 0.6$ ms). Analysis of these distributions leads to a confirmation of the rapid rate of the catalytic processes, whilst also lending weight to the method of alignment, and is presented in Appendix D.

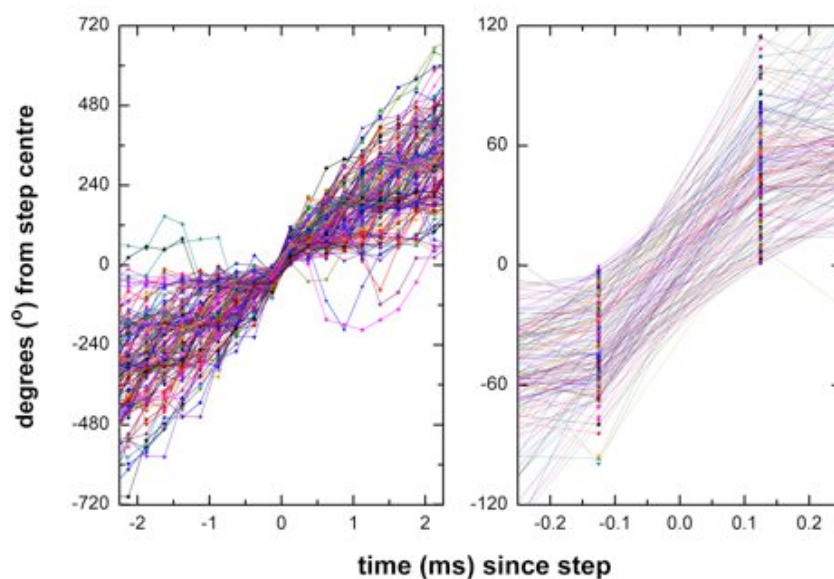


**Figure 3.19:** The alignment of 160 sequential  $120^\circ$  steps between catalytic pauses of EF<sub>1</sub> at 2mM ATP and sampled with a 4kHz camera. Steps were aligned by the angular data point closest to the centre between two angular states. Left: Nine frames either side of the step. After/before 9 frames from the step ( $\sim 2$ ms), the majority of data points are  $\pm 1$  revolution away. Right: The aligned steps viewing only the frames immediately before and after the step. There is a large spread in the data due to noise and the averaging effect of the camera. Obtaining the gradient of a best-fit line here is spurious as the true transition is likely to be much shorter than one frame.

### 3.6.7 A Summary of EF<sub>1</sub> Rotation Under Low-Load

In Sections 3.6–3.6.6, I have presented an analysis of EF<sub>1</sub> rotation data obtained in the low-load regime by Dr Mayumi Nakanishi-Matsui. During the analysis process, a method for determining dwell states in noisy F<sub>1</sub> data, named ‘Correlation Analysis’, has been developed and was presented here. It remains to be seen if the sheer quantity of data can be acquired to allow a rigorous testing of the method. However, the method works well on the simulated data presented and may prove to be a useful analytical tool in the future.

EF<sub>1</sub> rotation with a 60nm gold bead is fast ( $> 400$  rps) and noisy (as discussed previously) making analysis difficult. Unfortunately, the sampling rate we can use is limited by problems involving the removal of EF<sub>1</sub> from the glass surface. As a result, sufficient temporal resolution has not been achieved to accurately determine the distribution of the dwells observed due to the internal processes, the so-called catalytic dwells. Indeed, analysis reveals that each dwell has a contribution due to the bead’s transit from one state to the next, estimated to be  $\sim 0.05$ ms but lengthened due to the effect of camera sampling, and the catalytic processes lasting  $\sim 0.7$ ms and consisting of at least two events. The study of EF<sub>1</sub> at high speed is more difficult than TF<sub>1</sub> due to the greater rate of the catalytic process. TF<sub>1</sub> catalytic dwells last  $\sim 2$ ms and consist of two  $\sim 1$ ms processes [74]. In addition, TF<sub>1</sub> appears to be less flexible within its states. Perhaps this is due to deeper energy profiles within each state, required due to the high operating temperature TF<sub>1</sub> inhabits. Equally, the observed angular flexibility in EF<sub>1</sub> might be due to a more elastic linkage between the surface, enzyme and bead.

The slowly-hydrolyzing ATP analogue, ATP $\gamma$ S has been used to slow down the catalytic dwells of EF<sub>1</sub> to  $\sim 14$ ms. This approach appears to be the best method with which to observe the ATP-binding state and the catalytic state simultaneously. However, currently, no concrete examples

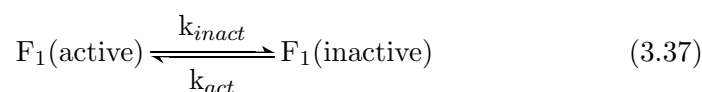
have been obtained.

Finally, alignment of 120° steps between catalytic dwells has been attempted. However, the true transition lasts only a fraction of one frame and therefore this method yields little insight into the processes occurring for EF<sub>1</sub>. The method has been employed in TF<sub>1</sub> studies [74], but in this study only a few transitions were recorded and a slightly higher sampling rate was used.

### 3.7 The Inhibited State of EF<sub>1</sub>

---

The rotation of EF<sub>1</sub> is unidirectional but not continuous. EF<sub>1</sub> switches stochastically from being in a rotating state to being in a paused, locked state, and vice versa, i.e.,



This process was observed in the first EF<sub>1</sub> rotation experiments using actin filaments [88,87] and in all subsequent studies. The time constant for both states is on the order of seconds. As a result, investigation of this process of inhibition must be done with long-term observation (on the order of minutes) and a large number of molecules. In terms of understanding the angular positions of dwell states in the EF<sub>1</sub> cycle, it was important to have a handle on the process and to quantify the behaviour.

There are mechanisms by which EF<sub>1</sub> could become paused that are external to the enzyme and involve transient interactions between the probe and the surface. There are two reasons for believing that the inactivation observed is the motor, namely, (1) the pausing frequency is independent of the size of the probe, and (2), in a majority of the molecules studied, the motor pauses at three preferential angles, separated by 120°.

Figure 3.20 shows the rotation and pausing of one EF<sub>1</sub> molecule. As

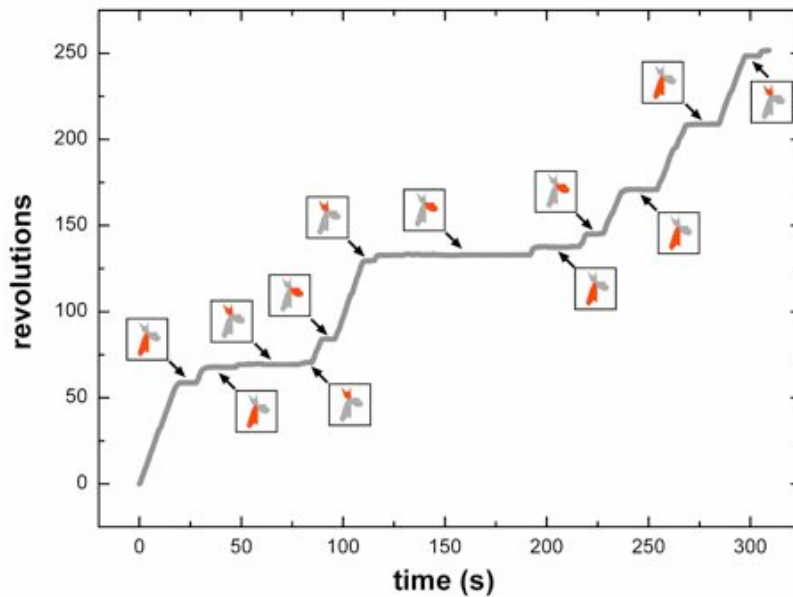


**Figure 3.20:** The unidirectional but non-continuous rotation of EF<sub>1</sub>. Single molecules of EF<sub>1</sub> are in dynamic exchange between an active, rotating state and a paused, locked state. Furthermore, in the majority of EF<sub>1</sub> molecules studied, the pausing angles were distributed preferentially to three positions separated by 120°. Shown in the insets is the radial angular histogram during the paused state. At each pause, the dominant position is indicated by the red sector of the histogram. The rotation rates in between pauses were generally constant indicating an on-off process of inactivation.

can be seen, the motor paused a number of times during the five minutes of recording. This molecule was slightly unusual in that the pauses are long but it is useful for illustrational purposes. During each pause, the motor resides within one of three preferential angles (indicated by the red sector of the radial angular histograms shown as insets).

In order to investigate the pausing of EF<sub>1</sub>, I observed the rotation of 72 molecules at 2mM ATP. Each molecule was recorded for 5–10 minutes, resulting in over seven hours of data to analyse.

### 3.7.1 An Automated Method for Determining Pauses

In order to analyze over seven hours of rotation data, an algorithm was developed to enable automatic collection of pause results. The algorithm involved fitting straight lines to segments of the data using a method that shall be referred to as the ‘Segmental Fit’ method, coded by Dr Richard Berry. The method works by moving forward through the data, fitting a continuous straight line until the mean squared error (mse) reaches a set threshold (mse=0.2rad<sup>2</sup>). At this point the algorithm divides the current segment into two smaller sections corresponding to the best fit of two lines with different slopes meeting at point  $(x_i, y_i)$ . The next iteration of the algorithm starts at point  $(x_i, y_i)$  and moves forward from there. By applying a threshold for the rotation rate of 0.4rps, sections were ascribed as rotating or paused. The thresholds were adjusted such that the pause allocation was deemed to be best by eye. To remove the effects of noise from this method, whilst conserving fast changes in speed, the data were pre-filtered with a median filter of rank-2 (i.e., with a window size of 5). Since the minimum sampling rate was 25Hz, this non-linear filtering should only cause effects on the scale of  $\sim 0.2$ s or less. It was noticed that rapid fluctuations within a paused state occasionally resulted in a long pause being split into two. A correction was added to the algorithm that rejoined adjoining pauses if they were found within one-third of a revolution from each other. Figure 3.21 shows the results of the automated pause detection using this algorithm on an example EF<sub>1</sub> motor. The algorithm recognizes long pauses very well but it is difficult to define pauses shorter than 1s (as shown in the inset of Figure 3.21). Indeed, occasionally the algorithm finds very short pauses ( $\sim 0.1$ s) that would not appear to be so by eye. In addition, large bead-duplexes have been used which will inevitably filter high frequency signals out of the observed data. With these factors in mind, it was decided that the Segmental Fit algorithm could only be used for the effective detection

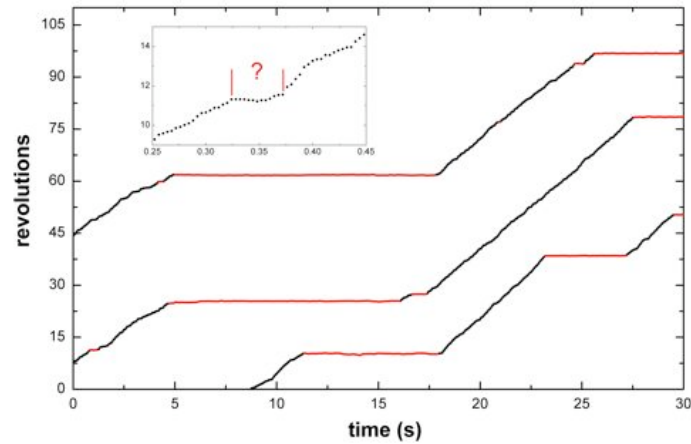


**Figure 3.21:** A detailed look at the effectiveness of the Segmental Fit method algorithm for automatic detection of inhibition pauses. Thresholds used in the algorithm are  $\text{mse}=0.2\text{rad}^2$  and  $\text{speed}=0.4\text{rps}$ . Regions determined to be rotating (black) and paused (red) for one EF<sub>1</sub> molecule are shown. The data are wrapped for illustrational purposes. The algorithm generally does well at finding long pauses but struggles to find pauses much shorter than 1s, as shown in the inset.

of pauses longer than 1s.

A different technique was also attempted with the aim of using an already developed methodology for determining speed changes. The technique used is known as the Switch-Time method, an algorithm developed by Dr Fan Bai and Richard Branch for the detection of switch events in the rotation of the bacterial flagellar motor. Although F<sub>1</sub>-ATPase does not switch its direction of rotation like the bacterial flagellar motor, it does switch between ‘on’ and ‘off’ states. Appendix E outlines my attempts to apply the algorithm to EF<sub>1</sub> rotation data. Unfortunately, the slow speed of EF<sub>1</sub> with 220–495nm bead-duplexes attached is such that the ‘on’ and ‘off’ states are poorly defined and the algorithm is greatly affected by the noise in EF<sub>1</sub> assays. Unfortunately, this means that the Switch-Time method cannot be used for F<sub>1</sub> data analysis and all analysis presented hereon is on data obtained using the Segmental Fit method algorithm presented earlier.

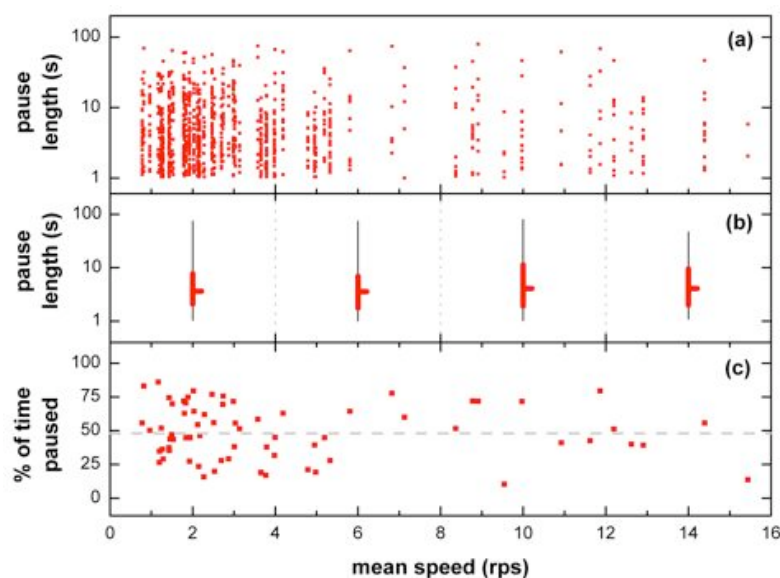


**Figure 3.22:** The effect of the viscous load of the attached probe on EF<sub>1</sub> pausing at 2mM ATP following an investigation of 72 molecules. (a) The pause length as a function of the rotation rate of the molecule. (b) A plot representing the pause distribution for molecules rotating between 0–4rps, 4–8rps, 8–12rps and 12–16rps. Data plotted are median, with lower and upper quartiles, in red and the full range of pauses in black. (c) The percentage of time paused as a function of rotation rate. Across all 72 molecules, EF<sub>1</sub> molecules were paused 48.6% of the time (indicated by the grey dotted line).

### 3.7.2 Load-Independent Pausing

To ensure that the inhibition was not due to some surface effect, a range of bead-duplexes was used (220–495nm). Assuming that EF<sub>1</sub> produces a constant torque,  $T$ , amongst all molecules, then the speed of rotation will just be inversely proportional to the viscous drag. Therefore, to assess the size of the load on the motor, we can simply look at its rotation rate. Figure 3.22a shows the length of the pauses against the speed of the motor for the 72 different molecules monitored at 2mM ATP. Only 0.3% of pauses lasted longer than 100s (6 out of 1884) and are not shown here. It is evident that the underlying pause length distribution is not Normal. To ensure that the shape of the distribution was not affected by the viscous load, the non-

parametric quantities of median, upper and low quartiles and range were computed for all molecules within the speed ranges 0–4rps, 4–8rps, 8–12rps and 12–16rps (shown in Figure 3.22b). The shapes of the distributions vary little with rotation rate, and hence, pause length is not dependent on load. Finally, to ensure that large loads did not simply result in more frequent pausing, the fraction of time paused against speed is shown in Figure 3.22c. The correlation coefficient is -0.03, indicating almost no relationship between the load and the rate of pausing.

### 3.7.3 The Distribution of Pause Lengths

The distribution of pause lengths shorter than 30s, at 2mM ATP, is shown in Figure 3.23a and is clearly a smoothly decaying function. The distribution is poorly described by a simple exponential fit due to a larger than expected number of long pauses ( $t > 20$ s), suggesting that the inhibited state is more complicated than a straightforward single molecule dissociation (ADP vacating the binding site) which would lead to Poisson statistics. The pause length distribution found is well fit by a probability distribution that allows the possibility of two unresolvable inhibited states (as found previously for TF<sub>1</sub> [75]), each decaying back to the active state by Poisson processes. Two inhibited states is consistent with the two forms of inhibition discussed in Section 3.4.1. Such a probability function is of the form

$$p(t) = p_1 e^{-\frac{t}{\tau_1}} + p_2 e^{-\frac{t}{\tau_2}} \quad (3.38)$$

where  $\tau_1$  and  $\tau_2$  are the time constants of the inhibited states 1 and 2 and  $p_1$  and  $p_2$  are the relative probabilities that the unresolved inhibited state is state 1 or state 2. Fitting Equation 3.38 to the obtained data gives the four parameters of Equation 3.38 and are shown in Table 3.5. At 2mM ATP, the time constants of the two inhibited states are  $2.3 \pm 0.3$ s and  $11.4 \pm 3.8$ s, with

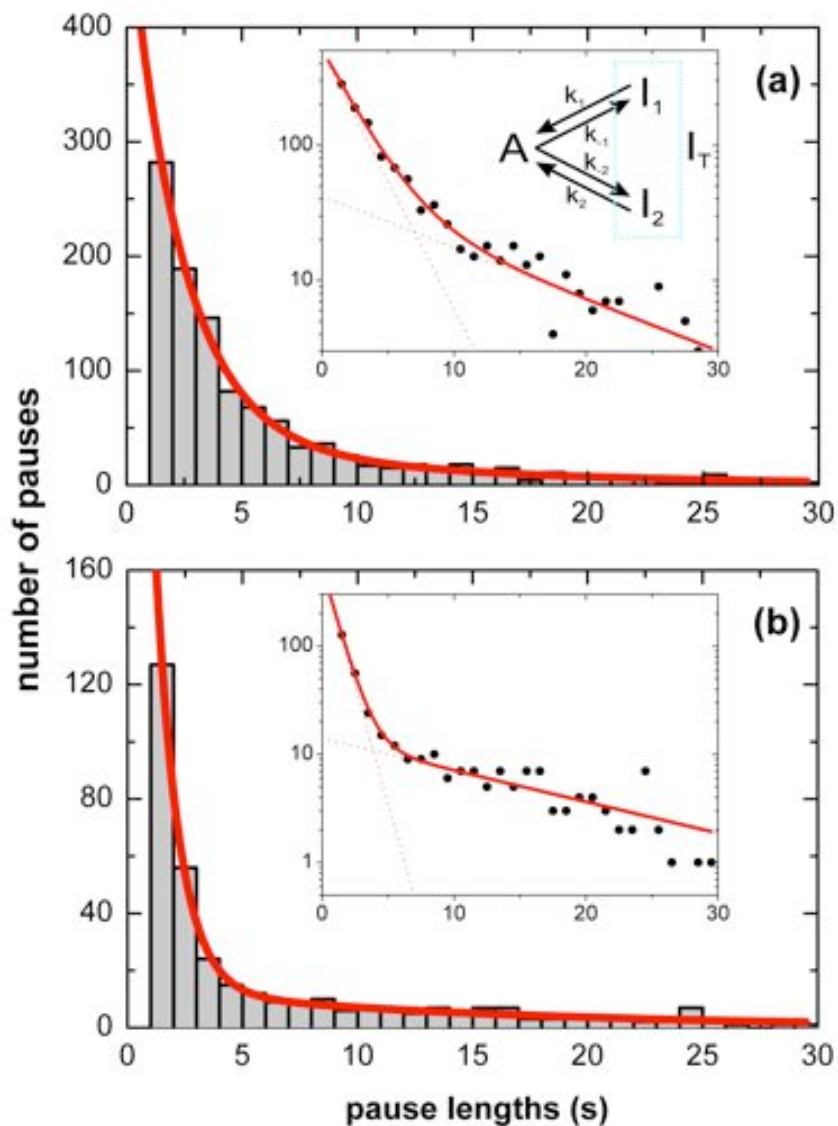


**Figure 3.23:** The distribution of pauses observed in the rotation of EF<sub>1</sub> at 2mM ATP (a) and at 20µM ATP (b). Pauses shorter than 1s were not accurately detected and are not plotted here. The distributions are not exponential but are described well by a scheme where the inhibited state, I<sub>T</sub>, is actually two unresolvable states, I<sub>1</sub> and I<sub>2</sub>. As a result, the inhibited pauses should have lengths described by Equation 3.38, where  $\tau_1$  and  $\tau_2$  are the characteristic time constants of each paused state. The thick red curves represent the fitted probability function with parameters given in Table 3.5. In both (a) and (b) the data is plotted on both a linear scale (main figures) and on a logarithmic scale (insets) to indicate the two rate processes observed.

|          | 2mM ATP           | 20 $\mu$ M ATP    |
|----------|-------------------|-------------------|
| $p_1$    | 0.30 $\pm$ 0.17   | 0.71 $\pm$ 0.18   |
| $\tau_1$ | 2.3 $\pm$ 0.3s    | 1.0 $\pm$ 0.1s    |
| $p_2$    | 0.027 $\pm$ 0.020 | 0.019 $\pm$ 0.006 |
| $\tau_2$ | 11.4 $\pm$ 3.8s   | 15.0 $\pm$ 2.5s   |

**Table 3.5:** The time constants and relative probabilities of the two inhibited states obtained from fitting Equation 3.38 to the data in Figure 3.23.

the shorter lasting state being  $\sim 2$  times more populous ( $\frac{p_1\tau_1}{p_2\tau_2}$ ). To check that this distribution fits all the pauses observed, not just those shorter than 30s, we can calculate the number of pauses expected to be longer than 30s by

$$p(t > 30) = \frac{\int_{30}^{\infty} p(t) dt}{\int_1^{\infty} p(t) dt} \quad (3.39)$$

From the parameters obtained, the percentage of pauses expected longer than 30s is 3.0%. The experimental percentage is 2.0% (52 from a total of 2670 pauses), suggesting that there are no other significant processes occurring.

In total, the percentage of time that EF<sub>1</sub> spent paused was 48.6%, however, this time does not include all of the pauses shorter than 1s. Therefore, correcting for these short but frequent pause events and assuming that there are no other processes occurring on time-scales shorter than 1s, the fraction of all pause time observed,  $f_p$ , will be given by

$$f_p = \frac{\int_1^{\infty} t p(t) dt}{\int_0^{\infty} t p(t) dt} \quad (3.40)$$

Using this expression indicates that the pauses shorter than 1s contribute little to the total time paused ( $f_p = 0.975$ ) and we can predict that EF<sub>1</sub> at 2mM ATP spends 50% of its time in the paused state.

To investigate if the characteristics of the inhibited state varied greatly with ATP concentration, I have also studied 40 molecules at 20 $\mu$ M ATP. The distribution of pauses observed at this ATP concentration is shown in Figure 3.23b and, again, the shape is best described by Equation 3.38. Similarly, a short state and a long state are observed, on this occasion with time constants  $1.0 \pm 0.1s$  and  $15.0 \pm 2.5s$  respectively. More pauses are observed at 20 $\mu$ M that last longer than 30s (9%) than at 2mM due to the increased length of the long pause state, in approximate agreement with the expected number (7.3%, 62 of 661 pauses). At 20 $\mu$ M, after correction, EF<sub>1</sub> spends 56% of its time in the inhibited state.

Ideally, we would investigate the rate at which EF<sub>1</sub> lapses into one of the two proposed inhibited states from the active state. Potentially, one of the rates might be dependent on the ATP concentration. Unfortunately, due to the numerous short pauses that we are unable to detect, it has not been possible to ascertain periods of rotation only and, as a result, we cannot accurately determine the length of times between pauses. However, from the proposed scheme in Figure 3.23, we *can* calculate the average rate that the active state decays into each of the inhibited states. If  $F_a$ ,  $F_1$  and  $F_2$  are the fraction of molecules in the active state, inhibited state 1 and inhibited state 2 respectively with  $F_a + F_1 + F_2 = 1$ , we know that in the steady-state, the relative populations of paused and rotating molecules is not changing. Therefore

$$F_a k_{-1} = k_1 F_1 \tag{3.41}$$

$$F_a k_{-2} = k_2 F_2 \tag{3.42}$$

$F_a$ ,  $F_1$  and  $F_2$  can be calculated from Equation 3.38 and the total fraction of time EF<sub>1</sub> spends paused including pauses shorter than 1s ( $f'_p$ ). Solving

Equations 3.41 and 3.42 gives

$$k_{-1} = \frac{p_1}{p_1\tau_1 + p_2\tau_2} \frac{f'_p}{1 - f'_p} \quad (3.43)$$

$$k_{-2} = \frac{p_2}{p_1\tau_1 + p_2\tau_2} \frac{f'_p}{1 - f'_p} \quad (3.44)$$

The lifetime of the active state prior to decay into the inhibited states 1 and 2 is calculated to be  $\sim 3.3$ s and  $\sim 37$ s at 2mM ATP respectively, and  $\sim 1.1$ s and  $\sim 41$ s at  $20\mu\text{M}$ . In total, the active state decays to the inhibited state with rate  $(k_{-1} + k_{-2})$ . The resulting time constant of the active state is 3.0s at 2mM ATP and 1.1s at  $20\mu\text{M}$ .

### 3.7.4 Angular Position Relative to ATP-Waiting and Catalytic States

The majority of the molecules analysed showed preferential angles for pausing, distributed at  $\sim 120^\circ$  separation around the orbit. To investigate the angle of these inhibited pauses relative to known states within the EF<sub>1</sub> catalytic cycle, molecules exhibiting  $120^\circ$  step-wise rotation, either due to slow ATP-binding or catalytic processes, were analyzed for obvious long pauses. Two examples are shown in Figure 3.24, one relative to the ATP-binding state and one relative to the catalytic state. Obtaining obvious pauses, that are clearly departed from the timescales of the other processes, is quite rare and, as a result, only 11 pauses relative to the ATP-binding state have been analyzed and only seven relative to the catalytic dwells. For these pauses, the inhibited state angular position was found to be at  $+82 \pm 3^\circ$  and  $+2 \pm 4^\circ$  relative to the ATP-binding state and catalytic state respectively. These angles are consistent with the catalytic state being at  $+80^\circ$  from the ATP-binding state, in agreement with the discussions of Section 3.6.5.

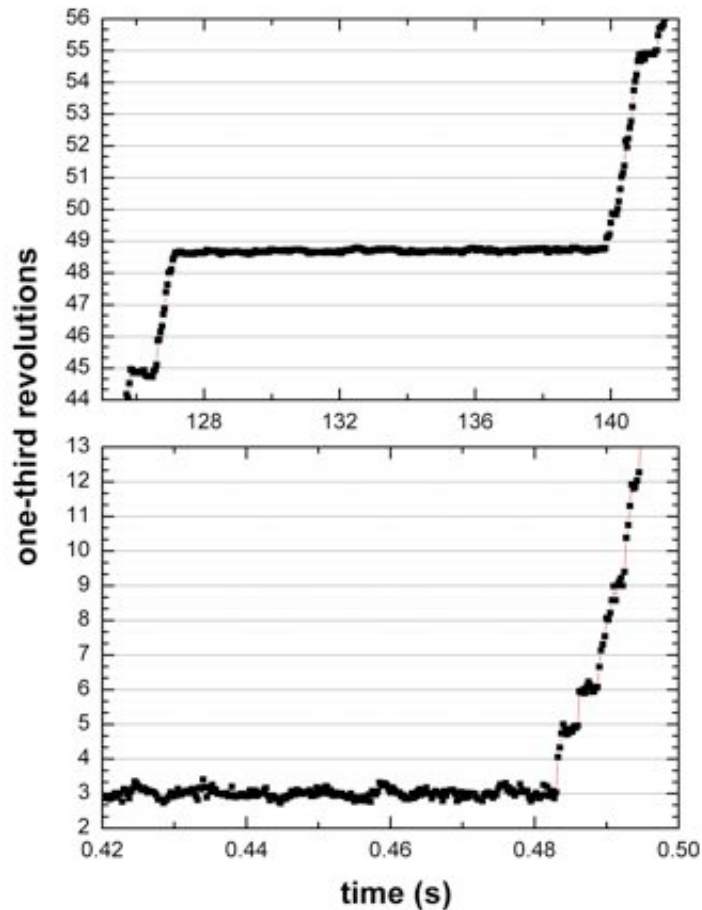


**Figure 3.24:** The angular position of the MgADP-inhibited pause relative to known states in the EF<sub>1</sub> catalytic cycle. Top: A long pause in the rotation of EF<sub>1</sub> at 50nM ATP with a 340nm bead-duplex attached. The ATP-binding states are aligned to the solid grey grid-lines which are separated by 120°. Typical ATP-binding dwells at this ATP concentration are ~0.5s and the probability of observing an ATP-binding event of 12s is estimated to be  $\sim 10^{-10}$ . Bottom: A long pause in the rotation of EF<sub>1</sub> at 2mM with a 60nm gold bead attached. Catalytic dwells last less than 1ms on average and are aligned to the solid grey grid-lines at 120° separation. This pause lasted for greater than 100ms (it was paused when the recording started) and therefore is very unlikely to be due to catalytic events. The probability of observing a 100ms dwell due to two sequential steps, each of less than 1ms, is less than  $10^{-43}$ .

### 3.7.5 Occasional Clicking Between States

During an inhibited pause, EF<sub>1</sub> dwells at three preferred positions separated by 120°. Each pause is normally held uniquely at one of the three angles. However, molecules have been observed where the EF<sub>1</sub> molecule appears to jump between the three angles. One example is shown in Figure 3.25. The radial angular histogram of the paused state demonstrates clear three-fold symmetry in the pause position. However, individual long pauses show transitions between the three positions in both the forwards and backwards direction. This stepping is unlikely to be due to loose attachment of the protein on the surface or the attachment of the bead-duplex to the enzyme since the angles are well-defined and three-fold. A mechanism for this jumping is not proposed but it does suggest that the enzyme has lapsed into a potential energy state that is three-fold symmetric about 360°.

### 3.7.6 A Summary of the Inhibited State of EF<sub>1</sub>

During ATP-driven rotation, EF<sub>1</sub> undergoes spontaneous, load-independent pausing. The actual state may be quite complex since, from analysis of the length of pauses and for ATP concentrations in the range of 20μM–2mM, the state appears to be two indistinguishable yet independent states, one of which is populous and decays with time constant 1–3s, while the other is less frequent with time constant 11–15s. Analysis of the pausing behaviour suggests that EF<sub>1</sub> spends about 50% of its time paused and not rotating, at both 20μM and 2mM ATP. The analysis of the paused state in TF<sub>1</sub> revealed a similar pattern with a short state of ~2s and a long state of ~30s at 2mM ATP, with TF<sub>1</sub> spending two-thirds of its time in the paused state [75].

The origins of the inhibited states are not conclusive. The propensity of TF<sub>1</sub> to lapse into the long pause was greatly increased by the presence of MgADP [75], suggesting that the long pause is due to MgADP-inhibition. It would appear likely that the long pause in EF<sub>1</sub> rotation is also due to

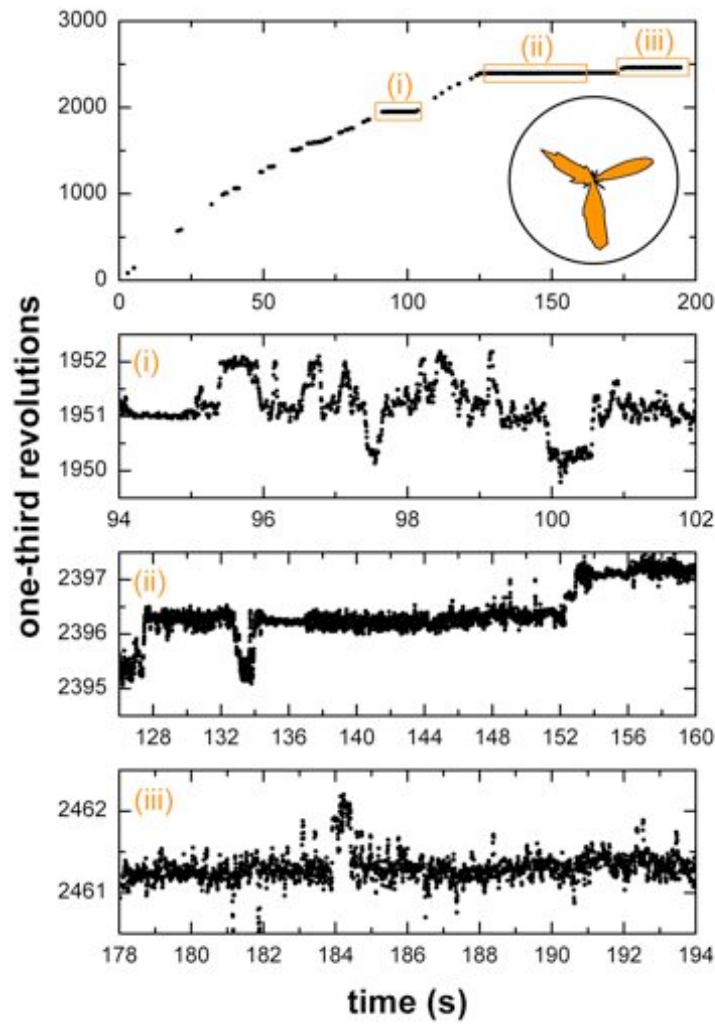


**Figure 3.25:** The observation of occasional transitions between paused states separated by  $120^\circ$  in  $EF_1$ . Top: The angular positions of pauses during rotation. The radial angular histogram shows clear preferred angles  $120^\circ$  apart. (i–iii) Three pauses are expanded that exhibit  $120^\circ$  steps between the three angles, in both the hydrolysis and synthesis direction. The mechanism of this ‘clicking’ is unclear.

MgADP-inhibition. It has been suggested that MgADP-inhibition would not be a feature of EF<sub>1</sub> because bacteria use F<sub>1</sub>F<sub>o</sub> to generate the membrane potential from ATP hydrolysis [173]. However, inhibition of EF<sub>1</sub> catalytic turnover has been observed in the presence of MgADP [102], albeit with excess Mg<sup>2+</sup> ions present, as is the case in these rotation assays. It is expected that MgADP, in general, can inhibit F<sub>1</sub> in two ways: firstly, binding competitively with MgATP, and secondly, by the spontaneous failure of F<sub>1</sub> to release the products of hydrolysis from the catalytic site [173]. There appears to be uncertainty since the ATPase rate of EF<sub>1</sub> has been reported to vary with Mg<sup>2+</sup> concentration [179] in an inhibitory manner [180]. Perhaps the short pause state observed here in EF<sub>1</sub> corresponds to inhibition by Mg<sup>2+</sup> ions, whereas the long pause corresponds to the MgADP-inhibited state reported for TF<sub>1</sub>. At both 2mM and 20μM, of all of the EF<sub>1</sub> molecules paused at any moment 70% are in the short pause whilst the remaining 30% are in the long pause. Future work looking at the effect of Mg<sup>2+</sup> or ADP concentration might help to elucidate the underlying origin of these states.

Importantly, the study of the paused state in EF<sub>1</sub> was attempted to obtain an angular marker in the EF<sub>1</sub> catalytic cycle for future torque measurements. The angle of long pauses (most likely corresponding to the ‘MgADP-inhibited’ long state) has been analysed here. Relative to the ATP-binding state, the paused state is at around the +80° position and, within experimental error, is coincident with the catalytic dwell state. Therefore, long pauses observed in the rotation of EF<sub>1</sub>, even at saturating ATP concentrations, could be used as effective angular markers in future studies.

### 3.8 Verification of the Rotary Nature of YF<sub>1</sub>

---

F<sub>1</sub> derived from yeast mitochondria (*Saccharomyces cerevisiae*) with three His<sub>6</sub>-tags on the β-subunit [181, 182] was sent to me by Prof David Mueller from Rosalind Franklin University, Chicago Medical School, US. Various

yeast mutants have been developed with the aim of relating single molecule rotation data to structural changes. In particular, mutants have been developed with the aim of understanding coupling between the  $\gamma$ -subunit and the  $\alpha\beta$ -stator. My role in the project was the initial verification of the rotary nature of YF<sub>1</sub>. Since then, the project has been taken on by Dr Bradley Steel, who is currently studying wild-type YF<sub>1</sub> and mutants under low-load.

YF<sub>1</sub> appears to be even less stable for rotation assays than EF<sub>1</sub>. The yields I obtained were substantially lower than for EF<sub>1</sub>. I found that pre-incubation of YF<sub>1</sub> with 2mM ATP prior to all assays improved the yield noticeably (not quantified).

Figure 3.26 shows the rotary nature of YF<sub>1</sub> with both 340nm and 495nm bead-duplexes attached. Only a small number of molecules have been analyzed that show stable rotation. The average rotation rates at 2mM ATP were  $2.2 \pm 0.3$ rps and  $4.6 \pm 0.2$  for 495nm bead-duplexes (four molecules) and 340nm bead-duplexes (six molecules).

It can be seen that YF<sub>1</sub> also undergoes frequent pausing during rotation similarly to EF<sub>1</sub>. Despite a relatively small number of molecules having been studied, there appears to be evidence that the pausing is, again, three-fold symmetric. One example is shown in the lower image of Figure 3.26.

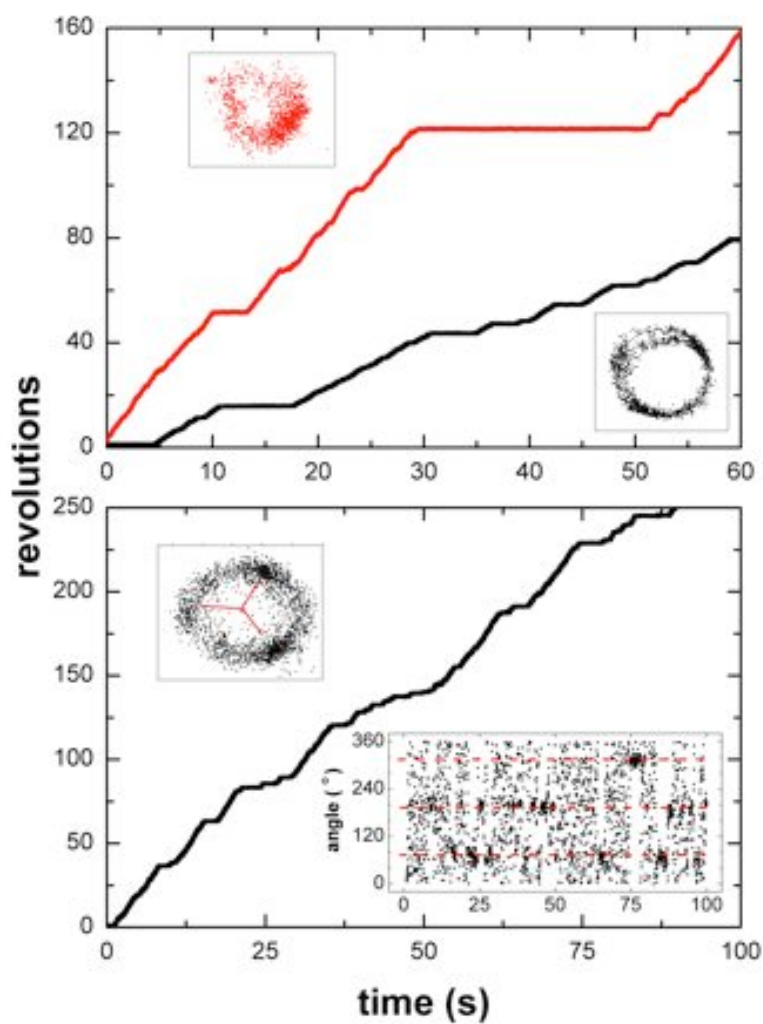


**Figure 3.26:** Verification of the rotary nature of YF<sub>1</sub>. Top: Two example molecules are shown at 2mM ATP with 495nm (black) and 340nm (red) bead-duplexes attached. Bottom: The rotation of YF<sub>1</sub> at 2mM ATP and with a 340nm bead-duplex appears to show a three-fold distribution of pausing angles, with the dominant angles indicated by the red lines.

# 4

## Applying External Torque with an Optical Trap

In this chapter I will present a summary of attempts to apply torque to  $F_1$  by means of an optical angle clamp. This section will be concerned with results obtained from a piece of hardware built and developed by Dr Teuta Pilizota throughout her DPhil. The vast majority of the work presented here was done in collaboration with Dr Pilizota whose knowledge and expertise on the apparatus has been invaluable. Dr Pilizota's thesis [183] detailed the development of the optical angle clamp, allowing a proof-of-concept for the application of torque to the bacterial flagellar motor and  $F_1$  [160]. This aspect of our work will be presented in Section 4.2.

This chapter will not follow experiment in a chronological manner. First, in Section 4.1.1, I will summarize my own contributions to the development of the second-generation angle clamp, including the addition of a new digital signal processing (DSP) board and the full-automation of a switch for turning the trap on and off. In Section 4.2, initial work regarding the stalling of rotating  $F_1$  and the difficulties encountered in trying to measure torques will be presented. Finally, in Section 4.3, I will detail my efforts to use the angle clamp to re-activate  $EF_1$  out of the inhibited state.

## 4.1 The Optical Angle Clamp

---

The optical set-up of the angle clamp was given in Section 2.7 and this section follows on from our discussions regarding force and torque measurements in Sections 1.3.1–1.3.3. Summarized, the optical angle clamp consists of a 633nm Helium-Neon laser for the detection of bead position by back-focal-plane interferometry and a 1064nm Ytterbium laser for optical trapping. Control of the optical trap position is achieved by the use of two acousto-optical deflectors (AODs). The AODs require a digital (15-bit) radio driving frequency input in the range of 60–90MHz and small frequency changes are sufficient to control the down-stream optical trap position in two dimensions. The AOD driver receives a digital signal corresponding to the driving frequency from the host PC and outputs it to the AODs. The host PC, containing a DSP board, handles the on-the-fly calculation of the required trap position and frequency. The interference pattern of the imaged bead is incident onto a quadrant photodiode (QD). The four output voltages from the QD are passed to the DSP board for calculation of bead position. The advantage of using a DSP board is not only rapid on-the-fly calculations but also the control of the timing of the data acquisition loop at a rate independent of the host PC. This means that, despite the PC running slow due to a heavy work-load, the DSP board still receives and processes data at the initialized rate. In this manner, control loops up to 100kHz can be obtained, where the maximal rate is determined by the size of the calculations required. Programming of the DSP board is achieved using QuVIEW (National Instruments), a set of C++ libraries incorporated into LabVIEW (National Instruments). The information flow circuitry is summarized in Figure 4.1a.

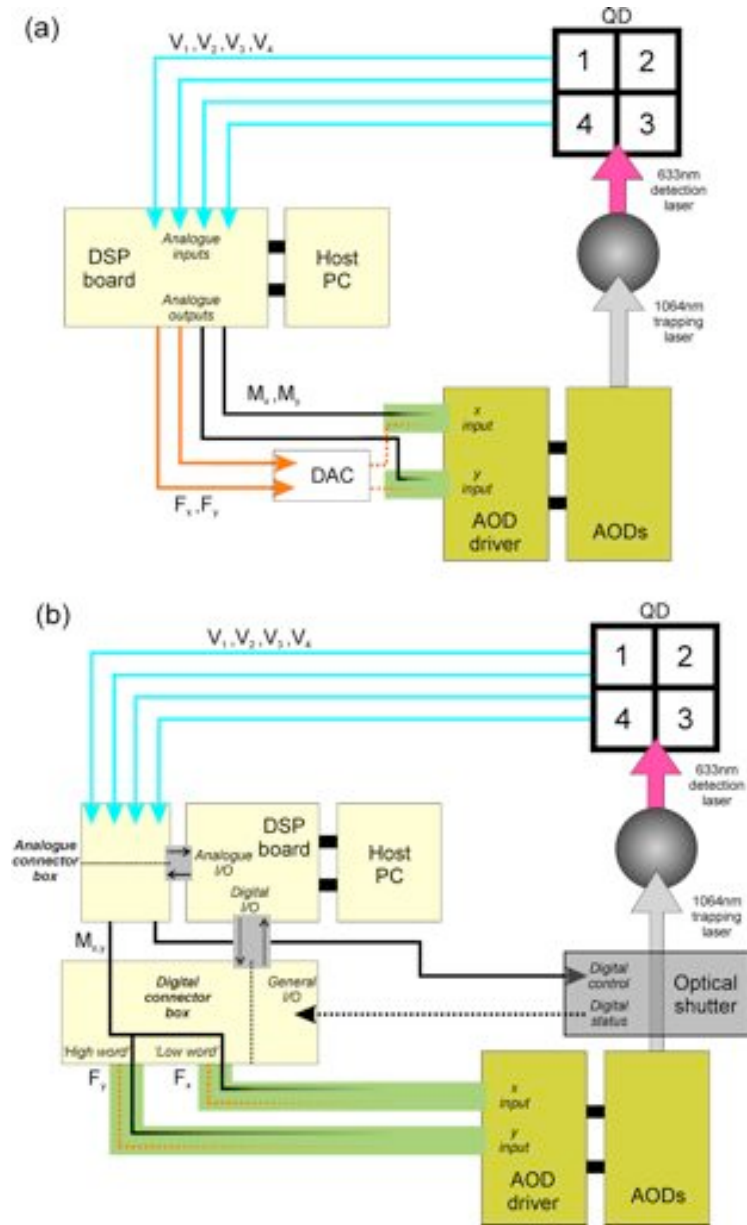


**Figure 4.1:** Schematic diagrams of the information flow within the first-generation (a) and second-generation (b) optical angle clamps. In (a), only the analogue channels of the DSP board can be used, resulting in few available channels and the need to use a digital-to-analogue converter (DAC). In (b), the new DSP board allows digital outputs, freeing up analogue outputs and allowing automated control of a shutter. Thick grey lines indicate connection buses to the DSP board. Solid and dashed flow-lines represent analogue and digital information flow respectively.  $V_{1 \rightarrow 4}$  represent the four quadrant voltages from the QD.  $M_{x/y}$  and  $F_{x/y}$  indicate the amplitude and frequency required by the AOD driver. The green box enclosing the digital  $F_{x/y}$  and analogue  $M_{x/y}$  indicate a 25-pin D-sub connector and ribbon (the precise wiring arrangement is given in Appendix F).

### 4.1.1 Programmable Control of the DSP Board

The ‘first-generation’ optical angle clamp [183,160] was controlled by a DSP board (SI-C33DSP-PCI; Sheldon Instruments) with 16 analogue input channels, 4 analogue outputs and 16 digital input/output (I/O) channels, capable of sampling rates of up to 50kHz. Unfortunately, some of the digital I/O channels never worked and the use of those that did as outputs resulted in a much reduced maximum sampling rate. Hence, only the 4 analogue channels could be used as outputs. The DSP board accepted the 4 voltages from the QD via 4 of the 16 analogue channels and computed the bead position and the desired trap position, using PI control from Equation 1.4 (i.e., with  $K_d = 0$ ). The DSP board then outputted the two frequency signals for control of the AOD deflection angle and two voltages required for the AODs to control the intensity of the transmitted beam. The analogue frequency signals were converted to 16-bit digital words by a custom-built analogue-to-digital converter. In this manner, simple position detection could be obtained at rates up to the maximal 50kHz but for the more intensive feedback programs, only 10kHz maximal rates were achievable.

To enable more automation and higher sampling rates a new DSP board, and host PC, were purchased (SI-Mod68xx-R09 with SI-Mod88xx expansion card; Sheldon Instruments), with up to 16 analogue inputs, 8 analogue outputs and 36 digital I/Os (4 general I/Os and a 32-bit word). This set-up will be referred to as the ‘second-generation’ optical angle clamp. The PCI card carries the analogue I/Os in the form of a 100-pin D-sub connector and the extension card carries the digital I/Os in a 68-pin D-sub connector. To make future reassembly of the set-up easier, I constructed two connection boxes to allow individual channel access through either BNC cables or 25-pin D-sub connectors. The exact nature of the wiring is included in Appendix F for future reference. The AOD driver requires 25-pin D-sub connectors including a 15-bit word describing the driving frequency and an analogue voltage

controlling the AOD transmittance for both the  $x$  and  $y$  axes. Again, this wiring pattern is included in Appendix F. Since  $x$  and  $y$  control is required, and in order to gain an extra analogue output, one analogue output has been wired directly into both of the 25-pin D-sub connectors to supply the transmittance voltage for both  $x$  and  $y$  deflection.

Despite both connection panels being connected to the computer ground, there is a slight issue with the behaviour of the analogue inputs. Even in the absence of signals, the analogue inputs have a small floating background of  $\sim 5\text{mV}$ . The origin of the background signal is not clear since all channels have been tested to make sure they are connected to the ground of the computer which, in turn, is connected to the mains ground (and was tested to be so). The background is small but non-negligible compared to the output signals from the QD of  $\sim 10\text{--}100\text{mV}$ . To remove this, I have taken care to include an option in all written software interfaces to re-calibrate the ‘zero-signal’ readings.

The second-generation set-up has similar sampling limitations as the first-generation set-up. The maximum sampling rate for the small detection programs is  $75\text{kHz}$ . However, the computationally-intensive feedback programs can only run at up to  $10\text{kHz}$ . Perhaps, with intensive attention to programmatic efficiency, these programs could be ‘thinned-down’ to run slightly faster.

### 4.1.2 Shutter Control

One of the difficulties encountered using the first-generation set-up was the lead-time between obtaining a suitable molecule and being able to apply torques with the trap. For example, for experiments where we wished to apply torques to  $\text{EF}_1$  molecules that had recently entered into the inhibited state, the time from noticing that the  $\text{EF}_1$  had paused, moving the angular position of the trap with the PC and then physically removing the beam

block from the trapping laser path was 10–20s, a period that is longer than most pauses (see Section 3.7).

The second-generation set-up has many more outputs available. One of the analogue outputs is used to provide the AOD transmittance voltage, leaving seven other analogue outputs available. I have used one of these analogue outputs to control a beam shutter (SH05; Thorlabs), via a shutter driver, with the aim of automating the initialization of the trap, substantially reducing experimental lead-times. Shutter opening is controlled by a digital TTL signal. Therefore, an analogue signal greater than +2.5V is sufficient to open the shutter. The shutter driver also outputs a TTL signal relating to the status of the shutter. A simple experiment was used to test the speed of the shutter response. The results are shown in Figure 4.2. With the set-up calibrated to remove the floating background signal and with the laser aligned with the QD, the shutter was opened by the PC and the QD output measured. There is a lag between the computer outputting a signal to open the shutter (at  $t = 5\text{ms}$  in Figure 4.2a) and for the shutter to begin opening (at  $t = 22\text{ms}$ ), presumably due to delays in the shutter driver circuitry. A similar delay is observed during closure. The results are highly-repeatable and, over many operations, the delay before opening is always 16–17ms and before closing 26–27ms. The shutter takes  $\sim 1\text{ms}$  to open fully across the width of the beam at its current position<sup>1</sup> and 1–2ms to close.

Since the shutter is controlled by a TTL signal, automated control is straightforward with the DSP board. Regular shutter cycles can be achieved, with varying opened-to-closed ratios, that will be extremely useful, not only in  $F_1$  experiments, but also in experiments on the bacterial flagellar motor.

Shutter control is just one of many devices where automaticity would prove to be useful. Indeed, control of laser drivers would allow automated

---

<sup>1</sup>For these experiments, the shutter was placed in a portion of the beam where the beam width was  $\sim 3\text{mm}$ . If the rise time due to the finite time to open is an issue, it could be reduced by placing the shutter in a plane conjugate to the image plane where the beam width is minimal.

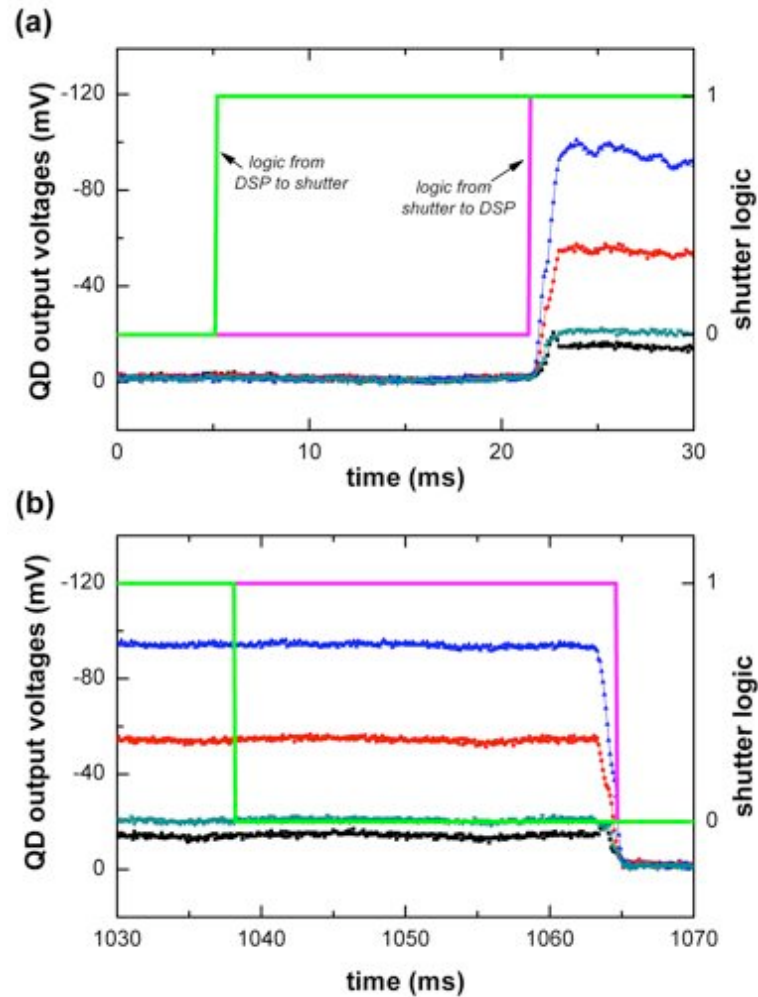


**Figure 4.2:** The speed of the shutter response during (a) opening and (b) closing. The four QD output voltages are shown in blue, red, dark green and black. The shutter was placed in the path of the laser. When the laser was shuttered, the QD voltages read  $\pm 1$  mV. There is a lag between the time for the PC to request the shutter to open (shown in light green) and for the shutter to actually open (magenta) of  $\sim 17$  ms. Similarly, there is a lag between requesting the shutter to close and for it to be fully shut,  $\sim 26$  ms. In line with the advertised specifications, the shutter takes  $\sim 1$  ms to open (as measured by the rise times of the QD voltages) and  $\sim 1$ – $2$  ms to close.

changes in laser intensity. *E. coli* cells expressing proteorhodopsin [184, 185, 186] are capable of generating a PMF from light. Therefore, control of an activating laser could be interesting in resurrection studies of the bacterial flagellar motor in these cells. A similar effect could be achieved by controlling a mechanical neutral density filter wheel by the DSP board, a piece of hardware that is commercially available.

## 4.2 Successful Stalling of $F_1$ with the Optical Angle Clamp

---

I mentioned earlier that this chapter would not be presented chronologically. The main reason for this being that preliminary results using the angle clamp on  $F_1$  were achieved early in the project but were hampered by some serious problems. These initial experiments turned out to be a proof-of-concept, verification that the experiment was feasible but dependent on the resolution of a number of the issues.

The initial results were obtained on both of the  $EF_1$  and  $YF_1$  enzymes, demonstrating that we could manipulate single molecules of  $F_1$  without causing mechanical damage. Experimentally,  $YF_1$  was found to be less affected by the 633nm laser, however the rotation of  $EF_1$  was more consistent. It should be noted that we did request the  $TF_1$  enzyme from the group of Prof Hiroyuki Noji but it was not forthcoming. One example of our manipulation is shown in Figure 4.3. The trap was used as a fixed clamp without feedback. We were able to successfully stall rotating  $YF_1$  and, upon release from the trap, the motor started to rotate at the same speed as pre-manipulation. In the example of Figure 4.3, eight successive stallings did not damage the enzyme. Furthermore, we moved the trap angularly during some of the stalls (see lower inset), both in the direction of hydrolysis and synthesis, verifying that this type of manipulation was possible.

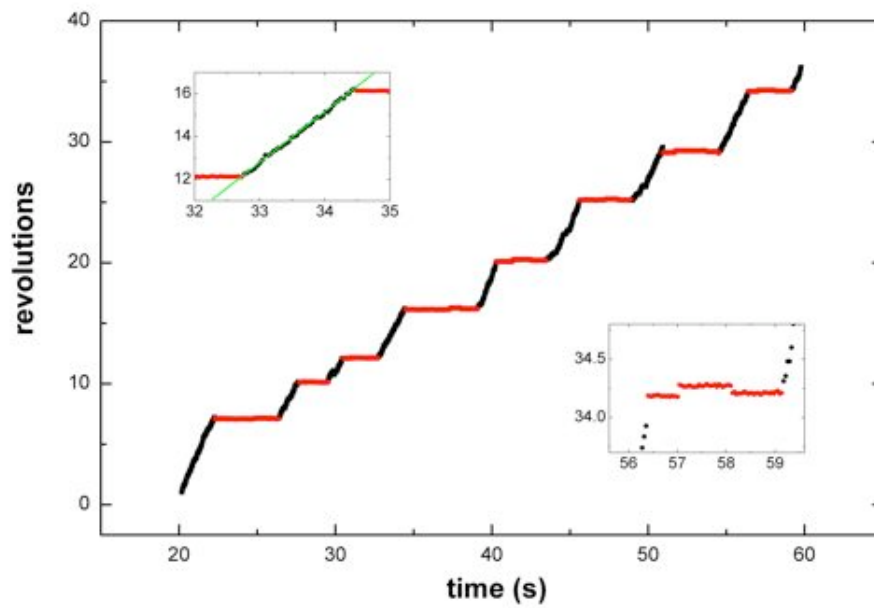


**Figure 4.3:** The sequential stalling of  $YF_1$  with the optical angle clamp at 2mM ATP. Periods without the trap present are shown in black and in red when the trap was used. A 495nm bead-duplex was used as the handle. The rotation rate of  $\sim 2.4$ rps (see green best-fit line in upper inset) did not change after manipulation with the trap. During stalls, we were able to move the bead-duplex angularly without mechanical damage (see lower inset).

### 4.2.1 The Use of Feedback

The most interesting aspect of the optical angle clamp set-up is the use of the feedback element. Feedback allows the direct measurement of motor torque, as described in Sections 1.3.2 and 1.3.3, providing that the trap stiffness can be calibrated. The use of the feedback element on  $F_1$  has been demonstrated, as is shown in Figure 4.4. The rotating  $EF_1$  motor was stalled with the angle clamp at 3.0s and then moved to the  $90^\circ$  position when feedback was turned on at 3.7s. The angular position of the bead-duplex was accurately kept at  $90^\circ$  throughout the period that feedback is on. After 5.9s and 6.75s the feedback was turned off and the angle clamp removed respectively. It is evident that there was no damage to the rotating  $EF_1$  motor upon release. The experiment illustrated in Figure 4.4 is ultimately the torque measurement assay that we plan. At the moment that feedback is turned on, the angular separation between the clamp angle and the bead angle is proportional to the torque produced by the motor. Unfortunately, the strength of the trap was not calibrated, i.e., we did not know the spring constant. In theory, the spring constant can be obtained from the Equipartition of Energy. However, the trap stiffness will change with angle and calibration has to be achieved using a motor not producing torque (i.e. a denatured or ‘dead’ protein). Therefore, calibration needs to be done after torque measurements have been carried out and in such a way as to stop  $F_1$  function prior to the measurement of the trap stiffness. In practice this could be achieved by rapid rotation of the bead-duplex with the trap (perhaps in the synthesis direction), to denature the protein, and then slowly moving the bead-duplex in a circle to obtain the angular trap stiffness. As might be imagined, this is all dependent on the enzyme remaining on the surface long enough for substantial manipulation with the trap.

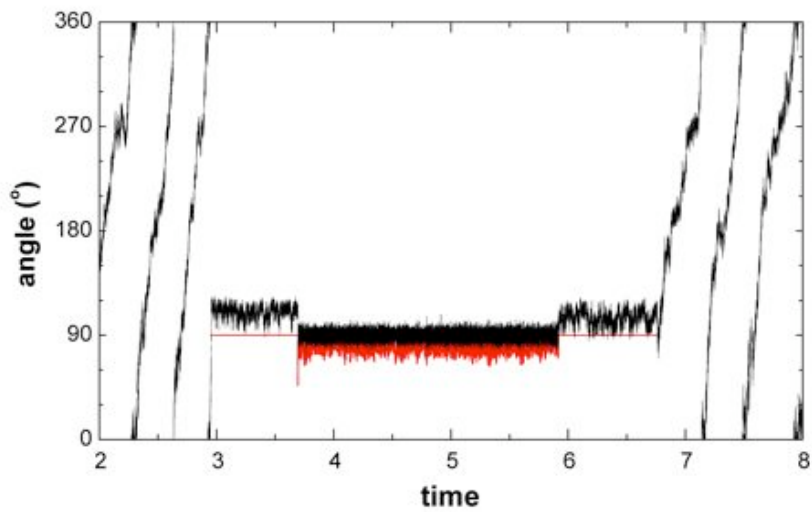


**Figure 4.4:** An example of the angle clamp with feedback being applied to  $F_1$ . The angular position of the bead-duplex is shown in black and the angular position of the angle clamp in red. An  $EF_1$  molecule, rotating at  $\sim 3$ rps at 2mM ATP, is stalled with the angle clamp at  $t = 3$ s. The trap angle is set at  $90^\circ$ . Due to the torque produced by  $EF_1$ , the actual position of the bead-duplex is  $\sim 110^\circ$ . At  $t = 3.7$ s, the feedback element is turned on and the bead-duplex moves to the  $90^\circ$  and the trap moves to oppose the direction of the motor torque. At  $t = 5.9$ s, the feedback is turned off and at  $t = 6.75$ s the trap is removed. The  $EF_1$  motor rotates at 3rps once again.

### 4.2.2 Issues Encountered

The main problem we found related to the attachment of the bead-duplexes to the surface. Frequently, during the application of the trap, the bead-duplexes were pulled off from the surface. The most likely cause for this is that the  $F_1$  itself was detaching from the surface since the bead-duplexes are attached to  $F_1$  via the strong biotin-streptavidin linkage. Furthermore, if the bead-duplex is not completely propellor-like ( $\theta = 0^\circ$  in Figure 3.1), there will be a force exerted on the bead-duplex further pulling it up from the surface due to the bead-duplex's tendency to align with its long axis along the optical axis [187, 188].

Figure 4.5 illustrates some of the issues we had when trying to apply the angle clamp, in this case during feedback on  $YF_1$ . The angle clamp was turned on to hold the 495nm bead-duplex at  $45^\circ$ . With feedback turned on, clear transient events in the trap position, and hence in the torque, can be seen. This type of transient event is exactly the aim of this project, since we hope to observe single molecule binding and/or hydrolysis on the enzyme. However, this may not be the case here. For this molecule, the transient increases in torque are accompanied by motion radially of the bead-duplex, as evident by the  $xy$  position plot. This motion should not be possible for a stably-anchored  $F_1$  molecule. It appears likely that we may actually be observing the transient detachment, and subsequent reattachment, of one or more of the  $YF_1$ 's His<sub>6</sub>-tags. In fact, the frequency of these transient events is roughly  $2s^{-1}$ , in agreement with the  $k_d$  of His<sub>6</sub>-tags from Ni<sup>2+</sup>-NTA discussed earlier in Section 3.2.

We therefore resolved to spend time improving the enzyme-surface interaction and the yield of the assay. An improved yield is important such that it is possible to only select propellor-like bead-duplexes to use. A summary of the different surface chemistries studied was given in Section 3.2. The best surface for the conventional rotation assay was found to be the Ni<sup>2+</sup>-

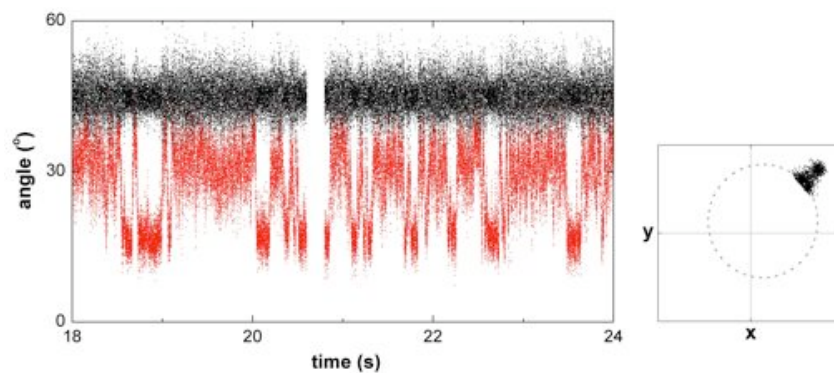


**Figure 4.5:** Observations of torque fluctuations produced by  $YF_1$  during stall. The bead-duplex angle is shown in black and the angular clamp position in red. Feedback was ‘on’, with parameters  $K_p = 0.8$  and  $K_i = 0.2$  from Equation 1.4. The bead-duplex was held fixed at  $45^\circ$  but fluctuations can be seen in the trap response, with occasional increases of  $\sim 2\times$ . One would expect to see transitions in the torque if  $F_1$  was stalled at an angle close to a power-stroke. However, in this instance, we cannot be confident since the fluctuations are accompanied by radial movements, as evident from the  $xy$  position image. The bead-duplex is only trapped angularly and is free to move radially. These transitions may possibly be due to dissociation of one of the  $\text{His}_6$ -tags from the glass surface. The approximate orbit of the bead-duplex during rotation is shown by the grey dashed line. The gap in the data at around 20.5s is due to two back-to-back files being recorded and this section corresponded to experimental dead-time.

NTA-silane surface, however, this surface does not fully resolve the issues of bead-duplex removal with the trap. Ideally, a more stable interaction than His<sub>6</sub>-tags on Ni<sup>2+</sup>-NTA could be used and a potential solution will be discussed in Section 5.2. I imagine that the improvement observed when using the Ni<sup>2+</sup>-NTA-silane surfaces compared to other surfaces considered is that there is a high density of Ni<sup>2+</sup>-NTA on the surface and therefore any dissociation of the His<sub>6</sub>-tags from Ni<sup>2+</sup>-NTA will be rapidly followed by re-attachment. The torques applied with the trap, however, may be such to stop this re-attachment. The switch from His<sub>6</sub>-tags to His<sub>10</sub>-tags (see Section 3.2) is only expected to make a small difference in this regard, in line with my own observations.

Finally, a separate issue we have encountered is that of possible laser damage by the 633nm laser during position detection. This effect has not been quantified and may be more of an issue for the EF<sub>1</sub> enzyme than YF<sub>1</sub> from my own observations during rotation assays. When put into the 633nm laser focus, some molecules became paused and stopped rotating. Occasionally, laser-paused molecules recovered when removed from the beam. Some molecules, however, showed little effect of the laser, whilst some detached from the surface when moved into the laser. For this reason, most of the large-load data presented in Chapter 3 was obtained with video recording and not by back-focal-plane detection. Laser-induced damage was most noticeable using the 633nm laser and not the 1064nm laser. Singlet oxygen scavengers have been used in previous TF<sub>1</sub> work [134, 123] but little improvement was observed when the ‘glucose oxidase - catalase’ system was tried [189]. Biological samples absorb less light as the wavelength moves towards the near-infrared [170] and for this reason the 1064nm laser was chosen as the strong trapping laser. However, all previous laser dark-field microscopy assays on TF<sub>1</sub> and EF<sub>1</sub> have used a 532nm laser and therefore the replacement of the 633nm laser with a 532nm laser might be an

idea to try in the future if laser damage is a continual problem. Equally, a laser in the range of 800–1000nm could be considered, provided that it can be satisfactorily separated from the 1064nm trapping laser with a dichroic filter.

### 4.3 Mechanical Activation

---

Mechanical activation of the inhibited state of  $\text{TF}_1$  has been studied using magnetic tweezers [82]. It was found that rotation of the  $\gamma$ -subunit in the hydrolysis direction increased the probability of the motor re-activating, presumably due to the loss of MgADP from the binding site. It has been postulated that the forced forward rotation of the  $\gamma$ -subunit results in the unzipping of the binding site holding the MgADP molecule [82].

Considering that  $\text{EF}_1$  shows similar pausing behaviour to  $\text{TF}_1$ , we have used the angle clamp to achieve mechanical activation of paused  $\text{EF}_1$ . We do not have the wealth of data yet to make any quantitative statements regarding the rate of mechanical activation with respect to external torque applied, except that it appears that the probability of re-activation increases markedly with the degree of external torque applied, in agreement with the  $\text{TF}_1$  results. I believe that our set-up has a distinct advantage over the magnetic tweezers technique and should allow more detailed measurements to be made. The main problem with the magnetic tweezers approach is that when the bead is rotated forwards, there is no knowledge of when the motor is activated. It is only when the trap is turned off that the motor status can be determined, i.e., if it has been reactivated by the mechanical manipulation it will be rotating when the trap is switched off. In our set-up, using the angle clamp with feedback, we should be able to tell the precise time during the manipulation that the motor re-activated, due to the increase in the relative torque measured. This experiment is now just at the stage where it is viable and it will be very interesting to see the results. Instead, I will

present here a few examples of our initial experiments which, in their own right, demonstrate the novel mechanical activation of EF<sub>1</sub>.

Of the 15 molecules that have been subjected to manipulation with the angle clamp in the static mode (i.e., with feedback ‘off’), eight ( $\equiv$  53%) were successfully re-activated from the paused state. All eight were manipulated more than once. The probability of activation appears to depend on the degree of forward rotation applied with the clamp. All eight molecules had failed activation attempts and successful attempts throughout multiple pauses. One example is shown in Figure 4.6 detailing an EF<sub>1</sub> motor rotating at 2.0rps in the presence of 20 $\mu$ M ATP and with a 495nm bead-duplex attached to the  $\gamma$ -subunit. Twice during rotation, the angle clamp was used to spin the bead-duplex at 1.7rps in the forwards (hydrolysis) direction. Removal of the trap resulted in rotation again at 2.0rps, indicating no mechanical damage. When the EF<sub>1</sub> motor entered into an inhibited pause, the clamp was used to move the bead-duplex in the forwards direction and, upon release from the trap, the motor began rotating at 2.0rps once again. It should be noted that some of the incremental movements with the trap were in the backwards direction. This was accidental and caused by the difficulty of controlling the angular position with the first-generation set-up. This has since been automated on the second-generation set-up and no user input will be required during the actual manipulation.

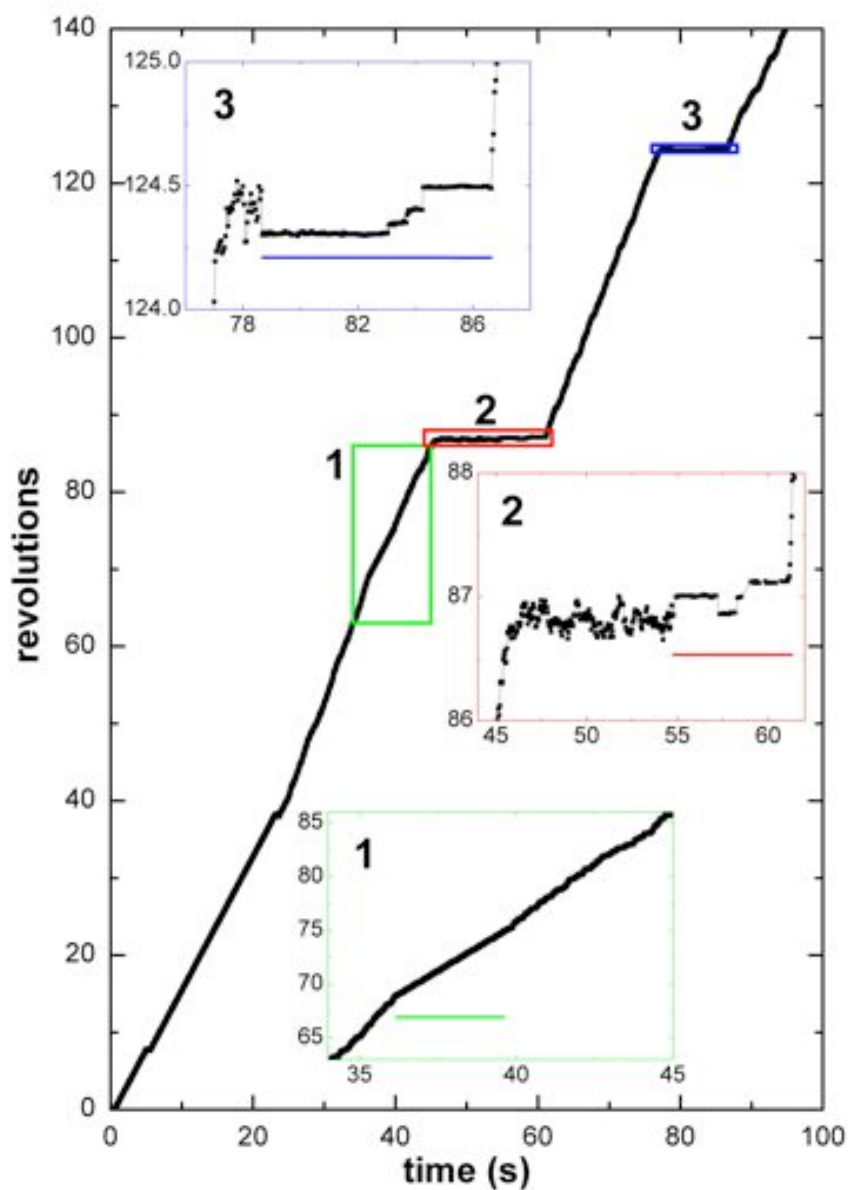


**Figure 4.6:** The activation of  $EF_1$  from the inhibited paused state by the application of external torque.  $EF_1$  was rotating in the presence of  $20\mu\text{M}$  ATP and a  $495\text{nm}$  bead-duplex. During rotation, the angle clamp can be used to manipulate the enzyme. These periods of manipulation are indicated by the horizontal lines in the insets. In this instance the feedback element of the angle clamp was not used. (1) Forced rotation at  $1.7\text{rps}$  with the trap in the hydrolysis direction does not hinder rotation after release from the trap. It should be noted that the molecule was also rotated forwards at  $1.7\text{rps}$  with the angle clamp between  $5\text{s}$  and  $22\text{s}$ . (2) The mechanical activation of  $EF_1$  from a pause by a forwards rotation of  $> 120^\circ$ . (3) The activation by forwards rotation of  $\sim 30^\circ$ . In (2) and (3) it is not possible to tell the exact point during manipulation that activation occurred.

# 5

## Discussions and Conclusions

The aim of this project was to measure the angular torque profile of  $F_1$ -ATPase through the application of external torque by an optical angle clamp. As we have discussed in previous chapters, this goal has still not been achieved but I believe that I have made substantial advancements to this end. I have demonstrated that we are capable of applying pN·nm torques to 495nm bead-duplexes attached to the  $\gamma$ -subunit of both  $EF_1$  and  $YF_1$ . A natural extension to this proof-of-concept work will be the measurement of torque produced by  $F_1$ , subject to calibration of the angle clamp for individual bead-duplexes and the stable attachment of the motors to the surface.

This thesis is mainly concerned with  $F_1$  derived from *Escherichia coli*. Compared to the raft of published literature describing the rotation of  $F_1$  from the thermophilic *Bacillus*, relatively little is known about  $EF_1$ . It is certainly not correct to assume that the two enzymes have the same characteristics, despite their related genealogy, since their physiological environments are substantially distinct. To this end, I have presented a detailed mechanical characterization of  $EF_1$  rotation.

The  $EF_1$  characterization has shown only small departures from that of  $TF_1$  and it appears that the two enzymes share a considerable number of

---

traits. The ATP-binding state, the catalytic binding state and the inhibited state of  $EF_1$  have been studied. The main difference was found to be the rate at which ATP-binding and the catalytic processes occur.  $EF_1$  rotates almost four times faster than  $TF_1$  at room temperature and, as a result, we have experienced issues with insufficient temporal resolution when  $EF_1$  rotates at full speed. The primary aim of the characterization of  $EF_1$  rotation was to obtain a detailed knowledge of available angular markers of the enzymatic catalytic cycle for use in the angle clamp experiments. I propose that these angular markers are either the ATP-binding dwell or the inhibited state. Considering the extremely low yield of rotating bead-duplexes obtained at a few nM, the most obvious candidate is the inhibited state.

With regards to the mechanical characterization of  $F_1$ , there are two points that I would like to raise here - neither qualify as rigorously scientific but they might make interesting points of discussion.

Firstly, the work presented here suggests that  $EF_1$  produces torque in the range of 33–40pN·nm. The previous studies of  $EF_1$  have predicted 40pN·nm [88] and 50pN·nm [87] using actin filaments. By comparison,  $TF_1$  has been reported to generate 40pN·nm using actin filaments [34, 73] and 20pN·nm using nano-engineered gold rods [60], whilst  $F_1$  from spinach chloroplasts was reported to produce torque in the range 10–40pN·nm [89]. Whilst acknowledging that this view is in contradiction to much of the work of the last decade, I believe that there is still uncertainty as to the precise value of the torque from  $F_1$ . It is my view that the value of 40pN·nm was published initially for  $TF_1$  [88] and all subsequent studies have said that their data support this value. Within each study, a wide range of torques or speeds are reported, typically varying from 10pN·nm up to ~60pN·nm. This is not to say that different molecules of a particular  $F_1$  produce variable torque, just that the experimental uncertainty is large. A natural question is: Does obtaining the exact torque value really matter? Well, yes. 40pN·nm

is the basis for the assertion that  $\text{TF}_1$  is a highly efficient motor, something that has previously been assumed to be required due to the reversibility of  $\text{F}_1$ . In turn, the  $\sim 100\%$  efficiency leads to a requirement of constant torque, something that has since been ‘shown’ by experiment. As I have mentioned in previous sections, non-constant torque over the  $120^\circ$  catalytic cycle can lead to  $\sim 90\%$  efficiency. I am not suggesting that  $40\text{pN}\cdot\text{nm}$  is wrong, indeed my own work on  $\text{EF}_1$  agrees with this value, however  $40\text{pN}\cdot\text{nm}$  appears to have entered into  $\text{F}_1$  folklore, despite the fact that it was only an estimate in the first rotation paper and that there is a large error associated with it. Furthermore, an adequate treatment of the surface effect on the drag coefficient of the observational probe has yet to be presented, increasing the uncertainty on the torque prediction.

My second aside, and one which is raised purely for purposes of discussion, is: Do  $\text{F}_1$  from all species rotate at the same speed at their correct physiological temperature and conditions? I ask this not because I think it is correct, but because there is such inherent beauty in the function and structure of  $\text{F}_1$  that, if it were true, I would not be surprised. The full speeds of  $\text{YF}_1$ ,  $\text{EF}_1$  and  $\text{TF}_1$  are  $\sim 600\text{rps}$  (B. Steel, unpublished data),  $450\text{rps}$  and  $130\text{rps}$  [74] respectively, whilst room temperature ( $23^\circ\text{C}$ ) departs from physiological temperatures by  $7\text{K}$ ,  $14\text{K}$  and  $\sim 50\text{K}$  respectively. It has been reported that  $\text{TF}_1$  rotates at  $\sim 700\text{rps}$  at  $50^\circ\text{C}$  and physiological rotation rates might be  $\sim 1000\text{rps}$  [81].  $\text{EF}_1$  and  $\text{YF}_1$  should be relatively easy to observe at physiological temperatures compared to the  $\text{TF}_1$  enzyme and this project could be attempted with our current set-ups.

## 5.1 Future Work

---

In terms of the characterization of  $\text{EF}_1$  rotation, there remain three aspects that, whilst unnecessary for the determination of angular markers with respect to the catalytic cycle, would be interesting subjects for future research.

Firstly, the simultaneous observation of the ATP-binding and catalytic dwells would allow a precise determination of the relative angles of the two states. I believe that 1–5 $\mu$ M ATP $\gamma$ S using a camera sampling rate of at least 1kHz should allow such observation. It would appear likely that the two states are distinct since, in light of our discussions in Chapter 3, there are many clues suggesting their relative position but with no definitive answer yet.

Secondly, the inhibited state of EF<sub>1</sub> will make a useful angular marker of EF<sub>1</sub> rotation but its chemical origin is not 100% clear. The long pause appears to behave very similarly to the long pause of TF<sub>1</sub>, shown to be due to MgADP-inhibition. Further work involving buffer exchange (attempted in this study but unsuccessfully) should allow determination of the origin of inhibition and a possible reaction scheme for entry into the inhibited states.

Thirdly, the rotation rate of EF<sub>1</sub> over a range of temperatures would be interesting. A temperature-controlling unit has been developed within the Molecular Motors group allowing either cooling of the sample down to 0°C or heating up to ~40°C. A new rate-limiting process has been observed in TF<sub>1</sub> at 4°C [93, 81], likely to be due to ADP release [81], but it has been predicted that much lower temperatures would be required to observe a similar effect in EF<sub>1</sub> [93] due to a lack of temperature dependence observed in bulk for EF<sub>1</sub> [190].

The obvious next experiment on EF<sub>1</sub> is the application of the angle clamp to EF<sub>1</sub>. Initially, the activation of EF<sub>1</sub> from the inhibited state should be attempted, using the angle clamp with feedback ‘on’. This technique has an obvious advantage over the previous TF<sub>1</sub> activation study [82] in that the precise moment of activation should be sensed by the feedback response. A more-detailed investigation of the inhibited state will be available using this technique. Furthermore, following my work on the second-generation angle clamp, full-automation of the system will allow a more intensive and

repeatable study of this process.

A significant advantage of the activation study with the angle clamp is the lack of requirement for rigorous calibration since activation will be observed simply by absolute changes in the trap angle. If the calibration issue can be resolved, the torque measurement is no more challenging than the activation experiment. Again, the improved automation of the second-generation system will allow easier control of the angle clamp in this study.

## 5.2 Other Ideas

---

The reliable application of the angle clamp to  $EF_1$  is still dependent on obtaining a more stable protein-surface attachment. We have discussed in previous sections that a His<sub>6</sub>-tag on a single Ni<sup>2+</sup>-NTA group dissociates about once every two seconds and that, if three Ni<sup>2+</sup>-NTA groups can be brought together with the correct topology, the dissociation of a His<sub>10</sub>-tag from one of the so-called TrisNTA groups occurs approximately once every six hours [168,191]. Whilst the Ni<sup>2+</sup>-NTA-silane surfaces we use have proved to be just sufficient for obtaining decent rotation assay data, the requirements of the angle clamp experiments are such that it would certainly be preferential to obtain a TrisNTA-coated surface.

TrisNTA was initially constructed using synthetic chemistry [168]. This option was considered but would have still resulted in the requirement to coat a glass surface with the synthesized TrisNTA group. Following discussion with Prof Andrew Turberfield and Dr Achillefs Kapanidis, a symbiotic scheme was borne out to construct TrisNTA onto a modified single-strand of DNA. The ability to attach a His-tagged protein to DNA in a non-transient manner is highly advantageous for possible drug delivery systems based on DNA nanostructures, for example, by using DNA as a cage [192,193,194,195]. One considerable advantage of using DNA is that three-dimensional structure can be engineered simply by careful choice of the

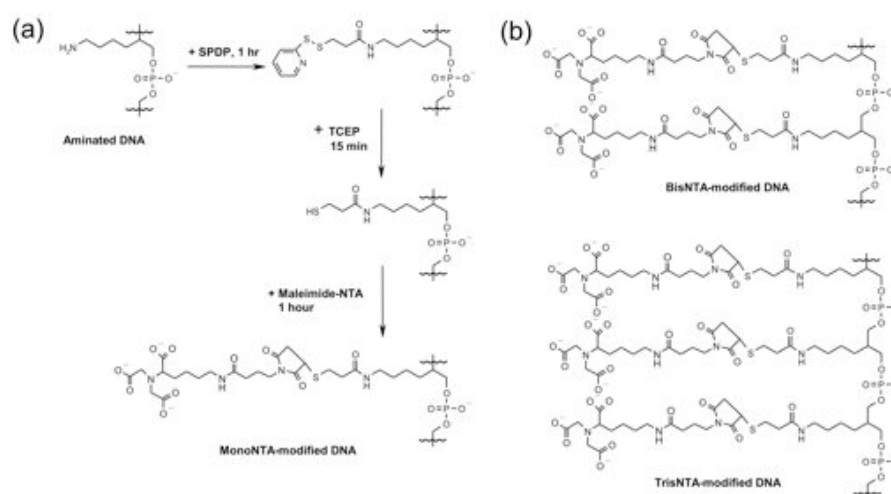


**Figure 5.1:** A scheme for the attachment of  $\text{Ni}^{2+}$ -NTA groups to modified DNA single-strands, leading to the construction of TrisNTA-DNA. The wiggly lines represent attached DNA oligonucleotides. (a) Modified DNA can be purchased commercially (Uni-Link amino modifier; IDT) that replaces the sugar component of the DNA backbone with an amino group on the end of a six carbon linker. Reaction with a functional cross-linker (SPDP) and subsequent reduction (TCEP) allows the attachment of maleimide-NTA. (b) Multiple  $\text{Ni}^{2+}$ -NTA groups can be introduced into the DNA strand in this manner, named BisNTA-DNA (two  $\text{Ni}^{2+}$ -NTA groups) and TrisNTA-DNA (three  $\text{Ni}^{2+}$ -NTA groups). Adapted from a figure by Dr Christoph Erben.

DNA sequence. Figure 5.1 outlines the synthesis of TrisNTA-DNA, worked carried out by Drs Russell Goodman and Christoph Erben in the group of Prof Andrew Turberfield, with fluorescence characterization achieved by Wei Meng Ho in the laboratory of Dr Achillefs Kapanidis [196]. Commercially-available DNA containing a modified aminated backbone can be sequentially reacted to attach maleimide-NTA. Either one, two or three consecutive modifications can be included in the designed DNA sequence to produce MonoNTA-DNA, BisNTA-DNA and TrisNTA-DNA respectively. TrisNTA-DNA has been found to have a similar equilibrium dissociation constant,  $K_D$ , to the original TrisNTA study [196, 168].

The issues we have observed when using the angle clamp on  $F_1$  range from apparent release of one or two His-tags (e.g., Figure 4.5) to the com-

plete dissociation of  $F_1$  from the glass surface. It is therefore apparent that, to obtain a stable attachment between the enzyme and the surface, all three His<sub>10</sub>-tags must be attached to a TrisNTA-DNA group. The task is therefore to obtain a sufficiently dense surface concentration of TrisNTA-DNA groups or to arrange three TrisNTA-DNA groups onto the surface in the correct geometry for  $F_1$ . Inspiration came from work within the group of Prof Andrew Turberfield by Dr Jonathan Malo on the construction of regular arrays of DNA, as shown in Figure 5.2. A simple Holliday junction consisting of four DNA oligonucleotides with complementary overhangs will self-assemble to form an extended lattice [197]. The initial aim was that the lattice could be used for the regular attachment of proteins in future crystallization studies. However, the spacing of the lattice is such that regular triangles of side length 8.8nm are arranged periodically. A central point along each edge of these triangles forms smaller triangular arrays of side length 4.4nm. Movement of the point from the centre to the vertex of the large triangles will vary the size of the smaller array from 4.4–8.8nm whilst maintaining three-fold symmetry. The size could therefore be tuned to match that of the His-tags in  $F_1$ . Alongside Dr Jonathan Malo, we made some initial attempts to visualize His<sub>10</sub>-tagged  $EF_1$  on the TrisNTA-DNA array using transmission Electron Microscopy (TEM) suggesting protein density at the expected attachment points but no conclusive results could be drawn (data not presented). We also attempted to attach the DNA arrays to Clean Glass by increasing the salt concentrations but the attachment was insufficient to leave arrays on the glass surface after a number of washing steps (arrays visualized with Sybr-Gold). These ideas have since been extended to use the DNA array template, incorporating TrisNTA-DNA, as a staple for structural determination of non-crystallizable His-tagged proteins with encouraging results (no method presented, patent pending - Daniele Selmi and Prof Andrew Turberfield). It is thought that this method will allow

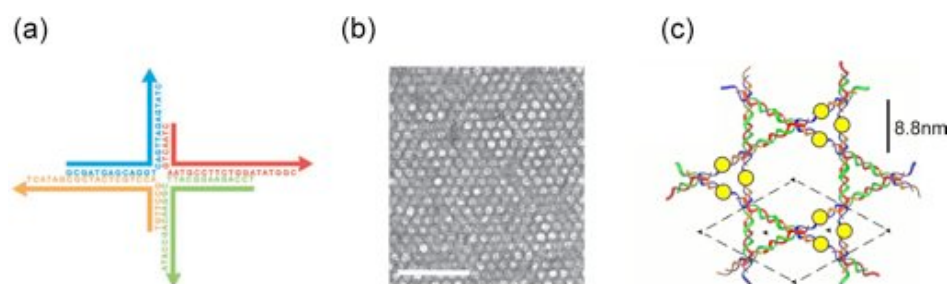


**Figure 5.2:** Regular arrays of DNA could be used for the immobilization of His-tagged proteins. (a) A Holliday junction formed from four complementary oligonucleotides. (b) The Holliday junction has sticky ends which allow their self-assembly into extended arrays forming a Kagome lattice. The size bar shown in white represents 100nm. (c) TrisNTA-DNA (indicated by the yellow circles) could be incorporated into two of the oligonucleotides to create a regular patterning of TrisNTA-DNA triangles with side length varying from 4.4–8.8nm. The dotted black line represents the unit cell of the lattice. (a) and (b) are adapted from [197] with permission.

protein structure determination by cryo-electron microscopy at resolutions better than 10Å.

The ability to pattern TrisNTA-DNA at a known periodicity with three-fold symmetry is an interesting development and could be used to form pseudo-crystals of  $F_1$ . However, for the case of rotation assays, a sparse distribution of  $F_1$  on the glass surface is desired. In this manner, DNA can still be used as a building-block but this time to obtain only occasional areas with three TrisNTA-DNA groups presented. This project was spawned from the DNA arrays idea and has since been taken on as a DPhil project by Shelley Wickham under the supervision of Prof Andrew Turberfield and Dr Richard Berry. The ability of creating bespoke two-dimensional patterns by DNA origami has been demonstrated [198] using a 7-kilobase viral DNA strand and in excess of 200 staple strands to construct self-assembled  $\sim 100$ nm tiles. A simple origami tile is shown in Figure 5.3a–c. Origami tiles produced by Shelley Wickham in a similar manner have been imaged by AFM (Figures 5.3d and 5.3e) and have been designed such that three of the staple strands present a TrisNTA-DNA group. The location of the three His<sub>10</sub>-tags on EF<sub>1</sub>

is not definitively known since the N-terminus of the  $\alpha$ -subunit has not been resolved in the 1.9Å MF<sub>1</sub> crystal structure [111]. The first resolved residue in the MF<sub>1</sub> structure is that of  $\alpha$ Asp-24 (corresponding to Glu-23 in the EF<sub>1</sub> structure). The His<sub>10</sub>-tags are therefore assumed to be located close to these resolved residues (Figure 5.3f) and form a triangle of side length 4.7–4.9nm. The design of the tiles is such that the TrisNTA-DNA groups are presented on the same face of the tile with this spacing. Other strands in the tile can be modified to include biotin tags for the attachment of the tiles to a streptavidin-coated coverslip, as shown in Figure 5.3g. Obviously, this double use of the biotin-streptavidin linkage may cause problems regarding to background attachment of biotinylated beads directly to the glass surface (i.e., not via F<sub>1</sub>). Future designs might wish to use a DNA-brush surface (for an example, see [199]) and ‘sticky overhangs’ on the origami tile for the surface attachment to avoid this potential issue.

If the origami tiles can be attached to the glass surface, this method might provide an ideal linkage for F<sub>1</sub> rotation studies. If the geometry is correctly designed, EF<sub>1</sub> should effectively be attached permanently to the surface. However, even if the origami tiles idea does not prove to be an effective solution (i.e., the correct geometry of TrisNTA-DNA can not be achieved or that F<sub>1</sub> does not rotate effectively upon the DNA origami tiles), TrisNTA-DNA could still be an effective linkage by the construction of a DNA brush onto the glass surface (for example, see [200,201]). Covalent attachment of the TrisNTA-DNA to the glass surface (either through a complementary strand to which TrisNTA-DNA can hybridize or directly to the surface itself) at a suitably high density should equally provide a permanent immobilization of F<sub>1</sub> onto the surface. My belief is that these spin-off projects will have a large influence as to the future success of angle clamp experiments on F<sub>1</sub>. If the use of DNA as a surface linker is to be successful, a significant amount of effort will need to be invested to ensure

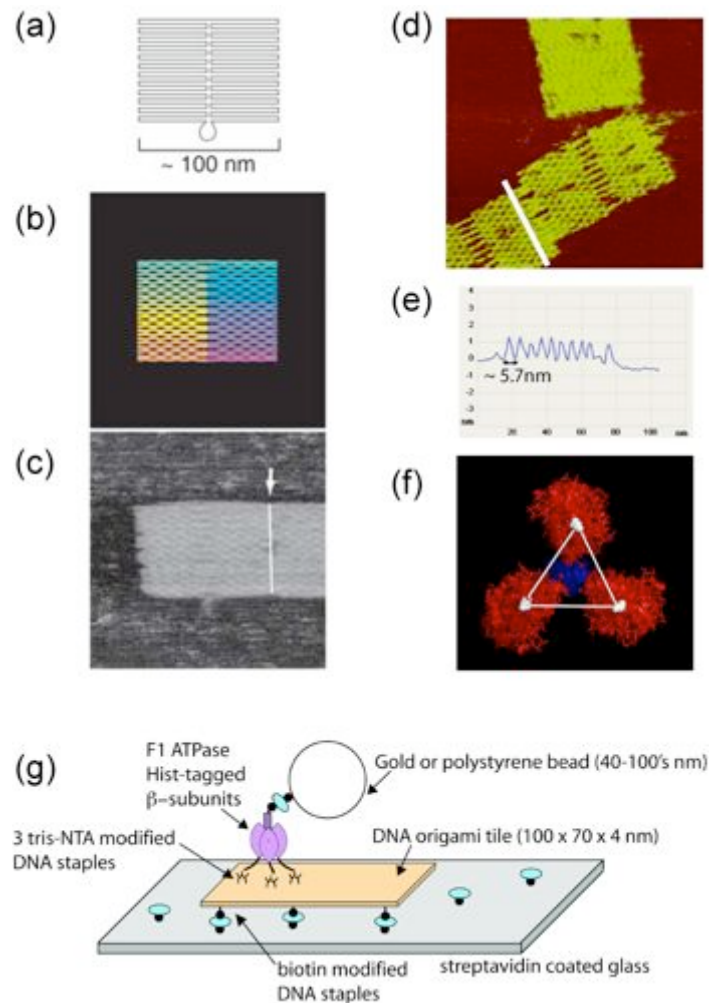


**Figure 5.3:** Constructing DNA origami tiles to act as surface linkers for the attachment of  $F_1$  to a glass surface. A 7-kilobase strand of viral DNA can be folded to create a  $\sim 100$  nm tile (a) by the addition of  $\sim 200$  short staple oligonucleotides (b). The resulting tiles can be visualized by AFM (c). (a-c) are adapted from [198] with permission. (d) An AFM image of a DNA origami tile produced by Shelley Wickham. (e) The characteristic spacing of the lattice is  $\sim 5.7$  nm along the cross-section of the white line in (d). (d) and (e) are from Shelley Wickham. (f) An approximate location of the three His-tags in  $F_1$ . The structure shown is that of  $MF_1$  at  $1.9\text{\AA}$  [111] (PDB code 2JDI) as viewed from the N-terminal end of the  $\alpha_3\beta_3$ -hexamer. The His<sub>6</sub>-tags are located at the N-terminus of the  $\alpha$ -subunit. The first 23 amino acids are not resolved in the crystal structure. The first residue in the structure is Asp-24, corresponding to Glu-23 in the  $EF_1$  sequence. Asp-24 is indicated in each of the  $\alpha$ -subunits (in red) by the white spheres. The residues form a triangle of side length 4.7–4.9 nm. Visualized using Pymol [112]. (g) A schematic of the possible attachment of  $F_1$  to a glass surface via an origami tile linker, drawn by Shelley Wickham.

that the yield of  $F_1$  rotating on DNA structures is adequate.

From an engineering point of view, developing a method with which to decorate a surface with TrisNTA groups with a predetermined geometry will be an interesting result in terms of nanotechnology. The origami tiles project could open up a whole new area of synthetic fabrication, including interesting ideas for creating teams of  $F_1$  rotating in series or for the co-localization of fluorescent phosphate-binding proteins and  $F_1$  for sensing the release of  $P_i$  from the nucleotide binding site during hydrolysis.

Finally, a brief mention should be made as to the ultimate goal of the single molecule field studying ATP synthase - namely, the observation of ion flux-driven rotation of  $F_1F_o$  in ATP synthesis mode. As we discussed in Section 1.2.2, the main challenges here revolve around obtaining a stable bilayer system and the reconstitution of  $F_1F_o$  into the bilayer. This project is being pursued by various researchers, including Wei Meng Ho in the Molecular Motors group who is attempting to use a newly-developed technique for the production of stable bilayers. Bilayers can be formed between aqueous droplets and a hydrated surface immersed in a lipid-oil mix [202]. This technique allows highly-stable bilayers of  $\sim 0.2\mu\text{m}$  in diameter within a droplet of less than  $1\mu\text{l}$ , with precise control of the bilayer location and size. Wei Meng Ho is currently attempting to obtain a perfusable system such that all reagents required for a rotation assay can be added in turn. It is hoped that *E.coli*  $F_1F_o$  reconstituted into vesicles will automatically insert into the bilayer. In this closed system, electronic contacts should be straightforward allowing control of the membrane voltage. This is an exciting development in our group and hopefully it is one that will yield interesting new results in the near future.

# A

## Purification of F<sub>1</sub>-ATPase from *Escherichia coli*

The following protocol for the purification of *E.coli* F<sub>1</sub>-ATPase is based on a protocol obtained from Professor Masamitsu Futai. The total method takes four days, two of which are spent growing cells. *E.coli* F<sub>1</sub> and F<sub>1</sub>F<sub>o</sub> are expressed by plasmids within *E.coli* cells modified to be resistant to ampicillin. The *E.coli* strains are discussed in Section 2.2.

### A.1 Buffers and Media Used

---

- **Luria-Bertani (LB) medium.** 1% (w/v) polypeptone, 0.5% yeast extract, 0.5% NaCl. In water.
- **Tanaka medium.** 64mM K<sub>2</sub>HPO<sub>2</sub>, 34mM KH<sub>2</sub>PO<sub>4</sub>, 20mM (NH<sub>4</sub>)<sub>2</sub>SO<sub>4</sub>, 1μM FeSO<sub>4</sub>, 10μM CaCl<sub>2</sub>, 1μM ZnCl<sub>2</sub>, 50mg/l L(+)-Isoleucine, 50mg/l L-Valine, 2mg/l Thiamine-HCl, 0.3mM MgCl<sub>2</sub>, 0.5% (w/v) glycerol, 0.1mg/ml ampicillin, at pH7.0.
- **TKG Buffer.** 20mM Tris-HCl pH8.0, 140mM KCl 10% (w/v) glycerol. In water.

- **TKDG Buffer.** TKG Buffer containing 0.5mM DTT.
- **TKDG-a Buffer.** TKG Buffer containing 0.5M DTT, 0.5 $\mu$ M phenylmethylsulfonyl fluoride (PMSF; Sigma), 0.5 $\mu$ g/ml leupeptin (Sigma), 0.5 $\mu$ g/ml pepstatin (Sigma) and 0.1 $\mu$ g/ml DNAase I (Roche Diagnostics).
- **TKDG-b Buffer.** As per TKDG-a Buffer except without DNAase I.
- **TKDG-e Buffer.** 50mM Tris-HCl pH8.0, 140mM KCl, 10% (w/v) glycerol, 1mM ethylenediaminetetraacetic acid (EDTA), 0.5mM DTT, 5 $\mu$ g/ml leupeptin, 5 $\mu$ g/ml pepstatin A (Sigma).
- **Buffer X.** 1mM Tris-HCl pH8.0, 0.5mM EDTA.
- **Buffer Y.** 20mM MOPS-NaOH pH8.0 50mM Na<sub>2</sub>SO<sub>4</sub>, 1mM ATP, 5 $\mu$ g/ml leupeptin, 5 $\mu$ g/ml pepstatin A.

## A.2 Day 1

---

**Overview:** The strains of F<sub>1</sub> (and F<sub>1</sub>F<sub>o</sub>) we have are all resistant to ampicillin and can therefore be grown with ampicillin present.

**Method:** Cell pre-cultures are grown in 20ml sterile Luria-Bertani (LB) medium containing 0.1mg/ml ampicillin at 37°C for ~16 hours.

## A.3 Day 2

---

**Overview:** The pre-cultures are inoculated and the cells collected.

**Method:** 8ml of the pre-culture is inoculated in 800ml Tanaka medium at 37°C, with shaking at ~150rpm, for around 16 hours, until the optical density at 600nm becomes >0.5. The culture is centrifuged for 23 minutes at 4°C and 6000g (using Beckman Coulter centrifuge, JLA9.1000 rotor at 5,800rpm). The supernatant is discarded and the pellet resuspended in

200ml 50mM Tris-HCl, pH8.0). The cells are again centrifuged for 23 minutes at 4°C and 6,000g (using Beckman Coulter centrifuge, JLA9.1000 rotor at 5,800rpm). The supernatant is removed and the pellet resuspended in 20ml TKDG Buffer. The cells are centrifuged for 12 minutes at 4°C and 6,000g (using Beckman Coulter centrifuge, JA12 rotor at 7,000rpm). The supernatant is discarded, the cells are weighed (measured to be  $x$  grams) and then frozen in liquid nitrogen, prior to storage overnight at -80°C.

## A.4 Day 3

---

**Overview:** The cells are disrupted and the membrane fragments (containing  $F_1F_o$ ) collected.

**Method:** The cells are thawed and then suspended in  $7x$  ml TKDG-a Buffer. The cells are broken using a French Press (Sim Amanco, SLM Instruments) with the pressure gauge set to 1,800kg/cm<sup>2</sup> (actual pressure is ~28,000psi) and kept on ice. The supernatant is centrifuged for 13 minutes at 4°C and 12,000g (using Beckman Coulter centrifuge, JA20 rotor at 12,400rpm). The supernatant is removed and then re-centrifuged using the same settings. *These two spins will removed intact cells, leaving membrane fragments in the supernatant. Next the membrane fragments are washed to remove non-membrane bound proteins.* The supernatant is removed and centrifuged for 1½hours at 4°C and 130,000g (Beckman Coulter L-XP ultracentrifuge, 70.1 TI rotor at 43,500rpm). The supernatant is discarded and the pellet resuspended  $7x$  ml TKDG-b Buffer. The suspension is centrifuged again for 1½hours at 4°C and 130,000g (Beckman Coulter L-XP ultracentrifuge, 70.1 TI rotor at 43,500rpm) The supernatant is removed and the pellet suspended in  $200x$   $\mu$ l on ice. A small amount of the suspension (~10 $\mu$ l) is removed in order to calculate the total protein concentration via the Lowry method [203]. The membrane fragment suspension is frozen in liquid nitrogen and then stored overnight at -80°C.

## A.5 Day 4

---

**Overview:** The ionic content of the medium is reduced, removing  $F_1$  from the membrane fragments. Biotin is attached to the  $\gamma$ -subunit due to a reaction between the mutant cysteine residues and biotin-maleimide.  $F_1$  is removed from other proteins present by separation through a glycerol gradient.

**Method:** The membrane fragment suspension is defrosted, suspended in  $14x$  ml TKDG-e Buffer and centrifuged for 1 hour at  $15^\circ\text{C}$  at  $150,000g$  (using Beckman Coulter L-XP ultracentrifuge, 70.1 rotor at  $46,700\text{rpm}$ ). The supernatant is discarded, the pellet resuspended in  $0.6x$  ml Buffer X and the suspension centrifuged at  $15^\circ\text{C}$  for 20 minutes at  $370,000g$  (Beckman Coulter L-XP ultracentrifuge, rotor TLA 100.2 at  $100,000\text{rpm}$ ). The supernatant is extracted and re-centrifuged at  $15^\circ\text{C}$  for 20 minutes at  $370,000g$  (Beckman Coulter L-XP ultracentrifuge, rotor TLA 100.2 at  $100,000\text{rpm}$ ). The supernatant is removed. MOPS-NaOH pH7.0 and  $\text{Na}_2\text{SO}_4$  are added to final concentrations of  $25\text{mM}$  and  $50\text{mM}$  respectively. Biotin-PEAC<sub>5</sub>-maleimide, leupeptin and pepstatin A are added, to final concentrations  $100\mu\text{M}$ ,  $5\mu\text{g}/\text{ml}$  and  $5\mu\text{g}/\text{ml}$  respectively, and the solution is incubated at room temperature for  $1\frac{1}{2}$  hours. A glycerol step gradient is created using (from bottom to top) 30%, 23.3%, 20%, 16.7% and 10% glycerol in Buffer Y. The  $F_1$  solution is added to the upper glycerol layer and the gradient is centrifuged at  $15^\circ\text{C}$  for 4 hours at  $250,000g$  (using Beckman Coulter ultracentrifuge, SW 55Ti rotor at  $51,300\text{rpm}$ ). A small hole is made at the bottom of the gradient tube and small fractions ( $\sim 300\mu\text{l}$  per fraction) are collected. The ATPase activity of each fraction is measured by  $P_i$  colouring (see Section 2.3.1) to find the peak fraction. The peak fraction is aliquotted into  $\sim 6\mu\text{l}$  aliquots which are frozen in liquid nitrogen and placed in a liquid nitrogen dewar for long-term storage.

# B

## A Guide to Nonlinear Curve Fitting

As experimental scientists we often wish to explain our data by a theoretical function described by a set of parameters. If the theoretical function is a probability distribution, we can obtain the parameters using a Maximum Likelihood approach. This technique, however, can be badly affected by occasional outliers, an all too common feature of experimental data at the single molecule level. A different approach, and the method that has been employed throughout this thesis, is to use nonlinear curve fitting. This technique is commonly available in commercial software packages (e.g., Origin) but, to be used with complex theoretical functions or for some other wish, it is often desirable to encode the method explicitly. Here I present a brief review of the theory behind nonlinear curve fitting to assist future researchers.

### **B.1 Likelihood Estimator**

---

Nonlinear curve-fitting describes the fitting of a function to the experimental data when the function is not a linear function of the parameters,  $a_1, a_2$  etc.. It should be noted that the dependence of the fitting function on the independent variable  $x$  does not affect the linearity of the fitting process.

We will assume that we have a set of  $n$  observed experimental measurements  $\{y_1, y_2, \dots, y_n\}$  due to an independent variable  $x$ , and that we know the standard deviation of each observation  $y_i$  to be  $\sigma_i$  (i.e., the standard error on the mean of repeat readings). In general we wish to fit the experimental data to an underlying theoretical model,  $f \equiv f(x_i, \mathbf{a})$  where  $\mathbf{a}$  is a vector of parameters controlling the model.

Qualitatively it is easy to say whether a theoretical function fits experimental data well or not. However, the ideal process should be more rigorous than this. The fitting procedure should provide: (1) the parameters describing the function; (2) an estimate of the error on each of the parameters; and (3) a statistical measure of the goodness of the fit. It is point (3) that quantitatively allows us to say whether the underlying theoretical function and the experimental data are a good match. If this is not satisfied, the parameters and relevant errors obtained in (1) and (2) are meaningless.

We wish to obtain a function that passes through, or close to, each of the observed measurements. In order to do this, we ask ourselves the following question: Given the presumed theoretical function, what is the likelihood that we should obtain our experimental results  $y_i$ ? Importantly, we know the standard deviation  $\sigma_i$ , and therefore the variance, associated with the observed values at each  $x_i$ . We will assume that at  $x_i$  the experimental result  $y_i$  is drawn from a normal distribution centred upon  $f(x_i)$  with standard deviation  $\sigma_i$ . Therefore, the probability of obtaining  $y_i$  at  $x_i$  will be

$$p(y_i | \mathbf{a}) \propto \exp \left[ -\frac{(y_i - f(x_i))^2}{2\sigma_i^2} \right] \quad (\text{B.1})$$

and the corresponding likelihood of observing all the experimental values will be

$$P(y_1, y_2, \dots, y_n | \mathbf{a}) \propto \prod_{i=1}^N \exp \left[ -\frac{(y_i - f(x_i))^2}{2\sigma_i^2} \right] \quad (\text{B.2})$$

Therefore, our quest must be to find the parameters  $\mathbf{a}$  that maximise  $P$ .

This is simplified if we take logs of Equation B.2.

$$\ln P = -\frac{1}{2} \sum_{i=1}^N \frac{(y_i - f(x_i))^2}{\sigma_i^2} + c \quad (\text{B.3})$$

To maximise P, we need to minimise  $\chi^2$  where

$$\chi^2 = \sum_{i=1}^N \frac{(y_i - f(x_i))^2}{\sigma_i^2} \quad (\text{B.4})$$

$\chi^2$  is derived from the maximum likelihood estimator approach but it should be noted that it is equivalent to the generic weighted least-squares minimization function but where the weighting is inversely proportional to the variance at each  $x_i$ .

## B.2 Minimization of $\chi^2$

---

Minimization routines are available in commercial packages and may employ different techniques to obtain a local minimum. Here I will present the main methods of local minimization. It should be noted that Origin and Labview use the Levenberg-Marquardt algorithm presented in Section B.2.3 by default, whilst minimization routines in Matlab (e.g. *fminsearch*, *lsqcurvefit*) use the Nelder-Mead downhill simplex method of Section B.2.4.

### B.2.1 Method of Steepest Descent

With an initial parameter vector  $\mathbf{a}$  the method of steepest descent finds the minimum of  $\chi^2$  by stepping off in a direction  $\delta\mathbf{a}$  where

$$\delta\mathbf{a} \propto \nabla\chi^2(\mathbf{a}) \quad (\text{B.5})$$

so that the input vector for the next iteration is  $\mathbf{a} + \delta\mathbf{a}$ . The problem with this method is that it is difficult to select a suitable step-size such that the minimum is not overshot.

### B.2.2 Newton's Method

At the minimum of  $\chi^2$ ,

$$\frac{\partial}{\partial a_j} [\chi^2(\mathbf{a})] = 0 = -2 \sum_{i=1}^N \frac{y_i - f(x_i)}{\sigma^2} \frac{\partial f(x_i)}{\partial a_j} \quad (\text{B.6})$$

and close to the minimum we can expand  $\chi^2$  by a Taylor's expansion

$$\chi^2(\mathbf{a} + \delta\mathbf{a}) = \chi^2(\mathbf{a}) + \sum_j \delta a_j \frac{\partial}{\partial a_j} [\chi^2(\mathbf{a})] + \sum_k \sum_l \frac{\delta a_k \delta a_l}{2} \frac{\partial^2}{\partial a_k \partial a_l} [\chi^2(\mathbf{a})] + \dots \quad (\text{B.7})$$

Newton's method involves taking an initial parameter vector  $\mathbf{a}$  and then seeking a new vector  $\delta\mathbf{a}$  that satisfies Equation B.6.

$$\frac{\partial}{\partial a_j} [\chi^2(\mathbf{a} + \delta\mathbf{a})] = 0 = \frac{\partial}{\partial a_j} [\chi^2(\mathbf{a})] + \sum_{k=1}^m \frac{\partial^2}{\partial a_j \partial a_k} [\chi^2(\mathbf{a})] \delta a_k \quad (\text{B.8})$$

where we assume that the vector change  $\delta\mathbf{a}$  is sufficiently small such that  $\chi^2(\delta a_j) \approx \frac{\partial \chi^2(a_j)}{\partial a_j} \delta a_j$  holds.

Solving Equation B.8 gives

$$c_j = \sum_{k=1}^m M_{j,k} \delta a_k \quad (\text{B.9})$$

where

$$c_j = -\frac{1}{2} \frac{\delta \chi^2}{\delta a_j} \quad (\text{B.10})$$

and

$$M_{j,k} = \frac{1}{2} \frac{\partial^2}{\partial a_j \partial a_k} [\chi^2(\mathbf{a})] = \sum_{i=1}^N \frac{1}{\sigma_i^2} \frac{\partial f(x_i)}{\partial a_k} \frac{\partial f(x_i)}{\partial a_j} - \sum_{i=1}^n \frac{y_i - f(x_i)}{\sigma_i^2} \frac{\partial^2 f(x_i)}{\partial a_j \partial a_k} \quad (\text{B.11})$$

It should be noted at this stage that the elements in  $M$  are just half

of those from the Hessian matrix  $H$  of  $\chi^2$  with respect to  $\mathbf{a}$  where  $H_{j,k} = \frac{\partial^2 \chi^2(\mathbf{a})}{\partial a_j \partial a_k}$ . Substituting  $c_j$  and  $M_{j,k}$  into Equation B.7 results in

$$\chi^2(\mathbf{a} + \delta\mathbf{a}) = \chi^2(\mathbf{a}) - 2\mathbf{a} \cdot \delta\mathbf{a} + \delta\mathbf{a}^\dagger \cdot M \cdot \delta\mathbf{a} + \dots \quad (\text{B.12})$$

Newton's method involves solving the linear system of Equation B.9 using

$$\delta\mathbf{a} = M^{-1}\mathbf{c} \quad (\text{B.13})$$

If the matrix  $M$  is singular then Equation B.13 cannot be formed and this method will not recover the minimum. Another possible problem with Newton's method is that unless the initial parameters  $\mathbf{a}$  were chosen to be close to the minimum, the solution of B.13 may lead to divergent oscillations away from the minimum.

### B.2.3 Levenberg-Marquardt Method

The Levenberg-Marquardt method (LM) is now taken to be the standard by which most nonlinear curve-fitting is achieved. LM uses the strength of the method of steepest descent to make large-scale steps towards the minimum and the accuracy of Newton's method close to the minimum by varying between the two extreme methods when far from the minimum (steepest descent method used) and when close (Newton's method).

The issues with the steepest descent method (the lack of an apparent length scale for each step) can be reduced by the knowledge that the diagonal elements of  $M$  set the length scale in question and thus a step-size is chosen that is very unlikely to overshoot the minimum [204]. Furthermore, the challenges arising from the Newton method (the potential singular matrix  $M$ ) can be overcome by ignoring the second derivative term in Equation B.8. This is probably acceptable in practice because the term multiplying

the second derivative  $[y_i - f(x_i)]$  should be the random error either side of the function line and should average to zero due to the lack of correlation between the data points.

A successful minimization routine by LM will afford the best-fit parameters  $\mathbf{a}$ , the corresponding value of  $\chi^2$  at the minimum and the matrix  $M$ .

### B.2.4 The Simplex Method

The advantage of the Nelder-Mead downhill simplex method [205] is that only function evaluations are required at each iteration rather than function derivatives. Unfortunately, and partly as a result, it is not as efficient as the Levenberg-Marquardt algorithm.

A simplex is a geometrical figure consisting of  $N + 1$  vertices in  $N$  dimensions. In the case of two parameter minimization, the simplex corresponds to a triangle. Ideally, the initial simplex chosen should be close to the true values to avoid local (non-global) minima. If one of the points of the initial simplex is chosen to be  $\mathbf{a}_0$  then the other  $N$  points of the initial simplex can be given by

$$\mathbf{a}_i = \mathbf{a}_0 + \lambda \hat{u}_i \tag{B.14}$$

where  $\hat{u}_i$  are  $N$  unit vectors in the parameter space and  $\lambda$  is a guess at the characteristic length scale of the minimization. The method takes a number of steps. At each step point, the function is evaluated at each of the simplex vertices. The majority of steps involve moving the point of the simplex where the function is greatest through the opposite face of the simplex. When it can do so, the method should expand the simplex in one or more dimensions to take larger steps [204].

### B.3 Obtaining a Measure of the Goodness of Fit

---

After obtaining the minimum  $\chi^2$  value, we have to be able to decide if the fit is quantitatively good. We need to define the number of degrees of freedom of the fitting process  $\nu$  to be equal to  $n_{data} - n_{parameters}$ , where  $n_{data}$  and  $n_{parameters}$  are the number of data points and fitting parameters respectively. If we had a large data set, we would expect that  $\chi^2 \approx \nu$  at the minimum, since each data point should contribute  $\sim 1$  to the  $\chi^2$  summation. A value for  $\chi^2$  much greater than  $\nu$  suggests that the experimental data points deviate from the assumed function more than expected from their associated standard deviations. A  $\chi^2$  value much less than  $\nu$  would likely be due to an underestimate of the errors on the data points.

If  $P(\chi^2 | \nu)$  is defined as the probability that the observed chi-squared value is less than a value  $\chi^2$ , then  $P(\chi^2 | \nu)$  will be given by

$$P(\chi^2 | \nu) = G\left(\frac{\nu}{2}, \frac{\chi^2}{2}\right) \quad (\text{B.15})$$

(for a proof, see [204]) where  $G$  is the incomplete gamma function defined by

$$G(a, x) \equiv \frac{\gamma(a, x)}{\Gamma(a)} \equiv \frac{1}{\Gamma(a)} \int_0^x e^{-t} t^{a-1} dt \quad (\text{B.16})$$

Therefore, the probability  $Q$  that the chi-squared value should exceed  $\chi^2$  by chance is given by  $1 - P$ . If  $Q$  is a small probability (say  $< 0.1$ ) then the fluctuations observed away from the fit are unlikely to be just down to random chance. They may be down to either an incorrect fitting function or that the associated errors on the experimental data are not normally distributed (in this case the fit may be accepted with slightly lower  $Q$  values,  $> 0.001$  say). A value of  $Q$  approaching 1 indicates that the experimental errors have been overestimated.

## B.4 Estimating the Errors on the Best-Fit Parameters

---

We have already mentioned that a rigorous fitting procedure should provide not only the best fit parameters  $\mathbf{a}$  and make a quantitative statement about the goodness of the fit but it should also make an estimate of the errors on the best fit parameters,  $\Delta\mathbf{a}$ .

The covariance  $V_{1,2}$  between two parameters  $a_1$  and  $a_2$  is given by the expectation value of the product of their deviations away from their means,  $\langle(a_1 - \bar{a}_1)(a_2 - \bar{a}_2)\rangle$ . Therefore, it is possible to construct a matrix  $V$  where each element is the covariance between the corresponding parameters.

$$V_{i,j} = \langle(a_i - \bar{a}_i)(a_j - \bar{a}_j)\rangle \quad (\text{B.17})$$

It should be noted that the diagonal elements  $V_{i,i}$  give the variance of parameter  $a_i$  by definition.

By considering small departures away from the minimum in terms of both the function parameters  $\mathbf{a}$  and the independent variables  $x_i$  it is possible to show (for a full derivation see [206]) that  $V$  is approximately equal to the inverse of the Hessian matrix of  $\chi^2$  with respect to the fitting parameters  $\mathbf{a}$  when evaluated at the minimum,  $\mathbf{a} = \mathbf{a}^*$ .

$$V \approx H(\mathbf{a}^*)^{-1} \quad (\text{B.18})$$

The LM method directly calculates the matrix  $M$  for the solving of Equation B.9 and therefore  $H$  and  $V$  can be readily found.

For the  $j$ th parameter, the associated standard deviation will be given by

$$\sigma_j = \sqrt{V_{j,j}} \quad (\text{B.19})$$

Finally, the degree of confidence level required will affect the amount of

the error stated on the parameters. If  $c_i$  is the confidence level, then the error in parameter  $j$  will be given by

$$\Delta a_j = \sqrt{c_i} \sqrt{V_{j,j}} \quad (\text{B.20})$$

where  $c_i = 1$  indicates a 68% confidence level,  $c_i = 2$  indicates 95%, etc..

## B.5 A Procedure for Fitting to Histogram Data

---

Until now, we have been concerned with fitting an experimental data set  $\{x_i, y_i, \sigma_i\}$  with a model function  $f(x_i, \mathbf{a})$ . This has assumed that the experimental data is measured at discrete values of the independent variable  $x_i$ . Quite often this is not true. More often than not, the data represents a statistical distribution expressed as a histogram, i.e. the true experimental results  $y_i$  will now be represented by the histogram function  $H(x_i)$ . In many cases, the shape of the histogram closely matches that of the underlying distribution but this observation is not exact. Importantly, the model function  $f(x_i)$  should undergo a transformation, akin to binning the data, to form a new histogram function  $g(x_i)$ . Each bin in a histogram represents the integral of the underlying distribution function over the bin width. Therefore, if the distribution function  $f(x_i)$  is integrable this can be achieved exactly, whereas if  $f(x_i)$  is not integrable, a numerical integral will be required.

If  $f(x_i)$  is integrable

$$f(x_i) \rightarrow g(x_i) = \frac{1}{\Delta x} \int_{x_i - \frac{\Delta x}{2}}^{x_i + \frac{\Delta x}{2}} f(x_i) dx \quad (\text{B.21})$$

where  $\Delta x$  is the bin width used in the histogram.

If  $f(x_i)$  is not integrable

$$f(x_i) \rightarrow g(x_i) = \frac{1}{n} \sum_{j=1}^n f \left( x_i + \Delta x \left( \frac{j-1}{n-1} - \frac{1}{2} \right) \right) \quad (\text{B.22})$$

where again  $\Delta x$  is the bin width used in the histogram and now  $n$  is the number of points within each bin over which to perform the numerical integration.

In each case, the  $\chi^2$  function to minimise is the same and given by

$$\chi^2 = \sum_{i=1}^N \frac{(H(x_i) - g_i(x_i))^2}{\sigma_i^2} \quad (\text{B.23})$$



## A Simulation of $F_1$ Rotation

$F_1$  data has been simulated using a simple model of  $F_1$  rotation. The simulation was encoded by Dr Bradley Steel.

The model is summarized in Figure C.1.  $F_1$  is considered to be a simple rotating unit, dragging a large viscous load (i.e., a bead) with drag coefficient,  $\zeta$ , through the medium (with viscosity  $\eta$ ) via an elastic linker with spring constant,  $k_s$ . The linkage has a characteristic Lorentzian corner frequency,  $f_c$ . The viscous load will be subject to Brownian motion determined by a Monte-Carlo process due to noise of RMS amplitude  $\sqrt{\frac{2k_B T t}{\zeta}}$ .  $F_1$  binds ATP at  $0^\circ$ ,  $120^\circ$  and  $240^\circ$  with a rate given by  $k_{on}[ATP]$ . Two sequential catalytic processes occur at each of  $80^\circ$ ,  $200^\circ$  and  $320^\circ$  with time constants of  $\tau_1$  and  $\tau_2$ . In the simulations presented in this thesis,  $\tau_1 = \tau_2 = 0.3\text{ms}$  has been used.  $F_1$  is modelled to rotate between states with a constant torque of  $T = 40\text{pNm}$  and the angular speed of rotation between states will be given by  $\omega = \frac{T}{\zeta}$ . To account for the fast-fluctuations occurring due to Brownian noise, the model generates the data at  $\sim 30\text{MHz}$ . The force on the bead,  $F_i$ , at time step  $t_i$  is related to the position of the bead,  $\theta_{i-1}$ , at time  $t_{i-1} = t_i + \Delta T$  is given by  $F_i = -k_s(\theta_i - \theta_{i-1}) + n\sqrt{\frac{2k_B T}{\zeta} \Delta t}$ , where  $n$  is a uniformly randomly generated number between -1 and +1. The effect of the camera sampling rate and the finite exposure are then computed by

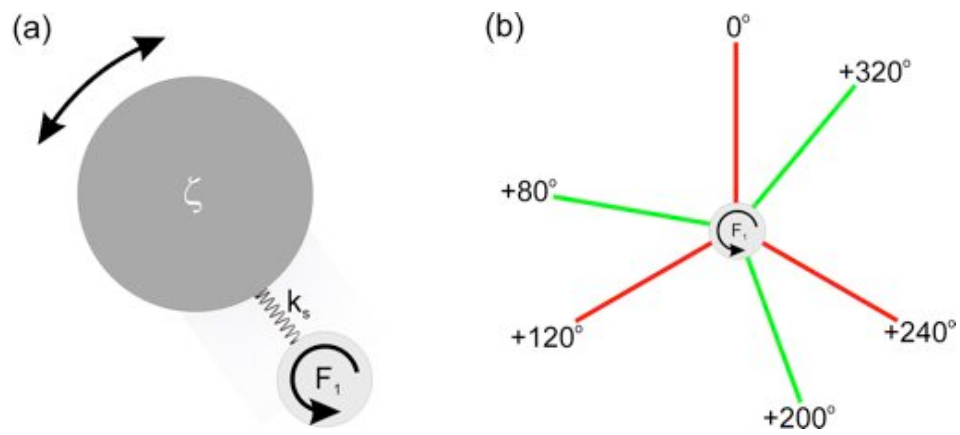


**Figure C.1:** A representation of the processes occurring during the simulated  $F_1$  rotation. (a) A bead with drag coefficient  $\zeta$  is attached to the rotating  $F_1$  motor via a flexible linker with spring constant  $k_s$ . (b) The ATP-binding state (indicated by the red lines) occurs at  $0^\circ$ ,  $120^\circ$  and  $240^\circ$ , whilst the catalytic dwells (indicated by the green lines) occur at  $80^\circ$ ,  $200^\circ$  and  $320^\circ$ . The rate of ATP-binding is given by  $k_{on}[\text{ATP}]$  and the two processes occurring at each catalytic dwell have time constants of  $\tau_1$  and  $\tau_2$ .

averaging all time steps within the camera exposure.

# D

## An Estimate of the Catalytic Process Length from Step Alignment

The alignment of catalytic steps is presented in Section 3.6.6. Here we look at the distributions of points away from the principal step at  $t = 0$ . If we assume that each catalytic dwell corresponds to two sequential events, as seen in Section 3.6.3 and in  $\text{TF}_1$ , and that both last a similar time,  $t_d$ . In this situation, after a time  $t$ , the probability of having undergone  $n$  steps away from the principal step is a Gamma function with shape parameters  $n$  and  $t_d$ . Therefore, we should expect to see a distribution of

$$N(n, t) \propto \frac{T^{2n} e^{-T}}{(2n - 1)!} \quad (\text{D.1})$$

where  $N(n, t)$  represent the observed distribution at time  $t$  and  $T = \frac{t}{t_d}$ . The distributions are observed to be symmetrical before and after the step. Figure D.1 shows the distributions observed from the step alignment of Figure 3.19.

Fitting the distributions with Equation D.1 and the fitted catalytic dwell length is shown in Figure D.2. Only a few frames away from the step, the fit is poor due to the lack of available data points. As we move further away

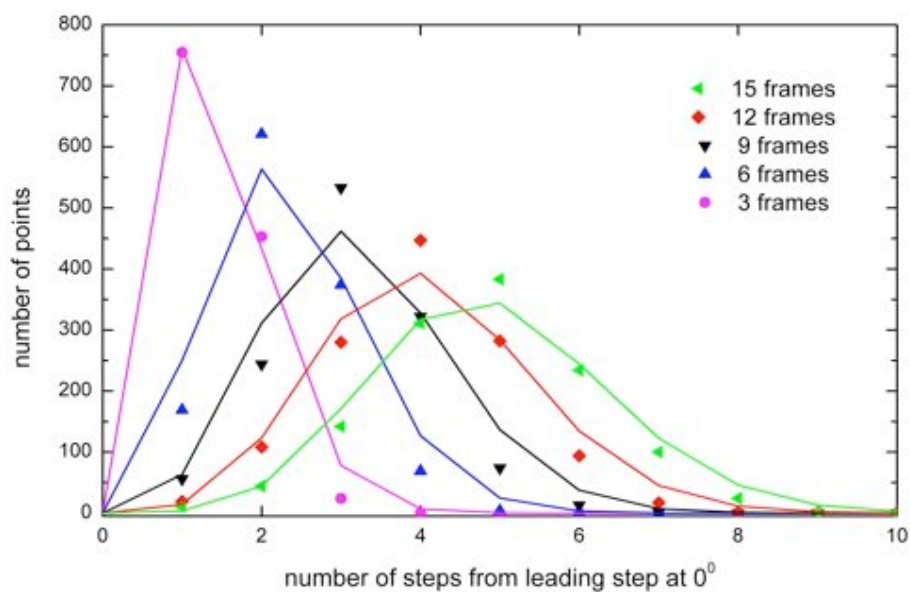


**Figure D.1:** The occupancy of states away from the leading step at  $0^\circ$  for up to 15 frames after the principal step. Shown by symbols are the experimentally obtained distributions for 3 frames (pink), 6 frames (blue), 9 frame (black), 12 frames (red) and 15 frames (purple). The solid lines represent the fits to the distributions using Equation D.1. Only distributions for times after the step event are shown for clarity, though it should be noted that the distributions prior to the step event are virtually symmetrical.

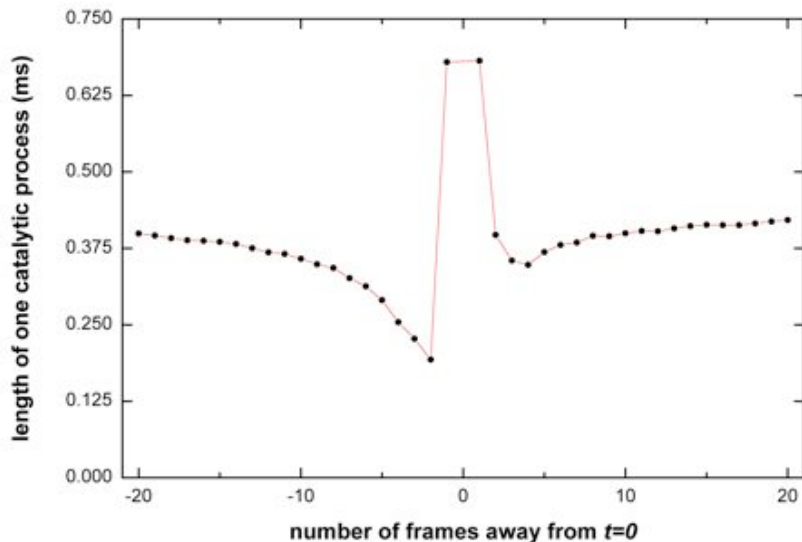


**Figure D.2:** An estimate of the length of the processes in the catalytic dwell obtained from step alignment, assuming that there are two processes per step of equal length. The obtained process length is unstable at low frame numbers due to the lack of data for the fitting. However, far from the step, the distributions suggest an average process length of  $\sim 0.4$ ms, consistent with the  $\sim 0.7$ ms dwells found in Chapter 3.

from  $t = 0$ , in this case out to 20 frames away from the step, Equation D.1 describes the distribution increasingly well. The distribution in Figure D.1 is always slightly narrower than that expected from the simple theory (especially when we consider that the fits should all be slightly greater in magnitude too), perhaps indicating that there are more than two catalytic processes during each dwell. However, we know from our discussions that there is a transit time included in each dwell but not in the theory. Far from  $t = 0$ , the fitted parameters are consistent with two  $\sim 0.4$ ms processes occurring at each catalytic dwell, in good agreement with the measured  $\sim 0.7$ ms dwells.

# E

## Applying the Switch-Time Algorithm to Rotation Data from EF<sub>1</sub>

Although F<sub>1</sub>-ATPase does not switch its direction of rotation like the bacterial flagellar motor, it does switch between ‘on’ and ‘off’ states and, as a result, the Switch-Time method, an algorithm developed by Dr Fan Bai and Richard Branch to locate switches in the rotation direction of the bacterial flagellar motor, can be extended to EF<sub>1</sub> pausing assays. The details of the method are summarized in Figure E.1. The raw angle data is numerically differentiated to calculate an instantaneous speed measurement. A rank-3 median filter is then used to remove outliers from the speed data. As you can see from Figure E.1a, for ideal rotation, this corresponds to well defined ‘on’ and ‘off’ states. Due to rapid speed fluctuations caused by detection noise and stochastic pausing, the ‘on’ state has a large spread, illustrated by the speed histogram. A double Gaussian function can be fit to these levels to determine the shape of the state distributions. In order to determine the times of switches between ‘on’ and ‘off’, two threshold levels are set at half a standard deviation away from the mean for each state, as shown in Figure E.1b. A rotating period is defined as the time from when the speed first goes above the upper threshold limit until it crosses below the lower threshold.

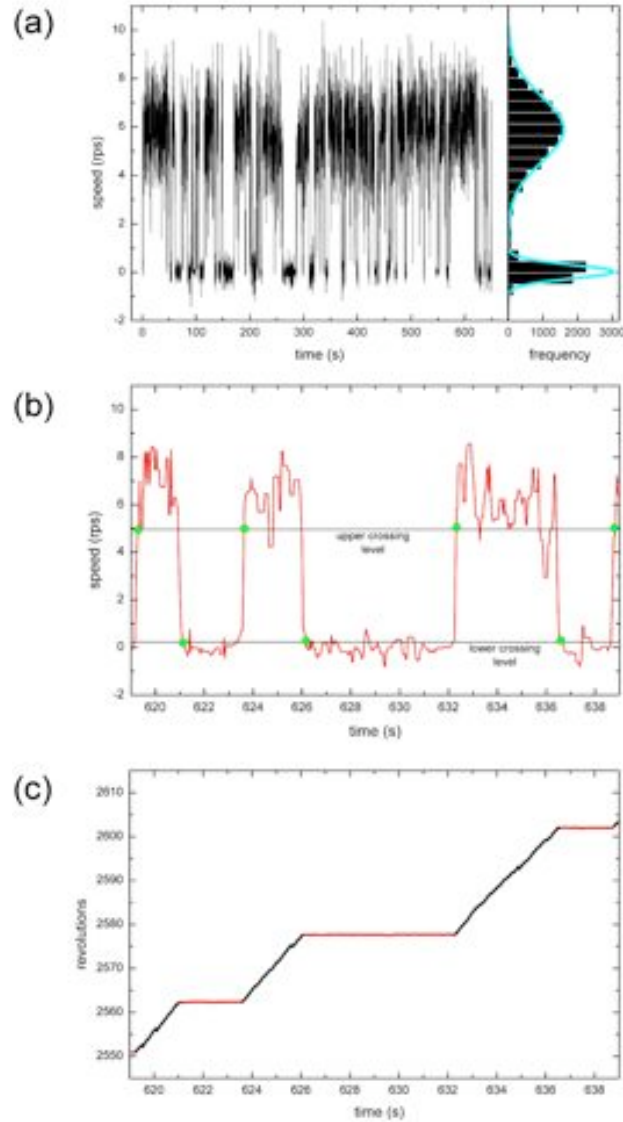


**Figure E.1:** Application of the Switch-Time algorithm to  $EF_1$  rotation data for the determination of pausing information. (a) The angle data is numerically differentiated point-by-point to obtain instantaneous speed, which is then passed through a median filter of rank-3 to remove outliers. The distributions of the ‘on’ and ‘off’ states are fitted with a double Gaussian function to determine the mean speed and standard deviation of each state. (b) Two thresholds are determined at half a standard deviation from the mean for each state. For a switching event to occur, the speed data has to move through both thresholds, defining the periods of pause and rotation. (c) The resulting rotating (black points) and pausing sections (red points) as determined by the Switch-Time algorithm.

---

Pauses are defined in the opposite manner. The result of this algorithm is shown in Figure E.1c. For very clean data, the Switch-Time method gives excellent agreement with sections determined by eye. However, for data with large amounts of noise, the ‘on’ state, in particular, becomes poorly-defined and the method breaks down. This is true for about two-thirds of all data and is due to the width of the ‘on’ state being comparable to the separation in the speeds between the two states. Conversely, for experiments on the bacterial flagellar motor, the two states are very distinct and have relatively small spread, and in these conditions, the algorithm is, no doubt, very powerful. Unfortunately, this means that the Switch-Time method cannot be used for the analysis of  $F_1$  data obtained at low speed.

# F

## Wiring Connection Panels for the Control of Hardware by the DSP Board

The use of digital and analogue connection panels allows direct access to each of the DSP channels. The 100-channel analogue and 68-channel digital panel diagrams are shown in Figure F.1 and Figure F.2 respectively.

The analogue channels are arranged such that BNC cables access the four analogue inputs and eight analogue outputs. Also available is BNC access of a channel allowing control of the DSP clocking method. Currently this channel is not being used.

The digital channels are used to provide the AOD driving frequency. The AOD driver receives one 25-pin D-sub connector for each of the  $x$  and  $y$  driving channels, called the ‘Low Word’ and ‘High Word’ respectively due to the manner in which they are programmed on the board. The pin numbering of a male D-sub connector is shown in Figure F.3. Pins 1–8 and 21–15 (in that order) are required to carry the 15-bit driving frequency, with Pin 1 representing the least significant bit and Pin 15 the most significant bit. The exact connection of the pins for the two 25-pin D-sub connectors to the digital connection panel is also shown in Figure F.3. Pin 13 provides the analogue AOD transmittance voltage and is shared between both D-sub

|       |                                  |                           |       |                                  |    |
|-------|----------------------------------|---------------------------|-------|----------------------------------|----|
| DB.1  | <b>DGND</b>                      | DB.35                     | DIO0  | 1                                |    |
| DB.2  | DIO1                             | 2                         | DB.36 | DIO2                             | 3  |
| DB.3  | DIO3                             | 4                         | DB.37 | DIO4                             | 5  |
| DB.4  | DIO5                             | 6                         | DB.38 | DIO6                             | 7  |
| DB.5  | DIO7                             | 8                         | DB.39 | DIO8                             | 21 |
| DB.6  | DIO9                             | 20                        | DB.40 | DIO10                            | 19 |
| DB.7  | DIO11                            | 18                        | DB.41 | DIO12                            | 17 |
| DB.8  | DIO13                            | 16                        | DB.42 | DIO14                            | 15 |
| DB.9  | DIO15                            | 10-12, 22-25 10-12, 22-25 | DB.43 | <b>DGND</b>                      |    |
| DB.10 | DIO17                            | 2                         | DB.44 | DIO16                            | 1  |
| DB.11 | DIO19                            | 4                         | DB.45 | DIO18                            | 3  |
| DB.12 | DIO21                            | 6                         | DB.46 | DIO20                            | 5  |
| DB.13 | DIO23                            | 8                         | DB.47 | DIO22                            | 7  |
| DB.14 | DIO25                            | 20                        | DB.48 | DIO24                            | 21 |
| DB.15 | DIO27                            | 18                        | DB.49 | DIO26                            | 19 |
| DB.16 | DIO29                            | 16                        | DB.50 | DIO28                            | 17 |
| DB.17 | DIO31                            | 14 14                     | DB.51 | DIO30                            | 15 |
| DB.18 | DIO_STRB_REQ (QE0_Index)         |                           | DB.52 | DIO_STRB_ACK (QE1_Index)         |    |
| DB.19 | • GPIO1 (AUXDIO1/PWMOUT0/QE0_a)  |                           | DB.53 | • GPIO0 (AUXDIO0/PWMIN0/QE0_b)   |    |
| DB.20 | • GPIO3 (AUXDIO3/PWMOUT1/QE1_a)  |                           | DB.54 | • GPIO2 (AUXDIO2/PWMIN1/QE1_b)   |    |
| DB.21 | -                                |                           | DB.55 | -                                |    |
| DB.22 | +5V (Optional from PC Supply)    |                           | DB.56 | +5Vdc (Optional from PC Supply)  |    |
| DB.23 | <b>DGND</b>                      |                           | DB.57 | <b>DGND</b>                      |    |
| DB.24 | <b>DGND</b>                      |                           | DB.58 | <b>DGND</b>                      |    |
| DB.25 | +12Vdc (Optional from PC Supply) |                           | DB.59 | +12Vdc (Optional from PC Supply) |    |
| DB.26 | -                                |                           | DB.60 | -                                |    |
| DB.27 | -                                |                           | DB.61 | -                                |    |
| DB.28 | -                                |                           | DB.62 | -                                |    |
| DB.29 | -                                |                           | DB.63 | -                                |    |
| DB.30 | -                                |                           | DB.64 | -                                |    |
| DB.31 | -                                |                           | DB.65 | -                                |    |
| DB.32 | -                                |                           | DB.66 | -                                |    |
| DB.33 | -                                |                           | DB.67 | -                                |    |
| DB.34 | -                                |                           | DB.68 | -                                |    |

**Figure F.1:** A diagram of the accessibility to the 68 digital channels via the connection panel. The connection panel communicates with the extension card via a 68-pin D-sub connector. The digital channels are used to provide the AOD driving frequency via two 25-pin D-sub connectors called ‘High Word’ and ‘Low Word’ due to the way they are programmed on the DSP board. The channels connected directly to the pins of the 25-pin D-sub connectors are indicated in red (low word) and green (high word). Also accessible are four general I/Os via BNC cables indicated by the blue dots.

connectors. The voltage is provided by analogue channel DB1.37 on the analogue connection panel (see Figure F.2).

|        |                |         |                 |
|--------|----------------|---------|-----------------|
| DB1.1  | IN0 / IN0+ ●   | DB1.51  | IN8 / IN0-      |
| DB1.2  | IN1 / IN1+ ●   | DB1.52  | IN9 / IN1-      |
| DB1.3  | IN2 / IN2+     | DB1.53  | IN10 / IN2-     |
| DB1.4  | IN3 / IN3+     | DB1.54  | IN11 / IN3-     |
| DB1.5  | IN4 / IN4+     | DB1.55  | IN12 / IN4-     |
| DB1.6  | IN5 / IN5+     | DB1.56  | IN13 / IN5-     |
| DB1.7  | IN6 / IN6+     | DB1.57  | IN14 / IN6-     |
| DB1.8  | IN7 / IN7+     | DB1.58  | IN15 / IN7-     |
| DB1.9  | AGND           | DB1.59  | AGND            |
| DB1.10 | IN16 / IN16+ ● | DB1.60  | IN24 / IN16-    |
| DB1.11 | IN17 / IN17+ ● | DB1.61  | IN25 / IN17-    |
| DB1.12 | IN18 / IN18+   | DB1.62  | IN26 / IN18-    |
| DB1.13 | IN19 / IN19+   | DB1.63  | IN27 / IN19-    |
| DB1.14 | IN20 / IN20+   | DB1.64  | IN28 / IN20-    |
| DB1.15 | IN21 / IN21+   | DB1.65  | IN29 / IN21-    |
| DB1.16 | IN22 / IN22+   | DB1.66  | IN30 / IN22-    |
| DB1.17 | IN23 / IN23+   | DB1.67  | IN31 / IN23-    |
| DB1.18 | AGND           | DB1.68  | AGND            |
| DB1.19 | IN32 / IN32+   | DB1.69  | IN40 / IN32-    |
| DB1.20 | IN33 / IN33+   | DB1.70  | IN41 / IN33-    |
| DB1.21 | IN34 / IN34+   | DB1.71  | IN42 / IN34-    |
| DB1.22 | IN35 / IN35+   | DB1.72  | IN43 / IN35-    |
| DB1.23 | IN36 / IN36+   | DB1.73  | IN44 / IN36-    |
| DB1.24 | IN37 / IN37+   | DB1.74  | IN45 / IN37-    |
| DB1.25 | IN38 / IN38+   | DB1.75  | IN46 / IN38-    |
| DB1.26 | IN39 / IN39+   | DB1.76  | IN47 / IN39-    |
| DB1.27 | AGND           | DB1.77  | AGND            |
| DB1.28 | IN48 / IN48+   | DB1.78  | IN56 / IN48-    |
| DB1.29 | IN49 / IN49+   | DB1.79  | IN57 / IN49-    |
| DB1.30 | IN50 / IN50+   | DB1.80  | IN58 / IN50-    |
| DB1.31 | IN51 / IN51+   | DB1.81  | IN59 / IN51-    |
| DB1.32 | IN52 / IN52+   | DB1.82  | IN60 / IN52-    |
| DB1.33 | IN53 / IN53+   | DB1.83  | IN61 / IN53-    |
| DB1.34 | IN54 / IN54+   | DB1.84  | IN62 / IN54-    |
| DB1.35 | IN55 / IN55+   | DB1.85  | IN63 / IN55-    |
| DB1.36 | AGND           | DB1.86  | AGND            |
| DB1.37 | DACOUT_0 ●     | DB1.87  | DACOUT_8        |
| DB1.38 | DACOUT_1 ●     | DB1.88  | DACOUT_9        |
| DB1.39 | DACOUT_2 ●     | DB1.89  | DACOUT_10       |
| DB1.40 | DACOUT_3 ●     | DB1.90  | DACOUT_11       |
| DB1.41 | AGND           | DB1.91  | AGND            |
| DB1.42 | DACOUT_4 ●     | DB1.92  | DACOUT_12       |
| DB1.43 | DACOUT_5 ●     | DB1.93  | DACOUT_13       |
| DB1.44 | DACOUT_6 ●     | DB1.94  | DACOUT_14       |
| DB1.45 | DACOUT_7 ●     | DB1.95  | DACOUT_15       |
| DB1.46 | AGND           | DB1.96  | AGND            |
| DB1.47 | DGND           | DB1.97  | DGND            |
| DB1.48 | -              | DB1.98  | -               |
| DB1.49 | -              | DB1.99  | -               |
| DB1.50 | -              | DB1.100 | SAMPLE_CLK_IO ● |

**Figure F.2:** A diagram of the accessibility to the 100 analogue channels via the connection panel. The connector panel communicates with the DSP card via a 100-pin D-sub connector. Four analogue inputs are marked by the red dots, eight analogue outputs are marked with the green dots and input for control of the DSP board internal timing clock is marked by the blue dot.

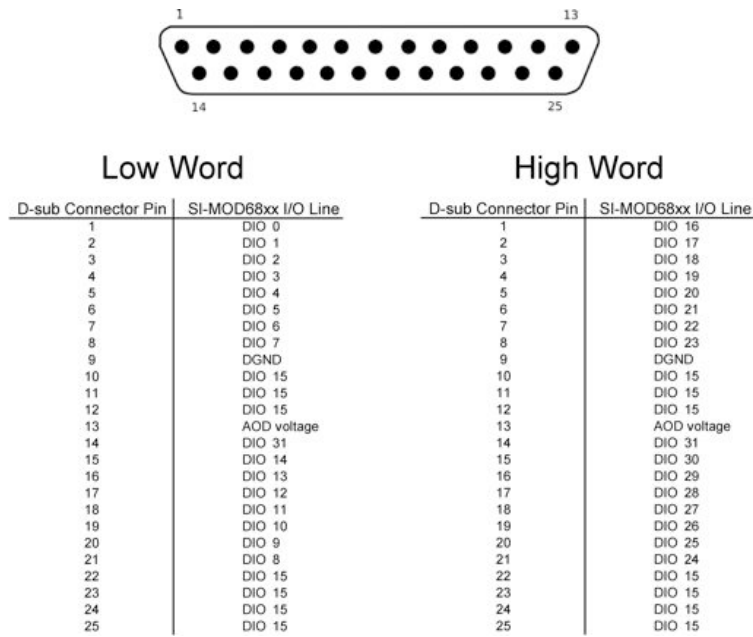


**Figure F.3:** Two 25-pin D-sub connectors control the  $x$  and  $y$  elements of the AODs. The pins include both analogue and digital inputs. The top image shows a diagram of the numbering system of a D-sub connector as if viewed looking at the pins. The D-sub connector called ‘Low Word’ controls the  $x$  AOD axis and ‘High Word’ controls  $y$ . Shown in the tables are the digital I/O channels each pin, except Pin 13, is connected to, corresponding to the channels shown in Figure F.1. Pins 1–8 and 21–15 are connected to supply the 15-bit driving frequency, with Pin 1 holding the least significant bit and Pin 15 the most significant bit. Pin 9 carries the digital ground. The digital I/O channel DIO15 is programmed to output a ‘0’, ensuring that Pins 10–12 and 22–25 also output ‘0’, as required by the AOD driver. Pin 13 carries the AOD transmittance voltage and receives its signal from analogue channel DB1.37 of Figure F.2.

# Bibliography

- [1] Philip Pullman. *The Amber Spyglass*. Scholastic, London, 2000.
- [2] C. Bustamante, D. Keller, and G. Oster. The physics of molecular motors. *Acc Chem Res*, 34(6):412–20, 2001.
- [3] H. Berg. *Random Walks in Biology*. Princeton University Press, Princeton, 1983.
- [4] Y. Sowa and R. M. Berry. Bacterial flagellar motor. *Q Rev Biophys*, 41(2):103–32, 2008.
- [5] J. S. Berg, B. C. Powell, and R. E. Cheney. A millennial myosin census. *Mol Biol Cell*, 12(4):780–94, 2001.
- [6] M. A. Geeves and K. C. Holmes. Structural mechanism of muscle contraction. *Annu Rev Biochem*, 68:687–728, 1999.
- [7] M. Schliwa. *Molecular Motors*. Wiley-VCH, Weinheim, 2003.
- [8] A. D. Mehta, R. S. Rock, M. Rief, J. A. Spudich, M. S. Mooseker, and R. E. Cheney. Myosin-V is a processive actin-based motor. *Nature*, 400(6744):590–3, 1999.
- [9] R. D. Vale, T. S. Reese, and M. P. Sheetz. Identification of a novel force-generating protein, kinesin, involved in microtubule-based motility. *Cell*, 42(1):39–50, 1985.
- [10] D. N. Richardson, M. P. Simmons, and A. S. Reddy. Comprehensive comparative analysis of kinesins in photosynthetic eukaryotes. *BMC Genomics*, 7:18, 2006.
- [11] A. Moore and L. Wordeman. The mechanism, function and regulation of depolymerizing kinesins during mitosis. *Trends Cell Biol*, 14(10):537–46, 2004.

- [12] A. Yildiz, M. Tomishige, R. D. Vale, and P. R. Selvin. Kinesin walks hand-over-hand. *Science*, 303(5658):676–8, 2004.
- [13] K. Svoboda, C. F. Schmidt, B. J. Schnapp, and S. M. Block. Direct observation of kinesin stepping by optical trapping interferometry. *Nature*, 365(6448):721–7, 1993.
- [14] D. L. Coy, M. Wagenbach, and J. Howard. Kinesin takes one 8-nm step for each ATP that it hydrolyzes. *J Biol Chem*, 274(6):3667–71, 1999.
- [15] S. M. Block, C. L. Asbury, J. W. Shaevitz, and M. J. Lang. Probing the kinesin reaction cycle with a 2D optical force clamp. *Proc Natl Acad Sci USA*, 100(5):2351–6, 2003.
- [16] K. Oiwa and H. Sakakibara. Recent progress in dynein structure and mechanism. *Curr Opin Cell Biol*, 17(1):98–103, 2005.
- [17] R. Mallik, B. C. Carter, S. A. Lex, S. J. King, and S. P. Gross. Cytoplasmic dynein functions as a gear in response to load. *Nature*, 427(6975):649–52, 2004.
- [18] G. H. Wadhams and J. P. Armitage. Making sense of it all: Bacterial chemotaxis. *Nat Rev Mol Cell Biol*, 5(12):1024–37, 2004.
- [19] D. F. Blair. How bacteria sense and swim. *Annu Rev Microbiol*, 49:489–522, 1995.
- [20] J. E. Segall, S. M. Block, and H. C. Berg. Temporal comparisons in bacterial chemotaxis. *Proc Natl Acad Sci USA*, 83(23):8987–91, 1986.
- [21] H. C. Berg and D. A. Brown. Chemotaxis in *Escherichia coli* analysed by three-dimensional tracking. *Nature*, 239(5374):500–4, 1972.

- [22] D. R. Thomas, N. R. Francis, C. Xu, and D. J. DeRosier. The three-dimensional structure of the flagellar rotor from a clockwise-locked mutant of *Salmonella enterica* serovar Typhimurium. *J Bacteriol*, 188(20):7039–48, 2006.
- [23] H. Suzuki, K. Yonekura, and K. Namba. Structure of the rotor of the bacterial flagellar motor revealed by electron cryomicroscopy and single-particle image analysis. *J Mol Biol*, 337(1):105–13, 2004.
- [24] S. W. Reid, M. C. Leake, J. H. Chandler, C. J. Lo, J. P. Armitage, and R. M. Berry. The maximum number of torque-generating units in the flagellar motor of *Escherichia coli* is at least 11. *Proc Natl Acad Sci USA*, 103(21):8066–71, 2006.
- [25] M. C. Leake, J. H. Chandler, G. H. Wadhams, F. Bai, R. M. Berry, and J. P. Armitage. Stoichiometry and turnover in single, functioning membrane protein complexes. *Nature*, 443(7109):355–8, 2006.
- [26] D. DeRosier. Bacterial flagellum: Visualizing the complete machine in situ. *Curr Biol*, 16(21):R928–30, 2006.
- [27] H. C. Berg and R. A. Anderson. Bacteria swim by rotating their flagellar filaments. *Nature*, 245(5425):380–2, 1973.
- [28] Y. Sowa, H. Hotta, M. Homma, and A. Ishijima. Torque-speed relationship of the  $\text{Na}^+$ -driven flagellar motor of *Vibrio alginolyticus*. *J Mol Biol*, 327(5):1043–51, 2003.
- [29] Y. Magariyama, S. Sugiyama, K. Muramoto, Y. Maekawa, I. Kawagishi, Y. Imae, and S. Kudo. Very fast flagellar rotation. *Nature*, 371(6500):752, 1994.

- [30] C. J. Lo, M. C. Leake, and R. M. Berry. Fluorescence measurement of intracellular sodium concentration in single *Escherichia coli* cells. *Biophys J*, 90(1):357–65, 2006.
- [31] C. J. Lo, M. C. Leake, T. Pilizota, and R. M. Berry. Nonequivalence of membrane voltage and ion-gradient as driving forces for the bacterial flagellar motor at low load. *Biophys J*, 93(1):294–302, 2007.
- [32] Y. Sowa, A. D. Rowe, M. C. Leake, T. Yakushi, M. Homma, A. Ishijima, and R. M. Berry. Direct observation of steps in rotation of the bacterial flagellar motor. *Nature*, 437(7060):916–9, 2005.
- [33] J. P. Abrahams, A. G. Leslie, R. Lutter, and J. E. Walker. Structure at 2.8Å resolution of F<sub>1</sub>-ATPase from bovine heart mitochondria. *Nature*, 370(6491):621–8, 1994.
- [34] H. Noji, R. Yasuda, M. Yoshida, and K. Kinosita Jr. Direct observation of the rotation of F<sub>1</sub>-ATPase. *Nature*, 386(6622):299–302, 1997.
- [35] R. K. Nakamoto, J. A. Baylis Scanlon, and M. K. Al-Shawi. The rotary mechanism of the ATP synthase. *Arch Biochem Biophys*, 476(1):43–50, 2008.
- [36] S. D. Dunn, L. A. Heppel, and C. S. Fullmer. The NH<sub>2</sub>-terminal portion of the alpha subunit of *Escherichia coli* F<sub>1</sub>-ATPase is required for binding the delta subunit. *J Biol Chem*, 255(14):6891–6, 1980.
- [37] R. J. Carbajo, F. A. Kellas, J. C. Yang, M. J. Runswick, M. G. Montgomery, J. E. Walker, and D. Neuhaus. How the N-terminal domain of the OSCP subunit of bovine F<sub>1</sub>F<sub>o</sub>-ATP synthase interacts with the N-terminal region of an alpha subunit. *J Mol Biol*, 368(2):310–8, 2007.

- [38] V. K. Dickson, J. A. Silvester, I. M. Fearnley, A. G. Leslie, and J. E. Walker. On the structure of the stator of the mitochondrial ATP synthase. *EMBO J*, 25(12):2911–8, 2006.
- [39] J. L. Rubinstein, J. E. Walker, and R. Henderson. Structure of the mitochondrial ATP synthase by electron cryomicroscopy. *EMBO J*, 22(23):6182–92, 2003.
- [40] D. Stock, A. G. Leslie, and J. E. Walker. Molecular architecture of the rotary motor in ATP synthase. *Science*, 286(5445):1700–5, 1999.
- [41] W. Jiang, J. Hermolin, and R. H. Fillingame. The preferred stoichiometry of c subunits in the rotary motor sector of *Escherichia coli* ATP synthase is 10. *Proc Natl Acad Sci USA*, 98(9):4966–71, 2001.
- [42] N. Mitome, T. Suzuki, S. Hayashi, and M. Yoshida. Thermophilic ATP synthase has a decamer c-ring: Indication of noninteger 10:3 H<sup>+</sup>/ATP ratio and permissive elastic coupling. *Proc Natl Acad Sci USA*, 101(33):12159–64, 2004.
- [43] H. Stahlberg, D. J. Muller, K. Suda, D. Fotiadis, A. Engel, T. Meier, U. Matthey, and P. Dimroth. Bacterial Na<sup>+</sup>-ATP synthase has an undecameric rotor. *EMBO Rep*, 2(3):229–33, 2001.
- [44] T. Meier, U. Matthey, C. von Ballmoos, J. Vonck, T. Krug von Nidda, W. Kuhlbrandt, and P. Dimroth. Evidence for structural integrity in the undecameric c-rings isolated from sodium ATP synthases. *J Mol Biol*, 325(2):389–97, 2003.
- [45] T. Meier, S. A. Ferguson, G. M. Cook, P. Dimroth, and J. Vonck. Structural investigations of the membrane-embedded rotor ring of the F-ATPase from *Clostridium paradoxum*. *J Bacteriol*, 188(22):7759–64, 2006.

- [46] J. S. Lolkema and E. J. Boekema. The A-type ATP synthase subunit K of *Methanopyrus kandleri* is deduced from its sequence to form a monomeric rotor comprising 13 hairpin domains. *FEBS Lett*, 543(1-3): 47–50, 2003.
- [47] J. M. Meyer Zu Tittingdorf, S. Rexroth, E. Schafer, R. Schlichting, C. Giersch, N. A. Dencher, and H. Seelert. The stoichiometry of the chloroplast ATP synthase oligomer III in *Chlamydomonas reinhardtii* is not affected by the metabolic state. *Biochim Biophys Acta*, 1659(1): 92–9, 2004.
- [48] D. Pogoryelov, J. Yu, T. Meier, J. Vonck, P. Dimroth, and D. J. Muller. The  $c_{15}$  ring of the *Spirulina platensis* F-ATP synthase:  $F_1/F_o$  symmetry mismatch is not obligatory. *EMBO Rep*, 6(11):1040–4, 2005.
- [49] D. Pogoryelov, C. Reichen, A. L. Klyszejko, R. Brunisholz, D. J. Muller, P. Dimroth, and T. Meier. The oligomeric state of c rings from cyanobacterial F-ATP synthases varies from 13 to 15. *J Bacteriol*, 189(16):5895–902, 2007.
- [50] M. Fritz, A. L. Klyszejko, N. Morgner, J. Vonck, B. Brutschy, D. J. Muller, T. Meier, and V. Muller. An intermediate step in the evolution of ATPases: A hybrid  $F_o$ - $V_o$  rotor in a bacterial  $Na^+$  f(1)f(0) ATP synthase. *FEBS J*, 275(9):1999–2007, 2008.
- [51] D. Pogoryelov, Y. Nikolaev, U. Schlattner, K. Pervushin, P. Dimroth, and T. Meier. Probing the rotor subunit interface of the ATP synthase from *Ilyobacter tartaricus*. *FEBS J*, 275(19):4850–62, 2008.
- [52] T. H. Stevens and M. Forgac. Structure, function and regulation of the vacuolar  $H^+$ -ATPase. *Annu Rev Cell Dev Biol*, 13:779–808, 1997.

- [53] T. Murata, I. Yamato, Y. Kakinuma, A. G. Leslie, and J. E. Walker. Structure of the rotor of the V-Type Na<sup>+</sup>-ATPase from *Enterococcus hirae*. *Science*, 308(5722):654–9, 2005.
- [54] H. Imamura, M. Nakano, H. Noji, E. Muneyuki, S. Ohkuma, M. Yoshida, and K. Yokoyama. Evidence for rotation of V<sub>1</sub>-ATPase. *Proc Natl Acad Sci USA*, 100(5):2312–5, 2003.
- [55] J. Bath and A. J. Turberfield. DNA nanomachines. *Nat Nanotechnol*, 2(5):275–84, 2007.
- [56] Y. Chen, M. Wang, and C. Mao. An autonomous DNA nanomotor powered by a DNA enzyme. *Angew Chem Int Ed Engl*, 43(27):3554–7, 2004.
- [57] J. Bath, S. J. Green, and A. J. Turberfield. A free-running DNA motor powered by a nicking enzyme. *Angew Chem Int Ed Engl*, 44(28):4358–61, 2005.
- [58] P. Yin, H. Yan, X. G. Daniell, A. J. Turberfield, and J. H. Reif. A unidirectional DNA walker that moves autonomously along a track. *Angew Chem Int Ed Engl*, 43(37):4906–11, 2004.
- [59] J. S. Shin and N. A. Pierce. A synthetic DNA walker for molecular transport. *J Am Chem Soc*, 126(35):10834–5, 2004.
- [60] R. K. Soong, G. D. Bachand, H. P. Neves, A. G. Olkhovets, H. G. Craighead, and C. D. Montemagno. Powering an inorganic nanodevice with a biomolecular motor. *Science*, 290(5496):1555–8, 2000.
- [61] M. Yoshida, N. Sone, H. Hirata, and Y. Kagawa. A highly stable adenosine triphosphatase from a thermophilic bacterium. Purification, properties, and reconstitution. *J Biol Chem*, 250(19):7910–6, 1975.

## BIBLIOGRAPHY

---

- [62] V. Kabaleeswaran, N. Puri, J. E. Walker, A. G. Leslie, and D. M. Mueller. Novel features of the rotary catalytic mechanism revealed in the structure of yeast F<sub>1</sub>-ATPase. *EMBO J*, 25(22):5433–42, 2006.
- [63] V. Kabaleeswaran, H. Shen, J. Symersky, J. E. Walker, A. G. Leslie, and D. M. Mueller. Asymmetric structure of the yeast F<sub>1</sub>-ATPase in the absence of bound nucleotides. *J Biol Chem*, 2009.
- [64] J. E. Walker, I. M. Fearnley, N. J. Gay, B. W. Gibson, F. D. Northrop, S. J. Powell, M. J. Runswick, M. Saraste, and V. L. Tybulewicz. Primary structure and subunit stoichiometry of F<sub>1</sub>-ATPase from bovine mitochondria. *J Mol Biol*, 184(4):677–701, 1985.
- [65] R. Lutter, J. P. Abrahams, M. J. van Raaij, R. J. Todd, T. Lundqvist, S. K. Buchanan, A. G. Leslie, and J. E. Walker. Crystallization of F<sub>1</sub>-ATPase from bovine heart mitochondria. *J Mol Biol*, 229(3):787–90, 1993.
- [66] A. J. Rodgers and M. C. Wilce. Structure of the gamma-epsilon complex of ATP synthase. *Nat Struct Biol*, 7(11):1051–4, 2000.
- [67] W. J. Wilbur and D. J. Lipman. Rapid similarity searches of nucleic acid and protein data banks. *Proc Natl Acad Sci USA*, 80(3):726–30, 1983.
- [68] M. A. Larkin, G. Blackshields, N. P. Brown, R. Chenna, P. A. McGettigan, H. McWilliam, F. Valentin, I. M. Wallace, A. Wilm, R. Lopez, J. D. Thompson, T. J. Gibson, and D. G. Higgins. Clustal W and Clustal X version 2.0. *Bioinformatics*, 23(21):2947–8, 2007.
- [69] P. D. Boyer. The binding change mechanism for ATP synthase - some probabilities and possibilities. *Biochim Biophys Acta*, 1140(3):215–50, 1993.

- [70] R. Rao and A. E. Senior. The properties of hybrid  $F_1$ -ATPase enzymes suggest that a cyclical catalytic mechanism involving three catalytic sites occurs. *J Biol Chem*, 262(36):17450–4, 1987.
- [71] T. M. Duncan, V. V. Bulygin, Y. Zhou, M. L. Hutcheon, and R. L. Cross. Rotation of subunits during catalysis by *Escherichia coli*  $F_1$ -ATPase. *Proc Natl Acad Sci USA*, 92(24):10964–8, 1995.
- [72] D. Sabbert, S. Engelbrecht, and W. Junge. Intersubunit rotation in active F-ATPase. *Nature*, 381(6583):623–5, 1996.
- [73] R. Yasuda, H. Noji, K. Kinosita Jr., and M. Yoshida.  $F_1$ -ATPase is a highly efficient molecular motor that rotates with discrete 120 degree steps. *Cell*, 93(7):1117–24, 1998.
- [74] R. Yasuda, H. Noji, M. Yoshida, K. Kinosita Jr., and H. Itoh. Resolution of distinct rotational substeps by submillisecond kinetic analysis of  $F_1$ -ATPases. *Nature*, 410(6831):898–904, 2001.
- [75] Y. Hirono-Hara, H. Noji, M. Nishiura, E. Muneyuki, K. Y. Hara, R. Yasuda, K. Kinosita Jr., and M. Yoshida. Pause and rotation of  $F_1$ -ATPase during catalysis. *Proc Natl Acad Sci USA*, 98(24):13649–54, 2001.
- [76] K. Adachi, H. Noji, and K. Kinosita Jr. Single-molecule imaging of rotation of  $F_1$ -ATPase. *Methods Enzymol*, 361:211–27, 2003.
- [77] M. Borsch, M. Diez, B. Zimmermann, R. Reuter, and P. Graber. Stepwise rotation of the gamma-subunit of  $EF_1F_o$ -ATP synthase observed by intramolecular single-molecule fluorescence resonance energy transfer. *FEBS Lett*, 527(1-3):147–52, 2002.
- [78] R. Yasuda, T. Masaike, K. Adachi, H. Noji, H. Itoh, and K. Kinosita Jr. The ATP-waiting conformation of rotating  $F_1$ -ATPase revealed by

- single-pair fluorescence resonance energy transfer. *Proc Natl Acad Sci USA*, 100(16):9314–8, 2003.
- [79] K. Kinosita Jr., R. Yasuda, and H. Noji. F<sub>1</sub>-ATPase: A highly efficient rotary ATP machine. *Essays Biochem*, 35:3–18, 2000.
- [80] K. Shimabukuro, R. Yasuda, E. Muneyuki, K. Y. Hara, K. Kinosita Jr., and M. Yoshida. Catalysis and rotation of F<sub>1</sub> motor: Cleavage of ATP at the catalytic site occurs in 1ms before 40 degree substep rotation. *Proc Natl Acad Sci USA*, 100(25):14731–6, 2003.
- [81] S. Furuike, K. Adachi, N. Sakaki, R. Shimo-Kon, H. Itoh, E. Muneyuki, M. Yoshida, and K. Kinosita Jr. Temperature dependence of the rotation and hydrolysis activities of F<sub>1</sub>-ATPase. *Biophys J*, 95(2):761–70, 2008.
- [82] Y. Hirono-Hara, K. Ishizuka, K. Kinosita Jr., M. Yoshida, and H. Noji. Activation of pausing F<sub>1</sub> motor by external force. *Proc Natl Acad Sci USA*, 102(12):4288–93, 2005.
- [83] Y. Rondelez, G. Tresset, T. Nakashima, Y. Kato-Yamada, H. Fujita, S. Takeuchi, and H. Noji. Highly coupled ATP synthesis by F<sub>1</sub>-ATPase single molecules. *Nature*, 433(7027):773–7, 2005.
- [84] H. Itoh, A. Takahashi, K. Adachi, H. Noji, R. Yasuda, M. Yoshida, and K. Kinosita. Mechanically driven ATP synthesis by F<sub>1</sub>-ATPase. *Nature*, 427(6973):465–8, 2004.
- [85] Y. Rondelez, G. Tresset, K. V. Tabata, H. Arata, H. Fujita, S. Takeuchi, and H. Noji. Microfabricated arrays of femtoliter chambers allow single molecule enzymology. *Nat Biotechnol*, 23(3):361–5, 2005.

- [86] R. Iino, Y. Rondelez, M. Yoshida, and H. Noji. Chemomechanical coupling in single-molecule F-type ATP synthase. *J Bioenerg Biomembr*, 37(6):451–4, 2005.
- [87] H. Omote, N. Sambonmatsu, K. Saito, Y. Sambongi, A. Iwamoto-Kihara, T. Yanagida, Y. Wada, and M. Futai. The gamma-subunit rotation and torque generation in F<sub>1</sub>-ATPase from wild-type or uncoupled mutant *Escherichia coli* end. *Proc Natl Acad Sci USA*, 96(14):7780–4, 1999.
- [88] H. Noji, K. Hasler, W. Junge, K. Kinosita Jr., M. Yoshida, and S. Engelbrecht. Rotation of *Escherichia coli* F<sub>1</sub>-ATPase. *Biochem Biophys Res Commun*, 260(3):597–9, 1999.
- [89] T. Hisabori, A. Kondoh, and M. Yoshida. The gamma subunit in chloroplast F<sub>1</sub>-ATPase can rotate in a unidirectional and counterclockwise manner. *FEBS Lett*, 463(1-2):35–8, 1999.
- [90] H. Konno, T. Murakami-Fuse, F. Fujii, F. Koyama, H. Ueoka-Nakanishi, C. G. Pack, M. Kinjo, and T. Hisabori. The regulator of the F<sub>1</sub> motor: Inhibition of rotation of cyanobacterial F<sub>1</sub>-ATPase by the epsilon subunit. *EMBO J*, 25(19):4596–604, 2006.
- [91] E. Meiss, H. Konno, G. Groth, and T. Hisabori. Molecular processes of inhibition and stimulation of ATP synthase caused by the phytotoxin tentoxin. *J Biol Chem*, 283(36):24594–9, 2008.
- [92] M. Nakanishi-Matsui, S. Kashiwagi, H. Hosokawa, D. J. Cipriano, S. D. Dunn, Y. Wada, and M. Futai. Stochastic high-speed rotation of *Escherichia coli* ATP synthase F<sub>1</sub> sector: The epsilon subunit-sensitive rotation. *J Biol Chem*, 281(7):4126–31, 2006.

- [93] R. Watanabe, R. Iino, K. Shimabukuro, M. Yoshida, and H. Noji. Temperature-sensitive reaction intermediate of  $F_1$ -ATPase. *EMBO Rep*, 9(1):84–90, 2008.
- [94] G. Kaim, M. Prummer, B. Sick, G. Zumofen, A. Renn, U. P. Wild, and P. Dimroth. Coupled rotation within single  $F_1F_o$  enzyme complexes during ATP synthesis or hydrolysis. *FEBS Lett*, 525(1-3):156–63, 2002.
- [95] M. Diez, B. Zimmermann, M. Borsch, M. Konig, E. Schweinberger, S. Steigmiller, R. Reuter, S. Felekyan, V. Kudryavtsev, C. A. Seidel, and P. Graber. Proton-powered subunit rotation in single membrane-bound  $F_1F_o$ -ATP synthase. *Nat Struct Mol Biol*, 11(2):135–41, 2004.
- [96] Y. Sambongi, Y. Iko, M. Tanabe, H. Omote, A. Iwamoto-Kihara, I. Ueda, T. Yanagida, Y. Wada, and M. Futai. Mechanical rotation of the c subunit oligomer in ATP synthase ( $F_1F_o$ ): Direct observation. *Science*, 286(5445):1722–4, 1999.
- [97] S. P. Tsunoda, R. Aggeler, H. Noji, K. Kinosita Jr., M. Yoshida, and R. A. Capaldi. Observations of rotation within the  $F_1F_o$ -ATP synthase: Deciding between rotation of the  $F_o$  c subunit ring and artifact. *FEBS Lett*, 470(3):244–8, 2000.
- [98] M. Tanabe, K. Nishio, Y. Iko, Y. Sambongi, A. Iwamoto-Kihara, Y. Wada, and M. Futai. Rotation of a complex of the gamma subunit and c ring of *Escherichia coli* ATP synthase. The rotor and stator are interchangeable. *J Biol Chem*, 276(18):15269–74, 2001.
- [99] O. Panke, D. A. Cherepanov, K. Gumbiowski, S. Engelbrecht, and W. Junge. Viscoelastic dynamics of actin filaments coupled to rotary F-ATPase: Angular torque profile of the enzyme. *Biophys J*, 81(3):1220–33, 2001.

- [100] H. Ueno, T. Suzuki, K. Kinoshita Jr., and M. Yoshida. ATP-driven stepwise rotation of  $F_1F_o$ -ATP synthase. *Proc Natl Acad Sci USA*, 102(5):1333–8, 2005.
- [101] H. Sielaff, H. Rennekamp, S. Engelbrecht, and W. Junge. Functional halt positions of rotary  $F_1F_o$ -ATPase correlated with crystal structures. *Biophys J*, 95(10):4979–87, 2008.
- [102] D. J. Hyndman, Y. M. Milgrom, E. A. Bramhall, and R. L. Cross. Nucleotide-binding sites on *Escherichia coli*  $F_1$ -ATPase. Specificity of noncatalytic sites and inhibition at catalytic sites by MgADP. *J Biol Chem*, 269(46):28871–7, 1994.
- [103] M. J. van Raaij, J. P. Abrahams, A. G. Leslie, and J. E. Walker. The structure of bovine  $F_1$ -ATPase complexed with the antibiotic inhibitor aurovertin B. *Proc Natl Acad Sci USA*, 93(14):6913–7, 1996.
- [104] J. P. Abrahams, S. K. Buchanan, M. J. Van Raaij, I. M. Fearnley, A. G. Leslie, and J. E. Walker. The structure of bovine  $F_1$ -ATPase complexed with the peptide antibiotic efrapeptin. *Proc Natl Acad Sci USA*, 93(18):9420–4, 1996.
- [105] G. L. Orriss, A. G. Leslie, K. Braig, and J. E. Walker. Bovine  $F_1$ -ATPase covalently inhibited with 4-chloro-7-nitrobenzofurazan: The structure provides further support for a rotary catalytic mechanism. *Structure*, 6(7):831–7, 1998.
- [106] K. Braig, R. I. Menz, M. G. Montgomery, A. G. Leslie, and J. E. Walker. Structure of bovine mitochondrial  $F_1$ -ATPase inhibited by  $Mg^{2+}$ ADP and aluminium fluoride. *Structure*, 8(6):567–73, 2000.
- [107] C. Gibbons, M. G. Montgomery, A. G. Leslie, and J. E. Walker. The structure of the central stalk in bovine  $F_1$ -ATPase at 2.4Å resolution. *Nat Struct Biol*, 7(11):1055–61, 2000.

- [108] R. I. Menz, J. E. Walker, and A. G. Leslie. Structure of bovine mitochondrial F<sub>1</sub>-ATPase with nucleotide bound to all three catalytic sites: Implications for the mechanism of rotary catalysis. *Cell*, 106(3): 331–41, 2001.
- [109] E. Cabezon, M. G. Montgomery, A. G. Leslie, and J. E. Walker. The structure of bovine F<sub>1</sub>-ATPase in complex with its regulatory protein IF<sub>1</sub>. *Nat Struct Biol*, 10(9):744–50, 2003.
- [110] R. Kagawa, M. G. Montgomery, K. Braig, A. G. Leslie, and J. E. Walker. The structure of bovine F<sub>1</sub>-ATPase inhibited by ADP and beryllium fluoride. *EMBO J*, 23(14):2734–44, 2004.
- [111] M. W. Bowler, M. G. Montgomery, A. G. Leslie, and J. E. Walker. Ground state structure of F<sub>1</sub>-ATPase from bovine heart mitochondria at 1.9Å resolution. *J Biol Chem*, 282(19):14238–42, 2007.
- [112] W. L. Delano. The PyMOL molecular graphics system, 2008.
- [113] J. E. Walker, M. Saraste, M. J. Runswick, and N. J. Gay. Distantly related sequences in the alpha- and beta-subunits of ATP synthase, myosin, kinases and other ATP-requiring enzymes and a common nucleotide binding fold. *EMBO J*, 1(8):945–51, 1982.
- [114] N. Sakaki, R. Shimo-Kon, K. Adachi, H. Itoh, S. Furuike, E. Muneyuki, M. Yoshida, and K. Kinosita Jr. One rotary mechanism for F<sub>1</sub>-ATPase over ATP concentrations from millimolar down to nanomolar. *Biophys J*, 88(3):2047–56, 2005.
- [115] K. Y. Hara, H. Noji, D. Bald, R. Yasuda, K. Kinosita Jr., and M. Yoshida. The role of the DELSEED motif of the beta subunit in rotation of F<sub>1</sub>-ATPase. *J Biol Chem*, 275(19):14260–3, 2000.

- [116] K. Y. Hara, Y. Kato-Yamada, Y. Kikuchi, T. Hisabori, and M. Yoshida. The role of the betaDELSEED motif of F<sub>1</sub>-ATPase: Propagation of the inhibitory effect of the epsilon subunit. *J Biol Chem*, 276(26):23969–73, 2001.
- [117] M. Clamp, J. Cuff, S. M. Searle, and G. J. Barton. The Jalview Java alignment editor. *Bioinformatics*, 20(3):426–7, 2004.
- [118] M. W. Bowler, M. G. Montgomery, A. G. Leslie, and J. E. Walker. How azide inhibits ATP hydrolysis by the F-ATPases. *Proc Natl Acad Sci USA*, 103(23):8646–9, 2006.
- [119] D. Okuno, R. Fujisawa, R. Iino, Y. Hirono-Hara, H. Imamura, and H. Noji. Correlation between the conformational states of F<sub>1</sub>-ATPase as determined from its crystal structure and single-molecule rotation. *Proc Natl Acad Sci USA*, 105(52):20722–7, 2008.
- [120] A. C. Hausrath, G. Gruber, B. W. Matthews, and R. A. Capaldi. Structural features of the gamma subunit of the *Escherichia coli* F<sub>1</sub>-ATPase revealed by a 4.4Å resolution map obtained by x-ray crystallography. *Proc Natl Acad Sci USA*, 96(24):13697–702, 1999.
- [121] A. C. Hausrath, R. A. Capaldi, and B. W. Matthews. The conformation of the epsilon- and gamma-subunits within the *Escherichia coli* F<sub>1</sub>-ATPase. *J Biol Chem*, 276(50):47227–32, 2001.
- [122] K. Adachi, K. Oiwa, T. Nishizaka, S. Furuike, H. Noji, H. Itoh, M. Yoshida, and K. Kinosita Jr. Coupling of rotation and catalysis in F<sub>1</sub>-ATPase revealed by single-molecule imaging and manipulation. *Cell*, 130(2):309–21, 2007.
- [123] T. Nishizaka, K. Oiwa, H. Noji, S. Kimura, E. Muneyuki, M. Yoshida, and K. Kinosita Jr. Chemomechanical coupling in F<sub>1</sub>-ATPase revealed

- by simultaneous observation of nucleotide kinetics and rotation. *Nat Struct Mol Biol*, 11(2):142–8, 2004.
- [124] H. Yagi, K. Tozawa, N. Sekino, T. Iwabuchi, M. Yoshida, and H. Akutsu. Functional conformation changes in the TF<sub>1</sub>-ATPase beta subunit probed by 12 tyrosine residues. *Biophys J*, 77(4):2175–83, 1999.
- [125] Y. Shirakihara, A. G. Leslie, J. P. Abrahams, J. E. Walker, T. Ueda, Y. Sekimoto, M. Kambara, K. Saika, Y. Kagawa, and M. Yoshida. The crystal structure of the nucleotide-free  $\alpha_3\beta_3$  subcomplex of F<sub>1</sub>-ATPase from the thermophilic *Bacillus* PS3 is a symmetric trimer. *Structure*, 5(6):825–36, 1997.
- [126] H. Wang and G. Oster. Energy transduction in the F<sub>1</sub> motor of ATP synthase. *Nature*, 396(6708):279–82, 1998.
- [127] G. Oster and H. Wang. Reverse engineering a protein: The mechanochemistry of ATP synthase. *Biochim Biophys Acta*, 1458(2-3):482–510, 2000.
- [128] K. Kinosita Jr., K. Adachi, and H. Itoh. Rotation of F<sub>1</sub>-ATPase: How an ATP-driven molecular machine may work. *Annu Rev Biophys Biomol Struct*, 33:245–68, 2004.
- [129] I. Antes, D. Chandler, H. Wang, and G. Oster. The unbinding of ATP from F<sub>1</sub>-ATPase. *Biophys J*, 85(2):695–706, 2003.
- [130] J. Xing, J. C. Liao, and G. Oster. Making ATP. *Proc Natl Acad Sci USA*, 102(46):16539–46, 2005.
- [131] T. Masaike, E. Muneyuki, H. Noji, K. Kinosita Jr., and M. Yoshida. F<sub>1</sub>-ATPase changes its conformations upon phosphate release. *J Biol Chem*, 277(24):21643–9, 2002.

## BIBLIOGRAPHY

---

- [132] K. Kinosita Jr., R. Yasuda, H. Noji, and K. Adachi. A rotary molecular motor that can work at near 100% efficiency. *Philos Trans R Soc Lond B Biol Sci*, 355(1396):473–89, 2000.
- [133] R. E. Thompson, D. R. Larson, and W. W. Webb. Precise nanometer localization analysis for individual fluorescent probes. *Biophys J*, 82(5):2775–83, 2002.
- [134] K. Adachi, R. Yasuda, H. Noji, H. Itoh, Y. Harada, M. Yoshida, and K. Kinosita Jr. Stepping rotation of F<sub>1</sub>-ATPase visualized through angle-resolved single-fluorophore imaging. *Proc Natl Acad Sci USA*, 97(13):7243–7, 2000.
- [135] K. C. Neuman and S. M. Block. Optical trapping. *Rev Sci Instrum*, 75(9):2787–809, 2004.
- [136] F. Gittes and C. F. Schmidt. Interference model for back-focal-plane displacement detection in optical tweezers. *Opt Lett*, 23(1):7–9, 1998.
- [137] D. J. Muller. AFM: A nanotool in membrane biology. *Biochemistry*, 47(31):7986–98, 2008.
- [138] R. M. Berry, L. Turner, and H. C. Berg. Mechanical limits of bacterial flagellar motors probed by electrorotation. *Biophys J*, 69(1):280–6, 1995.
- [139] Y. Harada, O. Ohara, A. Takatsuki, H. Itoh, N. Shimamoto, and K. Kinosita Jr. Direct observation of DNA rotation during transcription by *Escherichia coli* RNA polymerase. *Nature*, 409(6816):113–5, 2001.
- [140] A Ashkin. Acceleration and trapping of particles by radiation pressure. *Phys. Rev. Lett.*, 24(4):156–159, 1970.
- [141] A. Ashkin and J. M. Dziedzic. Optical trapping and manipulation of viruses and bacteria. *Science*, 235(4795):1517–20, 1987.

## BIBLIOGRAPHY

---

- [142] A. Ashkin, J. M. Dziedzic, and T. Yamane. Optical trapping and manipulation of single cells using infrared laser beams. *Nature*, 330(6150):769–71, 1987.
- [143] T. A. Nieminen, G. Knoner, N. R. Heckenberg, and H. Rubinsztein-Dunlop. Physics of optical tweezers. *Methods Cell Biol*, 82:207–36, 2007.
- [144] S. C. Kuo and M. P. Sheetz. Force of single kinesin molecules measured with optical tweezers. *Science*, 260(5105):232–4, 1993.
- [145] K. Svoboda and S. M. Block. Force and velocity measured for single kinesin molecules. *Cell*, 77(5):773–84, 1994.
- [146] K. Visscher, M. J. Schnitzer, and S. M. Block. Single kinesin molecules studied with a molecular force clamp. *Nature*, 400(6740):184–9, 1999.
- [147] M. J. Lang, C. L. Asbury, J. W. Shaevitz, and S. M. Block. An automated two-dimensional optical force clamp for single molecule studies. *Biophys J*, 83(1):491–501, 2002.
- [148] R. M. Simmons, J. T. Finer, H. M. Warrick, B. Kralik, S. Chu, and J. A. Spudich. Force on single actin filaments in a motility assay measured with an optical trap. *Adv Exp Med Biol*, 332:331–6; discussion 336–7, 1993.
- [149] C. Veigel, F. Wang, M. L. Bartoo, J. R. Sellers, and J. E. Molloy. The gated gait of the processive molecular motor, myosin V. *Nat Cell Biol*, 4(1):59–65, 2002.
- [150] C. Veigel, S. Schmitz, F. Wang, and J. R. Sellers. Load-dependent kinetics of myosin-V can explain its high processivity. *Nat Cell Biol*, 7(9):861–9, 2005.

## BIBLIOGRAPHY

---

- [151] R. M. Berry and H. C. Berg. Absence of a barrier to backwards rotation of the bacterial flagellar motor demonstrated with optical tweezers. *Proc Natl Acad Sci USA*, 94(26):14433–7, 1997.
- [152] John Bechhoefer. Feedback for physicists: A tutorial essay on control. *Rev. Mod. Phys.*, 77(3):783–836, 2005.
- [153] D. J. Klionsky, W. S. Brusilow, and R. D. Simoni. In vivo evidence for the role of the epsilon subunit as an inhibitor of the proton-translocating ATPase of *Escherichia coli*. *J Bacteriol*, 160(3):1055–60, 1984.
- [154] H. Hartman, M. Syvanen, and B. B. Buchanan. Contrasting evolutionary histories of chloroplast thioredoxins f and m. *Mol Biol Evol*, 7(3):247–54, 1990.
- [155] J. B. Sumner. A method for the colorimetric determination of phosphorus. *Science*, 100(2601):413–414, 1944.
- [156] M. E. Pullman, H. S. Penefsky, A. Datta, and E. Racker. Partial resolution of the enzymes catalyzing oxidative phosphorylation. I. purification and properties of soluble dinitrophenol-stimulated adenosine triphosphatase. *J Biol Chem*, 235:3322–9, 1960.
- [157] H. S. Penefsky, M. E. Pullman, A. Datta, and E. Racker. Partial resolution of the enzymes catalyzing oxidative phosphorylation. II. participation of a soluble adenosine triphosphatase in oxidative phosphorylation. *J Biol Chem*, 235:3330–6, 1960.
- [158] Y. Zhang, O. Marcillat, C. Giulivi, L. Ernster, and K. J. Davies. The oxidative inactivation of mitochondrial electron transport chain components and ATPase. *J Biol Chem*, 265(27):16330–6, 1990.

- [159] T. Cha, A. Guo, and X. Y. Zhu. Enzymatic activity on a chip: The critical role of protein orientation. *Proteomics*, 5(2):416–9, 2005.
- [160] T. Pilizota, T. Bilyard, F. Bai, M. Futai, H. Hosokawa, and R. M. Berry. A programmable optical angle clamp for rotary molecular motors. *Biophys J*, 93(1):264–75, 2007.
- [161] T. Sano, S. Vajda, and C. R. Cantor. Genetic engineering of streptavidin, a versatile affinity tag. *J Chromatogr B Biomed Sci Appl*, 715(1):85–91, 1998.
- [162] A. Holmberg, A. Blomstergren, O. Nord, M. Lukacs, J. Lundberg, and M. Uhlen. The biotin-streptavidin interaction can be reversibly broken using water at elevated temperatures. *Electrophoresis*, 26(3):501–10, 2005.
- [163] U. Bohme and U. Scheler. Effective charge of polyelectrolytes as a function of the dielectric constant of a solution. *J Colloid Interface Sci*, 309(2):231–5, 2007.
- [164] J. Y. Yoon, H. Y. Park, J. H. Kim, and W. S. Kim. Adsorption of BSA on highly carboxylated microspheres - quantitative effects of surface functional groups and interaction forces. *Journal of Colloid and Interface Science*, 177(2):613–620, 1996.
- [165] J. Y. Yoon, J. H. Kim, and W. S. Kim. Interpretation of protein adsorption phenomena onto functional microspheres. *Colloids and Surfaces B-Biointerfaces*, 12(1):15–22, 1998.
- [166] J. Y. Yoon, J. H. Kim, and W. S. Kim. The relationship of interaction forces in the protein adsorption onto polymeric microspheres. *Colloids and Surfaces a-Physicochemical and Engineering Aspects*, 153(1-3):413–419, 1999.

- [167] J. Hu, S. J. Li, and B. L. Liu. Adsorption of BSA onto sulfonated microspheres. *Biochemical Engineering Journal*, 23(3):259–263, 2005.
- [168] S. Lata, A. Reichel, R. Brock, R. Tampe, and J. Piehler. High-affinity adaptors for switchable recognition of histidine-tagged proteins. *J Am Chem Soc*, 127(29):10205–15, 2005.
- [169] J. Happel and H. Brenner. *Low Reynolds Number Hydrodynamics*. Martinus Nijhoff Publishers, The Hague, 1963.
- [170] K. Svoboda and S. M. Block. Biological applications of optical forces. *Annu Rev Biophys Biomol Struct*, 23:247–85, 1994.
- [171] J. Weber, S. Wilke-Mounts, R. S. Lee, E. Grell, and A. E. Senior. Specific placement of tryptophan in the catalytic sites of *Escherichia coli* F<sub>1</sub>-ATPase provides a direct probe of nucleotide binding: Maximal ATP hydrolysis occurs with three sites occupied. *J Biol Chem*, 268(27):20126–33, 1993.
- [172] M. K. al Shawi and A. E. Senior. Catalytic sites of *Escherichia coli* F<sub>1</sub>-ATPase. Characterization of unisite catalysis at varied pH. *Biochemistry*, 31(3):878–85, 1992.
- [173] A. E. Senior, S. Nadanaciva, and J. Weber. The molecular mechanism of ATP synthesis by F<sub>1</sub>F<sub>0</sub>-ATP synthase. *Biochim Biophys Acta*, 1553(3):188–211, 2002.
- [174] A. Cornish-Bowden. A simple graphical method for determining the inhibition constants of mixed, uncompetitive and non-competitive inhibitors. *Biochem J*, 137(1):143–4, 1974.
- [175] J. Weber and A. E. Senior. Bi-site catalysis in F<sub>1</sub>-ATPase: Does it exist? *J Biol Chem*, 276(38):35422–8, 2001.

- [176] S. H. Chung and R. A. Kennedy. Forward-backward non-linear filtering technique for extracting small biological signals from noise. *J Neurosci Methods*, 40(1):71–86, 1991.
- [177] M. Nakanishi-Matsui, S. Kashiwagi, T. Ubukata, A. Iwamoto-Kihara, Y. Wada, and M. Futai. Rotational catalysis of *Escherichia coli* ATP synthase F<sub>1</sub> sector. Stochastic fluctuation and a key domain of the beta subunit. *J Biol Chem*, 282(28):20698–704, 2007.
- [178] S. Kashiwagi, A. Iwamoto-Kihara, M. Kojima, T. Nonaka, M. Futai, and M. Nakanishi-Matsui. Effects of mutations in the beta subunit hinge domain on ATP synthase F<sub>1</sub> sector rotation: Interaction between Ser 174 and Ile 163. *Biochem Biophys Res Commun*, 365(2):227–31, 2008.
- [179] H. Kanazawa, Y. Horiuchi, M. Takagi, Y. Ishino, and M. Futai. Coupling factor F<sub>1</sub>-ATPase with defective beta subunit from a mutant of *Escherichia coli*. *J Biochem*, 88(3):695–703, 1980.
- [180] M. K. Al-Shawi, D. Parsonage, and A. E. Senior. Directed mutagenesis of the strongly conserved aspartate 242 in the beta-subunit of *Escherichia coli* proton-ATPase. *J Biol Chem*, 263(36):19633–9, 1988.
- [181] D. M. Mueller, N. Puri, V. Kabaleeswaran, C. Terry, A. G. Leslie, and J. E. Walker. Ni-chelate-affinity purification and crystallization of the yeast mitochondrial F<sub>1</sub>-ATPase. *Protein Expr Purif*, 37(2):479–85, 2004.
- [182] D. M. Mueller, N. Puri, V. Kabaleeswaran, C. Terry, A. G. Leslie, and J. E. Walker. Crystallization and preliminary crystallographic studies of the mitochondrial F<sub>1</sub>-ATPase from the yeast *Saccharomyces cerevisiae*. *Acta Crystallogr D Biol Crystallogr*, 60(Pt 8):1441–4, 2004.

## BIBLIOGRAPHY

---

- [183] T. Pilizota. *A Programmable Optical Angle Clamp for Rotary Molecular Motors*. PhD thesis, Oxford University, 2007.
- [184] O. Beja, L. Aravind, E. V. Koonin, M. T. Suzuki, A. Hadd, L. P. Nguyen, S. B. Jovanovich, C. M. Gates, R. A. Feldman, J. L. Spudich, E. N. Spudich, and E. F. DeLong. Bacterial rhodopsin: Evidence for a new type of phototrophy in the sea. *Science*, 289(5486):1902–6, 2000.
- [185] O. Beja, E. N. Spudich, J. L. Spudich, M. Leclerc, and E. F. DeLong. Proteorhodopsin phototrophy in the ocean. *Nature*, 411(6839):786–9, 2001.
- [186] A. Martinez, A. S. Bradley, J. R. Waldbauer, R. E. Summons, and E. F. DeLong. Proteorhodopsin photosystem gene expression enables photophosphorylation in a heterologous host. *Proc Natl Acad Sci USA*, 104(13):5590–5, 2007.
- [187] S. Bayouth, T. A. Nieminen, N. R. Heckenberg, and H. Rubinsztein-Dunlop. Orientation of biological cells using plane-polarized gaussian beam optical tweezers. *Journal of Modern Optics*, 50(10):1581–1590, 2003.
- [188] A. I. Bishop, T. A. Nieminen, N. R. Heckenberg, and H. Rubinsztein-Dunlop. Optical application and measurement of torque on microparticles of isotropic nonabsorbing material. *Physical Review A*, 68(3):–, 2003.
- [189] Y. Harada, K. Sakurada, T. Aoki, D. D. Thomas, and T. Yanagida. Mechanochemical coupling in actomyosin energy transduction studied by invitro movement assay. *Journal of Molecular Biology*, 216(1):49–68, 1990.
- [190] M. K. Al-Shawi, C. J. Ketchum, and R. K. Nakamoto. Energy coupling, turnover, and stability of the  $F_1F_o$  ATP synthase are dependent

- on the energy of interaction between gamma and beta subunits. *J Biol Chem*, 272(4):2300–6, 1997.
- [191] S. Lata, M. Gavutis, R. Tampe, and J. Piehler. Specific and stable fluorescence labeling of histidine-tagged proteins for dissecting multi-protein complex formation. *J Am Chem Soc*, 128(7):2365–72, 2006.
- [192] R. P. Goodman, I. A. Schaap, C. F. Tardin, C. M. Erben, R. M. Berry, C. F. Schmidt, and A. J. Turberfield. Rapid chiral assembly of rigid DNA building blocks for molecular nanofabrication. *Science*, 310(5754):1661–5, 2005.
- [193] C. M. Erben, R. P. Goodman, and A. J. Turberfield. Single-molecule protein encapsulation in a rigid DNA cage. *Angew Chem Int Ed Engl*, 45(44):7414–7, 2006.
- [194] C. M. Erben, R. P. Goodman, and A. J. Turberfield. A self-assembled DNA bipyramid. *J Am Chem Soc*, 129(22):6992–3, 2007.
- [195] R. P. Goodman, M. Heilemann, S. Doose, C. M. Erben, A. N. Kapanidis, and A. J. Turberfield. Reconfigurable, braced, three-dimensional DNA nanostructures. *Nat Nanotechnol*, 3(2):93–6, 2008.
- [196] R. P. Goodman, C. Erben, J. Malo, W. M. Ho, A. N. Kapanidis, and A. J. Turberfield. A facile method for reversibly linking a recombinant protein to DNA, 2009.
- [197] J. Malo, J. C. Mitchell, C. Venien-Bryan, J. R. Harris, H. Wille, D. J. Sherratt, and A. J. Turberfield. Engineering a 2D protein-DNA crystal. *Angew Chem Int Ed Engl*, 44(20):3057–61, 2005.
- [198] P. W. Rothemund. Folding DNA to create nanoscale shapes and patterns. *Nature*, 440(7082):297–302, 2006.

- [199] M. F. Hagan and A. K. Chakraborty. Hybridization dynamics of surface immobilized DNA. *Journal of Chemical Physics*, 120(10):4958–4968, 2004.
- [200] A. W. Peterson, R. J. Heaton, and R. M. Georgiadis. The effect of surface probe density on DNA hybridization. *Nucleic Acids Res*, 29(24):5163–8, 2001.
- [201] R. J. Heaton, A. W. Peterson, and R. M. Georgiadis. Electrostatic surface plasmon resonance: Direct electric field-induced hybridization and denaturation in monolayer nucleic acid films and label-free discrimination of base mismatches. *Proc Natl Acad Sci USA*, 98(7):3701–4, 2001.
- [202] A. J. Heron, J. R. Thompson, A. E. Mason, and M. I. Wallace. Direct detection of membrane channels from gels using water-in-oil droplet bilayers. *J Am Chem Soc*, 129(51):16042–7, 2007.
- [203] O. H. Lowry, N. J. Rosebrough, A. L. Farr, and R. J. Randall. Protein measurement with the folin phenol reagent. *J Biol Chem*, 193(1):265–75, 1951.
- [204] William H. Press. *Numerical Recipes in C++ : The Art of Scientific Computing*. Cambridge University Press, Cambridge, 2nd edition, 2002.
- [205] J. A. Nelder and R. Mead. A simplex-method for function minimization. *Computer Journal*, 7(4):308–313, 1965.
- [206] Yonathan Bard. *Nonlinear Parameter Estimation*. Academic Press, New York, 1974.